Three-pion dynamics at COMPASS: resonances, rescattering and non-resonant processes

Dissertation

zur

Erlangung des Doktorgrades (Dr. rer. nat.)

der

Mathematisch-Naturwissenschaftlichen Fakultät

der

Rheinischen Friedrich-Wilhelms-Universität Bonn

von

Mikhail Mikhasenko

aus

Verkhnyaya Salda, Russia

Bonn, 2019

Abstract

This thesis presents studies of the strong interaction in the non-perturbative regime by analyzing the properties of hadronic resonances. The basis for this research is the world's largest dataset on diffractive reactions, especially the $\pi^- p \to \pi^- \pi^+ \pi^- p$ channel with about $50\,\mathrm{M}$ events, measured with a high-energy pion beam by the COMPASS experiment at the CERN Super Proton Synchrotron. The three-pion final state couples to a variety of light isovector resonances, many of which are still poorly understood. Among these are a ground axial-vector state $a_1(1260)$, and the spin-exotic $\pi_1(1600)$ that is a prime candidate for the lightest hybrid meson with explicit gluonic degrees of freedom. Recently, a new resonance-like signal with axial-vector quantum numbers was reported by COMPASS at a mass of $1420\,\mathrm{MeV}$ and called $a_1(1420)$. This state, if confirmed, is to be regarded as a candidate for a light tetraquark or molecular state because of its proximity to the $a_1(1260)$ ground state. In order to disentangle the different spin-parity contributions to a given final state, a partial-wave analysis (PWA) of the data in small bins of the 3π invariant mass and of the momentum transfer squared t is performed. The results of this analysis are spin-density matrix elements, whose mass and t-dependences are subjected to phenomenological analysis to extract resonance parameters. We introduce the PWA technique and discuss several methods to obtain the resonance parameters. Instead of the traditional approach of coherently adding Breit-Wigner amplitudes, which violate the fundamental principle of unitarity, we study models that incorporate the unitarity constraints by construction and enable us to minimize systematic uncertainties of the pole positions of resonances.

Other effects which are traditionally ignored in the analyses are final-state interactions of the hadrons produced in the reaction. Due to the high energy of the beam particle, these effects are usually considered negligible. We show, however, that they do become important given the large datasets available. A distinct feature of the three-hadron final state that is not present in two-hadron final states is cross-channel rescattering. We find that a peculiar rescattering from $K^*\bar{K} \to f_0\pi$ in a triangle loop produces a resonance-like signal with exactly the mass and width of the new $a_1(1420)$. We calculate the amplitude for this and other rescattering processes using different techniques and demonstrate that the final-state-interaction hypothesis is consistent with the COMPASS observations. A simple approach applied to the data is matched to the unitarity-based dispersive framework, known as the Khuri-Treiman model, which gives access to the "higher orders" of the rescattering corrections beyond the triangle graph.

In diffractive reactions, an additional complication arises from a coherent physical background due to non-resonant production of the 3π system, the main part of which is the so-called Deck effect. We reveal its features using the COMPASS data and compare several theoretical models to describe it. This background accounts for a large fraction of the intensity in several important waves and has been one of the reasons for the poor knowledge of the $a_1(1260)$ from diffractive reactions. In order to obtain an independent extraction of a_1 pole parameters, we study the hadronic decays of τ-leptons from e^+e^- collisions, $\tau \to \pi^-\pi^+\pi^- \nu_\tau$, using data of the ALEPH experiment. In this case, the 3π-interaction is dominated by the $a_1(1260)$. Applying our unitarity approach we construct a K-matrix-based model and successfully extract the pole position of the $a_1(1260)$ for the first time.

Finally, using the S-matrix unitarity constraints for the system of three particles we derive a unified framework which combines the resonance physics (the short-range interaction) and the rescattering phenomena (the long-range exchanges). A factorization inspired by the Khuri-Treiman approach leads to a simplification of the three-body unitarity constraints and permits us to build a K-matrix-like model for the resonance physics with the rescattering terms entering the self-energy function.

Parts of this thesis have been published in the following articles:

- M. Mikhasenko, B. Ketzer, and A. Sarantsev, *Nature of the $a_1(1420)$*, Phys. Rev. **D91**.9 (2015) 094015, arXiv: `1501.07023` [hep-ph]

- M. Mikhasenko et al., *Pole position of the $a_1(1260)$ from τ-decay*, Phys. Rev. **D98**.9 (2018) 096021, arXiv: `1810.00016` [hep-ph]

- M. Aghasyan et al., *Light isovector resonances in $\pi^- p \to \pi^- \pi^- \pi^+ p$ at 190 GeV/c*, Phys. Rev. **D98**.9 (2018) 092003, arXiv: `1802.05913` [hep-ex]

- A. Jackura et al., *New analysis of $\eta\pi$ tensor resonances measured at the COMPASS experiment*, Phys. Lett. **B779** (2018) 464, arXiv: `1707.02848` [hep-ph]

Chapter 5 are Chapter 7 are being drafted for the publication during preparation of the thesis. The latter was published shortly after the thesis submission.

- M. Mikhasenko et al., *Three-body scattering: Ladders and Resonances*, JHEP **08** (2019) 080, arXiv: `1904.11894` [hep-ph]

Equations derived in Appendix C.3 were extended for particles with spin and published shortly after the thesis submission.

- M. Mikhasenko et al., *Dalitz-plot decomposition for three-body decays*, (2019), arXiv: `1910.04566` [hep-ph]

Some material of this work was presented at conferences and entered the proceedings:

- M. Mikhasenko et al., *Unitarity approach to the mass-dependent fit of 3π resonance production data from the COMPASS experiment*, EPJ Web Conf. **137** (2017) 05017

- M. Mikhasenko and B. Ketzer, *Beyond the isobar model: Rescattering in the system of three particles.*, PoS **BORMIO2016** (2016) 024

Some pieces of research that did not enter the thesis,

- M. Mikhasenko et al., *What is the right formalism to search for resonances?*, Eur. Phys. J. **C78**.3 (2018) 229, arXiv: `1712.02815` [hep-ph]

- M. Mikhasenko, *A triangle singularity and the LHCb pentaquarks*, (2015), arXiv: `1507.06552` [hep-ph]

Several other works with a significant personal contribution:

- J. Nys et al., *Features of $\pi\Delta$ Photoproduction at High Energies*, Phys. Lett. **B779** (2018) 77, arXiv: `1710.09394` [hep-ph]

- A. Rodas et al., *Determination of the pole position of the lightest hybrid meson candidate*, accepted by PRL (2018), arXiv: `1810.04171` [hep-ph]

- A. Pilloni et al., *What is the right formalism to search for resonances? II. The pentaquark chain*, Eur. Phys. J. **C78**.9 (2018) 727, arXiv: `1805.02113` [hep-ph]

- A. Jackura et al., *Phenomenology of Relativistic $3 \to 3$ Reaction Amplitudes within the Isobar Approximation*, (2018), arXiv: `1809.10523 [hep-ph]`

- M. Albaladejo et al., *Khuri–Treiman equations for $\pi\pi$ scattering*, Eur. Phys. J. **C78**.7 (2018) 574, arXiv: `1803.06027 [hep-ph]`

- A. Pilloni et al., *Amplitude analysis and the nature of the $Z_c(3900)$*, Phys. Lett. **B772** (2017) 200, arXiv: `1612.06490 [hep-ph]`

Acknowledgements

This thesis represents the combined effort of a number of people. For this reason, I have chosen to write it in first person plural. However, in the acknowledgments, I will be speaking solely about my experience and the people in my life who have made undertaking and completing this work possible.

First and foremost, I wish to express my heartfelt thanks to my advisor Bernhard Ketzer. Joining his group at Bonn was the most fortunate occurrence in my scientific life. Being actively involved in the COMPASS experiment, Bernhard opened a wide spectrum of possibilities for me: from hardware development to field-theoretical calculations. He was always open-minded and very supportive for new ideas. His high-class scientific attitude is inspiring. I am very glad that despite him being a hard-worker, he finds time for his lovely family and outside interests. His example is motivating me in pursuing a scientific carrier. I would also like to thank Bernhard for taking a great care about me and my wife just after our movement to the first foreign country.

I am indebted to Adam Szczepaniak who practically was my joined adviser. I am thankful for a chance to be a part of the Joint Physics Analysis Center lead and educated by Adam. Our Late-Tuesday meetings were always such an enormous dose of knowledge that takes the rest of the week to digest. The life speed and productivity of Adam seem to me the highest bar which can only be achieved asymptotically.

I want to thank my JPAC colleagues who become my big friends: Alessandro Pilloni, Andrew Jackura, Miguel Albaladejo, Cesar Fernández-Ramírez, Vincent Mathieu, Jannes Nys, and Arkaitz Rodas. It was a great pleasure to work in the nice group with these outstanding young professionals who share my interests and enthusiasm in solving physics riddles. Special thanks to Andrew Jackura, with whom I could always share my indignation of the difficulties of some equations and problems that I stumbled by. Many thanks to Alessandro Pilloni who is the most glorious and easy-to-work with colleague I had a chance to collaborate.

My sincere gratitude is reserved for my former advisers which gave me initial inspiration and the basis, on which the further knowledge could adhere. I am indebted to Anatoly Konstantinovich Likhoded for explaining to me that the best way to learn something is start working on a practical problem. He told that the difficult questions can only be solved by a scrupulous work, by a slow and consecutive unwinding the tangle. I thank him for always believing in me. Alexander Mikhailovich Zaitzev was the first who started planting the knowledge on the high energy physics in my head. He took a great care about my education and broadening experience. He knew answers to nearly all questions I could ask at that time. His sharp mind and brilliant memory are impressive. A few days before I left the IHEP he pointed the Ref. [17] to me which had largely determined the direction of my research for the next four years. Thank you, Alexander Mikhailovich, it was smart! I thank Anton Ivashin who was my mentor for all years in IHEP. I received the most of my practical experience due to Anton. An example of his zeal and motivation helped me to overcome many difficulties with the work. I would like to thank my Yuri Khokhlov for his supervision during several years in IHEP.

Contents

Introduction

The strong interaction is one of four fundamental interactions which govern the laws of nature. The universally established theory of strong interactions is Quantum Chromodynamics (QCD). It is responsible for generating all hadronic matter, hadrons, *e.g.* protons and neutrons. It is clear that the hadrons are confined bound states of elementary Quantum Chromodynamics (QCD) particles, quarks and gluons. However, a detailed understanding of internal QCD dynamics which leads to the emergence of hadrons is still missing. How exactly the intrinsic QCD degrees of freedom, quarks and gluons manifest themselves in a variety of the hadronic states puzzles several generation of physicists already.

One of the first clue for the fundamental theory of the strong interaction was observed in proton-proton and proton-electron collisions at high energies. On the one hand, pions produced in the proton-proton collisions did not have the phase-space like distribution, the momentum directions collinear to the initial proton were preferred (see Ref. [19], also an extensive review [20]). The production of pions with high transferred momentum were suppressed. On the other hand, in electron-proton scattering experiments, a large contribution to the total cross section was given by high transferred momentum, *i.e.* in hard scattering processes [21]. Moreover, at high momentum transferred the proton gets destroyed by the interaction, and many hadrons are produced. The *parton model* [22, 23] suggested by J. Bjorken and R. Feynman offered a simple reconciliation of the two observations. Protons are built of quarks, which carry electric charge, and gluons, which are responsible for gluing the quarks together. It was assumed that the quarks cannot exchange a high momentum in strong interactions. However, as they have an electric charge, the quarks can obtain a large transferred momentum from the scattered electrons. The kicked quark interacts with the remaining part of the proton and produces a hadronic jet in the direction of the original proton. The phenomena of quasi-free partons at a small distance, corresponding to large momentum transfers, was called *asymptotic freedom*. Several years later, asymptotic freedom was realized as a natural consequence in the non-abelian gauge theories by D. Gross, F. Wilczek, and D. Politzer [24, 25]. For the $SU_c(3)$ gauge group with n_f massless fermions (quarks) in the fundamental representation, the coupling α_s, called the *color*-charge, runs with the transferred momentum Q as

$$\alpha_s(Q^2) = \frac{\alpha_s(\mu^2)}{1 + \frac{\alpha_s(\mu^2)}{12\pi}(33 - 2n_f)\log(Q^2/\mu^2)},\tag{1.1}$$

with μ being the scale where $\alpha_s(\mu)$ is measured [26]. The coupling $\alpha_s(Q^2)$ vanishes at high energies for $n_f < 16$ and especially for $n_f = 6$, which is suggested by all experimental observations at the moment. In the opposite limit, for $Q^2 < 1\,\mathrm{GeV}^2$, [1] the strength of the interaction becomes very large which leads to the phenomenon of *confinement*. In this region, the interacting systems are confined to a very small distance scale, of about $\sim 10^{-15}\,\mathrm{m}$, staying color-neutral as a whole. Those color-neutral objects are the hadrons. Due to the strong coupling, the probability to exchange single gluons between quarks is negligibly smaller than the probability to exchange any large numbers of gluons. Therefore, the interaction between the quarks cannot be separated from the collective behavior of the gluons and quark-antiquark pairs, produced and absorbed incessantly. The main method applied in field-theoretical calculations, the method of perturbations, becomes untenable in this regime. No simple approach to calculate the net effect of the interaction between quarks has yet been found. In the non-perturbative regime, a representation of hadrons as simple objects composed of quarks and antiquarks becomes questionable, however, such an approach turned out to be constructive. Given that the quarks are transformed under the fundamental representation of $\mathrm{SU}_c(3)$ the color-neutral combinations can be constructed as $q\bar{q}$, qqq, $q\bar{q}q\bar{q}$, $qqqq\bar{q}$, etc as suggested by M. Gell-Mann [27], where q stands for the quark, and $\bar{q}$ for the antiquark constituent. One can also construct new states by adding to the latter constituent gluons, *i.e.* $q\bar{q}g$, $qqqg$, etc. [2] Surprisingly, the majority of the observed hadrons falls into two sets only: the conventional mesons, regarded as a $q\bar{q}$-system, and the conventional baryons, composed of three quarks, *i.e.* qqq or $\bar{q}\bar{q}\bar{q}$. This raised the question of why the states which contain a higher number of quark and/or gluonic components are not diversely present. Is there a principle emerging from the unsolved equations of QCD which excludes (suppresses) such states from existence or was the identification of the observed states not done correctly?

Those questions drive hadron spectroscopy. There is a global experimental effort aiming to establish the spectrum of hadrons. Many theoretical groups around the world are working on predictions and descriptions of the spectrum. However, as a simple direct connection between the hadronic spectrum and the fundamental theory is blocked by the confinement issue, establishing the nature of the observed states becomes very challenging. The main approaches over the last decades were phenomenological models adopted from solvable theories, like QED, which suggest a certain pattern to be recognized in the spectrum. For hadronic *bosons*, *i.e.* particles with integer spin, deviations from the assigned $q\bar{q}$ pattern become candidates for *exotic mesons*, which is a collective term for the non-conventional states. Following the simplistic picture, the exotic states are also classified to be *e.g.* tetraquarks $q\bar{q}q\bar{q}$, hybrids, $q\bar{q}g$, etc. The ideal, abstract, exotic hadrons are expected to form their own spectroscopic pattern which is attempted to be recognized in the experimental spectrum (*e.g.* see a spectrum of hadronic molecules in Ref. [30–32], a pattern of the exotic states in the light meson sector is discussed *e.g.* in Ref. [33–36]).

There are six quark types (*flavors*) distributed in three generations in pairs. The quarks u, d (first generation) and s (second generation) are referred to as the light quarks. The others c (second generation), also t and b (third generation) are called heavy quarks. The strong interaction is blind to flavor, *i.e.* invariant under flavor symmetry. Since the light quarks are nearly degenerate in mass [26], one can expect similarities in the spectrum of a $u\bar{d}$ system and a $s\bar{d}$ system (*i.e.* the mass degeneracy of the mesons as a consequence of the flavor symmetry group, $\mathrm{SU}_f(3)$). This symmetry was noticed

---

[1] Throughout this thesis we use natural units, $c = \hbar = 1$.

[2] The constituent gluons are introduced in quark models as an additional degrees of freedom associated with gluons (gluelump, glueballs) which contribute to the quantum numbers, see *e.g.* Ref. [28, 29].
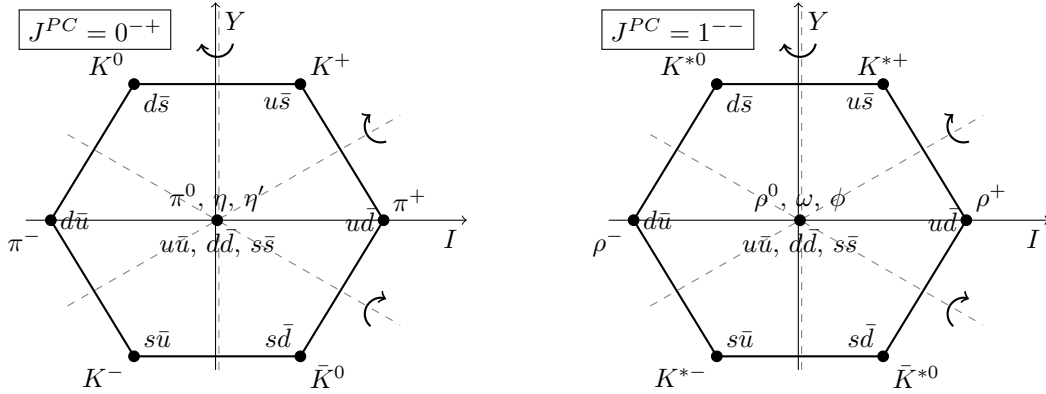
Figure 1.1: Light scalar (left) and vector (right) nonets of mesons. Flavor symmetry, *i.e.* the group $SU_f(3)$, transforms states to each other. The x axis gives the isospin quantum number, the hypercharge Y is shown along the y axis. Three common rotation axes that correspond to action of isospin, V-spin and U-spin generators are presented by dashed lines. Under exact symmetry, the properties of hadrons, with respect to the strong interaction, are degenerate.
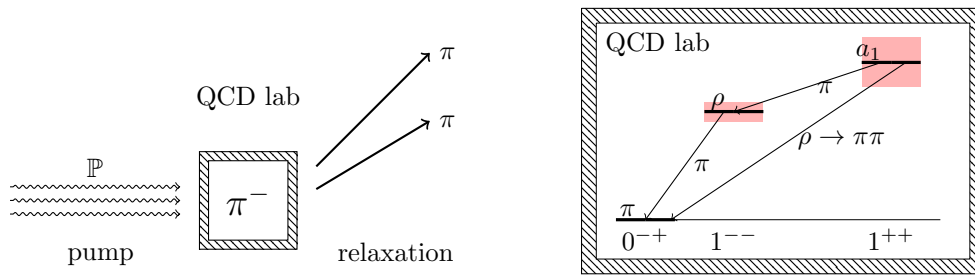
Figure 1.2: An analogy of the hadron scattering with an atomic spectroscopy setup. We consider an elementary hadron π^- as an isolated system. The system is excited by a gluonic field and relaxes by emitting particles. The excitation spectrum is obtained by measuring of the invariant mass spectrum of emitted particles.

first by M. Gell-Mann [27] and G. Zweig [37] and allowed them to guess the existence of quarks based on an emerging symmetry in the observed hadron multiplets as shown in Fig. 1.1. One important consequence of flavor $SU_f(3)$ symmetry is, that if the $q\bar{q}$ system permits an excitation, the whole nonet of excited states should emerge in the spectrum.

We label hadrons by their masses and quantum numbers J^{PC} where J is the total spin, P and C are the spatial parity and charge conjugation parity, respectively. Those properties are directly observable and assigned in the experiment. The quantum numbers J^{PC} are usually deduced from the hadron decay character, the mass is determined from the energy of the decay products. The other properties, as the internal composition, cannot be measured and must be inferred. Studies of the hadronic spectrum are performed in scattering experiments discussed in detail in this thesis. The excited states are often called *resonances*, due to the way they appear in the scattering experiment. The principle of the excitation can be viewed analogously to a setup of atomic spectroscopy as shown in Fig. 1.2. Identification of hadrons and extraction of their masses, however, becomes an extremely difficult problem for the excited states due to their short lifetime and, hence, large uncertainty on the total energy, called *width* of a hadron. By current understanding, the pattern of conventional $q\bar{q}$ states

3
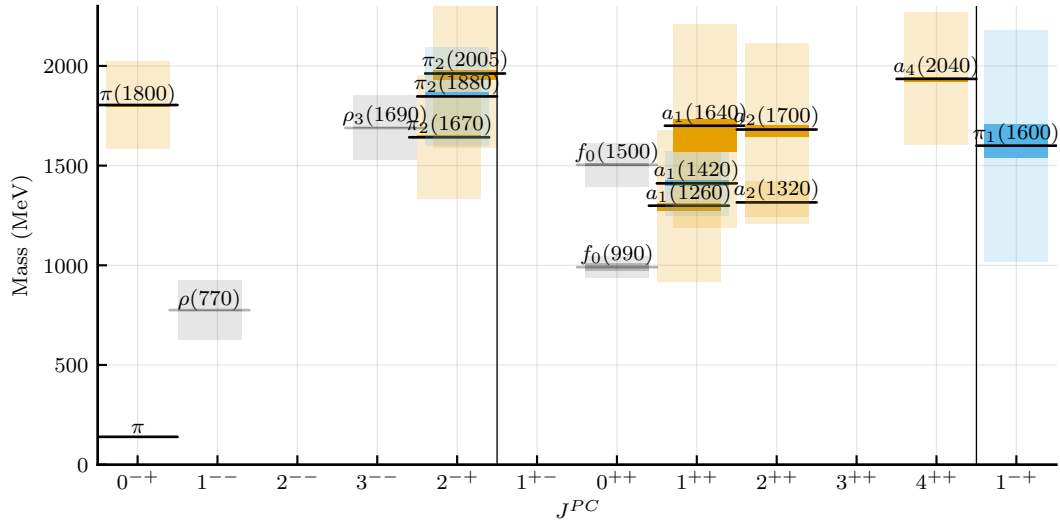
Figure 1.3: The plot shows the spectrum of a charged pion measured by excitation in a gluonic field at the COMPASS experiment [3]. The excited states are observed in decays to three charged pions. The lines indicate the estimated mass of the hadrons with the uncertainty shown by the filled colored box, while the transparent colored area shows the resonance width. The additional gray levels are possible intermediate two-pion states which can be seen in the decays.

roughly corresponds to the pattern of the hydrogen atom with its radial and orbital excitations. Fig. 1.3 shows the excitation spectrum of negatively charged pions measured at the COMPASS experiment [3]. The state $\pi_1(1600)$ falls out of the correspondence due to its quantum numbers, $J^{PC} = 1^{-+}$, *i.e.*, neither orbital nor radial excitation of a $q\bar{q}$ system can have this combination of spin and parities, as can be realized from simple algebra. [3] The other state suspected to be exotic is the $\pi_2(1880)$: this energy region is found to be too densely populated by resonances. The $a_1(1420)$ is another example of an interesting signal discovered by COMPASS. If it is a genuine state, it does not fit the $q\bar{q}$ pattern, however, it likely has a different origin [1] as discussed in this thesis.

Modern experiments have collected huge data samples, however, the identification of hadronic states and the extraction of their properties for light mesons became an essential difficulty. The main reason is the absence of a rigorous theoretical framework which would allow to address all complications of the non-perturbative hadronic interaction. The first complication as mentioned already is the short lifetime of hadronic excitations. Overlapping states which share the same J^{PC} interfere freely, hence, making it difficult to even count the number of resonances. As one generally cannot characterize the state by the peak position and width at half maximum, a revision of methods to extract resonance parameters is required. The decay of an excited hadron can proceed to multiple different final states. For various transitions, a resonance often manifests itself differently. One reason for this is the final-state interaction of hadrons, which is specific for every final state. In the system of three and more hadrons, the final-state interaction plays a very important role. If the transition

---

[3] The allowed quantum number for the conventional mesons are calculated by combining a quark state with the quantum numbers $J^P = (1/2)^-$ and an antiquark state with $J^P = (1/2)^+$. Hence, the combined parity is equal to $(-1)^{l+1}$, where l is the orbital angular momentum of the $q\bar{q}$ state. The charge conjugation, or C-parity is strictly defined for the neutral states only, $C = (-1)^{l+s}$. For the charge state (not an eigenstate of the charge conjugation), the C-parity of its neutral partner in the charge multiplet is attributed, it is found convenient in many situations.
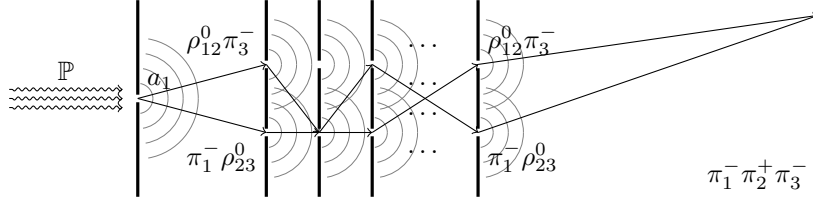
Figure 1.4: An analogy of the hadronic final-state interaction in the system $\pi^-\pi^+\pi^-$ and an infinite repetition of the double slit setup. There are two decay chains of the a_1 resonance to the $\pi_1^-\pi_2^+\pi_3^-$ final states: $\pi_1^-\rho_{23}^0[\to\pi_2^+\pi_3^-]$ and $\rho_{12}^0[\to\pi_1^-\pi_2^+]\pi_3^-$. The final-state interaction allows an infinite number of rescattering $\pi_1^-\rho_{23}^0\to\rho_{12}^0\pi_3^-$ via the pion exchange. The observed pattern is the interference of all outcomes added coherently.

from excited to the final state of three hadrons can proceed via two different decay chains as shown in Fig. 1.4, it is reminiscent of the double slit experiment due to the interference of several quantum outcomes. The hadronic interaction at the final state leads to an infinite repetition of the two chain bifurcation, as if in the double slit experiment, an infinite number of double-slit screens were installed. The approach pushed forward in this thesis is based on the general requirements of analytic S-matrix theory. A deductive S-matrix approach [38, 39] does not offer *ab initio* calculations. However, it gives a set of constraints, valid under the postulates of causality and probability conservation, and allows for an input which parametrizes internal QCD degrees of freedom. In this framework, the characteristics of the hadronic states are defined unambiguously. The approach to the problem of the final-state interaction based on the probability conservation offered by the S-matrix seems very promising.

In this thesis, we focus on the problems of the light-meson spectrum measured by the COMPASS experiment. Chapter 2 introduces the global theoretical framework of the analytic S-matrix. Using the example of $\eta\pi/\rho\pi$ scattering we outline the main concepts of the scattering and the production amplitude, the partial-wave expansion, dispersion relations and the resonance-pole search technique. In the further sections we depart from the two-particle scattering problem and discuss the three-pion system inferring and applying the consequences of the S-matrix postulates. Chapter 3 is dedicated to the partial-wave analysis technique used at COMPASS to study the following reaction: $\pi^- p \to \pi^-\pi^+\pi^- p$. We guide the reader through the ideas of the isobar model, the extended likelihood fit, and the freed-isobar analysis. We summarize the classical method of extracting parameters of hadron states based on an approximation of the isolated resonances (Breit-Wigner approach). The physics of the resonance-like phenomenon $a_1(1420)$ is discussed in Chapter 4. We consider singularities of the scattering amplitude and show how the logarithmic branching point due to the final-state interaction unavoidably emerges and leads to a consistent description of the $a_1(1420)$ signal. In Chapter 5, we address a known difficulty in the peripheral production of hadronic states, the so-called Deck process (after R. Deck [40]). The process functions as a coherent background which interferes with resonances and may mimic their appearance. Three approaches which model the one-pion exchange process differently are projected to partial waves and compared with COMPASS data. We discard one model and establish uncertainties on the partial wave projections. The Deck process is significant for nearly all J^{PC} sectors, however, its effects are largest for the $J^{PC} = 1^{++}$ sector, where the $a_1(1260)$ and $a_1(1420)$ were observed. Due to the Deck effect, the mass and the width of the axial ground state $a_1(1260)$ cannot be measured precisely. Therefore, we perform an analysis of the decay $\tau \to 3\pi\,\nu_\tau$, where the same hadronic state $a_1(1260)$ appears in a clean

environment. The extraction of the mass and width of the $a_1(1260)$ in a model based on analyticity and unitarity is performed for the first time. The last Chapter (Chapter 7) is dedicated to a proposal for a model which bridges the phenomenon of final-state interactions with the physics of three-body resonances. Starting from the general three-body unitarity requirements, we construct the $3 \rightarrow 3$ scattering amplitude, which enables to incorporate separately the long-range interactions as a reason of the final-state interaction and the short-range QCD dynamics which is expected to govern the resonance formation. The unified model can be reduced to the approaches used for the investigation of the $a_1(1420)$ effect, as well as the analysis of the $a_1(1260)$ properties in its limiting cases. The Deck effect can be incorporated to the production amplitude consistently fulfilling probability conservation.

S-matrix constraints to the scattering amplitude

As perturbation theory was found not to be applicable for the strong interaction at the low energies, an alternative approach was required. Active attempts to construct a consistent theory based on the general principles of the S-matrix were made the 60s [38]. The S-matrix theory, suggested by Heisenberg [41–43] in 1943, grew up from the idea that the interacting fields themselves are of little interest; the main objects of the theory are the transition amplitudes, *i.e.* the elements of the S-matrix. Based on the general properties of the scattering theory the transition amplitudes were tried to be calculated directly. A consistent self-contained formalism has not been found: although the consequences of the S-matrix requirements are fundamental, the theory requires an input attributed to the internal QCD dynamics (*e.g.* see discussion about Castillejo-Dalitz-Dyson poles in Ref. [44], chapter 8, section 3.3). The modern approach goes along these lines and uses the properties and consequences of the S-matrix theory as a set of constrains which restrict a possible functional form of the amplitude. The remaining freedom is fixed using experimental observations.

The scattering matrix is defined as the expectation value of the transition operator, S:

$$S_{if} \equiv \langle f | S | i \rangle , \qquad (2.1)$$

where $|i\rangle$ and $\langle f| = |f\rangle^\dagger$ are non-interacting asymptotic initial and final states of the reaction $i \to f$ which contain several particles. The S-matrix element, $\langle f | S | i \rangle$ is an amplitude for the initially prepared state $|i\rangle$ to be observed in the final state in a configuration $|f\rangle$. There are two distinct ways how the transition can happen: first, particles do not interact (*disconnected* transition), and the probability is given by an overlap of the states, $\langle f | i \rangle$. The other way is through an actual interaction introduced by the operator T (*connected* transition); the transition amplitude is written as $i \langle f | T | i \rangle$. The basic splitting of the S-matrix operator reads: [1]

$$S = 1 + iT, \qquad (2.2)$$

where 1 is the identity operator, $1 |i\rangle = |i\rangle$.

As suggested in Ref. [38], important assumptions (postulates) to the S-matrix theory are *Lorentz invariance*, *conservation of probability* (related to unitarity of S), *causality* (related to analyticity of

---

[1] The connectedness structure is believed to be a sure assumption as stated in Ref. [38]. It is further explored for the $3 \to 3$ process in Sec. 7.

the transition amplitude), the *short-range* character of strong force [2] and the *superposition principle* of quantum mechanics. The most nontrivial consequences are derived from the unitarity and analyticity principles. On the one hand, the unitarity constraint ensures that no single reaction channel exceeds the limit set by the probability conservation, while on the other hand, it is used as a principle that enables to identify peaks and dips in cross-sections with the hadronic resonances, as we introduce below.

The unitarity constraint to the operator S, $S^\dagger S = 1$, leads to a relation for the operator T,

$$T - T^\dagger = iT^\dagger T, \tag{2.3}$$

which becomes very practical as soon and it is sandwiched by the initial and the final states, $\langle f|$ and $|i\rangle$. In the next two sections we consider two most important examples: first, in Sec. 2.1 we discuss the *elastic scattering amplitude*, that is a transition matrix between a few strongly coupled channels. Second, an amplitude for one of these channels being produced in a more complex reaction, the *production* amplitude is discussed in Sec. 2.2.

2.1 The elastic scattering amplitude

To introduce a concept of the unitary model and the theoretical framework we follow a general discussion with a concrete example of a scattering problem in a system of two coupled channels, $\eta\pi$ and $\rho\pi$ (this model was developed for studies of Ref. [4]). As an example, we focus on interactions with the $J^{PC} = 2^{++}$ quantum numbers known to contain the $a_2(1320)$ resonance. The considered model can be further simplified by assuming the ρ-meson to be a stable, scalar particle. [3] The $2 \to 2$ scattering reaction reads,

$$\xi(q)\pi^-(p) \to \xi'(q')\pi^-(p'), \tag{2.4}$$

where ξ refers to either ρ^0 or η, q and p are the four-momenta of ξ and π, respectively. The primed (unprimed) momenta denote to the final- (initial-) state quantities. The matrix element T_{if} is defined as follows,

$$\langle f| T |i\rangle = T_{if}(s,t) (2\pi)^4 \delta^4(P - P'), \tag{2.5}$$

where P and P' are the total momenta in the initial and the final states, i, f are either $\eta\pi$ or $\rho\pi$ in the case at hand. Due to the Lorentz invariance and the energy-momentum conservation, the matrix element can be expressed via two independent kinematic variables. A convenient choice for these variables is the Mandelstam variables s and t: $s = (p + q)^2$ and $t = (q - q')^2$. The variable $u = (q - p')^2$ is not independent, since $u = m_\xi^2 + m_{\xi'}^2 + 2m_\pi^2 - t - s$. For brevity of notations we introduce $T(s,t) \equiv T_{if}(s,t)$, meaning that $T(s,t)$ is a matrix in the channel space.

The considered reaction $\xi\pi^- \to \xi'\pi^-$ is called the s-channel process. The t-channel process

---

[2] According to Eden *et at.* [38], there is at present no S-matrix theory which *properly* includes photons. Authors point that the essential problem is related to the infrared divergence of perturbation theory and unmeasurable number of photons. It does not mean, however, that the S-matrix is not applicable to reactions which involve the electromagnetic interaction. For example, one finds many useful consequences the S-matrix principles to the electromagnetic form factors as well as dip inelastic scattering processes (see Ref. [39]).

[3] Formation of the $J^P = 2^+$ state from ρ and π, with quantum numbers $J^P = 1^-$ and 0^-, is only possible in D-wave. The same orbital angular momentum (D-wave) is required for the scalar ρ-meson. The spin and finite width of the ρ are critical below and close to the nominal $\rho\pi$ threshold. Above 1 GeV, the simplification is well justified.
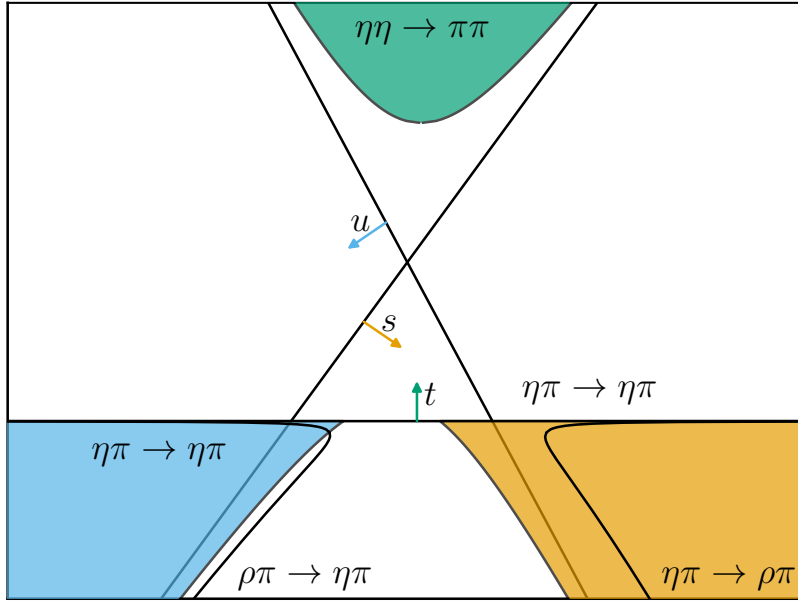
Figure 2.1: The Mandelstam plane for the reaction $\eta\pi \to \eta\pi$ in s-channel. The u-channel for the $\eta\pi \to \eta\pi$ is the same reaction since π and η coincide with their anti-particles, it is shown by the blue area. The kinematic border of the t-channel scattering ($\eta\eta \to \pi\pi$) is shown by blue region. The phase space for the reaction $\eta\pi \to \rho\pi$ present in the s-, and u-channels is shown by the dashed line.

corresponds to $\xi\xi' \to \pi^+\pi^-$ scattering. [4] The u-channel process is the same as the s-channel process despite that the pion charge must be flipped ($\xi\pi^+ \to \xi'\pi^+$). For the s-channel reaction, the physical values of t and u are below zero as shown in the Fig. 2.1. There is a domain of the amplitude when s is negative and t is positive which is unphysical for the s-channel, however, it represents the physical region of the t-channel reaction.

The analyticity of the scattering amplitude states that the s-, t-, and u- cross-channel amplitudes in their physical domains are analytically connected, *i.e.* the analytic amplitude (if exists) describes a complete Mandelstam plane. Moreover, this amplitude is analytic in the upper part of the complex plane (positive imaginary part) of the variables s or t (a proof of this fact is cumbersome, see *e.g.* Ref. [45]). An extension of the analyticity domain to the lower part of complex plane (negative imaginary part) is done using the Schwarz reflection principle (see the mathematical statement for a single-variable analytic function in Ref. [46], discussions about application to the physical processes in Ref. [47]). In the s-channel physical region (there are no t-channel-related singularities), it states:

$$T^*(s,t) = T(s^*,t) \tag{2.6}$$

Particularly, Eq. (2.6) means, that as soon as the amplitude has an imaginary part, it is not continuous on the real axis of the complex s-plane. As we will see below, the unitarity principle requires the scattering amplitude to have a finite imaginary part in the physical region, hence, a discontinuity. We use a common $+i\epsilon$ prescription, which suggests that the physical value of the amplitude is calculate

---

[4] Strictly speaking, the particles have to be replaced with antiparticles when applying crossing symmetry, however, meson antiparticles belongs to the same isospin multiplet, hence, those are essentially the same particles.

above the unitarity cut.

$$T(s,t) = \lim_{\epsilon \to 0} T(s + i\epsilon, t) \equiv T(s_+, t), \qquad (2.7a)$$

$$T(s^*, t) = \lim_{\epsilon \to 0} T(s - i\epsilon, t) \equiv T(s_-, t), \qquad (2.7b)$$

where the boundary of the complex function is indicated by the $\pm$ sign. For the s-channel physical region we assume that there are no singularities in the variable t.

The expectation value of the operator $T^\dagger$ is calculated using the hermitian property of the operator T: $\langle f | T^\dagger | i \rangle = \langle i | T | f \rangle^*$. Using the time-reversal symmetry, $T_{if}(s,t) = T_{fi}(s,t)$, we obtain [5]

$$\langle f | T^\dagger | i \rangle = T(s^*, t) \, (2\pi)^4 \delta^4(P - P'). \qquad (2.10)$$

An application of the unitarity relation of Eq. (2.3) to the amplitude $T(s,t)$ reads,

$$\langle f | T - T^\dagger | i \rangle = i \sum_m \int \prod_{j=1}^m \frac{\mathrm{d}^3 \mathbf{p}_j}{(2\pi)^3 2E_j} \, \langle f | T^\dagger | m \rangle \langle m | T | i \rangle, \qquad (2.11)$$

where $\sum_m$ denotes a sum over all possible on-shell intermediate states with m particles, all momentum states have to be integrated over. Substituting Eq. (2.5) we see that on the right-hand side, the delta functions ensure energy momentum conservation between the initial, the intermediate and the final state. Due to the delta functions, the integral over intermediate momenta gets reduced to the phase space.

$$\mathrm{d}\Phi_m \equiv \int \prod_{j=1}^m \frac{\mathrm{d}^3 \mathbf{p}_j}{(2\pi)^3 2E_j} (2\pi)^4 \delta^4(P_m - P), \qquad (2.12)$$

where P_m is the total momentum of the intermediate state equal to the sum of momenta q_m, and P is an external total momentum.

In our example of the two coupled channels, the intermediate state contains either a $\rho\pi$ or an $\eta\pi$ state. Therefore, Eq. (2.3) gives a constraint to the matrix $T(s,t)$.

$$T(s_+, t) - T(s_-, t) = i \sum_m \int \mathrm{d}\Phi_2 \, T(s_-, t'_m) T(s_+, t_m) \theta(s - s_{\text{th}}^{(m)}), \qquad (2.13)$$

where $t_m = (q - q_m)^2$, and $t'_m = (q' - q_m)^2$. We dropped the channel indices for brevity of notations. $s_{\text{th}}^{(m)}$ is a physical threshold for the channel m.

It is convenient to expand the amplitude $T(s,t)$ into partial waves

---

[5] Eq. (2.10) holds in the more general context of the field theory without requiring the time-reversal symmetry, As proven by D. Olive [48] (see also a later work of J. Miramontes [49]), "If the function T_{if} is a boundary value of the analytic function of complex invariants, then T_{fi}^* is an opposite boundary value." It means,

$$\langle f | T^\dagger | i \rangle = T(s^*, t^*) \, (2\pi)^4 \delta^4(P - P'). \qquad (2.8)$$

This condition is known as the *hermitial analyticity*. If follows that for the scattering of scalar particles, under the time-reversal symmetry,

$$T^*(s,t) = T(s^*, t^*). \qquad (2.9)$$

Eq. (2.9) extends the Eq. (2.6) to the region where s- and t-channel-related singularities overlap.
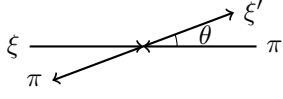
$$T(s,t) = \sum_{l=0}^{\infty} (2l+1)T_l(s)P_l(\cos\theta), \qquad (2.14)$$

where θ is a scattering angle in the s-channel rest frame, $P_l(\cos\theta)$ is the Legendre Polynomial of l-th order, and $T_l(s)$ is a matrix (in the channel space) of the scattering amplitudes projected to the partial waves. The two-body phase space integral in Eq. (B.3) includes an integral over directions of $\mathbf{q}_m$. In the partial wave basis the angular integral can be solved analytically ensuring orthogonality of different partial waves [6].

$$T_l(s_+) - T_l(s_-) = i\,T_l(s_-)\,\rho(s)\,T_l(s_+), \qquad (2.15)$$

where $\rho(s) = \mathrm{diag}(\rho_1, \rho_2)$ is a matrix of the phase-space factors with $\rho_i = \lambda^{1/2}(s, m_i^2, m_\pi^2)/(8\pi s)$, $m_i \in \{m_\eta, m_\rho\}$. The left part of Eq. (2.15) is often written as the discontinuity of the amplitude $d_s T_l(s) \equiv T_l(s_+) - T_l(s_-)$. Using the Schwarz reflection principle we obtain $T_l(s_-) = T^*(s)$. The unitarity relation then reads:

$$2\,\mathrm{Im}\,T_l(s) = T_l^*(s)\,\rho(s)\,T_l(s). \qquad (2.16)$$

We showed that the unitarity of the S-operator inferred a constraint to the partial wave amplitude $T_l(s)$. The matrix S_{if}, however, contains a delta-function from the disconnected term, $\langle f\,|i\rangle$. The unitary matrix for the partial wave amplitude $S_l(s)$, can also be defined as follows [26],

$$S_l(s) = 1 + i\sqrt{\rho(s)}\,T_l(s)\,\sqrt{\rho(s)}. \qquad (2.17)$$

S_l is indeed unitary since the constraint $S_l^\dagger S_l = 1$ leads to the condition (2.15). In our example, S_l belongs to the U(2) group. Hence, a general expression for S_l is

$$S_l = e^{i\phi} \begin{pmatrix} a & b \\ -b^* & a^* \end{pmatrix}, \qquad (2.18)$$

where $|a|^2 + |b|^2 = 1$. When time-reversal symmetry holds, the $T_l(s)$ as well as the S_l matrix are both symmetric. Hence, b is purely imaginary. A common parametrization of the S_l-matrix in terms of the *inelasticity* $\eta = |a|$ and phases, ϕ_1 and ϕ_2, reads,

$$S_l = \begin{pmatrix} \eta e^{i\phi_1} & i\sqrt{1-\eta^2}\,e^{i\phi} \\ i\sqrt{1-\eta^2}\,e^{i\phi} & \eta e^{i\phi_2} \end{pmatrix}, \qquad (2.19)$$

where ϕ_1 and ϕ_2 are scattering phases of the diagonal elements of the $S_l(s)$, $\phi = (\phi_1 + \phi_2)/2$.

Fig. 2.2 shows the Argand diagrams for the diagonal elements of the coupled-channel amplitude $T_2(s)$ for the $\eta\pi$, $\rho\pi$ scattering in D-wave (see details of the model in Appendix A.1). For convenience the amplitude multiplied to the phase space is plotted; in this representation the shaded area in Fig. 2.2 is forbidden by the unitarity condition in Eq. (2.16). Due to the phase-space factors, the amplitude curves start at 0 at the corresponding thresholds, $\sqrt{s_{\mathrm{th}}^{(1)}} = m_\eta + m_\pi$ (for the left panel)

---

[6] The derivation is straightforward and can be found e.g. in any of the classical books [39, 44, 47]
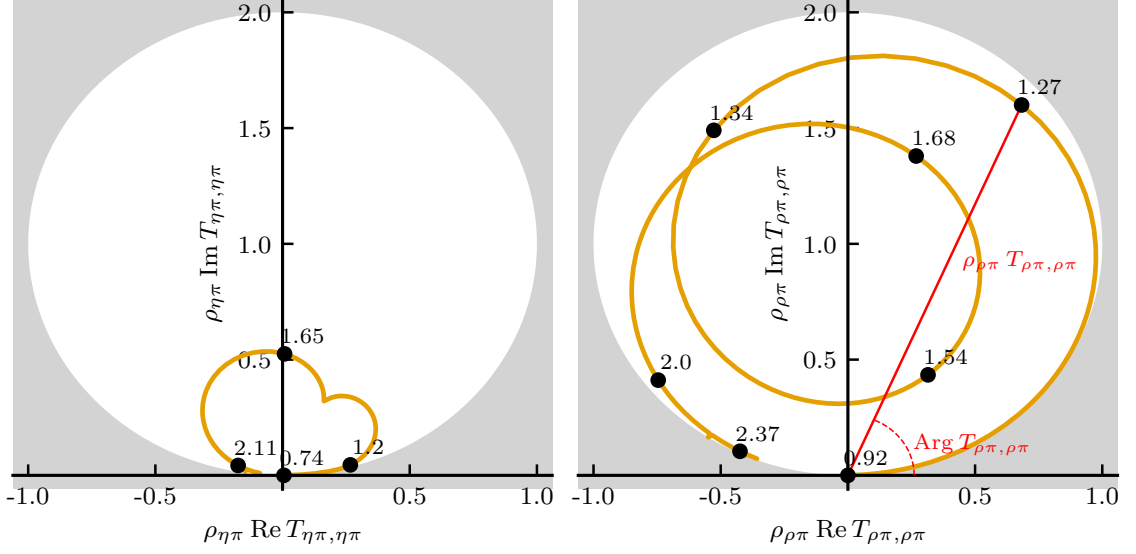
Figure 2.2: The Argand diagrams of the $\eta\pi/\rho\pi$ scattering model obtained with the COMPASS data (see details in Appendix A.1): the left (or right) plot shows a trajectory of the $\rho_{\eta\pi}T_{\eta\pi,\eta\pi}$ (or $\rho_{\rho\pi}T_{\rho\pi,\rho\pi}$) amplitude as a function of the invariant mass, $m_{\xi\pi} \equiv \sqrt{s}$, $\xi \in \{\eta, \rho\}$. The labeled dots indicate the values of the invariant mass of the system in GeV. The gray area represents the region of the complex plane which is forbidden by unitarity.

and $\sqrt{s_{\text{th}}^{(2)}} = m_\rho + m_\pi$ (for the right panel). The model for the scattering amplitude contains two resonances, $a_2(1320)$ and $a_2(1700)$. Both amplitudes in Fig. 2.2, $T_{\eta\pi,\eta\pi}$ and $T_{\rho\pi,\rho\pi}$ show a double peak structure in the absolute vales as the invariant mass of the system is varied (one can see it in the Argand diagram as a distance of the points on the orange lines to zero). One other important indication of a resonance is a motion of the scattering phase. As well seen on the right panel of Fig. 2.2 the amplitude develops two circles, the phase of the amplitude $T_{\rho\pi,\rho\pi}(s)$ has two regions of a fast movement, when the orange line crosses the imaginary axis; it decreases in between. The left panel of Fig. 2.2 shows an example of more complicated behavior, the phase of the scattering amplitude $T_{\eta\pi,\eta\pi}(s)$ rises although it does not have a classical circular behavior.

2.2 Analytic continuation and pole search

The analytic structure of the partial wave amplitude is more complicated since all physical singularities of the cross channels (thresholds openings, bound states) get projected to the complex s-plane. However, the analytic structure around the physical region is still simple as it is controlled by unitarity (2.16). The right-hand-side singularities are branch points related to thresholds. Since the left-hand-side singularities are cumbersome, for practical applications, they are often artificially modeled [4, 12, 50]. Eq. (2.16) does not fully determine the scattering amplitude, however, it gives a robust constraint. To obtain the unitary model, the constraint (2.16) is built in using one of a few known approaches. Here we comment on the K-matrix approach [47, 51–53], a complementary N-over-D approach is discussed in Ref. [47, 54, 55].

The unitarity condition (2.15) gets simpler for the inverse amplitude. When Eq. (2.15) is multiplied

by $T_l(s_-)^{-1}$ from the left side and by $T_l^{-1}(s_+)$ from the right side, it becomes,

$$T_l^{-1}(s_+) - T_l^{-1}(s_-) = -i\rho(s)\theta(s - s_{\text{th}}). \tag{2.20}$$

Eq. (2.20) is fulfilled for the model:

$$T_l^{-1} = K^{-1} - i\rho/2, \tag{2.21}$$

where K^{-1} must be a real function on the real axis above the threshold. Possible singularities of K are poles on the real axis and left-hand-side singularities. The function ρ defined below Eq. (2.15) has a square-root singularity. By drawing the cut from the threshold to the positive real axis, we make the function $i\rho$ hermitian analytic (see Eq. (2.8)). $i\rho$ flips the sign when one crosses the cut, therefore, the discontinuity matches Eq. (2.20). The expression for T_l obtained by an inversion of Eq. (2.22),

$$T_l = K \left[1 - i\rho K/2 \right]^{-1} = \quad K \quad + \quad K(i\rho/2)K \quad + \quad K(i\rho/2)K(i\rho/2)K \quad + \quad \ldots, \tag{2.22}$$

$$\tag{2.23}$$

where we also provide a correspondence with a simple diagrammatic interpretation. We notice that in this form of Eq. (2.22), the rank of the matrix K is not restricted. Often the rank of K is less than its dimension, hence K is degenerate. When K describes a single interaction between two particles, the function $i\rho/2$ stands for a loop as shown in Eq. (2.23). A common form of the K-matrix is a sum of pole terms,

$$K_{ij} = \sum_r \frac{g_i^{(r)} g_j^{(r)}}{m_r^2 - s}, \tag{2.24}$$

which are called *bare* poles. The bare pole position m_r^2 and the bare couplings $g_l^{(r)}$ do not have any physical meaning. They are used as a flexible parametrization.

One disadvantage of the parametrization in Eq. (2.22), is that the T_l contains left-hand-side singularities which are artistically penetrated in the model via the phase-space factor ρ. Indeed, the factor $\rho(s)$ can be written as (the definition of the Källén function)

$$\rho(s) = \frac{\sqrt{(s - (m_\xi + m_\pi)^2)(s - (m_\xi - m_\pi)^2)}}{8\pi s}, \tag{2.25}$$

where we clearly identify the square-root branch point at so-called pseudo-threshold, $s_{\text{pth}} = (m_\xi - m_\pi)^2$ and a pole at $s = 0$ in addition to the threshold singularity, $s_{\text{th}} = (m_\xi + m_\pi)^2$. In the diagrammatic correspondence in Eq. (2.22), $i\rho/2$ represents a loop, however, it is precisely equal to the imaginary part of a bubble loop integral [39]: As it can be shown by direct calculations, the expression for the scalar two-particle loop has only the right-hand cut and its imaginary part coincides with $\rho/2$. Using the knowledge of the analytic structure and the expression for the imaginary part, a complete function for the scattering loop can be recovered by means of the *dispersion relations*.

The dispersion relations establish a relation between the scattering amplitude and its discontinuities, and residuals of the non-analytic structures by use of Cauchy's integral theorem. In order to derive the relation one equates a value of the function, $f(s)$ to an integral of $f(s')/(s' - s)$ over s', along the

circular contour in the vicinity of s, which encloses s. Then, the circular integration contour is blown to an infinity wrapping around all non-analytic structures. As soon as the contribution to the integral from the blown circle is negligible, the value of the function $f(s)$ is equal to the sum of integrals around the non-analytic structures which we stumbled upon while blowing the contour. For example, if a function contains a single channel branch point at s_{th}, and the cut attached to it goes to $+\infty$ along the real axis, it admits a representation,
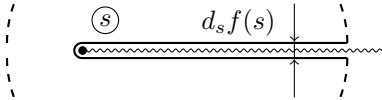
$$f(s) = \frac{1}{2\pi i} \int_{s_{\text{th}}}^{\infty} \frac{d_s f(s')}{s' - s} \mathrm{d}s', \tag{2.26}$$

where $d_s f(s) \equiv f(s_+) - f(s_-)$ is a discontinuity of the function $f(s)$ on the cut. In order to drop the circular part of the integral we have assumed that the function $f(s)$ vanishes at $s \to \infty$ faster than $1/s$. If the function does not vanish at $s \to \infty$, and it still does not grow faster than a polynomial of the order $(n - 1)$, the relation (2.26) can still be used for the *n-times subtracted function*,

$$\tilde{f}(s) = \frac{1}{(s - s_0)^n} \left(f(s) - \sum_{k=0}^{n} \frac{(s - s_0)^k}{k!} f^{(k)}(s_0) \right), \tag{2.27}$$

where $f^{(k)}(s_0)$ is the k-th derivative of the function $f(s)$ calculated at the subtraction point s_0. Using Eq. (2.26) for the function $\tilde{f}$, one can obtain an expression for $f(s)$, which, however, requires an input on the derivatives at the subtraction point, $f^{(k)}(s_0)$. The most practically used case is the once-subtracted relation. For a function with a single cut from s_{th} to ∞, it reads,

$$f(s) = f(0) + \frac{s}{2\pi i} \int_{s_{\text{th}}}^{\infty} \frac{d_s f(s')}{s'(s' - s)} \mathrm{d}s', \tag{2.28}$$

where we used $s_0 = 0$ as the subtraction point. As we see, Eq. (2.26) and Eq. (2.28) are purely mathematical consequences of analyticity. It was first applied to a physical system by Kronig [56] and Kramers [57] who were studying analytic properties of the refractive index for the passage of electromagnetic radiation through matter as a function of frequency. From that time, they are called the *Kramers-Kronig relations* of the *dispersion relation* [47, 58].

Returning to the scalar two particle loop function we use the dispersion relations from Eq. (2.28) to write

$$\mathcal{C}_1(s) = \frac{s}{2\pi} \int_{(m_\xi + m_\pi)^2}^{\infty} \frac{\rho(s')}{s'(s' - s)} \mathrm{d}s', \tag{2.29}$$

where the once subtracted dispersion integral converges since the function $\rho(s)$ from Eq. (2.25) approaches a constraint value when $s \to \infty$. The subtraction constant $\tilde{\rho}(0)$ is set to 0. Eq. (2.29) gives an exact expression for a scalar bubble diagram up to a renormalization constant related to the ultraviolet divergence (constant in Eq. (2.28)) [59]. The integral (2.29), also known as *Chew-Mandelstam function* [60–62], or *Self-Energy* function [26] can be analytically solved and expressed
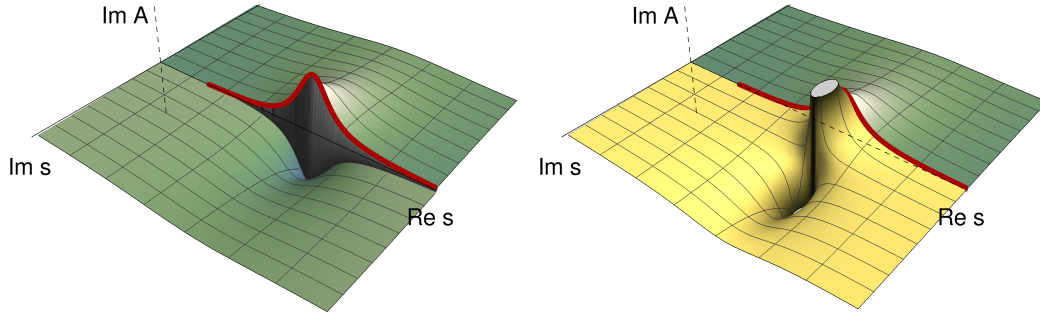
Figure 2.3: Complex plane of the elastic scattering amplitude which contains a single isolated resonance. The left plot shows the imaginary part of the amplitude in the complex plane on the first Riemann sheet (green surface). By means of analytic continuation the amplitude is calculated on the second sheet as shown on the right plot. One finds the origin of the resonance enhancement on the real axis in the pole located on the second sheet.

through elementary functions as shown in Ref. [61].

$$
\mathcal{C}_1(s) = \frac{1}{16\pi^2}\left[\frac{\lambda^{1/2}(s, m_\xi^2, m_\pi^2)}{s}\log\frac{m_\xi^2 + m_\pi^2 - s + \lambda^{1/2}(s, m_\xi^2, m_\pi^2)}{2m_\xi m_\pi}\right.
$$
$$
\left. + \frac{m_\xi^2 + m_\pi^2}{m_\xi^2 - m_\pi^2}\log\frac{m_\xi}{m_\pi} - \frac{m_\xi^2 - m_\pi^2}{s}\log\frac{m_\xi}{m_\pi} - 1\right]. \quad (2.30)
$$

The imaginary part of the function $\mathcal{C}_1(s)$ above the threshold $s > (m_\xi + m_\pi)^2$ comes from the first term of Eq. (2.30) for which the imaginary part of the logarithmic expression is simply $i\pi$, since the argument of the log is negative, and hence, $\operatorname{Im}\mathcal{C}_1(s_+) = i\rho/2$. The Chew-Mandelstam function is often used in the construction of the amplitude in Eq. (2.22) instead of $i\rho/2$. In that case the amplitude $T_l(s)$, has only the right-hand cut. It is still a model because the "correct" amplitude must contain the left singularities from the cross-channel physical processes. However, this model is somewhat better since the first Riemann sheet does not contain the pseudo-threshold branch point singularity, the presence of which cannot be motivated.

The unitarity cut which starts at the threshold and goes to real $+\infty$ splits the complex plane and introduces the Riemann sheets [46]. As we can see from Eq. (2.20), the two particle threshold is a square-root singularity and, hence, it defines the two-sheet Riemann surface. The causality principle forbids additional singularities to be present on the first Riemann sheet (an accessible derivation can be found in Sec. 5.3 of Ref. [45]). Hence, the singularities which rule the amplitude behavior along the real axis are located on the higher lying Riemann sheets. Fig. 2.3 displays the Riemann sheet structure for the amplitude which describes an isolated two particle resonance. An analysis of the singularities of the unphysical sheets, leads to a unambiguous definition of the hadronic resonances. The resonances are identified with the poles of the amplitude $T(s)$, *i.e.* terms $1/(s - s_p)$ in the Laurent

expansion [39]. The locations of the poles are related to the mass and width of the resonances,

$$s_{\mathrm{p}} = (m_p - i\Gamma_p/2)^2. \tag{2.31}$$

The analytic continuation of the model, which is constructed based on the unitarity requirement, straightforwardly follows from Eq. (2.20). We consider the function $T_{II}^{-1}(s) = T^{-1}(s) - i\rho$ and notice that $T^{-1}(s+i\epsilon) = T_{II}^{-1}(s-i\epsilon)$, where ϵ is an infinitesimal positive number. Since the function $T_{II}^{-1}(s)$ match $T^{-1}(s)$ along the real axis above the threshold, it gives a unique analytic continuation to the unphysical sheet [46]. The expression for the amplitude $T_{II}(s)$ reads,

$$T_{II}(s) = T(s) \left[1 - i\rho(s)T(s)\right]^{-1}. \tag{2.32}$$

One can realize that $\rho(s)$, which previously served as the imaginary part only has to be analytically continued, *i.e.* evaluated for the complex argument. Therefore, even when the pseudo-threshold branch point is removed from the first sheet using Eq. (2.30), it appears on the higher lying Riemann sheets. The question of extracting resonance parameters of the amplitude T, is reduced to a numerical problem of identifying poles of Eq. (2.32), which is equivalent to finding zeros of $1/\det T_{II}(s)$ in the coupled channel case.

2.3 The production amplitude

A pure meson-meson scattering reaction is in practice difficult to observe and reproduce in laboratory conditions since there are no stable (enough) mesons. However, this interaction can be studied as a subprocess of more complicated reactions. The matrix element of the reaction, in which the meson system is produced, can be related to the elastic scattering amplitude using the unitarity principle. The meson pair $\eta\pi$ from our example can be seen in the reaction $\pi\,p \to \eta\pi\,p$ measured at the COMPASS experiment [63] or in the reaction $\gamma\,p \to \eta\pi\,p$ measured at the GlueX experiment [64]. For both reactions, there is a kinematic domain when the $\eta\pi$ system is well isolated from the recoiling proton (*e.g.* peripheral production: high energy in the center of mass, low transferred momentum between the beam to the target). In that case the meson interaction can be factorized [65] and considered as produced from a source. Schematically the production amplitude is introduced as follows.

$$\langle\xi\pi|\,T\,|\text{source}\rangle = F(s,t)\,(2\pi)^4\delta^4(\text{four-momentum conservation}), \tag{2.33}$$

where in general F might depend on more variables as the production reaction can have more degrees of freedom (see discussion in Sec. 3.2).

Using Eq. (2.3) with the corresponding initial and final states from Eq. (2.33), we obtain the unitarity constraint for the production amplitude. For a complete set of states which we insert in Eq. (2.11) we include only the strongly coupled channels to the sum. Then, the partial-wave expansion is introduced in the same way as in Eq. (2.14). Omitting the straightforward calculations, we arrive at the unitarity equation for the partial wave production amplitude.

$$F_l(s) - F_l^*(s) = i\,T_l^*(s)\,\rho(s)\,F_l(s)\,\theta(s - s_{\mathrm{th}}), \tag{2.34}$$

where F_l is a vector of the partial wave amplitudes which, for the example of $\eta\pi/\rho\pi$ production, has two components. T_l is the elastic scattering matrix (2.14).

Eq. (2.34) establishes an important relation with the scattering amplitude T_l, which allows us to extract the resonance physics, an attribute of the scattering amplitude, from the production process accessible in the experiment. There are two common methods to express the production amplitude F_l through the scattering amplitude T_l: the method of the production vector with slight variations of P-vector and Q-vector [52, 66] and the approach to which we refer as the *unitarized background* construction (*a.k.a.* Deck-type production [66]).

The simplest construction of the production amplitude reads:

$$F_l(s) = T_l(s)\alpha(s), \tag{2.35}$$

where α is a vector of functions which does not have a right-hand cut, *i.e.* $\alpha(s) - \alpha^*(s) = 0$ for $s > s_{\text{thr}}$.[7] To demonstrate that the constraint (2.34) is satisfied we just need to plug Eq. (2.35) into Eq. (2.34) and use $d_s F_l(s) = d_s T_l(s)\alpha(s)$ and the unitarity of T_l, *i.e.* Eq. (2.15). The functions α_i are customarily parameterized by a polynomial [66], a combination of left poles [4] or a set of the left-hand cuts [68].

The second method was proposed in a way we consider it here in Ref. [62]. The amplitude F_l can be written as a sum of two terms: the first one, $G_l(s)$ contains the right-hand cut, and the second one, $B_l(s)$ which has only the left-hand cuts/singularities,

$$F_l(s) = G_l(s) + B_l(s). \tag{2.36}$$

$B_l(s)$ could be a given vector of the 'background' terms. In order to satisfy unitarity $G_l(s)$ should obey the following equation.

$$d_s G_l(s) = i\, T_l^*(s)\rho(s)\left(G_l(s) + B_l(s)\right), \tag{2.37}$$

which is known as the Riemann-Hilbert problem [46], or in particular Omnès problem [69]. The amplitude $G_l(s)$ is constructed in the form $G_l(s) = T_l(s)c_l(s)$ where $c_l(s)$ is a production vector.[8] In contrast to the previous case, $c_l(s)$ is not arbitrary, its right-hand cut is constrained by unitarity (2.34). To find the constraint we related the discontinuity of G_l to the discontinuity of $c_l(s)$ as follows.

$$
\begin{aligned}
G_l(s) - G_l^*(s) &= T_l(s)c_l(s) - T_l^*(s)c_l^*(s) \\
&= (T_l(s) - T_l^*(s))c_l(s) + T_l^*(s)(c_l(s) - c_l^*(s)) \\
&= i\,T_l^*(s)\rho(s)T_l(s)c_l(s) + T_l^*(s)(c_l(s) - c_l^*(s)) \\
&= i\,T_l^*(s)\rho(s)G_l(s) + T_l^*(s)(c_l(s) - c_l^*(s)).
\end{aligned}
\tag{2.38}
$$

where we used a zero addition $(0 = T_l^*(s)c_l(s) - T_l^*(s)c_l(s))$ in the second line and the unitarity of the matrix T_l at the third line. Then, by comparing Eq. (2.38) to the left part of Eq. (2.37), we find:

$$c_l(s) - c_l^*(s) = i\,\rho(s)\,B_l(s). \tag{2.39}$$

---

[7] Since $\alpha(s)$ is real above the threshold, the phase of F_l is the same as the phase of $T_l(s)$. It is known as the Watson's theorem after Ref. [67].

[8] We notice that the solution is not unique since the left-hand cut of G_l is not constrained. In Ref. [69] R. Omnès presented a construction of G_l that is required to contain only the right-hand cut. This solution is determined up to an arbitrary polynomial.

This equation can be satisfied by the dispersive-integral construction,

$$c_l(s) = \beta(s) + \frac{1}{2\pi} \int_{s_{\text{th}}}^{\infty} \frac{\rho(s')\, B_l(s')}{s' - s} \mathrm{d}s',$$ (2.40)

where $\beta(s)$ is a function without the left-hand cut as in Eq. (2.35). We see that for a specific background amplitude $B_l(s)$, the function $c_l(s)$ contains a compensating dispersive term, which keeps the unitarity constraint satisfied. For the final form of the model we indicate a common terminology used to refer to the different terms:

$$F_l(s) = \underbrace{B_l(s)}_{\text{Background}} + \underbrace{\frac{T_l(s)}{2\pi} \int_{s_{\text{th}}}^{\infty} \frac{\rho(s')\, B_l(s')}{s' - s} \mathrm{d}s'}_{\text{Unitarization}} + \underbrace{T_l(s)\beta(s)}_{\text{Direct production}},$$ (2.41)

It is important to mention that a separation between the "background" and the "direct production" does not have a strict physical meaning, the amplitude is equivalent to Eq. (2.35) as can be shown by simple algebraic manipulations [70]. However, the parametrization (2.41) has an interesting property emphasized in Ref. [62]: in the limit $T_l \to 0$ the amplitude F_l reduces to B_l.

Studies of the three-pion system at COMPASS

3.1 Introduction to the COMPASS experiment

The COMPASS experiment is a fixed-target experiment located at CERN, aiming to develop a better understanding of the structure and dynamics of hadrons. The experiment operates with a pion or a muon beam with energies up to 190 GeV which is scattered off a liquid hydrogen or solid nuclear targets. The hadronic program of COMPASS includes precision spectroscopy of light mesons, identification and studies of exotic states with gluonic degrees of freedom or multiquark configurations as well as tests of chiral dynamics. Tracking over a wide angular and momentum range and hermetic calorimetry allows for exclusive measurements of the mutli-hadron final states. Due to high beam energy the production reaction is clean: the excited meson system is boosted forward, it is kinematically separated from the baryon vertex, the recoil proton occupies a rapidity domain disjoint with the final state mesons. The muon program is focused on the investigation of the spin structure of nucleon via measurements of the Deep Inelastic Scattering (DIS) processes. [1]

The setup is modified as per the demands of the physical program. Fig. 3.1 shows the setup for measurements with hadron beams starting in 2008, an extensive description of the COMPASS instrumentation can be found in Ref. [72], specifically for physics with hadron beams in Ref. [73]. The 50 m long apparatus starts with the beam section where the beam particle is tracked by silicon microstrip detectors and identified by a pair of differential Cherenkov counters (CEDAR). The Beam Momentum Station (BMS), dedicated to determination of the incident momentum for studies with the muon beam, is moved out of the beam line to minimize amount of material along the beam path. The following target region contains the target filled with liquid hydrogen and the time-of-flight detector that is called Recoil Proton Detector (RPD). The RPD plays an important role in both the trigger formation and offline analyses to ensure exclusivity of the reactions under investigation. One unique feature of COMPASS is that the spectrometer has two stages which cover different ranges of momenta and scattering angles of the produced particles. Essentially, the classical sequence of particle detectors (dipole magnet surrounded by the tracking devices, also calorimetry, and muon ID systems) is replicated twice. The first stage, named *Large Angle Spectrometer*, serves to measure particles which leave the target region with large angles up to 180 mrad (mostly particles with low

---

[1] COMPASS experiment was upgraded in 2010-2012 years and named COMPASS-II [71]. In addition to the measurements of the DIS processes and tests of chiral dynamics, the physical program included studies of the Deeply Virtual Compton Scattering processes with the muon beam, and the Drell-Yan muon pair production processes with the pion beam.
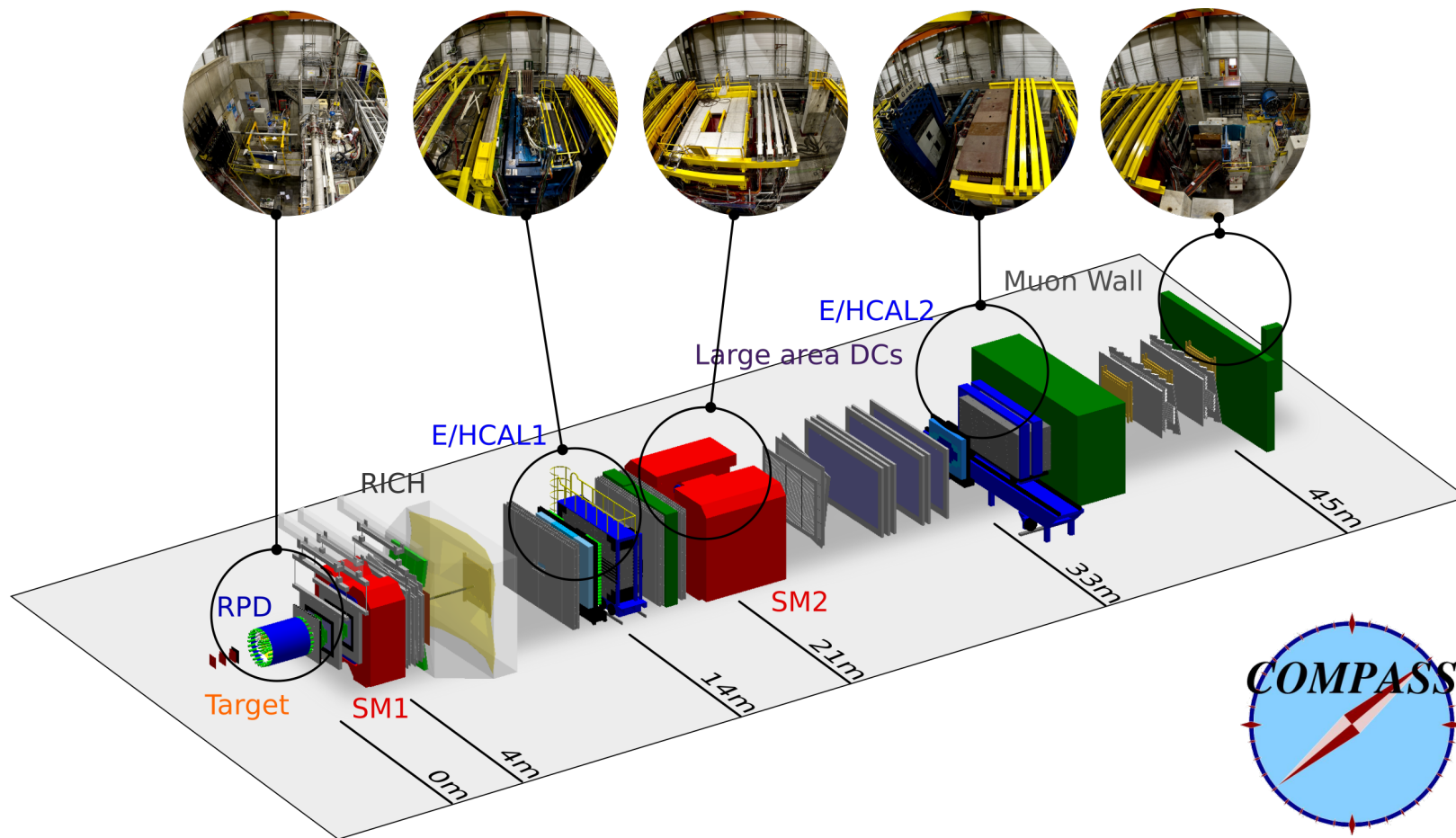
Figure 3.1: A schematic view of the COMPASS experiment setup of 2008. The 3D-model is exported from the `GEANT4`-based simulation program, `TGeant` described in details in Ref. [74, 75]. The panoramic photos can be found in the CERN PhotoLab, see Ref. [76].

momenta). It is also equipped with the Ring-Imaging Cherenkov detector (RICH) where changed particles with the momentum up to 50 GeV can be identified as pions, kaons or antiproton. The calorimeters and muon filters of the first stage have large windows in the middle, so particles with small angles less than approximately 70 mrad can pass through. The second stage is called *Small Angle Spectrometer*, it covers the largest part of the experiment acceptance. The significant longitudinal scale of COMPASS facilitates a good momentum resolution for the charged particles. The calorimeters have a fine granularity: the central regions of the ECAL1 and ECAL2 contain the lead glass and the shashlik type modules, respectively, with the cell size, 3.8 cm.

A large data set with a 190 GeV pion beam was collected during the summer of 2008. The 40 cm long liquid hydrogen target was installed used. A key advantage of COMPASS over the previous experiments is a high beam intensity of up to 10^8 particles per spill of 9.6 s. The physical events were recorded with a dedicated DT0 trigger which required: a beam signal determined by a coincidence of scintillating fiber detectors (SciFi) with a small scintillating disc (Beam Counter), a signal in the RPD (scintillator slabs surrounding the target), and a signal from Veto System. This system contains three components: three hodoscopes upstream the target, large lead-scintillator detector, and two scintillating counters, located exactly on the track of the non-interacting beam at the end of the experiment. With this trigger setup the recorded data was enriched with the diffractive scattering events. A rate of approximately 180 000 events per 10 s spill was reached [73]. The measured final states mostly contain charged pions, kaons, as well as photons from the decay of neutral pion and eta-mesons. The target recoil proton takes up the momentum transferred from the beam. In order to produce a trigger signal, this recoil proton needs to pass through the target material and the cryostat pipe and cross both scintillator rings of RPD. It limits the momentum of observable recoil protons to values larger than 250 MeV, which is equivalent to a proton kinetic energy of 30 MeV. The associated transferred momentum squared, t is defined as the squared difference between four-momentum of the target proton p_t and recoil proton p_r, $t = (p_r - p_t)^2$. It is limited to $t < -0.065\,\mathrm{GeV}^2$.

The elastic $\pi^- p$ scattering has the highest cross section and dominates the collected data set. The diffractive production $\pi^- p \to 3\pi\ p$ has the second largest cross section. The COMPASS experiment has a large acceptance and a high efficiency for the charge configuration $\pi^- \pi^+ \pi^-$: the efficiency for tracking and vertexing for particles with momentum above 3 GeV is above 94% as shown in Ref. [73], the averaged acceptance for the reaction $\pi^- p \to \pi^- \pi^+ \pi^-\ p$ is 50% (see Ref. [77]). The pions are reconstructed using tracking detectors. The interaction vertex position is determined by track extrapolation to the target area. The recoil proton is measured in the RPD, however, since the reaction is over-constrained, the RPD measurements are used to suppress non-exclusive background.

The analysis is based on 10^9 events recorded during four two-weeks periods of beam time in 2008. A set of selection criteria is employed to isolate a clean sample of exclusive $\pi^- p \to \pi^- \pi^+ \pi^-\ p$ events. The details of the event selection are described in Ref. [77] and just briefly listed below:

1. DT0 trigger bit must be set.

2. The event must contain exactly three outgoing particles with a total charge of -1.

3. The position of the interaction vertex found by the reconstruction algorithm must be located inside the fiducial volume of the target (38 cm × ⌀3.2 cm).

4. The energy of the beam calculated from the energies and momenta of the outgoing particles is required to be within a window of ± 3.78 GeV around the nominal beam momentum of

191 GeV, which corresponds to two standard deviations (see Fig. 3.2). [2]

5. The event must have exactly one recoil particle detected by the RPD whose the azimuthal coordinate is required to be opposite to the one for the outgoing 3π system within the azimuthal resolution of the RPD (In Ref. [77] it was found in the range from $5°$ to $9°$ depending on the crossed slab of the RPD rings).

6. The event is rejected if the beam particle is identified as a kaon by the two beam Cherenkov detectors or if at least one of the outgoing particles is identified as a kaon, proton, electron, or the "noise" by the forward RICH detector [78].

7. In order to suppress the background from central production reactions $\pi^- p \to \pi_{\text{fast}}^- \pi^+ \pi^- p$ the event is required to have a Feynman-x below 0.9, where x is defined by the ratio of the longitudinal momentum of the fast negatively charged pion in the beam-target rest frame to it maximal value approximated by $\sqrt{s_0}/2$.

$$x = \frac{2|(\vec{p}_{\text{fast}})_z^{(\text{CM}_0)}|}{\sqrt{s_0}},$$

where the z-direction in set by the beam particle.

Approximately 50×10^6 events passed all selection cuts and were used in the further analysis.

3.2 Physics of the three-pion system

The reaction $\pi^- p \to \pi^- \pi^+ \pi^- p$ has a $2 \to 4$ signature. Therefore, it is completely defined by 8 quantities. [3] These 8 quantities can be either invariant variables or any other frame-dependent observables, as long as the frame is unambiguously specified. To facilitate further discussions on the 3π angular analysis we parametrize the kinematics by the invariant mass squared of the 3π system denoted by $s = (p_1 + p_2 + p_3)^2$, 5 variables which completely describe the orientation of the three pions ($5 = 9 - 4$, three particles with three d.o.f. and four constraints for the energy-momentum conservation), and the two Mandelstam variables related to the $2 \to 2$ production reaction ($\pi^- p \to X^- p$ with $X = 3\pi$), which are the total invariant mass squared $s_0 = (p_b + p_t)^2$ and the transferred momentum squared, $t = (p_r - p_t)^2$, as introduced above. We also use $t' = |t| - |t|_{\text{min}}$, the reduced transferred momentum squared beyond the kinematic limit.

Fig. 3.3 shows the general diagram for a $2 \to 4$ reaction where the shaded interaction area contains all possible dynamics. The COMPASS experiment is set up to study a specific kinematic region of the reaction with its dominant production mechanism as shown in Fig. 3.4. Due to the high value of the total invariant mass, the reaction is dominated by long-range exchange processes between the

---

[2] The energy of the beam particle is calculated based on the constraint on the mass of the recoil particle as follows. The recoil four-vector is fully defined by $p_b + p_t - p_X$, where p_b is the beam vector for which the magnitude is unknown, the target proton four vector p_t, is assumed to be $(m_p, 0, 0, 0)$, and p_X is the sum of the pion four-momenta. By imposing the constraint $p_r^2 = m_p^2$, the energy of the beam can be calculated. A check of exclusivity is done by restricting the energy sum of pions. The deviation from the expected energy of the beam cannot be large since the recoil energy is small and has an exponentially falling spectrum (see Fig. 3.2, $t' \approx -t = 2mT_r$, where T_r is the recoil kinetic energy).

[3] Six particles with fixed masses have $6 \cdot 3 = 18$ degrees of freedom, which are constrained by four energy-momentum conservation laws, the other six degrees of freedom are taken out by fixing the frame (three rotations and three boosts).
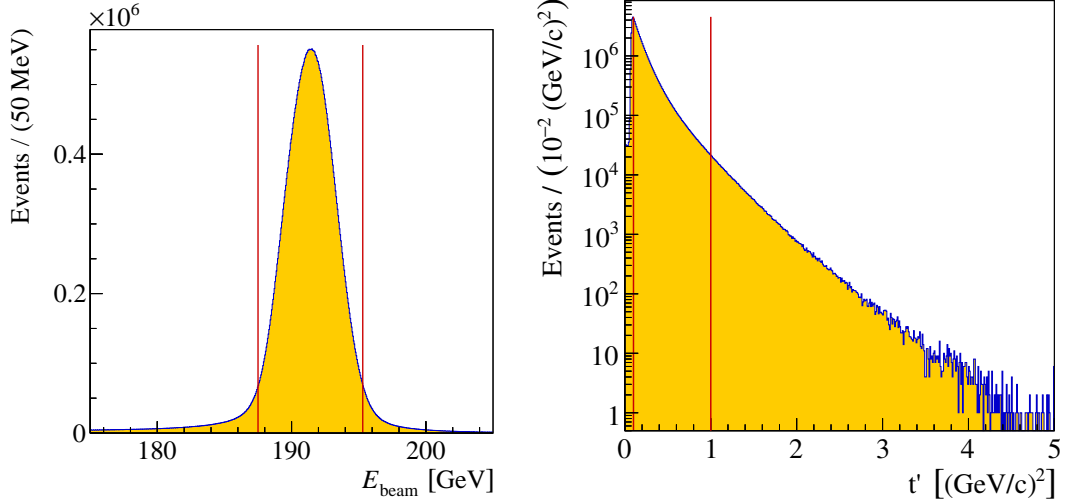
Figure 3.2: Kinematic distributions for the reaction $\pi^- p \to \pi^- \pi^+ \pi^- p$. The left plot shows the exclusivity check, the calculated energy of the beam is restricted in the range indicated by the red lines. The right plot presents the spectrum of the reduced transferred momentum squared beyond the kinematic limit, $t' = |t| - |t|_{\min}$; the red lines show a range used in the discussed analysis. The plots are from Ref. [78]
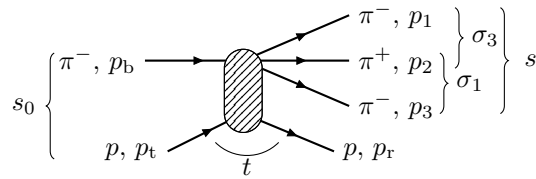
Figure 3.3: A general schematic diagram for the reaction $\pi^- p \to \pi^- \pi^+ \pi^- p$. The beam momentum is denoted by p_{b}, while p_{t} and p_{r} are the four-momenta of the target proton and the recoil proton, respectively. The pion four-momenta are p_i, where $i = 1, 2, 3$. The invariants are shown by curly braces, s_0 is the total invariant mass of the reaction, s is the invariant mass of the three-pion system, t stands for the transferred momentum square. The invariant masses in the two pion subchannels are defined in a circular convention $\sigma_k = (p_i + p_j)^2$, where (ijk) are $\in \{(123), (231), (312)\}$.
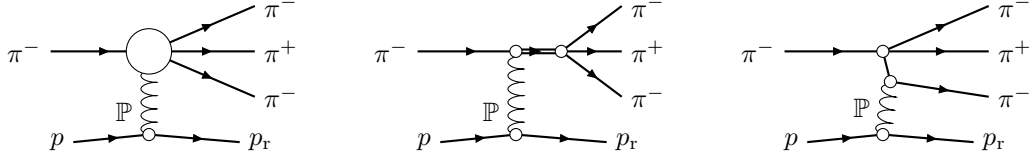
Figure 3.4: Production regimes for the reaction $\pi^- p \to \pi^- \pi^+ \pi^- p$. The left diagram represents diffractive reaction, where the proton stays intact. The reaction is the dominant process at COMPASS due to the high energy of the beam, $\sqrt{s_0} \approx 19\,\text{GeV}$ and the RPD-based COMPASS trigger. The middle and the right diagrams show further specification of the dynamics: when the invariant mass of the 3π system is relatively small, $\sqrt{s} \equiv m_{3\pi} < 3\,\text{GeV}$ the production is dominated by resonances (middle plot), for high values of $\sqrt{s}$ exchange dynamics dominated by pion the exchange takes over (right plot).

pion beam and the target proton. Further insight into the exchange dynamics can be obtained in the framework of Regge theory [39, 79]. The exchange particles are classified by Regge trajectories $\alpha(t)$ (approximately linear relation between the angular momentum of the exchange particle, $J = \alpha$, and its mass squared t), and there is a simple asymptotic expression for the amplitude of the reaction $\pi^- p \to \pi^- \pi^+ \pi^- p$ at high energies:

$$A(s_0, t) \propto s_0^{\alpha(t)}, \tag{3.1}$$

where one assumes the dominance of a single trajectory $\alpha(t)$. For the COMPASS setup, $s_0 \approx 360\,\text{GeV}^2$, the Pomeron trajectory is supposed to dominate. The Pomeron is a special flavorless gluonic object which was introduced to describe the elastic scattering at high energies, *e.g.* pp, $p\bar{p}$, $p\pi$, $\pi\bar{p}$ [26] as well as diffractive dissociation [80]. The trajectory has the highest *intercept*, $\alpha(0) \approx 1$, hence the fastest rise of the forward ($t \to 0$) scattering amplitude. The conventional Reggeon-exchange trajectories are suppressed for processes with low transferred momentum squared, t. The Pomeron dominance leads to the decomposition shown in the left plot of Fig. 3.4, where the 3π production dynamics is reduced to the $\pi\mathbb{P} \to 3\pi$ interaction blob. For the latter, analogously, there are two distinguishable production mechanisms: low energies $\sqrt{s} \equiv m_{3\pi} < 3\,\text{GeV}$ governed by the short-range interaction in the system $\pi\,\mathbb{P}$ (hadronic resonances as in the middle plot of Fig. 3.4), and at high energies $\sqrt{s} > 3\,\text{GeV}$ ruled by the long-range exchange forces as shown in the right plot of Fig. 3.4.

The spectrum of the low-energy region is very rich. The 3π invariant mass distribution shown in Fig. 3.5 (right) exhibits many peaks, which correspond to different resonance excitations. Resonances are also present in the $\pi^+\pi^-$ subchannels, as can be seen in Fig 3.5 (left). These are later referred to as ξ. While looking at the raw spectrum, one can already identify a few well-known mesons $\rho(770)$ and $f_2(1270)$. Less evidently, $f_0(980)$ enhances the right tail of the $\rho(770)$. The kinematics of the system of three particles is completely determined by 5 variables which are chosen to be the $\pi^+\pi^-$ invariant mass squared, σ, and two pairs of spherical angles as shown in Fig. 3.6. The vectors p_{b}, p_{t} define the production plane in the 3π rest frame. The orientation of the frame is fixed by the Gottfried-Jackson (GJ)-convention [81]: The beam vector defines the z_{GJ}-axis, the y_{GJ}-axis is oriented along the normal to the production plane ($\vec{y_{\text{GJ}}} = \vec{p_{\text{t}}} \times \vec{p_{\text{b}}}$). The pion momenta are p_k, where $k \in \{1, 2, 3\}$, the pions are labeled as $\pi_1^- \pi_2^+ \pi_3^-$ as shown in Fig. 3.3. We adopt the *spectator notation* (also called "odd-man-out" notation in Ref. [82]), where the pion pair associated with the spectator π_k is labeled by the index k.
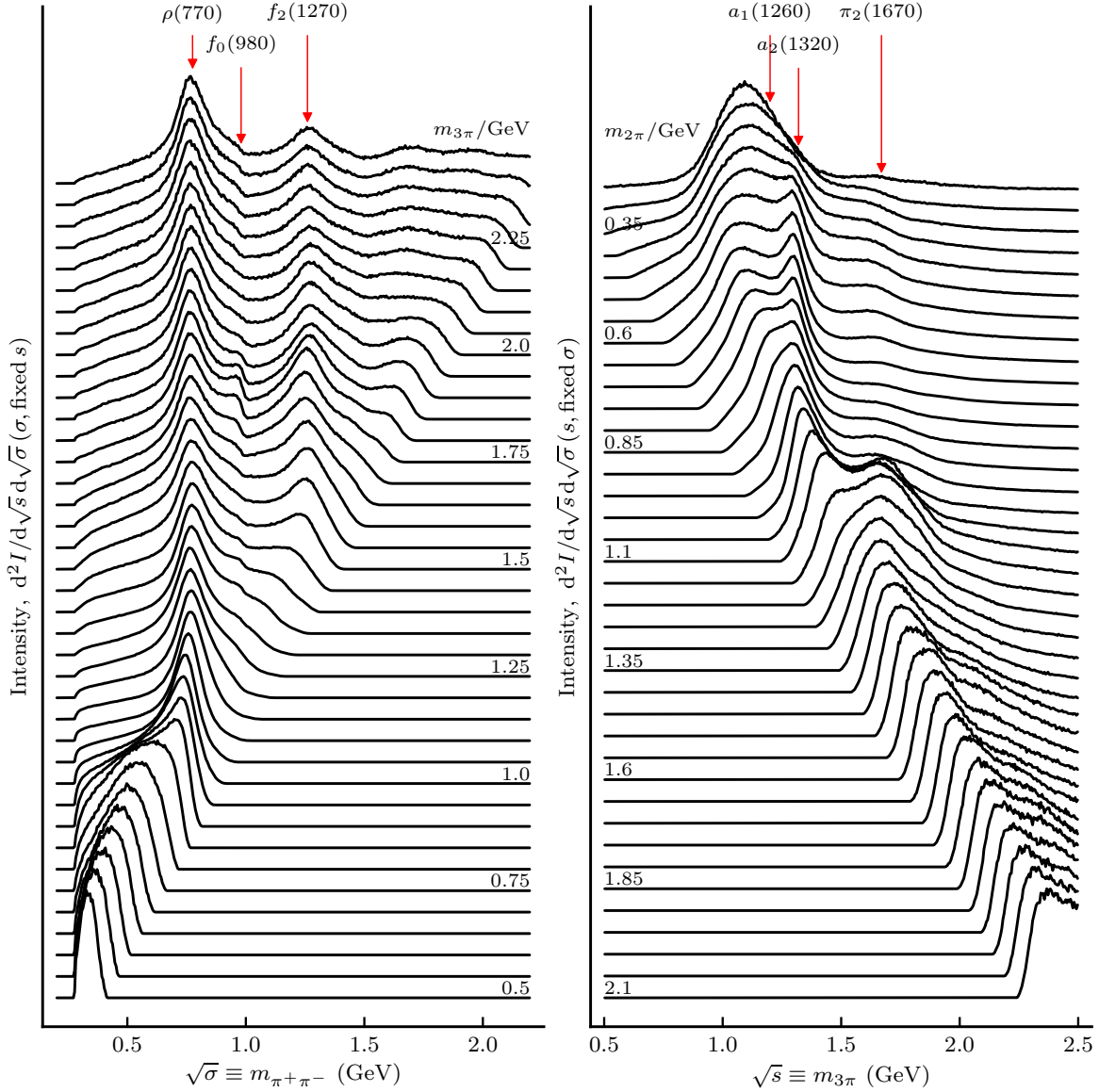
Figure 3.5: A representation of the correlation between the $\pi^+\pi^-$ invariant mass and the 3π invariant mass for the final event sample after all selection cuts (the sample was selected by F. Haas, see Ref. [77]). For the left plot, the $m_{\pi^+\pi^-}$ spectrum is presented in slices of $m_{3\pi}$ invariant mass. The centers of some slices are shown on the right of the plot panel. For the right plot, the slices of the $m_{\pi^+\pi^-}$ are used to present the $m_{3\pi}$ invariant mass spectrum. The central value of the $m_{\pi^+\pi^-}$ in some slices are depicted of the left of the plot panel.
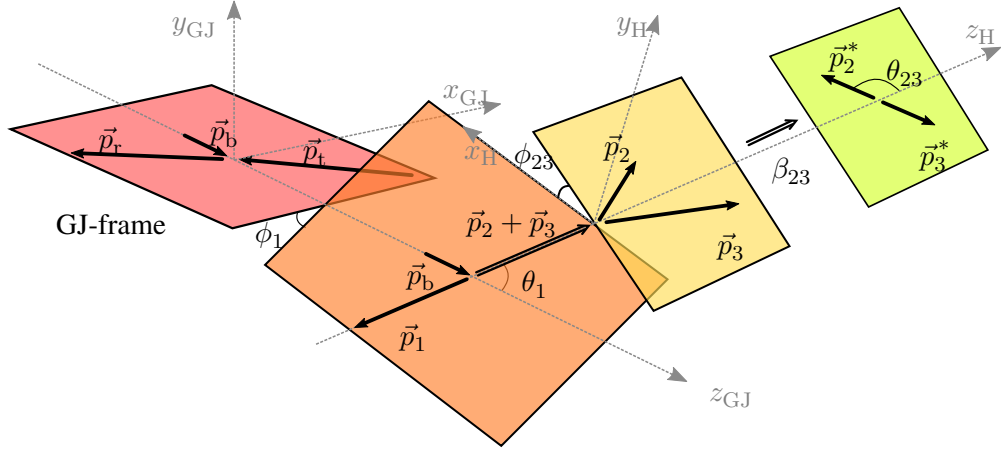
Figure 3.6: Definition of angles in the GJ and the (23)-helicity frames

Thus, $\sigma_k = (p_i + p_j)^2$ is the (ij)-subchannel invariant mass squared where the indices (ijk) stand for the even permutations of (123), *i.e.* $(ijk) \in \{(123), (231), (312)\}$. It allows us to define the set of kinematic variables τ_k unambiguously for any chosen spectator index $k \in \{1, 2, 3\}$.

$$\tau_k = (\sigma_k, \Omega_k, \Omega_{ij}), \tag{3.2}$$

the angles $\Omega_k = (\theta_k, \phi_k)$ are the polar and the azimuthal angles of **the pion pair momentum**, *i.e.* $\vec{p}_i + \vec{p}_j$, in the 3π Center-of-Momentum (CM)-frame; the $\Omega_{ij} = (\theta_{ij}, \phi_{ij})$ are the spherical angles of **the pion i** in the helicity frame of the pion pair (ij). It is important to realize that the sets of variables τ_1, τ_2, and τ_3 are completely equivalent and can be transformed to each other as shown in Appendix C.3. Nevertheless, a formulation of the amplitude dominated by interaction in $\pi_1^- \pi_2^+$ ($\pi_2^+ \pi_3^-$) subchannel is extremely convenient in terms of τ_3 (τ_1). [4] For illustration, the observed distributions of the angular variables Ω_1, Ω_{23} for events with 3π invariant mass near $a_1(1260)$ are shown in Fig. 3.7. The intensity, indicated by the color of the plots is proportional to the square of the amplitude integrated over the remaining kinematic variables. The dominant decay chain in the mass range $1.26 < m_{3\pi} < 1.28 \, \text{GeV}$ selected for Fig. 3.7 is $\rho\pi$ S-wave, where the ρ decays to two pions in a P-wave. However, it is difficult to recognize a simple angular dependence due to the identity of the two negatively charged pions. Indeed, the $\pi_2^+ \pi_1^-$-distribution, dominated by a ρ-meson being projected to the $\cos\theta_{23}$-axis produces an intensity enhancement around 0 along this variable on the right panel of Fig. 3.7.

There are no evident resonance peaks for $m_{3\pi} > 2 \, \text{GeV}$ (see right panel of Fig. 3.5), the high-energy region exhibits new phenomena induced by the long-range exchange shown on the right plot of Fig 3.4. As the $\pi^+\pi^-$ spectrum is still dominated by the resonances (see Fig. 3.9), one of these can be selected for the investigation of the scattering angle distribution in quasi-two-body kinematics $\pi\mathbb{P} \to \xi\pi$. Fig. 3.8 shows the distribution of the scattering angle $\cos\theta_k$, for the production of $\rho\pi$ ($\xi = \rho$ selected by a cut over the $\pi^+\pi^-$ invariant mass $|m_\rho - m_{\pi^+\pi^-}| < 0.2 \, \text{GeV}$) against the invariant mass of the $\xi\pi$ system. For high 3π masses, the events are concentrated in the forward region, $\cos\theta_k \approx 1$

---

[4] We notice that the set τ_2 would useful to study the $\pi^-\pi^-$ interaction with isospin $I \geq 2$, however, this studies are not practical in the system $\pi^-\pi^+\pi^-$ since the $\pi^+\pi^-$ interaction significantly dominates the process.
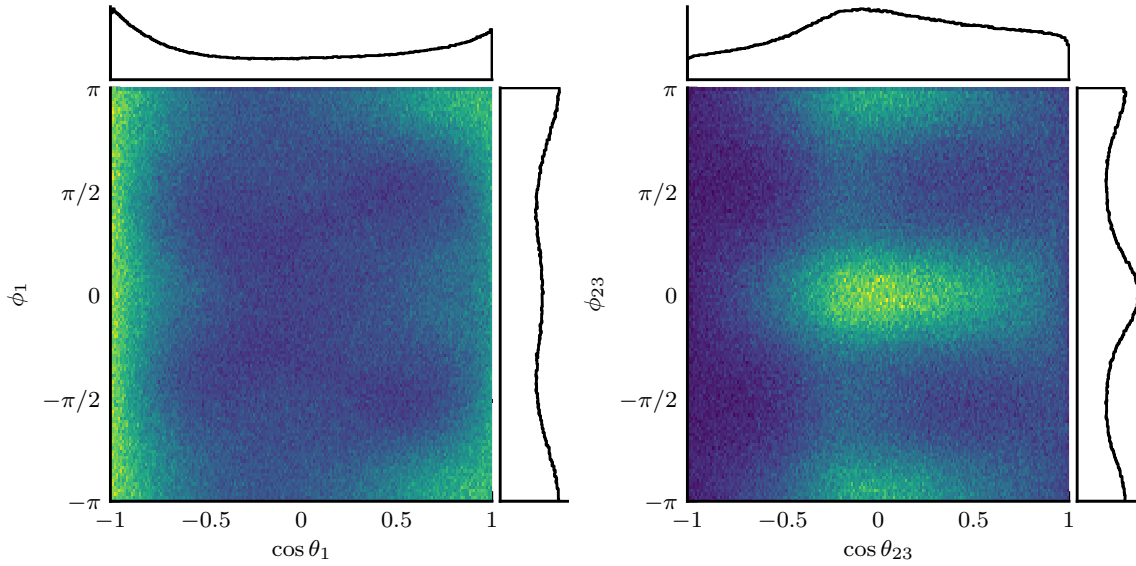
Figure 3.7: Angular distribution of the 3π system selected in the range $1.26 < m_{3\pi} < 1.28 \, \text{GeV}$. The left plot shows the distribution of $\Omega_1 = (\cos\theta_1, \phi_1)$, *i.e.* the direction of the subsystem $\pi^+\pi^-$ in the GJ frame. The right plot shows the distribution of $\Omega_{23} = (\cos\theta_{23}, \phi_{23})$, those are the angles of the π^+ in the $\pi^+\pi^-$ helicity frame. Since the two negative pions are experimentally indistinguishable, the distributions of the τ_1 variables cannot be viewed separately from τ_3 variables, thus, there are two entries per event in each histogram.

($\pi^+\pi^-$-system goes forward in GJ-frame and has high momentum in the laboratory frame in contrast to the bachelor pion which goes backward in the GJ-frame and is therefore rather slow in the laboratory frame), and in the backward region with $\cos\theta_k \approx -1$ (fast π^- and slow $(\pi^+\pi^-)$).

The forward scattering has a rather clear explanation. The pion exchange production shown on the right plot of Fig 3.4 has a high cross section due to the small mass of the pion and contributes exactly to the forward region [40, 83]. The squared transferred momentum between the beam pion and the $\pi^+\pi^-$-system, $t_k = (p_b - p_i - p_j)^2$, can be expressed as a function of the scattering angle as

$$t_k = \sigma_k + m_\pi^2 - \frac{(s + \sigma_k - m_\pi^2)(s + m_\pi^2 - t)}{2s} + \frac{\lambda^{1/2}(s, \sigma_k, m_\pi^2)\lambda^{1/2}(s, m_\pi^2, t)}{2s} \cos\theta_k$$
$$\approx -\frac{s}{2}(1 - \cos\theta_k), \quad s \gg m^2, \sigma_k, t \tag{3.3}$$

where $\lambda(x, y, z)$ is the Källén function. The pion exchange produces a pole in the scattering amplitude by the exchange propagator $1/(m_\pi^2 - t_k)$. While t_k is smaller than zero, it is very close to the pole, $t_k = m_\pi^2$ in the forward region. A quantitative analysis of the pion exchange process is performed in Sec. 5. The backward region is more complicated as it has two structures as shown in Fig. 3.8 (a dip between the broader peak and the narrow spike is made by the selection cut on the Feynman-x variable) and does not have a straightforward interpretation. The possible explanation of the backward events are ρ-exchange processes as well as the central production of the $\pi^+\pi^-$ system, *i.e.* a double diffractive process [84]. In addition, the backward region contains a background from the forward region scattering due to π^- symmetrization, although, its fraction is reduced by the cut on the invariant mass of the pion pair (see caption of Fig. 3.8). It can be understood as follows: for events with forward
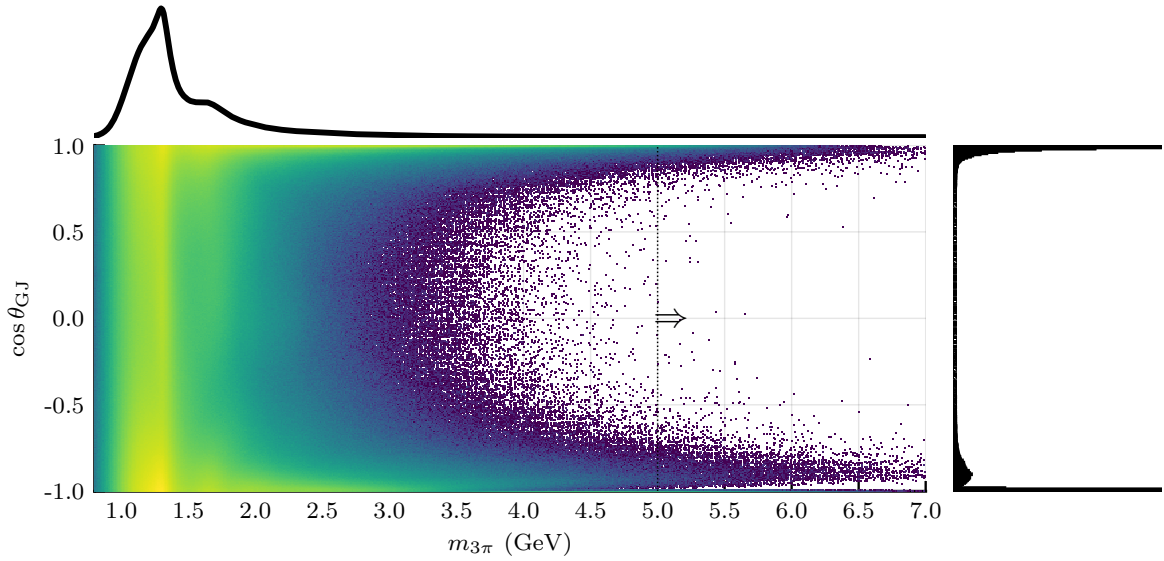
Figure 3.8: A distribution of the events in the variables $\cos\theta_k$, $k = 1, 3$ (denoted on the plot as $\cos\theta_{\mathrm{GJ}}$) and $\sqrt{s} \equiv m_{3\pi}$. There are two entries per event due to the indistinguishable negative pions. The ρ-meson is isolated by cutting on the $\pi^+\pi^-$-invariant mass, $|m_\rho - \sqrt{\sigma_k}| < 0.2\,\mathrm{GeV}$, where $k = 1, 3$. The upper panel shows the projection of the distribution to the s-variable. The events above $5\,\mathrm{GeV}$ (see dashed line) are projected to the $\cos\theta_k$-variable and are shown in the right panel.

$\rho(\to \pi_2^+\pi_3^-)$, the vector of the pion pair $(\pi_1^-\pi_2^+)$ might happen to point backward, however, the invariant mass squared σ_3 is high in this case, therefore, background is significantly diminished by the restriction of $\sqrt{\sigma_3}$ to be in the region of the ρ-meson resonance mass. Fig. 3.9 shows the invariant mass of the $\pi^+\pi^-$ system in three regions of the scattering angles with a band indicating the cut. All plots demonstrate a significant resonance content which confirms that there are forward-backward physical scattering processes. The exchange processes dominate at high energies, moreover, their contribution to the resonance region is significant. The resonance signals are always "sitting" on the coherent irremovable background. Precise studies of the resonances properties require a deep understanding of the exchange dynamics. Therefore, Sec. 5 returns to the subject for a detailed discussion of the pion exchange process shown on the right plot of Fig. 3.4.

3.3 COMPASS Partial Wave Analysis

The Angular analysis, Dalitz plot analysis and the Partial Wave Analysis (PWA) are the main tools in spectroscopy studies. They exploit the same technique of decomposing the reaction amplitude to a set of partial waves based on angular distributions and differ by number of the explored dimensions (a separation is not strict). The partial-wave decomposition helps to identify hadronic resonances and to establish their quantum numbers. These techniques are used by nearly all hadron-spectroscopy experiments (see a few examples from BaBar [85, 86], LHCb [87, 88], CLEO [89]).

The development of the partial-wave analysis technique for the three-pion final state goes back to the 70s to the Brookhaven National Laboratory, bubble chamber experiments and the works of the Illinois
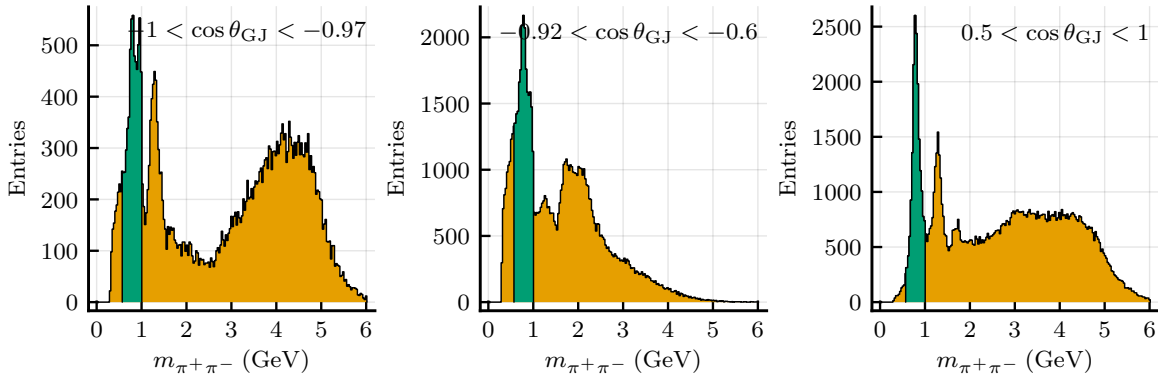
Figure 3.9: Double entered histograms of the $\pi^+\pi^-$ invariant mass in the high-energy range $m_{3\pi} > 5\,\text{GeV}$ for the different changes of the scattering angles $\cos\theta_k$. The green area indicates the cut applied to select ρ-meson, $|m_\rho - \sqrt{\sigma_k}| < 0.2\,\text{GeV}$. Left plot: events in the forward region $\cos\theta > 0.5$, one finds the resonances ρ, f_2 and ρ_3, the pile above $2.5\,\text{GeV}$ is a reflection of the cross channel backward events. Middle plot: events which lead to the broad backward structure in Fig. 3.8, $-0.92 < \cos\theta < -0.6$. Right plot: events in the narrow backward region $\cos\theta < -0.97$. The ρ-meson contribution is small and the f_2 peak is well pronounced. The additional narrow structure at $0.9\,\text{GeV}$ cannot be assigned to known resonances. It requires a dedicated investigation.

group [90, 91]. Both the formalism and the model are quite complicated at first glance, there are many details and aspects to it which we will see in Sec. 3.3.1. However, the main idea is straightforward and can be demonstrated in a rather compact way (see an example of the implementation in Ref. [92]). The three-pion state is characterized by a set of quantum numbers $w = (J^P M \ldots)$, which includes the total spin and parity of the state J^P, the spin projection M, and the relative angular momenta between the pions. Since the 3π resonances appear in states with well defined J^{PC}, the matrix element for the reaction $\pi^- p \to \pi^- \pi^+ \pi^- p$ contains a coherent composition of the three-pion states with these quantum numbers projected into kinematic variables. The essence of the PWA technique is an estimation of the relative contribution of the individual states by a fit to the data. We make a model for the matrix element in a way that,

$$A(t, s, \tau) = \sum_w F_w(t, s) \Psi_w(\tau), \tag{3.4}$$

where $\Psi_w(\tau)$ is a known function of the kinematic variables τ, which are naively the matrix elements of the cascade reaction shown in Fig. 3.10, $F_w(t, s)$ are the weights [5] to be estimated for every value of t and s (the data is binned in s and t). We notice that this expansion (3.4) maps the continuous angular variables τ to the discrete indices w, similarly to the Fourier transformation or an expansion in the Legendre series. The square of the amplitudes $F_w(t, s)$ determines the fraction of the pion states with quantum numbers w in the observed events. In order to find $F_w(t, s)$, the amplitude is squared and fitted to the data using the event-based Likelihood method. The resonances properties are then extracted by detailed analysis of the intensities $I_w \sim |F_w(t, s)|^2$ and relative phase motions $e^{\Delta\phi_{wq}} \sim F_w^*(t, s) F_q(t, s)$ as discussed in Sec. 3.3.3.

---

[5] Strictly speaking these coefficients are allowed to be complex. The complex phases are very significant bits of extracted information as discussed later in the text.
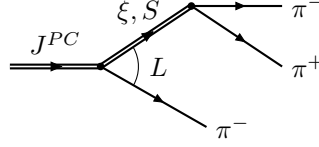
Figure 3.10: A notation of the $J^{PC} M^\epsilon \xi \pi L$ quantum numbers for the cascade decay $X \to 3\pi$. The subchannel $\pi^+\pi^-$ is set in the intermediate state denoted by ξ with spin S. The orbital angular momentum between the Isobar ξ and the bachelor pion is L.

3.3.1 Partial-wave analysis technique of $\pi^- p \to \pi^- \pi^+ \pi^- p$

The amplitude $A_{\lambda'\lambda}(t', s, \tau_1)$ characterizes the transition from $\pi^- p$ to $\pi^- \pi^+ \pi^- p$. In principle, it depends on s_0, however, this variable is fixed by the beam momentum to $s_0 \approx (19 \,\text{GeV})^2$, it will be omitted in the further discussions. $A_{\lambda'\lambda}(t', s, \tau_1)$ is given by the matrix element:

$$\langle 3\pi, p, \lambda' | \, T \, | \pi, p, \lambda \rangle = A_{\lambda'\lambda}(t', s, \tau_1) \, (2\pi)^4 \delta^4(p_\text{b} + p_\text{t} - p_1 - p_2 - p_3 - p_\text{r}), \qquad (3.5)$$

where T is the strong interaction operator, λ (λ') is the helicity of the target (recoil) proton. The helicities are not measured but rather averaged (summed) incoherently.

In the isospin limit the pions are identical particles. The most general decomposition of the $|3\pi\rangle$ state is provided in Appendix C.1. It is very helpful to compare various charge configurations. However, for the $\pi^-\pi^+\pi^-$ system, the interaction dynamics is only significant in the $\pi^+\pi^-$ subsystem, hence, the amplitude is only symmetric with respect to permutations of the π^--momentum. The General Isobar Model explicitly incorporates the $\pi_1^- \pi_3^-$ Bose-symmetry.

$$A_{\lambda'\lambda}(s, \tau) = A^{(3)}_{\lambda'\lambda}(s, \tau_3) + A^{(1)}_{\lambda'\lambda}(s, \tau_1). \qquad (3.6)$$

The amplitude $A^{(k)}_{\lambda'\lambda}$, *i.e. the isobar amplitude*, includes only the subchannel interaction in the $\pi_i \pi_j$ leaving the pion indexed k as a bachelor pion. In Eq. (3.6), we did not add the term for the (31)-system because the interaction in the $\pi^-\pi^-$ subchannel is known to be weak. The kinematic variables τ, in the argument of the full amplitude τ refers to any τ_i, $i \in \{1, 2, 3\}$ as those are equivalent, while there are certain advantages of using the variables τ_k for $A^{(k)}_{\lambda'\lambda}$.

Partial-wave expansion

The $A^{(k)}_{\lambda'\lambda}$ are projected to the partial waves in the canonical basis as described in Appendix C.1 (see also Ref. [47, 79]),

$$A^{(k)}_{\lambda'\lambda} = \sum_{JMLS,I} \frac{1 + (-1)^{S+I}}{2} C^{(k)}_I \, Z^{JM}_{LS}(\Omega_k, \Omega_{ij}) \, (A_{\lambda'\lambda})^{JM}_{LS}(t, s, \sigma_k), \qquad (3.7)$$

where J and M are the total spin of the state and the spin projection, respectively, S is the orbital angular momentum in the two-pion subsystem (also is equal to spin of isobar), and L is the orbital angular momentum in the isobar-bachelor system. $C^{(k)}_I$ is the isospin factor for the coupling of two

pions to the Isobar isospin state, and the Isobar and the bachelor to the state $|1, -1\rangle$:

$$C_I^{(k)} = \langle 1, \mu_i; 1\mu_j \, | I, 0 \rangle \, \langle I, 0; 1, -1 \, | 1, -1 \rangle \, , \tag{3.8}$$

where μ_i and μ_j are the isospin projections of the pions π_i and π_j, respectively. The Isobar is always neutral, so its isospin state is $|I, 0\rangle$. The total $\pi^- \pi^+ \pi^-$ state is assumed to be of isospin 1, since states with higher values have not been observed and can thus be safely neglected. The isobar projected amplitude $A_{LS}^{JM}(s, \sigma_k)$ does not contain the isospin index I for simplicity. Due to the factor $1 + (-1)^{S+I}$, the odd waves contain only isovector interactions, while the even waves contain the isoscalar isobars. The function Z_{LS}^{JM} is the angular decay function for the decay chain shown in Fig. 3.10

$$Z_{LS}^{JM}(\Omega_k, \Omega_{ij}) = \sqrt{(2L+1)(2S+1)} \sum_\lambda \langle L, 0; S, \lambda \, | J, \lambda \rangle \, D_{M\lambda}^{J*}(\Omega_k) D_{\lambda 0}^{S*}(\Omega_{ij}), \tag{3.9}$$

The Clebsch-Gordan coefficient in Eq. (3.9) reflects the recoupling of the system from the helicity basis to the canonical basis. The Wigner functions, $D_{m_1 m_2}^J$ of two angles $\Omega = (\theta, \phi)$ are defined by $D_{m_1 m_2}^J(\Omega) = D_{m_1 m_2}^J(\phi, \theta, 0)$ (see more details in Appendix C.2).

Parity constraints

Before proceeding to the final expression, we explore the parity conservation of the three-pion state $|3\pi\rangle$ expanded in the canonical basis $|JMLS\rangle$ (see Appendix C.1). We perform a linear transformation of the three-pion state vectors $|JMLS\rangle$ introducing the *reflectivity* index ϵ,

$$\left| J^P M \epsilon, \dots \right\rangle = \theta(M) \left[\left| J^P M, \dots \right\rangle - \epsilon P (-1)^{J-M} \left| J^P - M, \dots \right\rangle \right], \tag{3.10}$$

where ϵ is either $(+1)$ or (-1), the dots stand for other quantum numbers of the state, $\theta(M)$ is zero for negative M, while it is equal to $1/2$ for $M = 0$ and $1/\sqrt{2}$ for positive M. The basis has two advantages: Firstly, in the high-energy limit, the *reflectivity* in the GJ-frame is related to the *naturality* of the exchange [93, 94]. Secondly, different reflectivities are forbidden to interfere by the parity of the production reaction [95]. The *reflectivity* representation of the Wigner D-functions is given by

$$^\epsilon D_{M\lambda}^J(\Omega) = \theta(M) \left[D_{M\lambda}^J(\Omega) - \epsilon P (-1)^{J-M} D_{-M\lambda}^J(\Omega) \right]. \tag{3.11}$$

The decay function $Z_{LS}^{JM\epsilon}(\Omega_k, \Omega_{ij})$ is introduced analogously to Eq. (3.9) with the replacement $D_{M\lambda}^J(\Omega) \to \,^\epsilon D_{M\lambda}^J(\Omega)$. The parity reflection in the new basis relates different helicities (see equation 3.10 of Ref. [96]),

$$(A_{\lambda'\lambda}^\epsilon)_{LS}^{JM} = P\epsilon \, (-1)^{1+\lambda'+\lambda} (A_{-\lambda'-\lambda}^\epsilon)_{LS}^{JM}, \tag{3.12}$$

however, it does not change the other quantum numbers. There are only two independent configurations $(\lambda'\lambda) = (++)$ or $(+-)$, where $\pm$ stands for the spin projection $\pm 1/2$. The amplitudes for the configurations are referred to as the helicity flip and the helicity non-flip amplitudes.

Isobar dynamics

The COMPASS model of the Isobar decay dynamics assumes factorization in the variables s and σ,

$$(A_{\lambda'\lambda})^{JM\epsilon}_{LS}(s,\sigma) = (\mathcal{A}_{\lambda'\lambda})^{JM\epsilon}_{LS}(s) f_S(\sigma)\, h_L(s,\sigma), \tag{3.13}$$

where we introduce the *amputated amplitude* $(\mathcal{A}_{\lambda'\lambda})^{JM\epsilon}_{LS}(s)$, and the Isobar decay function $f_S(\sigma)$, which is customarily parametrized by Breit-Wigner propagators; $h_L(s,\sigma)$ is a function which combines the threshold factor for the $\xi\pi$ L-wave state and the barrier (centrifugal) factor which regularizes the high-energy behavior. In the COMPASS analysis, we use the Blatt-Weisskopf factors for h_L [97, 98] which are discussed in Appendix E.3.

The final expression for the amplitude expansion is found by combining Eq. (3.6) and Eq. (3.7).

$$A_{\lambda'\lambda} = \sum_{\epsilon} \sum_{JMLS} (\mathcal{A}^{\epsilon}_{\lambda'\lambda})^{JM}_{LS}(t,s) \Psi^{JM\epsilon}_{LS}(s,\tau). \tag{3.14}$$

where the basis functions $\Psi^{JM\epsilon}_{LS}$ reads,

$$\Psi^{JM\epsilon}_{LS}(s,\tau) = C^{(1)}_I Z^{JM\epsilon}_{LS}(\Omega_1, \Omega_{23})\, h_L(s,\sigma_1) f_S(\sigma_1)$$
$$+ C^{(3)}_I Z^{JM\epsilon}_{LS}(\Omega_3, \Omega_{12})\, h_L(s,\sigma_3) f_S(\sigma_3).$$

We can explicitly demonstrate that this basis function respects the permutation symmetry of the negatively charged pions. From the symmetry of the Clebsch-Gordan coefficients in Eq. (3.8), we derive a relation between the isospin coefficients: $C^{(3)}_I = (-1)^I C^{(1)}_I$. Using the properties of the Wigner D-functions discussed in Appendix C.2, we can show that $Z^{JM}_{LS}(\Omega_3, \Omega_{12}) = (-1)^S Z^{JM}_{LS}(\Omega_3, \Omega_{21})$. Since only waves with even sum $(S+I)$ are allowed in Eq. (3.7), the phase factors from the isospin coefficient and the angular dependence cancel each other.

The COMPASS analysis [78] uses Ψ, written in the form,

$$\Psi^{JM\epsilon}_{LS}(s,\tau) = Z^{JM\epsilon}_{LS}(\Omega_1, \Omega_{32})\, h_L(s,\sigma_1) f_S(\sigma_1) + Z^{JM\epsilon}_{LS}(\Omega_3, \Omega_{12})\, h_L(s,\sigma_3) f_S(\sigma_3), \tag{3.15}$$

where the numerical factor $C^{(1)}_I$ is dropped, the positive pion is used to determine the spherical angles for the decay of the isobar in both chains, $k = 1,3$. We note, however, that this convention leads to a shift in the relative phases of the waves with different spin of isobars due to the sign of $C^{(1)}_I$, sign $C^{(1)}_I = (-1)^I$.

Partial-waves intensities

The expression for the squared amplitude averaged over the spin projection of the target proton reads

$$\frac{1}{2}\sum_{\lambda'\lambda} |\mathcal{A}_{\lambda'\lambda}|^2 = \frac{1}{2}\sum_{\lambda'\lambda}\sum_{\epsilon} \left| \sum_{JMLS} (\mathcal{A}^{\epsilon}_{\lambda'\lambda})^{JM}_{LS} \Psi^{JM\epsilon}_{LS} \right|^2 \equiv \sum_{b} \left| \sum_{w} \mathcal{A}^{b}_{w} \Psi_{w} \right|^2, \tag{3.16}$$

where for brevity of notation we introduce a short wave lower index $w = (JM\epsilon LS)$, and the upper index b for the non-interfering blocks of the waves, *i.e.* independent helicity configurations (due to the

factor $1/2$) and the two reflectivities, $\epsilon = \pm 1$.

Investigating the three-pion spectrum for a fixed value of the squared transferred momentum we define the intensity distribution as the most convenient representation. The *intensity* is defined as the differential cross-section normalized by the number of observed events,

$$I(t,s) \equiv \frac{\mathrm{d}^2 N}{\mathrm{d}t\,\mathrm{d}s} = c_N \int \mathrm{d}\Phi_3 \sum_b \left| \sum_w \mathcal{A}_w^b \Psi_w \right|^2, \tag{3.17}$$

$$I_{m_{3\pi}}(t,\sqrt{s}) \equiv \frac{\mathrm{d}^2 N}{\mathrm{d}t\,\mathrm{d}\sqrt{s}} = 2\sqrt{s}\, c_N \int \mathrm{d}\Phi_3 \sum_b \left| \sum_w \mathcal{A}_w^b \Psi_w \right|^2, \tag{3.18}$$

$\mathrm{d}\Phi_3$ is the differential three-body phase space, c_N accounts for luminosity and kinematic s_0-dependence (*cf.* Appendix B); it does not depend on s and t. The intensity in the variable $\sqrt{s} \equiv m_{3\pi}$ is more presentative, but it has an additional Jacobian factor $2\sqrt{s}$ with respect to the simple Eq. (3.17) for the differential intensity $I(t,s)$.

Binning

When we consider a narrow bin in $s \times t$, the total number of events can be calculated by integrating Eq. (3.17), and is denoted as the number of *produced* events, $I_{\mathrm{prd}}^{(\mathrm{bin})}$, *i.e.* events which would have happened for a given cross section and integrated luminosity. Clearly, it is different to the number of events expected to be registered, $I_{\mathrm{exp}}^{(\mathrm{bin})}$, due to acceptance effects and efficiencies of the experimental setup denoted by the function $\eta(t,s,\tau)$.

$$I_{\mathrm{prd}}^{(\mathrm{bin})} = c\,\Delta s\,\Delta t \sum_{wq} \mathcal{A}_w^*(\bar{t},\bar{s})\mathcal{A}_q(\bar{t},\bar{s}) \int \Psi_w^*(\tau)\Psi_q(\tau)\,\mathrm{d}\Phi_3, \tag{3.19a}$$

$$I_{\mathrm{exp}}^{(\mathrm{bin})} = c\,\Delta s\,\Delta t \sum_{wq} \mathcal{A}_w^*(\bar{t},\bar{s})\mathcal{A}_q(\bar{t},\bar{s}) \int \Psi_w^*(\tau)\Psi_q(\tau)\eta(t,s,\tau)\,\mathrm{d}\Phi_3, \tag{3.19b}$$

where the amplitude squared integrated over the $s \times t$ bin is written as the averaged value $\mathcal{A}_w^*(\bar{t},\bar{s})\mathcal{A}_q(\bar{t},\bar{s})$ multiplied by the bin size $\Delta s\,\Delta t$. The bins in $m_{3\pi}$ are narrow, therefore one can assume that $\bar{s}$ corresponds to the center of the bin. For $\bar{t}$, however, one has to indeed average due to the rapid behavior of the amplitude. The acceptance function $\eta(t,s,\tau)$ gives a number between 0 and 1 as the probability to observe an event described by variables t, s, and τ. Practically the integrals are calculated using the Monte-Carlo (MC) method. In the narrow $s \times t$ bin, the product of basis functions is averaged over a wider set of observables including the vertex position, the beam energy and direction as well as the remaining s and t dependence inside of the bin. We introduce the matrices B_{wq} and $B_{wq}^{(\eta)}$ as the matrices of integrals over the basis functions,

$$B_{wq} = \int \Psi_w^*(\tau)\Psi_q(\tau)\,\mathrm{d}\Phi_3 \approx \frac{\Phi_3(s)}{N_{\mathrm{MC}}} \sum_{e=1}^{N_{\mathrm{MC}}} \Psi_w^*(\tau_e)\Psi_q(\tau_e), \tag{3.20a}$$

$$B_{wq}^{(\eta)} = \int \Psi_w^*(\tau)\Psi_q(\tau)\eta(t,s,\tau)\,\mathrm{d}\Phi_3 \approx \frac{\Phi_3(s)}{N_{\mathrm{MC}}} \sum_{e=1}^{N_{\mathrm{MC\,acc}}} \Psi_w^*(\tau_e)\Psi_q(\tau_e), \tag{3.20b}$$

where the sum in the second line includes only MC events which passed the reconstruction and the data selection chain. $B_{wq}^{(\eta)}$ gives the averaged value of the COMPASS acceptance for the $\pi^- p \to \pi^- \pi^+ \pi^- p$ reaction with pions in a specific angular combination, it is of the order of 0.5 for most of the waves.

Likelihood fit

After the data have been binned in $t \times s$, the angular analysis (PWA) is performed on the selected sample of events independently bin-by-bin. The *expected* number of events in the bin according to the model is denoted μ. The normalization $c \, \Delta s \, \Delta t$ can be absorbed into the amplitude $\mathcal{A}_w(t, s)$,

$$a_w(\bar{t}, \bar{s}) = \mathcal{A}_w(\bar{t}, \bar{s})/\sqrt{c \, \Delta s \, \Delta t}, \quad \Rightarrow \quad I_{\text{exp}}^{(\text{bin})} = \sum_{wq} a_w^* B_{wq}^{(\eta)} \, a_q, \tag{3.21}$$

such that the expression for $I_{\text{prd}}^{(\text{bin})}$ is a simple bilinear form of amplitude values a_w, which make a vector of parameters for a given bin. For a data set of N events we define the likelihood function which estimates our model specified by a vector of parameters a_w.

$$\mathfrak{L}_0 = \prod_{e=1}^{N} \mathcal{P}(\tau_e), \qquad \mathcal{P}(\tau_e) = \sum_{wq} \frac{a_w^* \Psi_w^*(\tau_e) \, a_q \Psi_q(\tau_e) \, \eta(\tau_e)}{\sum_{wq} a_w^* B_{wq}^{(\eta)} a_q}, \tag{3.22}$$

where τ_e is the set of kinematic variables specified in Eq. (3.2) for the eth event in the set. By maximizing the function $\mathfrak{L}_0$ we can obtain an estimate for the parameters a_w. However, the estimator $\mathfrak{L}_0$ has a little disadvantage: a normalization of parameters a_w is set. Indeed, the likelihood function in Eq. (3.22) is invariant under simultaneous scaling of all parameters, $a_w \to \alpha a_w$. Hence, after the parameters are estimated by maximizing $\mathfrak{L}_0$ one has to adjust the scale α to enforce $I_{\text{exp}}^{(\text{bin})} \to N$. The Extended Likelihood estimator is defined by adding the Poisson distribution function which achieves the maximum only when the constraint $I_{\text{exp}}^{(\text{bin})} = N$ is satisfied [99].

$$\mathfrak{L} = \frac{e^{-\mu} \mu^N}{N!} \prod_{e=1}^{N} \mathcal{P}(\tau_e), \tag{3.23}$$

where we use the Poisson mean value $\mu = I_{\text{exp}}^{(\text{bin})}$ for brevity. The Poisson factor is justified as a probability to observe exactly N events with the mean μ in the model. Practically, we minimize the Negative Log-likelihood Function, which reads,

$$-\log \mathfrak{L} = -\sum_{e=1}^{N} \log \left| \sum_w a_w \Psi_w(\tau_e) \right|^2 + \sum_{wq} a_w^* B_{wq}^{(\eta)} a_q + \text{const.} \tag{3.24}$$

The terms which do not have a dependence on a_w are pulled to the irrelevant constant as they play no role in finding the minimum. The minimum is found by running the gradient minimization provided by external packages as `Minuit` [100] or `NLopt` [101]. The estimated parameters are used to calculate the number of events which can be attributed to the individual wave, *the wave intensity*, using the integral matrix, as $a_w^* B_{ww} a_w$. The Spin Density Matrix (SDM) is defined by the outer product of

parameter vectors normalized by the integrals B_{wq},

$$(\text{SDM})_{wq} = a_w^* a_q \sqrt{B_{ww} B_{qq}}. \tag{3.25}$$

The diagonal elements of the SDM are the wave intensities, and the off-diagonal elements are referred to as the *interference terms*. The matrix defined in Eq. (3.25) is degenerate. It becomes clear if we notice that all column (also rows) of this matrix are proportional to the vector $a_q \sqrt{B_{qq}}$. Rank of such matrix is 1 since the space of the column vectors can be spanned by a single basis vector. A simple example of rank-2 matrix is $v_w^* v_q + v_w'^* v_q'$: the basis of the column vectors is spanned now by two vectors, v_q and v_q'. For the complete SDM defined with respect to Eq. (3.16), the total rank is given by the number of terms in the sum over the index b. Since the different reflectivities, $\epsilon = (\pm 1)$ form orthogonal spaces of parameter vectors, it is reasonable to speak about the rank of the positive reflectivity sector and the negative reflectivity sector separately. The maximal value of the rank motivated by the sum over proton helicity configurations in Eq. (3.16) is 2. However, there is no reason for a difference between the helicity flip and the helicity non-flip amplitudes for the fixed value of t' under assumption of the Pomeron exchange. Therefore, the rank-1 approach is expected to be a good approximation.

Error estimation

Errors for the a_w parameters are estimated using the Hessian matrix, *i.e.* the matrix of second derivatives in the minimum [99, 102, 103].

$$C_{\text{stat}} = H^{-1}, \quad H_{wq} = - \frac{\text{d}^2 \log \mathfrak{L}}{\text{d}a_w \text{d}a_q}\bigg|_{\text{min}}, \tag{3.26}$$

where C_{stat} is the covariance matrix for the parameter vector a. The crude assumption of a parabolic shape of the minimum made in the hessian approach is a known issue of the current PWA procedure [104]. The propagation of the errors of a_w to the SDM is done numerically by generating a sample of variables a_w^{MC} with the mean $a_w|_{\text{min}}$ and the covariance C_{stat} using a multidimensional Gaussian (see Cholesky decomposition [99]). The mean and the root mean square of the obtained distributions for the SDM elements are used as main uncertainties of the PWA results.

3.3.2 The main COMPASS model and results

The main model includes 88 waves.

$$
\begin{aligned}
a_w = (\,a_1, & \quad a_2, \ldots a_{81}, & \quad a_{82}, \ldots, a_{88}, & \quad a'_{82}, \ldots, a'_{88}) \\
\Psi_w = (\,\underbrace{\Psi_1}_{\text{FLAT}}, & \quad \underbrace{\Psi_2, \ldots \Psi_{81}}_{\epsilon=(+1)}, & \quad \underbrace{\Psi_{82}, \ldots, \Psi_{88}}_{\epsilon=(-1)}, & \quad \underbrace{\Psi_{82}, \ldots, \Psi_{88}}_{\epsilon=(-1)}),
\end{aligned}
$$

where a_w and a'_w are complex numbers which are fixed by a fit to data. The block of positive reflectivities is the main physical component of the model. The basis function for the FLAT wave is constant $\Psi_{\text{FLAT}} = 1$, it represents an incoherent background distributed according to the phase space in all kinematic variables τ. In addition, the model includes 7 waves with negative reflectivity
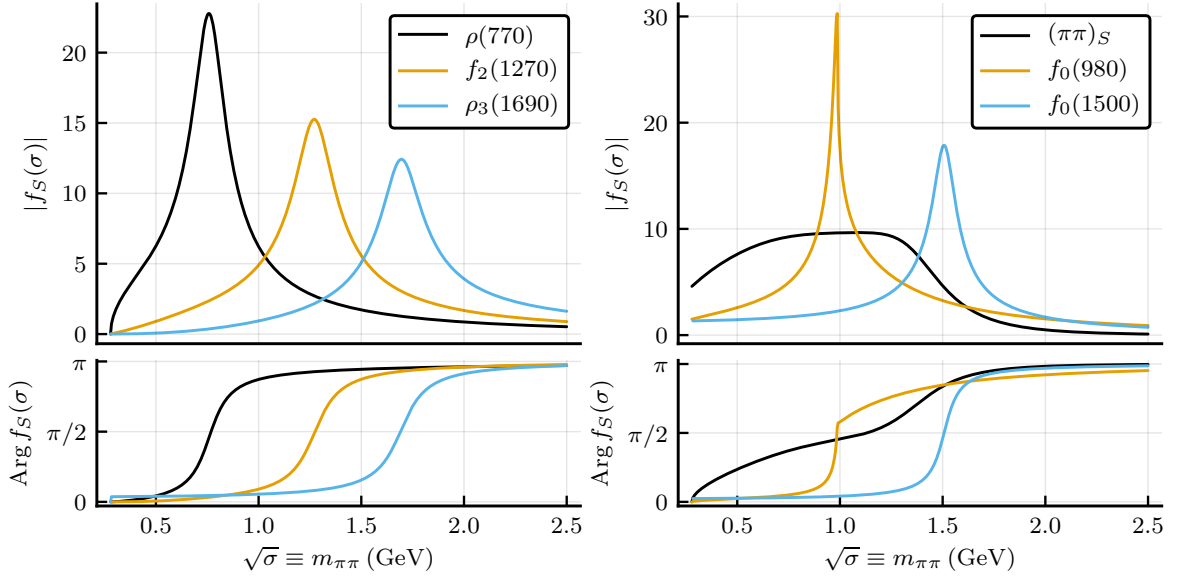
Figure 3.11: The parametrization of the $\pi\pi$ isobars used in COMPASS analysis. Plots in the top row show the absolute value of the amplitude $f_S(\sigma)$, plots on the bottom present the phases. The amplitudes for the non-scalar waves, $S > 0$, are shown in the left column. Components of the $[\pi\pi]_S$ parametrization are shown on the right. The intensities are normalized by a total integral as shown in Eq. (D.3).

which are incorporated with the rank-2, *i.e.* the basis functions are repeated twice with different sets of parameters. Practically, those three blocks (FLAT and $\epsilon = (-1)$) serve to account parasitic effects such as a lack of acceptance description, resolution effects, and a background *e.g.* from the central production. They make the fit more stable, and the intensity which goes to those blocks does not exceed 10 %. The waves between different blocks are forbidden to interfere. The parameters a_i are complex in general. The overall phase freedom at every non-interfering block is removed by fixing the phase of one wave to zero. The total number of the free parameters is 186 for every $t \times s$ bin. [6]

The waves are labeled by the set $J^{PC} M^\epsilon \xi\pi L$, where ξ shows the resonance in the $\pi^+\pi^-$ subchannel. A list of all waves is given in the Appendix D. J varies between 0 and 6, for both parities P (except $J^{PC} = 0^+$ and 5^-). The change states are not eigenstates of C parity, however, $C = (+)$ can be inferred from the G-parity and the total isospin 1; it corresponds to the proper C-parity eigenvalue of the neutral component in the isospin triplet. The projection M is less than 2. The analysis include six $\pi^+\pi^-$ isobars, which are shown in Fig. 3.11, the expressions are given in Appendix D. The $\rho(770)$ parametrizes the $[\pi\pi]$ P-wave, the $[\pi\pi]$ D-wave contains the $f_2(1270)$, the $\rho_3(1670)$ Breit-Wigner-amplitude is a model for the $[\pi\pi]$ F-wave. The S-wave interaction is split into 3 resonances which are incorporated independently: the $f_0(500)$ is parametrized by I. Kachaev's modification of the Au-Morgan-Pennington solution [105, 106], while the $f_0(980)$ is parametrized by the Flatté formula [107] and $f_0(1500)$ is given by the Breit-Wigner amplitude. The basis does not include $f_0(1370)$ and $\rho(1700)$ as these resonances are not significantly seen in the COMPASS data.

The big data sample of 50×10^6 events is divided in 11 slices in t' such that each slice contains

---

[6] Strictly speaking, for bins with low $m_{3\pi}$ the number of free parameters is less since some coefficients are enforced to be zero. The parameters a_w, a'_w are related above the individual thresholds indicated in Table D.1.
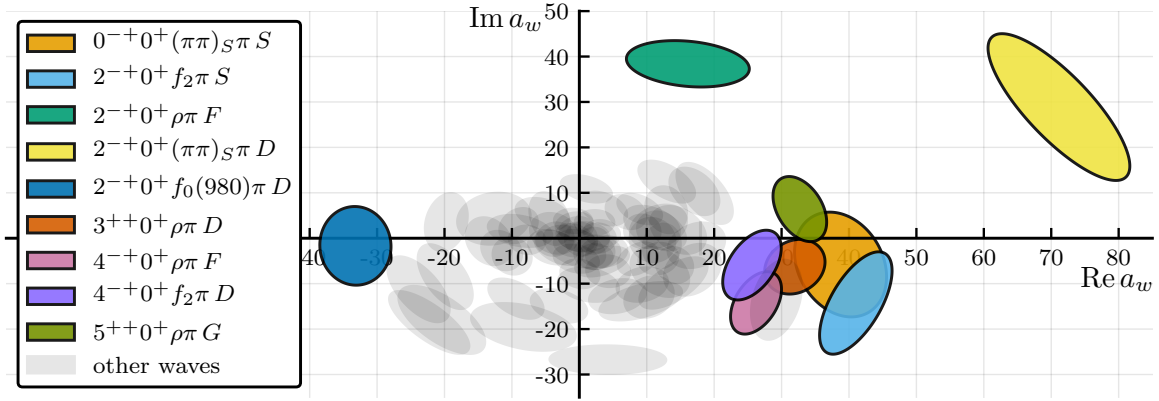
Figure 3.12: The results of the PWA in a single bin (the first t' bin, and $1.54 < \sqrt{s} < 1.56\,\text{GeV}$) in the polar representation. The plotted quantities are $(\text{SDM})_{w_0,i}/(\text{SDM})_{w_0,w_0}^{1/2}$ where w_0 is the reference wave $1^{++}0^+\,\rho\pi\,S$ fpr $i = 1, \ldots, 88$. The square root of intensities determines the distance from zero, the angle is given by the relative phase. The phase of the reference wave $1^{++}0^+\,\rho\pi\,S$ is 0; this error ellipse is degenerate and not visible at the plot. The ellipses represent 1σ contours of the statistical uncertainty.

roughly the same number of events, and in 100 equidistant $\sqrt{s} \equiv m_{3\pi}$ bins with a width of $20\,\text{MeV}$. The results of a single PWA (*i.e.* in a single $t \times s$ bin) are intensities and relative phases of the waves as shown in Fig. 3.12.

Repeating the fit bin-by-bin, the PWA is performed on all 11×100 bins independently. Fig. 3.13 shows the expansion of the total intensity into intensities of the individual waves. Using the PWA
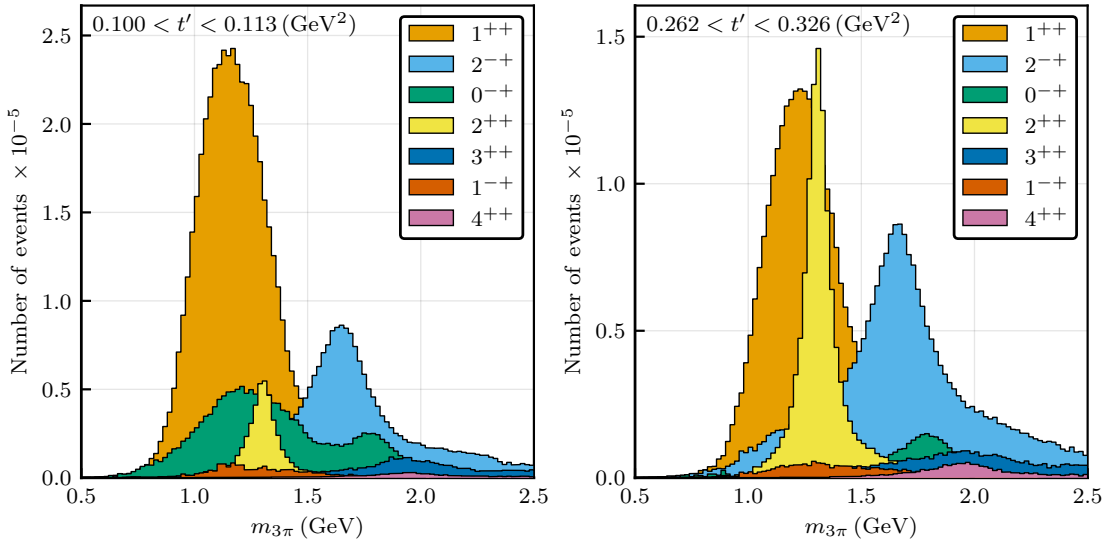
Figure 3.13: Results of the mass-independent PWA (the data are from Ref. [78]). The plots show intensity in $20\,\text{MeV}$ bins of the main J^{PC} sectors as functions of the 3π invariant mass for two different t' slices indicated in the panels.

technique we disentangle the contributions of different waves making further resonance analysis

possible. The largest contribution comes from the waves with $J^{PC} = 1^{++}$ where the $\rho\pi$ S-wave dominants. The broad resonance-like structure is known as the $a_1(1260)$. The blue filled area is the intensity of the $J^{PC} = 2^{-+}$ where a detailed analysis allows us to observe three π_2 resonances (see Appendix A.2). The 2^{++} sector shown by the yellow distribution presents a clean and narrow $a_2(1320)$ resonance. The 0^{-+} structure shown in green is likely a composition of a broad non-resonant scattering at $m_{3\pi} \approx 1.3\,\text{GeV}$ which dies out at high t' (in the analysis [3] the state $\pi(1300)$ has not been found), and the hadronic state $\pi(1800)$ which is seen as the second bump in the intensity. The 4^{++} clearly shows the highly excited axial fourth-order tensor state $a_4(2040)$. The wave with exotic quantum numbers 1^{-+} obtains a significant intensity. The resonance signal was confirmed in the recent analysis [3, 108, 109].

3.3.3 Extraction of the resonance parameters

To interpret the s and t'-dependence of the partial waves, a dynamical model is introduced and fitted to the data [3]. From the pool of 88 waves used in the mass-independent analysis, a subset of 14 major waves are selected, amounting to $\sim 57\%$ of the total intensity (see Table II of Ref. [3]). The simultaneous fit of all 88 waves was not possible due to poor understanding of physics in high partial waves which do not manifest a resonance pattern. In addition the fit has technical limitations because the number of free parameters rapidly grows and this makes the fit unstable and computationally expensive. For the selected subset of the data all t'-slices were fitted simultaneously; the resonance parameters were assumed to be independent of the production mechanism. The model includes 11 resonances in 6 orthogonal J^{PC} sectors which are required for a good description of the data

$$
\begin{aligned}
0^{-+} &: \quad \pi(1800), \\
1^{-+} &: \quad \pi_1(1600), \\
1^{++} &: \quad a_1(1260),\ a_1(1420),\ a_1(1640), \\
2^{-+} &: \quad \pi_2(1670),\ \pi_2(1880),\ \pi_2(2005), \\
2^{++} &: \quad a_2(1320),\ a_1(1700), \\
4^{++} &: \quad a_4(2040),
\end{aligned}
$$

where the well-known resonances are written in black, the less known states (which are still in the PDG [26]) are shown in gray. The resonance-like signal $a_1(1420)$ is shown in red and discussed in detail in Chapter 4 of this thesis.

A model for the partial-wave-Isobar amplitude is written as a sum of the resonance component and the coherent background.

$$
A(s) = \sum_i C_i D_i^{\text{R}}(s) + C_{\text{NR}} D^{\text{NR}}(s), \tag{3.27}
$$

where C_i, C_{NR} are complex constants, which are free parameters of the fit, $D_i^{\text{R}}(s)$ parametrizes the resonance term, and $D^{\text{NR}}(s)$ is an amplitude for the non-resonant term. A simple Breit-Wigner amplitude with a constant width is used for all resonances, except a few exceptions discussed below.

$$
D^{\text{R}}(s) = \frac{1}{m^2 - s - im\Gamma}, \tag{3.28}
$$

where the mass m and the width Γ are left free in the fit. The non-resonant term reads

$$D^{\mathrm{NR}}(s) = \left(\frac{\sqrt{s} - m_{\mathrm{thr}}}{m_{\mathrm{thr}}} \right)^b e^{-(c_0 + c_1 t' + c_2 t'^2)} \tilde{q}_w^2(s) \tag{3.29}$$

where m_{thr} is empirically fixed to $0.5\,\mathrm{GeV}$, the parameters b, c_0, c_1, c_2 are free parameters of the fit[7], $\tilde{q}_w$ is a quantity inspired by the break-up momentum between the isobar and the bachelor which is smooth and non-zero below the nominal isobar-bachelor threshold. The expression for $\tilde{q}_w$, $\tilde{q}_w(s) = 4\pi\sqrt{s}B_{ww}(s)$ is simply found by equating the effective phase space B_{ww}, that is calculated numerically as the diagonal element of the integral matrix in Eq. (3.20a), to the expression for the two-body phase space.

$$B_{ww}(s) = \frac{1}{8\pi} \frac{2\tilde{q}_w(s)}{\sqrt{s}}$$

The analysis attempts to describe the spectrum in partial waves in a mass range as large as possible having minimal number of resonances. Hence, the mass range for every partial wave is adjusted individually, however it is kept the same for different t'-slices. The low limit is set around $1\,\mathrm{GeV}$ depending on the two-body threshold for the nominal masses, $m_\pi + m_\xi$. The high range is pushed to high values of the 3π invariant mass as far as possible until the non-resonant background starts dominating or the fit curve departs significantly from the data due to higher resonances which are not included in the model. The detailed discussion about the fit threshold is given in the original Ref. [78]. The fit is performed by minimizing the deviations of the model from the values of the SDM. For all waves in the selected subset, the intensities, real and imaginary parts of all possible interference terms are used in construction of the penalty function χ^2-inspired representing the deviation of the model from the SDM-data.

We present here a selected part of the fit results that is closely related to the further discussion in this thesis. The resonance $a_1(1260)$ dominates the $J^{PC}M^\epsilon = 1^{++}0^+$ $\rho\pi$ S-wave. The $J^{PC}M^\epsilon = 2^{++}1^+$ $\rho\pi$ D-wave contains the narrow $a_2(1320)$ resonance as shown in Fig. 3.14. The relative phase between the D-wave and the S-wave goes down at first, below $1.25\,\mathrm{GeV}$, due to the a_1 resonance. The a_2 resonance is responsible for the fast positive phase motion around $1.3\,\mathrm{GeV}$. The a_1 state is parametrized by a Breit-Wigner amplitude with energy-dependent width, as suggested by M.G. Bowler [110].

$$D_{a_1}(s) = \frac{1}{m_{a_1}^2 - s - im\Gamma(s)}, \quad \Gamma(s) = \Gamma_{a_1} \frac{m_{a_1}\rho_a(s)}{\sqrt{s}\rho_a(m_{a_1}^2)}, \tag{3.30}$$

where the mass m_{a_1} and the width Γ_{a_1} are free parameters in the fit, $\rho_a = B_{w_0 w_0}$ for w_0 being the $1^{++}0^+$ $\rho\pi$ S-wave. The a_2 energy-dependent width takes into account the two dominant decay channels: $\rho\pi$ and $\eta\pi$ D-waves.

$$\Gamma(s) = \Gamma_{a_2} \frac{m_{a_2}}{\sqrt{s}} \left[(1-x) \frac{q_{\rho\pi}(\sqrt{s})}{q_{\rho\pi}(m_{a_2})} \frac{h_2^2(q_{\rho\pi}(\sqrt{s})R)}{h_2^2(q_{\rho\pi}(m_{a_2})R)} + x \frac{q_{\eta\pi}(\sqrt{s})}{q_{\eta\pi}(m_{a_2})} \frac{h_2^2(q_{\eta\pi}(\sqrt{s})R)}{h_2^2(q_{\eta\pi}(m_{a_2})R^2)} \right], \tag{3.31}$$

---

[7] for most of the waves $b = c_1 = c_2 = 0$. The exceptions are waves with high intensity or/and strong non-resonant component: $J^{PC}M^\epsilon = 1^{++}0^+$ $\rho\pi$ S-wave with $a_1(1260)$, $J^{PC}M^\epsilon = 2^{++}1^+$ $\rho\pi$ D-wave with $a_2(1320)$, $J^{PC}M^\epsilon = 2^{-+}0^+$ $f_2\pi$ S-wave with $\pi_2(1670)$, $J^{PC}M^\epsilon = 1^{-+}1^+$ $\rho\pi$ P-wave with $\pi_1(1600)$
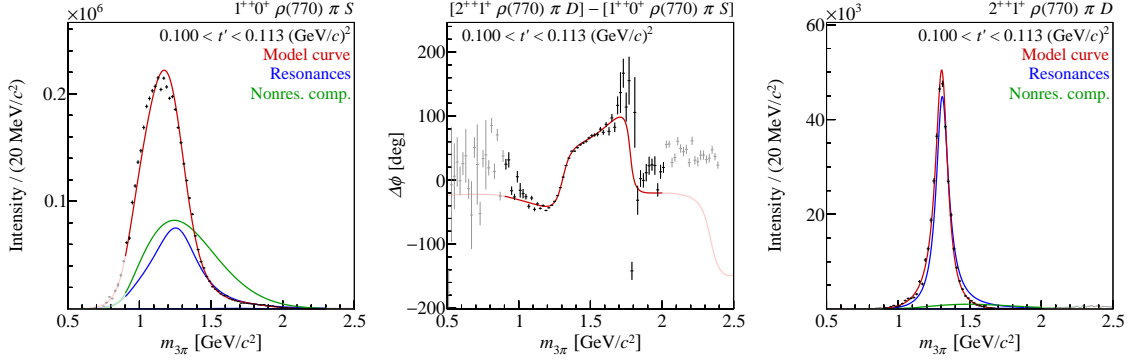
Figure 3.14: Selected results of the COMPASS mass-dependent fit from Ref. [3]: the intensity of $J^{PC}M^\epsilon = 1^{++}0^+\ \rho\pi$ S-wave, the relative phase between $J^{PC}M^\epsilon = 2^{++}1^+\ \rho\pi$ D-wave and $J^{PC}M^\epsilon = 1^{++}0^+\ \rho\pi$ S-wave, and the intensity of $J^{PC}M^\epsilon = 2^{++}1^+\ \rho\pi$ D-wave are presented in the panels from left to right, respectively. The red curve presents the complete model in Eq. (3.27), the blue (green) line shows the intensity of the resonance signal (background).

where x is the relative branching fraction of $\eta\pi$ fixed to 20%. $q_{\xi\pi}$, $\xi \in \{\eta, \rho\}$ is a break-up momenta, $q_{\xi\pi}(s) = \lambda^{1/2}(s, m_\xi^2, m_\pi^2)/(2\sqrt{s})$, where $\lambda(x, y, z)$ is the Källén function, m_ξ is a nominal mass of the state ξ. h_2 are the Blatt-Weisskopf factors discussed in E.3.

All 11 t' slices are fitted simultaneously. Since the resonance parameters are kept independent of t', changes in the intensity distribution and the phase are forced to be adjusted by the background term. This strong constraint significantly reduces the uncertainties of the obtained resonance parameters. However, the large systematic uncertainties due to the unconstrained intensity of the non-resonant component remain.

The analysis [3] developed the most comprehensive resonance model for $\pi^-\pi^+\pi^-$ system. The Breit-Wigner parameter of the $a_1(1420)$, $a_2(1320)$, $a_4(2040)$, $\pi(1800)$, $\pi_2(1670)$ were reliably extracted with relatively small uncertainties. The extracted Breit-Wigner parameters of the $a_2(1320)$ resonance,

$$m_{\text{BW}}^{(a_2)} = (1314.5^{+4}_{-3.3})\,\text{MeV}, \quad \Gamma_{\text{BW}}^{(a_2)} = (106.6^{+3.4}_{-7})\,\text{MeV},$$

are consistent with previous measurements [26]. The parameters of the $a_1(1260)$,

$$m_{\text{BW}}^{(a_1)} = (1299^{+12}_{-28})\,\text{MeV}, \quad \Gamma_{\text{BW}}^{(a_1)} = (380 \pm 80)\,\text{MeV},$$

have large systematic uncertainties due the crucial importance of the non-resonant background.

Pole positions of the resonances

One essential difficulty of hadron spectroscopy is that the line shape of the resonance depends on the specific production mechanism and the observed final state. Various functional forms can be used to parametrize the resonance phenomena, but being dependent on a specific set of parameters, they cannot give a common knowledge about the resonance nature for various reactions. An alternative approach to characterize a resonance structure discussed in Sec. 2.2, is to find out the position of the resonance pole at the complex plane of the scattering energy (see also Ref. [39, 79]). The resonance poles are expected to be located in the region below the real axis, which is smoothly attached to it.

The position of the pole in the complex energy plane gives a natural characterization of the resonance phenomenon. The mass and width of the hadronic state from the pole position is defined by Eq. (2.31).

An important property analytic functions is that, if two functions are exactly equal on an open set (*e.g.* the real axis), they are equal everywhere in the domain of analyticity. It tells that as soon as an exact analytic parametrization is given on the real axis, the function is known in the domain of analyticity, together with the positions of its singularities. However, in practical applications this is never the case, since the scattering amplitude is never known exactly. Nevertheless, the closer the explored complex region to the real axis is, the smaller are the uncertainties caused by variation of the function along the real axis. The amplitude in Eq. (3.27) is written as a sum of the resonant terms and the non-resonant background. Therefore, the expression for the sum contains at most all singularities of individual terms. The non-resonant term does not have any pole-like singularities: since it is written as a product of a polynomial and an exponential, the equation $1/D^{\text{NR}}(s) = 0$ can only have a solution at complex infinity. The Breit-Wigner amplitudes used for the resonance part have pole singularities which are straightforward to find.

The majority of the resonances are parametrized by the Breit-Wigner formula with a constant width shown in Eq. (3.28), which has a pole at $s_p = m^2 - im\Gamma$. Comparing this to Eq. (2.31) we find:

$$m_p = \text{Re}\ \sqrt{m^2 - im\Gamma}, \quad \Gamma_p = -2\,\text{Im}\ \sqrt{m^2 - im\Gamma}, \tag{3.32}$$

Systematic uncertainties dominate the errors, hence we only propagate them. The systematic error for pole positions is found based on the image of the rectangular error box in the $m \times \Gamma$ space as shown in Fig. 3.15.

We see that the pole position listed in Table 3.1 does not coincide with the Breit-Wigner parameters, however the difference is rather small and lies within the errors. A difference between the Breit-Wigner

Table 3.1: The pole positions of the resonances studied in Ref. [3]. The results for all resonances except $a_2(1320)$ are found using Eq. (3.32). The pole position of the $a_2(1320)$ is obtained using a dedicated procedure of the analytic continuation described in the text.

state	m, GeV	Γ, GeV	m_p, GeV	Γ_p, GeV
$\pi(1800)$	1804^{+6}_{-9}	220^{+8}_{-11}	1807^{+6}_{-9}	220^{+8}_{-11}
$\pi_1(1600)$	1600^{+110}_{-60}	580^{+100}_{-230}	1625^{+117}_{-75}	571^{+96}_{-223}
$\pi_2(1670)$	1642^{+12}_{-1}	311^{+12}_{-23}	1649^{+13}_{-2}	310^{+12}_{-23}
$\pi_2(1880)$	1847^{+20}_{-3}	246^{+33}_{-28}	1851^{+21}_{-4}	245^{+33}_{-28}
$\pi_2(2005)$	1962^{+17}_{-29}	371^{+16}_{-120}	1971^{+18}_{-34}	369^{+16}_{-119}
$a_1(1420)$	1411^{+4}_{-5}	161^{+11}_{-14}	1413^{+4}_{-5}	161^{+11}_{-14}
$a_1(1640)$	1700^{+35}_{-130}	510^{+170}_{-90}	1719^{+48}_{-135}	504^{+163}_{-88}
$a_2(1700)$	1681^{+22}_{-35}	436^{+20}_{-16}	1695^{+23}_{-36}	432^{+20}_{-16}
$a_4(2040)$	1935^{+11}_{-13}	333^{+16}_{-21}	1942^{+12}_{-14}	332^{+16}_{-21}
$a_2(1320)$	1315^{+4}_{-3}	107^{+3}_{-7}	1307^{+4}_{-3}	105^{+3}_{-7}

mass and the pole mass is the larger, the wider the resonance is, since $m^2 = m_p^2 - \Gamma_p^2/4$. The
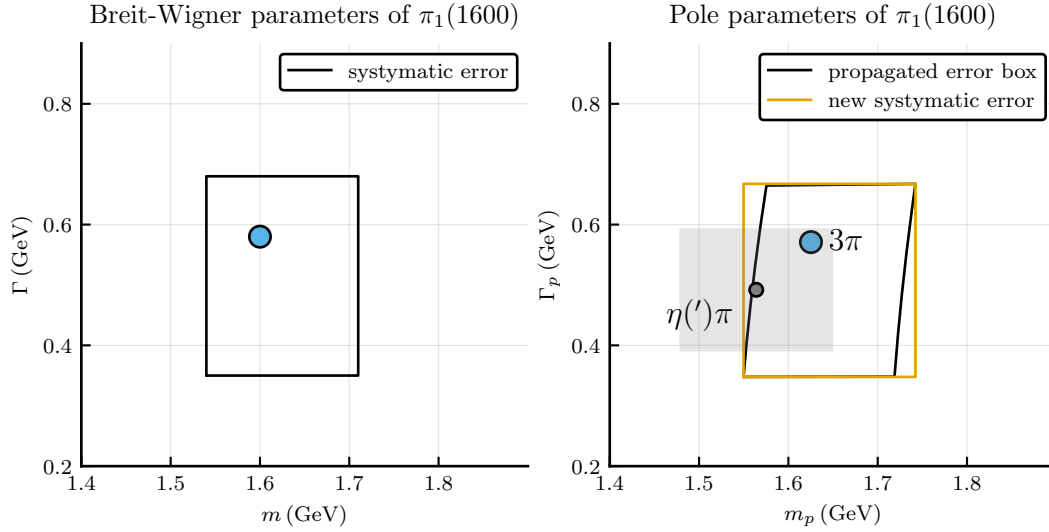
Figure 3.15: Parameters of the $\pi_1(1600)$: the Breit-Wigner mass and width found in the analysis [3] are shown in the left panel, the corresponding pole parameters are shown on the right plot. The blue dots show the central values (labeled by "3π" on the right panel). The black rectangle on the left panel presents the systematic uncertainties (see Ref. [3]). The systematic uncertainty of the pole position presented on the right panel by the orange rectangle are found by drawing a minimal rectangular area which includes an image of the error from the left panel. The pole position of $\pi_1(1600)$ obtained in the recent analysis of $\eta^{(\prime)}\pi$ systems [12] is shown by the gray dot with the gray rectangle representing the systematic uncertainty (labeled by "$\eta^{(\prime)}\pi$").

pole mass is always bigger than the Breit-Wigner mass; For the width, the following relation holds: $m\Gamma = m_p\Gamma_p$. Hence, the relative shift of the mass and width is approximately the same with the opposite sign, $\Delta\Gamma/\Gamma \approx -\Delta m/m$, *i.e.* the Breit-Wigner pole width is usually smaller than the width parameter.

The energy-dependent width of the a_2 resonance is given by Eq. (3.31). The analytic continuation is performed by calculating the amplitude with complex values for the energy. One does not need to add a discontinuity as discussed in Sec. 2.2 since the Breit-Wigner amplitude with the width from Eq. (3.31) does not have discontinuity on the real axis above the thresholds. [8] By minimizing the expression $|m^2 - (x + iy/2)^2 - im\Gamma((x + iy/2)^2)|^2$ in the domain $x \in [1,2]$, $y \in [-1,0]$ we find a single pole, which is identified with the a_2 resonance. The result is shown in Table 3.1. Since the $a_2(1320)$ is quite narrow, we observe again that the Breit-Wigner parameters are very close to the pole position. Interestingly, the pole mass is slightly smaller than the Breit-Wigner mass in contrast to the other parametrization.

We have performed a formal exercise: for given analytic parametrizations on the real axis, we found

---

[8] To avoid a possible confusion, we would like to stress that the construction in Eq. (3.31) does have branch points at both thresholds, $s = (m_\xi + m_\pi)^2$, $\xi \in \{\eta, \rho\}$ which produce cuts. However, in the standard definition of the break-up momentum, $q_{\xi\pi}(s) = \sqrt{\lambda(s, m_\xi^2, m_\pi^2)}/(2\sqrt{s})$, the cuts are directed to the left. To transform the complex structure of the a_2 propagator to the conventional representation (unitarity cut goes to the right from the threshold branch point), we could modify the break-up momentum definition, $q_{\xi\pi}(s) = i\sqrt{-\lambda(s, m_\xi^2, m_\pi^2)}/(2\sqrt{s})$. It would introduce a discontinuity and would hide poles on the second Riemann sheet. The analytic continuation in this case would require adding the discontinuity to the amplitude as discussed in Sec. 2.2.
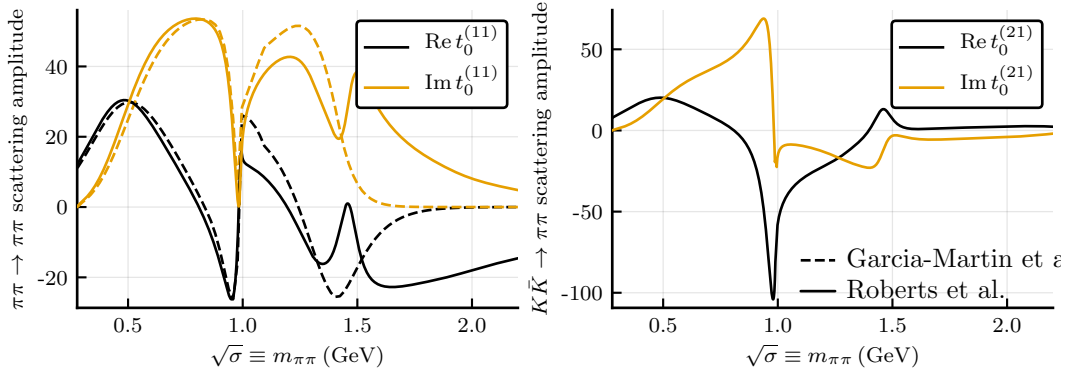
Figure 3.16: The real and imaginary part of the scattering amplitude $\pi\pi \to \pi\pi$ (left) and $K\bar{K} \to \pi\pi$ (right) extracted in the analysis of Ref. [115]. For comparison the dashed line shows the commonly used parametrization from Ref. [116] which is claimed to be valid up to $1.2\,\text{GeV}$.

the poles in the complex plane. One might argue that the original model is not unitary, and is suited for the description of the data along the real axis only. However, we put forward an argument of uniqueness of the analytic continuation which is difficult to oppose. Indeed, the unitarity condition is not incorporated into the model, manifestly; it can be shown that the sum of Breit-Wigner functions violate unitarity requirement for the scattering amplitude (see Eq. (2.16)). But, the amplitude, we are dealing with, is supposed to obey the production unitarity constraint (see Eq. (2.34)), which is not easy to validate. In this respect, when resonances are studied far from relevant thresholds, there is nothing immediately wrong in writing the production amplitude as a sum of several Breit-Wigner functions. On the other side, the unitarity conditions (Eq. (2.16) and Eq. (2.34)) give a clear way to incorporate new open-channel thresholds and constrain the relative strengths of the production amplitudes in coupled-channel problems assuming that all significant channels are known. There is a hope that using the unitarity constrains, one is able to reduce the systematic errors for the pole positions.

3.4 Remaining questions and further improvements

$f_0(500)/f_0(980)$ separation

The partial-wave model with fixed shapes of the isobars has difficulties describing the $\pi\pi$ interaction in the S-wave which is actually important for most J^{PC}-sectors of the 3π data. A part of the problem comes from the strong coupling between the $\pi\pi$ and $K\bar{K}$ systems. The $\pi\pi$ scattering amplitude known from CERN-Munich studies [111–113], has a sharp dip at $1\,\text{GeV}$ representing the $f_0(980)$ resonance. However, even the raw $\pi\pi$ spectrum in Fig. 3.5 measured by COMPASS shows a shoulder, not a depletion, around $1\,\text{GeV}$. One mechanism of turning the $f_0(980)$ peak into a dip is related to the production process [114, 115]. When the source of the $\pi\pi$ interaction is a light quark-antiquark current, $n\bar{n} = (u\bar{u} + d\bar{d})/2$, the amplitude exhibits a dip, while when the pion pair is produced by an $s\bar{s}$ current, the production amplitude looks like a narrow peak as shown in Fig. 3.16. Often, it is convenient to formulate the production amplitude in terms of form factors (see Ref. [114]) which are
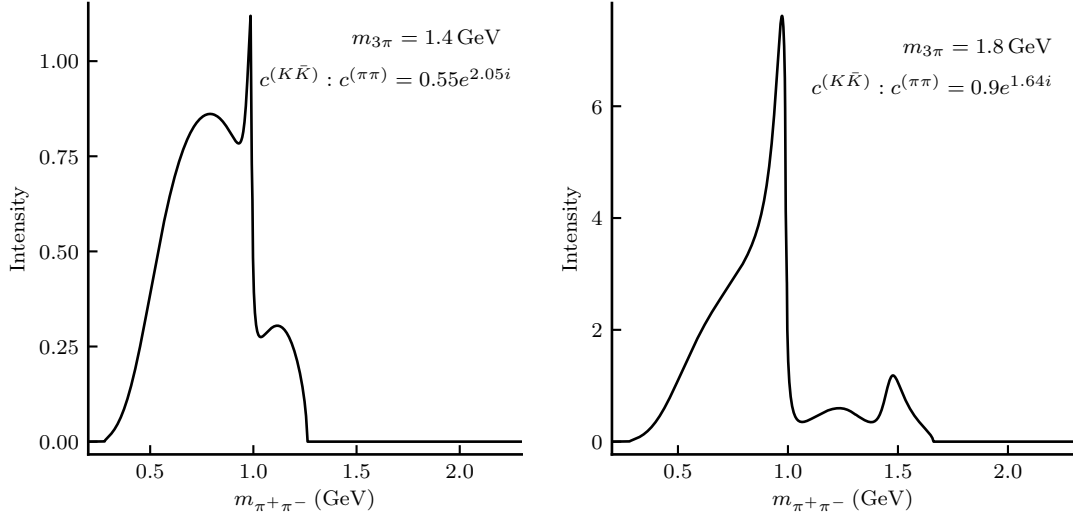
Figure 3.17: Examples of the $\pi^+\pi^-$ spectrum for different ratios of the strange and the non-strange currents. Intensity defined in Eq. (3.36) are calculated using the amplitude from Eq. (3.34) for the different source vectors $c^{(i)}$ where $i \in \{(\pi\pi), (K\bar{K})\}$. The relative strength and the phase of $c^{(i)}$ are indicated on the plot. For this exercise instead of Ω_0 in Eq. (3.34) we used the scattering matrix t_0 extracted in the analysis of Ref. [115] which is presented in Fig. 3.16.

introduced as,

$$\Gamma_\pi^q(\sigma) \propto \langle \pi^+\pi^- | n\bar{n} | 0 \rangle,$$
$$\Gamma_K^q(\sigma) \propto \langle K\bar{K} | s\bar{s} | 0 \rangle,$$

where σ is the squared invariant mass of the system, $n\bar{n}$ and $s\bar{s}$ are the isoscalar scalar currents for the light non-strange and the strange quarks, respectively. Since the form factors possess the right-hand cut only (there is no cross channel which would produce the left-hand cut), they are expressed in the following form, using the unitarity constraints in the form of Eq. (2.34):

$$\begin{pmatrix} \Gamma_\pi^q(\sigma) \\ \Gamma_K^q(\sigma) \end{pmatrix} = \begin{pmatrix} \Omega_0^{(\pi\pi,\pi\pi)}(\sigma) & \Omega_0^{(\pi\pi,K\bar{K})}(\sigma) \\ \Omega_0^{(K\bar{K},\pi\pi)}(\sigma) & \Omega_0^{(K\bar{K},K\bar{K})}(\sigma) \end{pmatrix} \begin{pmatrix} c^{(\pi\pi)}(\sigma) \\ c^{(K\bar{K})}(\sigma) \end{pmatrix}, \tag{3.34}$$

where the matrix Ω_0, known as the Omnès-matrix, is a construction which satisfies unitarity Eq. (2.34) and has only the right had cut [69, 114], $c^{(i)}(\sigma)$ are polynomials in σ. When the left singularities of the scattering matrix are far away from the physical region, the Omnès matrix, resembles the scattering matrix t_0 (we use the scattering matrix instead of the Omnès matrix, Ω_0 for simplicity in the numerical exercise in Fig. 3.17). For the $\pi\pi$, $K\bar{K}$ scattering in S-wave the approximation is rather crude, however, it will allow us to demonstrate the scale of variations of the measured $\pi\pi$ line shape. A slight admixture of the strange source leads to a large variation of the $\pi\pi$ production amplitude. Changing the couplings $c^{(\pi\pi)}$ and $c^{(K\bar{K})}$, and the relative phase between them, one obtains a set of various shapes of the $\pi\pi$ spectrum as shown in Fig. 3.17.

Clearly, the S-wave parametrization requires a flexibility in order to describe the data. In COMPASS

basis, it consists of three components: a broad $(\pi\pi)_S$ amplitude with slow phase motion, a sharp structure at 1 GeV parameterized by the Flatté model, which is referred to as the $f_0(980)$ component, and a Breit-Wigner amplitude for the $f_0(1500)$ (see Appendix D). This choice of the basis leads to systematic uncertainties discussed in Ref. [77] which cannot be removed in the current model of the PWA.

Freed-isobar fit

The problem of the fixed isobar shape is solved with an advanced analysis method, called freed-isobar PWA [117]. It was realized that the line shape of the isobars can be extracted from the data by parameterizing the general partial amplitude $(A_{\chi'\chi})_{LS}^{JM}(t, s, \sigma)$ introduced in Eq. (3.7) as a combination of independent complex amplitudes, each of which is nonzero only in a finite bin in σ. For a single $s \times t'$ bin we have

$$A_w^b(s, t', \sigma) = \sum_\beta \omega_\beta^{w,b}(s, t') \mathbb{I}_\beta(\sigma), \tag{3.35}$$

where w and b are combined indices (see Eq. (3.16)), the label β numbers successive bins of the two-pion mass range, $\omega_\beta^{w,b}(s, t')$ is the value of the amplitude for the given $t \times s \times \sigma$ bin, $\mathbb{I}_\beta(\sigma)$ is an indicator function which is 1 if σ is inside the bin and zero otherwise.

The waves, for which the continuous fixed shape is replaced by the combination of $\omega_\beta^{w,b}$, are called freed-isobar waves. In Ref. [78] the three waves with scalar isobars were freed and the line shape of the $[\pi\pi]_S$-wave was extracted. Recently, a fit with 11 freed-isobar waves was performed [118].

For convenience the freed-isobar amplitude is also normalized by the number of events, *cf.* Eq. (3.18),

$$I_{m_{3\pi} \times m_{2\pi}}(t, \sqrt{s}, \sqrt{\sigma}) \equiv \frac{\mathrm{d}^3 N}{\mathrm{d}t \, \mathrm{d}\sqrt{s} \, \mathrm{d}\sqrt{\sigma}} \propto 4\sqrt{\sigma s} \left| A_w^b(s, t', \sigma) \right|^2 \frac{\lambda^{1/2}(\sigma, m_\pi^2, m_\pi^2)\lambda^{1/2}(s, \sigma)}{\sigma s}. \tag{3.36}$$

The intensity correlations between $m_{2\pi}$ and $m_{3\pi}$ extracted from the freed-isobar fit are shown in Fig. 3.18 (left column). The distribution for the $J^{PC}M^\epsilon = 1^{++}0^+ [\pi\pi]_{0^{++}} \pi$ P-wave (the upper row) is dominated by a broad spot around $s \times \sigma = 1.2 \times 0.6 \,\mathrm{GeV}^2$. Naively, it could be entirely attributed to the $a_1(1260)$ resonance decaying into the $(\pi\pi)_S \pi$ P-wave. But, in Sec. 5, we will demonstrate that a significant part of this intensity spot should be associated with the non-resonant production. As a function of the $\pi^+\pi^-$ invariant mass, the intensity also has a spectacular behavior: there is a broad peak structure around 0.7 GeV, that reminds of $\pi\pi \to \pi\pi$ scattering amplitude from Fig. 3.16; it is followed by a sharp peak at 1 GeV, that indicates a non-trivial $\pi\pi \leftrightarrow K\bar{K}$ scattering (compare to the left plot of Fig. 3.17). The analogous distributions for the $J^{PC}M^\epsilon = 0^{-+}0^+ [\pi\pi]_{0^{++}} \pi$ P-wave (the lower row) look significantly different. The 3π spectrum is dominated by the $\pi(1800)$ resonance; the $\pi^+\pi^-$ invariant mass distribution in addition to the non-trivial interplay around 1 GeV indicates $f_0(1500)$ as a little enhancement around 1.45 GeV (compare to the right plot of Fig. 3.17).

Questions to the dynamic model

The mass-dependent fit of the SDM describes the data rather well, however, it leaves a list of questions about the model used. The Breit-Wigner amplitude is a good model for a single isolated two-particle resonance which is far from threshold. In the COMPASS analysis, none of the waves are isolated
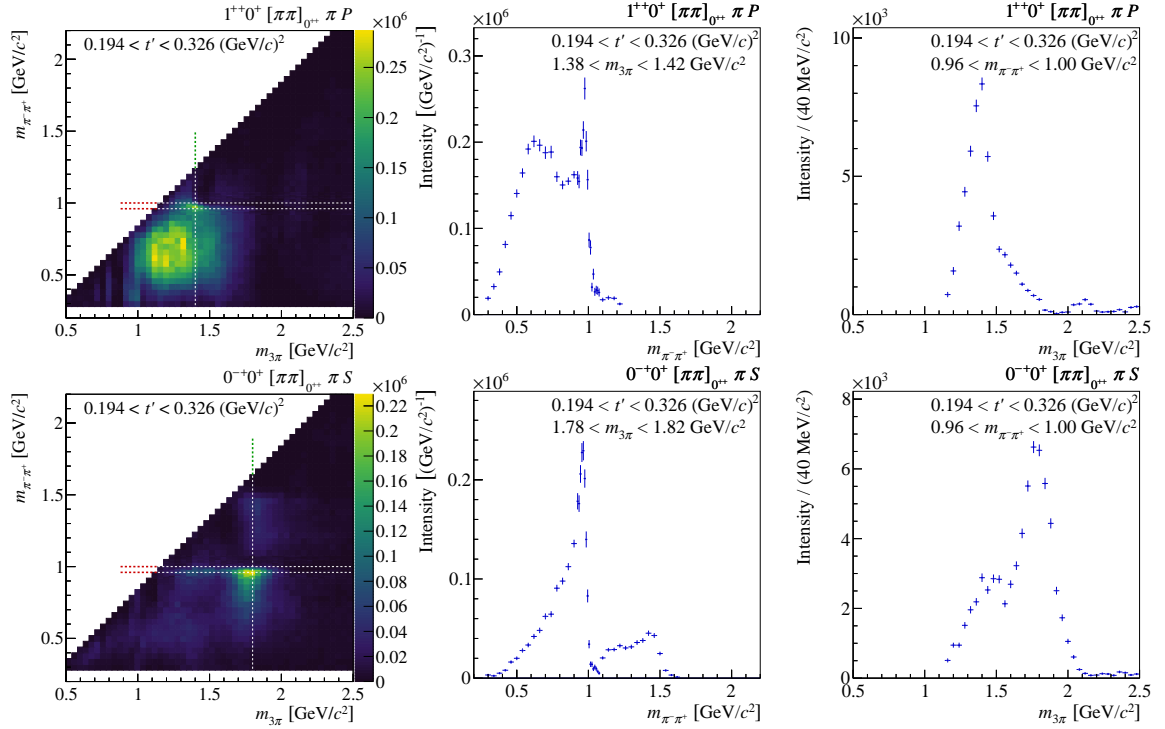
Figure 3.18: The results of the freed-isobar analysis from Ref. [78] for two selected waves. Intensity of the $[\pi\pi]_S\,\pi\,P$-wave of the $J^{PC}M^\epsilon = 1^{++}0^-$ (upper row) and the $J^{PC}M^\epsilon = 0^{-+}0^-$ (lower row) freed-isobar waves obtained in the fits in a single t'-slice as indicated on the plots. Left column: two-dimensional representation of the intensity of the wave as a function of $\sqrt{\sigma} \equiv m_{\pi\pi}$ and $\sqrt{s} \equiv m_{3\pi}$. Middle column: the intensity as a function of $m_{\pi\pi}$ for the $m_{3\pi}$-bin indicated by the vertical line in the left plot. Right column: the intensity as a function of $m_{3\pi}$ summed over a range of several $m_{\pi\pi}$-bins indicated by horizontal lines in the left plot. The $\pi\pi$ mass is binned in $10\,\mathrm{MeV}$ wide intervals around the $f_0(980)$ and $40\,\mathrm{MeV}$ otherwise.

due to the presence of a coherent non-resonant background, there are multiple thresholds related to different 3π-waves and inelastic channels, the $1^{++}\,\rho\pi\,S$-wave serves as a good example of the former point. The performed mass-dependent analysis suggests a nearly equal contribution of the background and the resonance signal. These effects make the extracted resonance parameters model- and process-dependent. Nevertheless, the discussed approach is a common practice established in the past; the results can be directly compared with the previous studies of diffractive three-pion production [108, 119–121]. The Breit-Wigner parameters for various resonances dominate the PDG listings [26]. Going beyond the "Breit-Wigner + Background" parametrization and constructing a more theoretically-sound approach is one of the goals of this thesis.

Rescattering corrections:
the $a_1(1420)$ phenomenon [1]

Identification of hadronic states in the invariant mass spectrum of particles produced in the experiments can be a simple problem. If one observes a narrow isolated peak in the spectrum, it most likely corresponds to a resonance, *i.e.* a hadronic state. More often, however, the situation is more complicated: many broad resonances largely overlap and interfere. It is a problem especially in the light-quark sector. But even in the charmonium region, the interpretation of X, Y, Z as hadronic states is not straightforward. The second very prominent feature of a resonance is, that the phase of the transition amplitude develops a rapid motion near the resonance. In case of an isolated resonance, the phase rises approximately by π as a function of energy and passes $\pi/2$ at the mass of the resonance (the isobar amplitudes for $S > 0$ shown in Fig. 3.11 serve as good examples). The phase differences between several transition amplitudes are often observable, and they can be used for the investigation of resonance phenomena (one example is discussed in Sec. 3.3.3 and shown in Fig. 3.14). The information on the intensity and the phase helps to identify the resonance states in complex situations like, for example, S-wave interaction of two pions where the $f_0(980)$ is seen as a dip (see Fig. 3.16). For many years, it was commonly accepted that a combination of a rather narrow structure in the spectrum (either a peak or a dip) and a rapidly changing phase is a clear sign of a hadronic state in the scattering process [122, 123]. The $a_1(1420)$ phenomenon discussed in this chapter seems to bring in a spectacular exception to this rule.

4.1 First observation of the $a_1(1420)$ and interpretations

One unexpected result of the conventional PWA performed by the COMPASS collaboration was the observation of a resonance-like behavior in the $J^{PC}M^{\epsilon} = 1^{++}0^+$ $f_0\pi$ P-wave near 1.4 GeV [124]. The results were confirmed by the VES collaboration [125] shortly after. A clear peak structure and a rapid phase motion, with respect to the $J^{PC}M^{\epsilon} = 1^{++}0^+$ $\rho\pi$ S-wave, suggested the presence of a new resonance in the $J^{PC} = 1^{++}$ sector, different to the well-known $a_1(1260)$. Following the nomenclature, the resonance-like signal was called $a_1(1420)$ due to its quantum numbers. Although the signal contributes just a tiny fraction to the total intensity as shown in Fig. 4.1, the observation has

---

[1] A part of this chapter has been published in Ref. [1] in the collaboration with Andrey Sarantsev and Bernhard Ketzer.

statistical significance far above 5σ (see discussion in Ref. [124]). It was found to be stable under various model modifications (the list of systematic studies can be found in Ref. [78]), and confirmed in the advanced freed-isobar analysis [126] as well as in a simple cut-based analysis as discussed below.
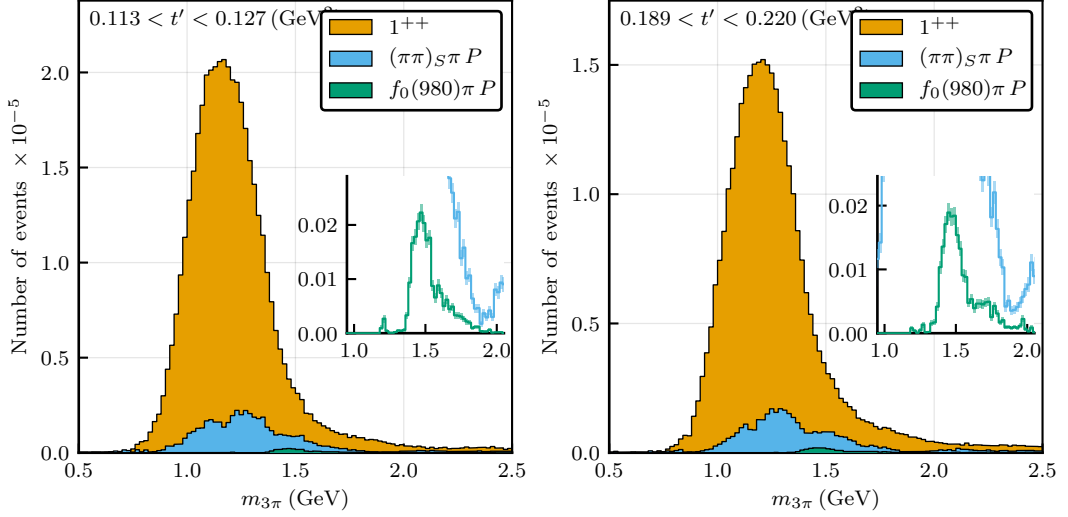
Figure 4.1: The plots summarize the results of the PWA for the $J^{PC}M^\epsilon = 1^{++}0^+$ sector in the second (left) and the sixth (right) t'-bin: the total intensity as a function of 3π-invariant mass is shown by the orange filled area, the blue area presents the $J^{PC}M^\epsilon = 1^{++}0^+$ $(\pi\pi)_S\pi$ P-wave, the green distribution is the intensity of the $J^{PC}M^\epsilon = 1^{++}0^+$ $f_0\pi$ P-wave. The inset plot makes a zoom to emphasize the $a_1(1420)$ signal.

In the conventional PWA, the mass-dependent fit with the model described in Sec. 3.3.3 was performed for a subset of three waves [124]. This subset includes the $J^{PC}M^\epsilon = 1^{++}0^+$ $f_0\pi$ P-wave with the resonance assumption for the $a_1(1420)$, and two waves with a very low background contribution: the $J^{PC}M^\epsilon = 2^{++}1^+$ $\rho\pi$ D-wave with two a_2-resonances and the $J^{PC}M^\epsilon = 4^{++}1^+$ $\rho\pi$ G-wave with one a_4-resonance. The last two waves are rather well described by the resonance model with a small coherent background, hence, they serve as a good reference. The resonance model for the $J^{PC}M^\epsilon = 1^{++}0^+$ $f_0\pi$ P-wave is well supported by the phase motion observed in the interference of this set of waves (see Fig. 4.2). The intensity and the phase is rather well reproduced by the mass-dependent fit suggesting the presence of a new, previously unobserved $a_1(1420)$ axial-vector resonance. The Breit-Wigner parameters obtained from the fit are $m_{a_1(1420)} = 1411^{+15}_{-13}\text{MeV}$, and $\Gamma_{a_1(1420)} = 153^{+8}_{-23}\text{MeV}$ [3].

Potential issues of the conventional PWA due to the limited basis and the fixed parametrization of the S-wave isobars has been addressed by the freed-isobar analysis discussed in Sec. 3.4. Fig. 3.18 shows the results for the $J^{PC}M^\epsilon = 1^{++}0^+[\pi\pi]_{0^{++}}\pi$ P-wave. The selected interval around $f_0(980)$, projected to the 3π-mass, is shown in the middle panel of Fig. 3.18. The intensity distribution projected to the 3π-mass for a selected interval around $f_0(980)$ has the same feature (a narrow isolated peak around $1.4\,\text{GeV}$) as the $J^{PC}M^\epsilon = 1^{++}0^+$ $f_0\pi$ P-wave spectrum in the conventional PWA (see Fig. 3.13). This demonstrates that the observed $a_1(1420)$ signal is not an artifact of the model used in the analysis. Looking at the intensity distribution as a function of the $\pi\pi$ invariant mass for $m_{3\pi}$ around $1.4\,\text{GeV}$, as shown in the middle plot of Fig. 3.18, we notice that the $f_0(980)$ resonance shows up as a peak. One possible reason for this behavior, as we discussed in Sec. 3.4, is a dominant
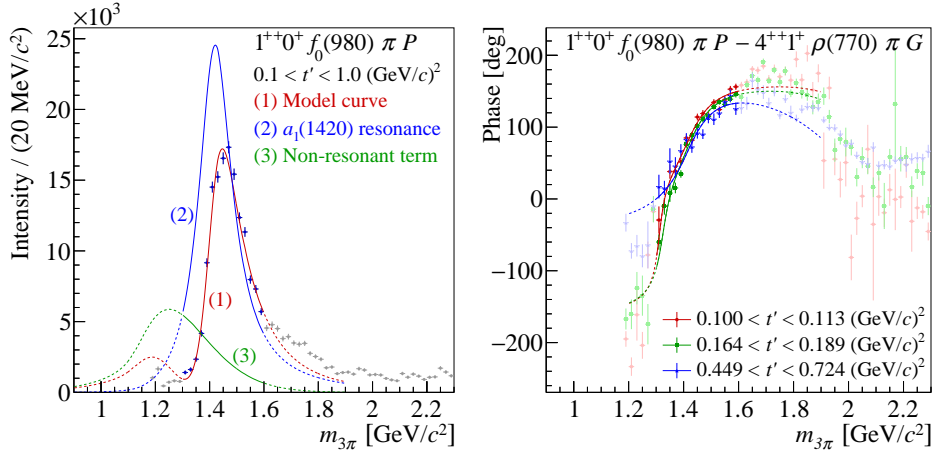
Figure 4.2: Results of the PWA in $m_{3\pi}$ bins (the PWA technique is introduced in Sec. 3.3.1) The left plot shows the intensity distributions of the $J^{PC}M^\epsilon = 1^{++}0^+ f_0\pi$ P-wave incoherently summed over all $11\, t'$-slices (black crosses). The fit with the $a_1(1420)$ resonance model is shown by the red line. The model for the $J^{PC}M^\epsilon = 1^{++}0^+ f_0\pi$ P-wave includes two components: the Breit-Wigner amplitude for which the intensity is shown by the blue line, and the non-resonance component with the intensity shown by the green line. The right plot shows the relative phase between $J^{PC}M^\epsilon = 1^{++}0^+ f_0\pi$ P-wave and $J^{PC}M^\epsilon = 4^{++}1^+ \rho\pi$ G-wave by the black crosses together with the model curves for different t'-slices as indicated in the plots' legend. The plots are from Ref. [124].

$K\bar{K}$-source of the $\pi\pi$ pair in this wave.

We have also found that the enhancement of the $a_1(1420)$ can be seen by applying simple cuts to the Dalitz plot of 3π. A quick analysis might be useful for a first rough check, *e.g.* for the $\tau \to 3\pi\,\nu_\tau$-reaction. The idea is to select the f_0 band in the Dalitz plot and exclude the dominating ρ-meson in the cross channel as shown in Fig. 4.3. The strength of the bump in the right panel roughly matches the height of the $a_1(1420)$ signal, which is approximately 1% of the height of the total intensity in the 1^{++} sector. Having the partial-wave analysis results at hand, we validate that the enhancement seen in the data is indeed caused by the $J^{PC}M^\epsilon = 1^{++}0^+ f_0\pi$ P-wave, while the other 87 waves give a smooth background in this mass region.

There are several issues which make the observation of this structure extremely interesting:

- The $a_1(1420)$ is very close to the ground axial-vector state $a_1(1260)$. The difference in the mass is only roughly $150\,\text{MeV}$.

- The width of the $a_1(1420)$ is much smaller than the width of the $a_1(1260)$ which contradicts the expectation for ordinary mesons (the excited states are expected to have larger width).

- The $a_1(1420)$ does not appear in lattice calculations [127] of excited hadronic states.

- There is no indication of the $a_1(1260)$ in the $J^{PC}M^\epsilon = 1^{++}0^+ f_0\pi$ P-wave, although the $a_1(1260)$ is allowed to decay to the this wave.

- The position of the peak is very close to the $K^*\bar{K}$ threshold, which is approximately at $1.39\,\text{GeV}$ for the nominal mass of the K^*.
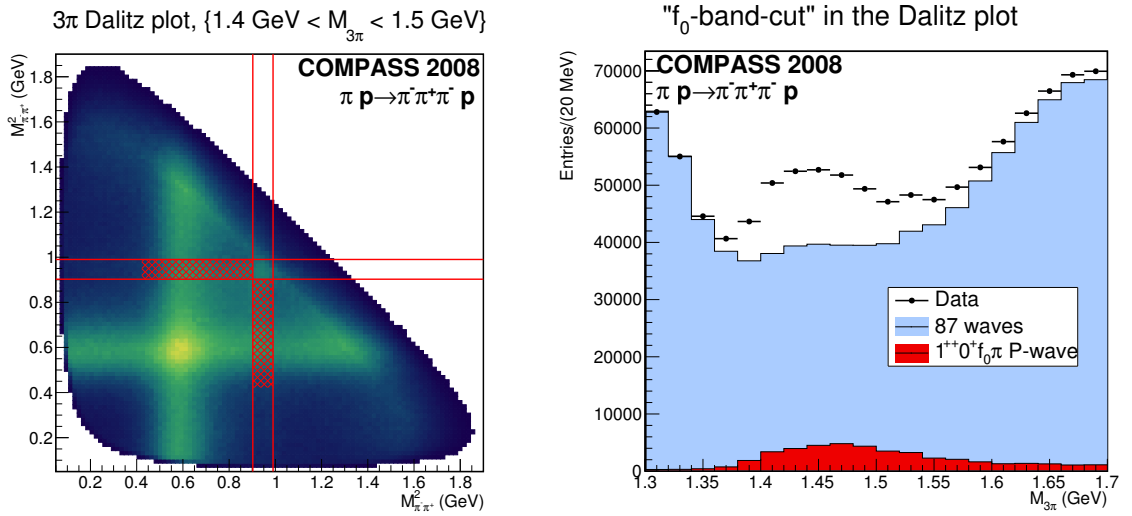
Figure 4.3: A recipe to produce the $a_1(1420)$ enhancement using a simple dissection analysis. The left panel presents the Dalitz plot for 3π system (a double-entered histogram for correlation of the two $\pi^+\pi^-$ invariant masses squared) integrated over t'. The red lines indicate the cuts applied. The f_0 band is selected in the range $950 < \sigma_i < 995\,\mathrm{MeV}$ with $i = 1, 3$. In order to suppress the background from the ρ-meson the shaded area, $650 < \sigma_i < 950\,\mathrm{MeV}$ is excluded. The right panel shows the 3π spectrum obtained for the selected region. The black crosses show the number of event per $m_{3\pi}$-mass bin which passed the selection. The colored areas represent the event rate of the phase-space MC events selected analogously and weighted with a specific model. The model for the blue area is taken from the PWA but excludes the $J^{PC}M^\epsilon = 1^{++}0^+\,f_0\pi$ P-wave (the wave amplitude is set to zero). The model for the red area includes only the $J^{PC}M^\epsilon = 1^{++}0^+\,f_0\pi$ P-wave, the other waves are set to zero.

All these items suggest that the $a_1(1420)$ is an exceptional phenomenon which does not fit the conventional $q\bar{q}$ pattern. Several interpretations have been suggested in the scientific community shortly after the release of the $a_1(1420)$ observation. We comment on the possible explanations in the following paragraphs.

Genuine state: $q\bar{q}$, hadronic molecule, tetraquark

The unconventional nature of the potential state is supported by a more indirect argument. Most of the conventional resonances lie on the radial excitation trajectory (the principle quantum number of the excitation level against its mass squared) as well as on the Regge trajectory (the total angular momentum of the excitation level against its the mass squared). The trajectories with light isovector states with unnatural parities from Refs. [128, 129] are shown in Fig. 4.4. There is obviously no room for the $a_1(1420)$.

An interpretation of the $a_1(1420)$ as a counter-partner of the $f_1(1420)$ was suggested in the original COMPASS paper [124]. The microscopic nature could not be addressed based on the experimental data, however, it was suspected to be either a tetraquark or a hadronic molecule. The molecular interpretation of the $a_1(1420)$ was supposed since the mass of the peak is found relatively close to the $K^*\bar{K}$ threshold. Let's suppose that $K^*\bar{K}$ are bound by a pion exchange potential. Such molecules would decay to the $\pi[\pi\pi]$ final state by rearrangement of the strangeness via kaon exchange. The
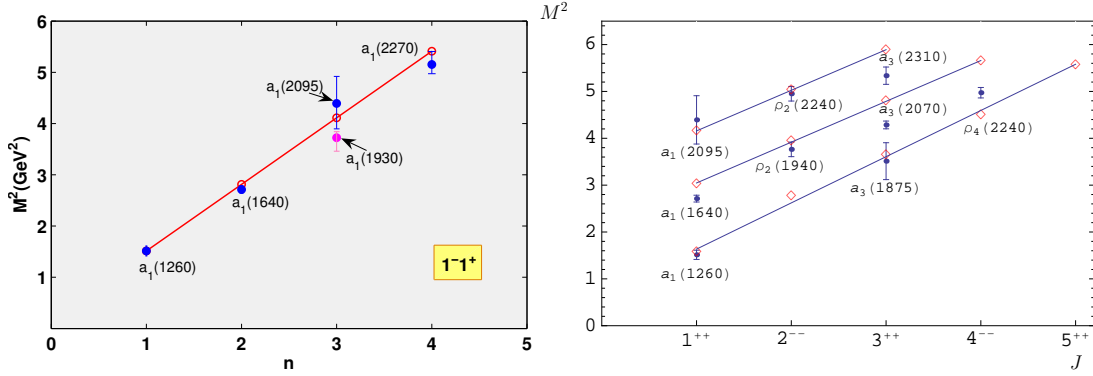
Figure 4.4: Left plot: the radial excitation trajectory of axial-vector states from Ref. [129]. n along the x-axis is the principle quantum number of the excited state (since n is cannot measured, the known states are ordered by their masses. Then, the numbers are assigned). Right plot: the Regge trajectories for the light isovector mesons with unnatural parity from Ref. [128]. J along the x-axis is the total angular momentum (simply spin) of the state. The invariant mass squared along the y-axis is given in unites of GeV^2.

first problem of the molecular interpretation is the fact that the $a_1(1420)$ is above the nominal $K^*\bar{K}$ threshold, while the positive binding energy requires the level to be below the threshold. If we ignore this problem in the molecular interpretation for a moment (one can agrue that the $a_1(1420)$ peak actually overlaps with the nominal $K^*\bar{K}$ threshold, the K^* is not stable) we can discuss a possibility for such a molecule to be bound. [2] It is known that the pion exchange, which would be a dominant interaction mechanism between K^* and $\bar{K}$, creates an attractive potential [130]. This force is also partially responsible for binding a proton and a neutron to a deuteron [131, 132]. It is also suggested to be responsible for the forming of $D^*\bar{D}$-molecules observed as the $X(3872)$ [133–135]. The binding in the $K^*\bar{K}$ system is expected to be even weaker for the following reason. Assuming a molecular nature of the $X(3872)$, the binding energy in the $D^{0*}\bar{D}^0$-system is measured to be at most a few hundred KeV [26]. In the classical picture of an attractive potential binding two mesons, the momentum of the mesons, p is of the order of the inverse size of the potential well, $1/a$ (since $pa = \pi/2 + \pi n$, with $n \in \mathbb{N}$, see *e.g.* Ref. [136]). Hence, it does not depend on the meson mass, m. The energy given by $p^2/2m$ is the larger the lighter the particles are. And since the binding energy is the difference between the attractive energy and the kinetic energy of the mesons, the binding in the strange sector should be less than in the charm sector. Therefore, it is very unlikely that the binding is sufficiently strong. The two arguments we have listed remove the molecular interpretation from the list of main hypotheses.

The tetraquark state proposed in Ref. [137–139] is not easy to rule out or support since the existence of the tetraquark states has not been established yet. However, we notice a practical difficulty in validating this hypothesis. A manifestation of a state (including the tetraquark state) would be an observation of a pole in the $f_0\pi$ scattering amplitude. Due to the strong coupling of the f_0 to kaons, the coupled-channel problem of $K\bar{K}\pi$ and 3π has to be considered and analyzed for a presence of the resonant pole. Moreover, this possible resonant pole is not the only singularity which might be present in the amplitude. In the next section, we find that the other "strong" singularities (logarithmic branch points) due to various exchanges have to be located close to the physical sheet. They already

---

[2] Thanks to conversation with Marek Karliner whom I met at the ICNFP2017 conference.

produce an enhancement in the amplitude even without the necessity of an additional pole singularity.

Basdevant-Berger: interference with the background

The observation of the $a_1(1420)$ phenomenon was quickly followed by the work of J.-L. Basdevant and Ed. Berger [140] who suggested a very peculiar dynamic interpretation. A key component of their explanation was the non-resonant production term, known as the Deck amplitude. The model developed by the same authors in 1977 includes a possible additional background in a way to satisfy the quasi-two-body unitarity requirement [62, 141]. This method is described in Sec. 2.3 as the *unitarized background method* (see Eq. (2.41)).

In the Basdevant-Berger approach, the scattering matrix T_l is considered to be elastic in the space of two channels, $\rho\pi$ S-wave and $f_0\pi$ P-wave. The interaction is parameterized by a single resonance, $a_1(1260)$, incorporated via a single-pole K-matrix of dimension 2 (see Eq. (2.22)). The phase-space factors are calculated in an approximation with stable ρ and f_0 particles as two-body phase space. The Deck amplitude (see details in Chapter 5) was approximated in the limit of small transferred momentum allowing the authors to carry out the partial-wave projection integrals analytically as shown in Ref. [142]. According to authors of Ref. [140], "a major clue" to the investigation is the fact that the background amplitude projected to the P-wave, being real, crosses zero at $1.38\,\mathrm{GeV}$. When the projection changes the sign, the phase jumps from -180° to 0° and makes a sudden change of the relative phase between the S-wave and the P-wave projections. The full production amplitude is constructed from the background projections and the scattering matrix using the unitarization procedure as given in Eq. (2.41). Authors show that the peak in the intensity of the $f_0\pi$ P-wave calculated from the full amplitude can be adjusted to $1.4\,\mathrm{GeV}$, to the place of $a_1(1420)$. However, the unitarization changes a location of the phase movement. The relative phase of the two production amplitudes still has a large motion but approximately at the position of the K-matrix pole, which is fixed by the $a_1(1260)$ peak at $\rho\pi$ S-wave at approximately $1.3\,\mathrm{GeV}$. There is a clear contradicts the COMPASS observation, which authors have not solved. Moreover, as we demonstrate in Chapter 5, the model of the Deck process used by the authors (we call it the "Standard Deck") in not supported by the COMPASS data at the high energies. Hence, the "major clue" is likely invalid.

The triangle singularity

In Ref. [1], we suggested a dynamic explanation of the phenomenon which does not require a genuine resonance. The key mechanism for the explanation is the final-state interaction between the 3π and $K\bar{K}\pi$ systems. We showed that a scattering $K^*\bar{K} \to f_0(980)\pi$ via K exchange has a very peculiar resonance-like behavior exactly at the mass of the observed $a_1(1420)$ signal. When in the $K^*\bar{K}$ system is produced in the decay of $a_1(1260)$, the simplest diagram the rescattering process contains a triangle loop. One finds that by integrating over the loop momentum the amplitude contain a logarithmic singularity. In honor of the leading singularity of the triangle diagram, the effect is often called the *triangle singularity*(TS). The following section is dedicated to a detailed discussion of the rescattering effect and the interpretation of the $a_1(1420)$.
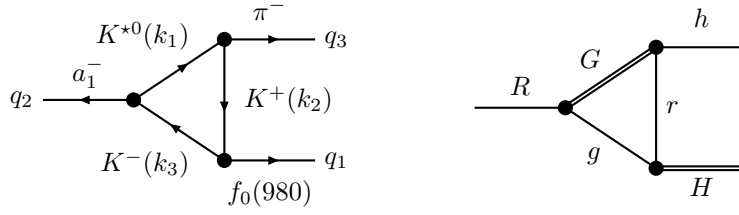
Figure 4.5: Left plot: the decay $a_1 \to f_0\pi$ proceeding via the triangle diagram with kaons. The four-momenta of the external particles are q_1, q_2, and q_3, the intermediate particle momenta are k_1, k_2, and k_3. Right plot: a diagram representing a general decay $R \to Hh$ where G, g, and r are intermediate particles in the loop. G and H stand for subchannel resonances.

4.2 The rescattering interpretation [3]

Our primary goal is to understand the dynamics which are relevant for the partial-wave isobar amplitude $F_w(s,t)$ where the wave index $w \sim J^{PC} = 1^{++} f_0\pi P$. As we announced already, we will primarily focus on the triangle diagram shown in Fig. 4.5, [4] addressing the first corrections to the naive model of the decay to non-interacting particles. The simplest way to investigate loop diagrams is the method of Feynman parameters and Wick rotation [59]. Using this method we calculate the loop and identify its singularities following the work of L. Landau [144]. R. Cutkosky developed a technique which permits us to calculate the imaginary part of a loop diagram based on the discontinuities across the cuts in the complex plane, related to the particle thresholds [145]. The studies of the discontinuities will lead us to the dispersive representations of the amplitude and allow us to relate the perturbative methods of Feynman diagrams with the non-perturbative relations of the S-matrix theory. The Feynman-diagrams-based method can be motivated in effective theories based on Chiral Lagrangians (*e.g.* Ref. [146]). However, in the energy region of the $a_1(1420)$ their applicability becomes questionable. Using the S-matrix principles we consider the unitarity-based approach and perspectives on calculating the complete rescattering series.

4.2.1 Kinematic conditions for a triangle singularity

It is well known that a logarithmic singularity arises in the triangle loop diagram [38, 39]. As was shown by a general analysis of singularities in scalar theory [144], the amplitude behavior near the branching point of a cut is $\propto \log(s - s_0)$, where s is an external invariant. The position of the singularity s_0 can be obtained from the simple condition that all intermediate particles are on mass shell and collinear to each other. This is given by the system of Landau equations:

$$\begin{cases} k_i^2 = m_i^2, & i = 1 \ldots 3, \\ x\, k_{1\mu} + y\, k_{2\mu} + z\, k_{3\mu} = 0, & x, y, z \in [0,1], \\ x + y + z = 1, \end{cases} \tag{4.1}$$

---

[3] A large part of this chapter has been published in Ref. [1].

[4] We restrict consideration to the process with the charge kaon exchange. The isospin-conjugated process $K^{*-}\bar{K}^0 \to f_0\pi^-$ via K^0 exchange is also possible. However, the calculation of the loop diagram with the $K^{-*}K^0\bar{K}^0$ internal particles is analogous to case presented in this chapter. More details can be found in Ref. [1, 143].

Figure 4.6: The kinematics of the decay $a_1 \rightarrow K^*[\rightarrow K\pi]\,\bar{K}$. Left plot: the possible directions of K in the a_1 rest frame, with respect to the decay $a_1 \rightarrow K^*\bar{K}$ are shown by the dashed ellipse. The energy of the system, $\sqrt{s_2} = 1.41\,\text{GeV}$. An alignment of $\bar{K}$ and K momenta is kin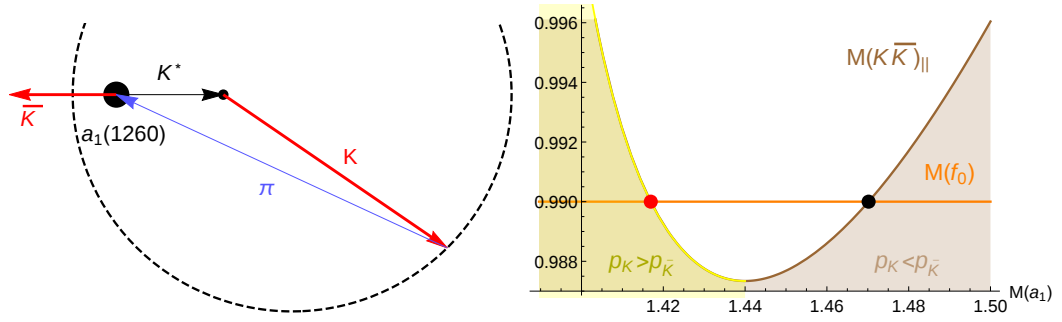ematically allowed, moreover, the K is faster than $\bar{K}$. Right Plot: the invariant mass of the $K\bar{K}$ pair as a function of the a_1 invariant mass for the situation when the K vector is aligned with the $\bar{K}$ vector. The horizontal line indicates the $f_0(980)$ mass. In the yellow (brown) region K is faster (slower) than $\bar{K}$.

where k_i and m_i are the 4-momenta and masses of intermediate particles, respectively (see Fig. 4.5). x, y, and z are the Feynman parameters which are unknown variables in this system of equations. By multiplying the second equation with k_i ($i = 1, 2, 3$) and expressing the scalar products $(k_i\,k_j)$ through the invariant variables $s_1 = q_1^2$, $s_2 = q_2^2$, and $s_3 = q_3^2$, we obtain three equations, which, together with the condition $x + y + z = 1$, make the system of equations overdetermined:

$$
\begin{pmatrix}
k_1^2 & k_1 k_2 & k_1 k_3 \\
k_2 k_1 & k_2^2 & k_2 k_3 \\
k_3 k_1 & k_3 k_2 & k_3^2 \\
1 & 1 & 1
\end{pmatrix}
\begin{pmatrix}
x \\
y \\
z
\end{pmatrix}
=
\begin{pmatrix}
0 \\
0 \\
0 \\
1
\end{pmatrix}
\tag{4.2}
$$

where $k_i k_j = (s_n - m_i^2 - m_j^2)/2$ with (ijn) being even permutations of the numbers (123). The system is solvable only in exceptional cases, under the adjustment of the external parameters s_i and m_i. When a solution exists, the condition $x, y, z > 0$ has to be checked in addition. Equivalently, we can check that the pair (x, y) belongs to the triangle domain ($x > 0$, $y > 0$, $x + y < 1$) shown in Fig. 4.7.

For the decay $a_1^-(1260) \rightarrow f_0(980)\pi^-$ through intermediate kaons, as shown in Fig. 4.5, we fix the invariant masses of the external particles with momenta q_1 and q_3 to the pion mass and the nominal mass of the $f_0(980)$, respectively, and study the solutions of Eq. (4.2) while varying the invariant mass s_2. Using a set of algebraic manipulations we find that the system (4.2) is solvable only for two values of s_2, namely $\sqrt{s_2} = m_{1,2}^{(\text{ts})}$, where $m_1^{(\text{ts})} = 1.42\,\text{GeV}$, and $m_2^{(\text{ts})} = 1.46\,\text{GeV}$. The points are shown as dots in the right bottom panel of Fig. 4.7. However, the condition $x, y, z \in [0, 1]$ is only satisfied for the first solution as can be seen in this figure.

There is a simple kinematic explanation for the appearance of the singularity illustrated on Fig. 4.6. The initial state $a_1(1260)$ with $J^{PC} = 1^{++}$ can decay $K^*\bar{K}$ on mass shell starting from the threshold $\sqrt{s_2} = 1.39\,\text{GeV}$. Then, K^* decays to K and π on mass shell. We notice that the K from K^* decay can go to the same direction as the $\bar{K}$, the ratio of velocities of $\bar{K}$ and K is a function of $\sqrt{s_2}$. The invariant mass of the $\bar{K}K$ system, when the kaons vectors are aligned, is only equal to the mass of f_0 if $\sqrt{s_2} = m_{1,2}^{(\text{ts})}$. For $\sqrt{s_2} = m_2^{(\text{ts})}$, however, $\bar{K}$ is faster than K and thus K cannot catch up with $\bar{K}$

to form f_0. Only for $\sqrt{s_2} = m_1^{(\text{ts})}$, is K faster than the $\bar{K}$. The discussed kinematics demonstrate a very peculiar situation in the decay of the $a_1(1260)$ to $K^*\bar{K}$: just above the two-body threshold, the rescattering in the triangle can happen with particles on mass shell. The relation between on-shellness of the process and the singularities of loop diagrams was noticed by Coleman and Norton in Ref. [147].

4.2.2 Feynman method

Once the positions of the singularities are established we can calculate and plot the amplitude and validate the findings. We start from the simple case of scalar particles, and discuss the spin in Sec. 4.5. For simplicity we use a scalar coupling g for all vertices

$$\mathbb{M}_{a_1 \to f_0 \pi}^{(\text{sc})} = g^3 \int \frac{\mathrm{d}^4 k_1}{(2\pi)^4 i} \frac{1}{(m_1^2 - k_1^2 - i\epsilon)(m_2^2 - (q_2 - k_1)^2 - i\epsilon)(m_3^2 - (k_1 - q_1)^2 - i\epsilon)}. \quad (4.3)$$

We calculate the integral using the technique of Feynman parameters [38, 39]

$$\mathbb{M}_{a_1 \to f_0 \pi}^{(\text{sc})} = \frac{g^3}{16\pi^2} \int_0^1 \mathrm{d}x \int_0^1 \mathrm{d}y \int_0^1 \mathrm{d}z \, \frac{\delta(x + y + z - 1)}{\Delta(x,y,z) - i\epsilon} \quad (4.4\text{a})$$

$$= \frac{g^3}{16\pi^2} \int_0^1 \mathrm{d}x \int_0^{1-x} \frac{\mathrm{d}y}{\Delta_{xy} - i\epsilon}, \quad (4.4\text{b})$$

$$= \frac{g^3}{16\pi^2} \int_0^1 \frac{\mathrm{d}x}{s_1(y_+(x) - y_-(x))} \left(\log \frac{1 - x - y_+(x)}{-y_+(x)} - \log \frac{1 - x - y_-(x)}{-y_-(x)} \right), \quad (4.4\text{c})$$

where $\Delta(x, y, z)$ is a polynomial in x, y and z which parametrically depends on invariant masses

$$\Delta(x, y, z) = xm_1^2 + ym_2^2 + zm_3^2 - xys_3 - yzs_1 - zxs_2, \quad (4.5)$$

the z-integral is solved using the delta function. Using the condition $x + y + z = 1$, we define $\Delta_{xy} = \Delta(x, y, 1 - x - y)$. The curve $\Delta_{xy} = 0$ shown in Fig. 4.7 gives the singularities of the integrand in Eq. (4.4b). The y integral is evaluated using a partial fraction decomposition, since Δ_{xy} is a second order polynomial in y. The $y_\pm$ are the solutions of the equation $\Delta_{xy} = 0$, *i.e.*

$$s_1 y^2 + (m_2^2 - m_3^2 - s_1 + xs_2 - xs_3 + xs_1) y + xm_1^2 + (1 - x)m_3^2 - x(1 - x)s_2 = 0.$$

Eq. (4.4c) is evaluated numerically; the real and imaginary parts are shown in Fig. 4.8. The imaginary part starts to grow rapidly from the $K^*\bar{K}$ threshold s_2^{th} ($s_2^{\text{th}} = m_K + m_{K^*}$); it goes to infinity when $\sqrt{s_2} = m_1^{(\text{ts})}$. The real part has a cusp at the threshold, then sharply drops below zero at $\sqrt{s} = m_1^{(\text{ts})}$ and becomes stable for higher values of $\sqrt{s}$. To take the finite width of the intermediate particles into account, we shift the masses to the complex plane by substituting $m_j^2 \to m_j^2 - im_j\Gamma_j$. Such substitutions do not lead to a correct analytic structure of the amplitude in the variables s_i, however, it gives a good estimation of the smearing due to the finite width. The changes of the K^* propagator in Eq. (4.3) results in a smoother behavior of the amplitude, as shown in the right panel of Fig. 4.8. The effect singularity at $\sqrt{s} = m_1^{(\text{ts})} = 1.42\,\text{GeV}$ is now limited, the amplitude scales proportionally to $\log \Gamma_{K^*}$.
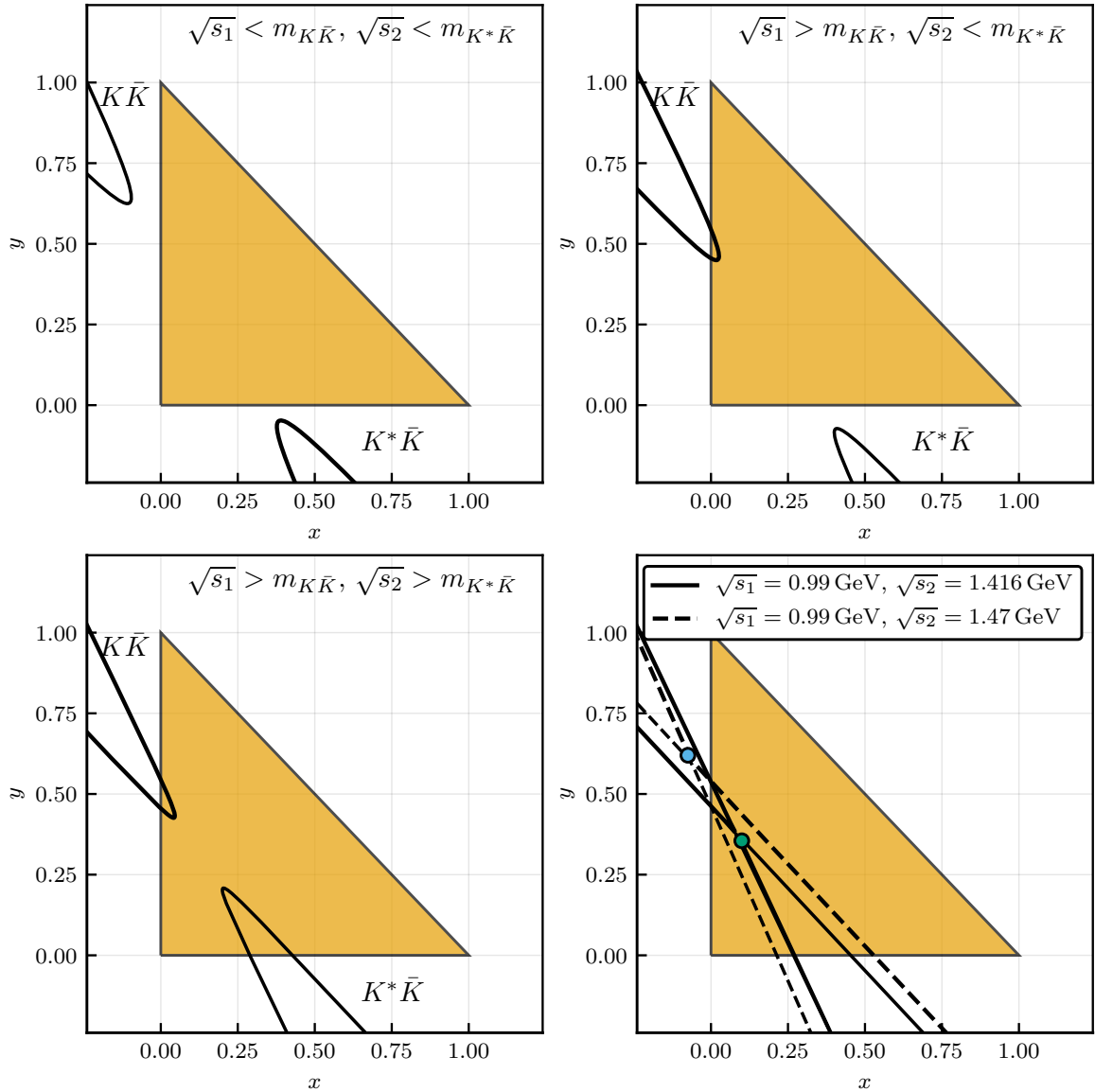
Figure 4.7: Diagrams illustrating the positions of the singularities of the integrand of Eq. (4.4b) in the plane of the Feynman variables x and y. The orange triangle is the kinematically allowed region. The dots are pinch singularities, corresponding to $\sqrt{s_2} = m_1^{(\text{ts})}$ (lower dot) and $\sqrt{s_2} = m_2^{(\text{ts})}$ (upper dot), respectively. The curves are the solutions of $\Delta_{xy} = 0$ (see Eqs. (4.4) and (4.5)) for $\sqrt{s_2} = m_1^{(\text{ts})}$ (solid line) and $\sqrt{s_2} = m_2^{(\text{ts})}$ (dashed line).
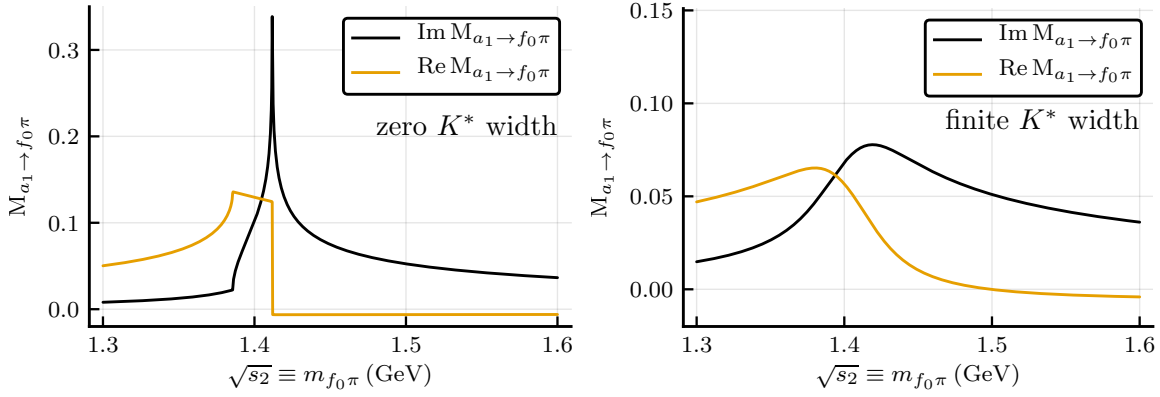
Figure 4.8: The left panel shows the real (orange) and imaginary (black) parts of $\mathbb{M}^{(sc)}_{a_1 \to f_0 \pi}(s)$ for infinitesimal width of K^*. The right panel shows the same amplitude smeared by the finite width of K^*.
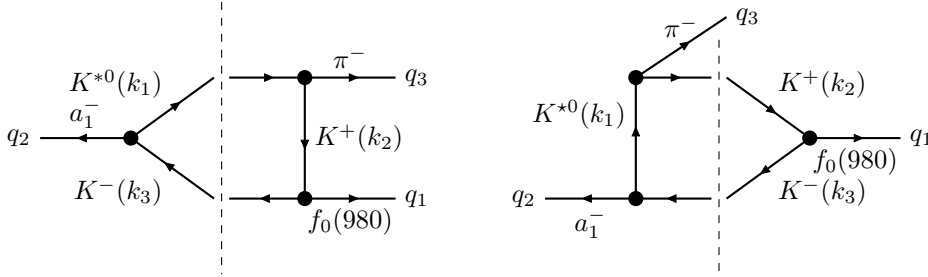
Figure 4.9: Two possible cuts which contribute to the imaginary part of the matrix element of the process $a_1^-(1260) \to f_0(980)\pi^-$.

4.2.3 Dispersive approach

The amplitude $\mathbb{M}^{(sc)}_{a_1 \to f_0 \pi}(s_1, s_2, s_3)$ in Eq. (4.4c) is an analytic function with a rather simple analytic structure: there is a unitarity cut in each variable s_i related to the production of intermediate particles in the triangle $q_n \to k_i, k_j$ (as before (ijn) are even permutations of (123)) [38, 145]. Hence, in order to recover the complete amplitude, one needs to only know the discontinuity on the cut. The latter can be calculated by a simple method developed by Cutkosky [145]. The representation of the amplitude via the Cauchy integral is referred to as the *dispersive representation*. This representation helps us to relate the model based on the single triangle rescattering to the more general approach discussed in Sec. 4.5 and Sec. 7.

Imaginary part of the amplitude

Expressions for the Feynman loop diagrams are real analytic functions, *i.e.* they obey the Schwarz reflection principle and stay real when all variables s_i are below the corresponding thresholds. In the kinematic domain of our interest s_2 is above the $K^*\bar{K}$ threshold, and s_1 is above the $K\bar{K}$ threshold therefore the amplitude is complex. The imaginary part of the amplitude $\mathbb{M}$ of the diagram in Fig. 4.5

is related to the discontinuity across the cuts shown in Fig. 4.9 by [145]

$$\text{Im}\,\mathbb{M}^{(\text{sc})}_{a_1 \to f_0 \pi} = \frac{1}{2i}\left(\text{Disc}^{(\text{sc})}_{K\bar{K}} + \text{Disc}^{(\text{sc})}_{K^*\bar{K}}\right). \tag{4.6}$$

To calculate the discontinuities, we use the following expression

$$\text{Disc} = \int \prod_{\text{cut}} \frac{\mathrm{d}^3 k_i}{(2\pi)^3 2E_i^{(k)}} \times \left(\sum_{\text{polarization}} \mathbb{M}_1 \cdot \mathbb{M}_2^*\right) \times (2\pi)^4 \delta^4(\text{mom.cons.}), \tag{4.7}$$

where $\mathbb{M}_{1,2}$ are the matrix elements for processes on the left- and right-hand side of the cutting line, respectively (see Fig. 4.9). We are calling particles which are crossed by the cutting line cut particles. The integration is performed over the total momentum space of the cut particles, k_i are the momenta of the cut particles, and $E_i^{(k)}$ are the corresponding energies.

Simple model with scalar intermediate particles

For the case of scalar intermediate particles, the expressions for the discontinuities are:

$$\text{Disc}^{(\text{sc})}_{K^*\bar{K}} = g^3 \int \frac{\mathrm{d}^3 k_1}{(2\pi)^3 2E_1^k} \frac{\mathrm{d}^3 k_3}{(2\pi)^3 2E_3^k} \times \frac{1}{m_2^2 - k_2^2 + i\epsilon} \times (2\pi)^4 \delta^4(q_2 + k_1 - k_3), \tag{4.8}$$

$$\text{Disc}^{(\text{sc})}_{K\bar{K}} = g^3 \int \frac{\mathrm{d}^3 k_2}{(2\pi)^3 2E_2^k} \frac{\mathrm{d}^3 k_3}{(2\pi)^3 2E_3^k} \times \frac{1}{m_1^2 - k_1^2 - i\epsilon} \times (2\pi)^4 \delta^4(q_1 + k_3 - k_2), \tag{4.9}$$

where the products of matrix elements $\mathbb{M}_1 \cdot \mathbb{M}_2^*$ are given by the coupling constants at the three vertices, which are set to g, and the propagator, which is a function of the angle between $\vec{k}_1$ and $\vec{q}_3$ in (4.8) and a function of the angle between $\vec{k}_3$ and $\vec{q}_3$ in (4.9). For both discontinuities, the cut particles (K^*, K^- and K^+, K^-, respectively) are set on their mass shells. The integration with the delta function in (4.9) is performed in the f_0 rest frame. After carrying out the integration we arrive at the following expression:

$$\text{Im}\,\mathbb{M}^{(\text{sc})}_{a_1 \to f_0 \pi} = \frac{g^3}{16\pi\lambda^{1/2}(s_2, s_3, s_1)}\left[\underbrace{\log\frac{\tilde{A} + 1 + i\epsilon}{\tilde{A} - 1 + i\epsilon}}_{\text{from Disc}^{(\text{sc})}_{K^*\bar{K}}} + \underbrace{\log\frac{\tilde{C} + 1 - i\epsilon}{\tilde{C} - 1 - i\epsilon}}_{\text{from Disc}^{(\text{sc})}_{K\bar{K}}}\right], \tag{4.10}$$

where the coefficients $\tilde{A}$, $\tilde{C}$ originate from the propagators,

$$\tilde{A} = \frac{2s_2(m_2^2 - m_1^2 - s_3) + (s_2 + m_1^2 - m_3^2)(s_2 + s_3 - s_1)}{\lambda^{1/2}(s_2, m_3^2, m_1^2)\lambda^{1/2}(s_2, s_3, s_1)}, \tag{4.11}$$

$$\tilde{C} = \frac{2s_1(m_1^2 - m_3^2 - s_2) + (s_1 + m_3^2 - m_2^2)(s_1 + s_2 - s_3)}{\lambda^{1/2}(s_1, m_2^2, m_3^2)\lambda^{1/2}(s_1, s_2, s_3)}. \tag{4.12}$$

Here, $q_i^2 = s_i$, $k_i^2 = m_i^2$, and $\lambda(x, y, z)$ is the Källén function. In the denominators of Eq. (4.11) and Eq. (4.12) one can recognize the break-up momenta calculated in the a_1 rest frame for $\tilde{A}$, and in the
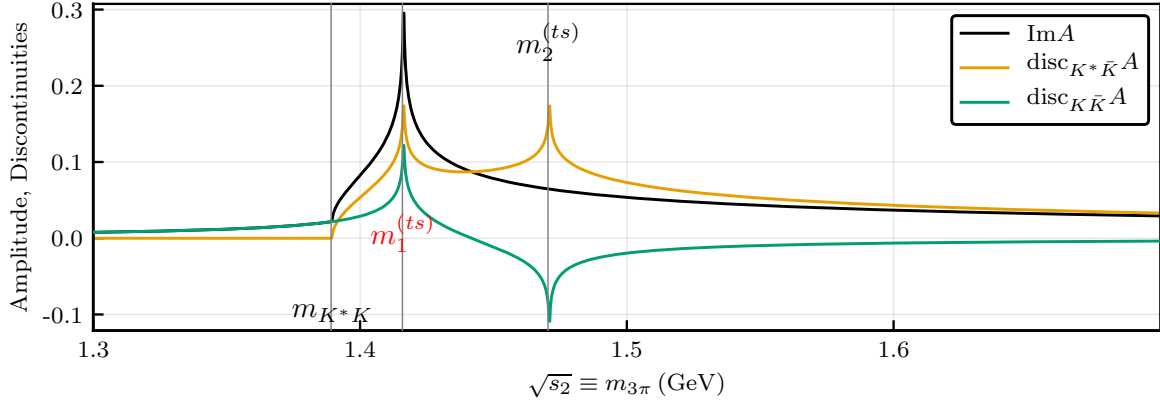
Figure 4.10: The imaginary part of the matrix element $\operatorname{Im} \mathbb{M}^{(\mathrm{sc})}_{a_1 \to f_0 \pi}(s)$ as a function of the $f_0 \pi$ invariant mass is shown by the black line. The contributions of the discontinuities for $K^* \bar{K}$ and $K\bar{K}$ are shown by the orange and the green lines, respectively.

f_0 rest frame for $\tilde{C}$. The products of two expressions in parentheses in the numerators come from the product of energies of the particles with momenta k_1 and q_3 in Eq. (4.11) and the particles with momenta k_3 and q_3 in Eq. (4.12) calculated in the corresponding frames. The real parts of expressions (4.8) and (4.9) compensate each other and consequently the expression for the imaginary part (4.10) is real.

The imaginary part of the amplitude, $\operatorname{Im} \mathbb{M}^{(\mathrm{sc})}_{a_1 \to f_0 \pi}(s)$, and the contributions from the individual discontinuities are shown in Fig. 4.10. One can clearly see two singularities at $\sqrt{s_2} = m^{(\mathrm{ts})}_{1,2}$ for the discontinuities. The imaginary part, however, is smooth at $\sqrt{s_2} = m^{(\mathrm{ts})}_2$ as expected from the kinematic analysis of Sec. 4.2.1. One can also notice that the imaginary part is not zero below the $K^* \bar{K}$ threshold. This contribution comes from $\operatorname{Disc}^{(\mathrm{sc})}_{K\bar{K}}$, because the mass m_{f_0} is above the $2m_{K^\pm}$ threshold.

Recovering the full amplitude using the dispersive integral

As we stated before, the amplitude of the triangle diagram can be recovered using the knowledge of the analytic structure and the discontinuities calculated in Eq. (4.8) and (4.9). Assuming that the analytic structure in s_1 is a cut, which starts at threshold $s_1^{\mathrm{th}} = 4m_K^2$ and runs to infinity, we write the dispersive integral (see Eq. (2.26)) as follows,

$$\mathbb{M}^{(\mathrm{sc})}_{a_1 \to f_0 \pi}(s_1, s_2) = \frac{1}{2\pi i} \int_{4m_K^2}^{\infty} \frac{\operatorname{Disc}^{(\mathrm{sc})}_{K\bar{K}}(s_1', s_2)}{s_1' - s_1 - i\epsilon} \mathrm{d}s_1'. \tag{4.13}$$

Similarly, we can write the expression for the amplitude using the s_2-discontinuity.

$$\mathbb{M}^{(\mathrm{sc})}_{a_1 \to f_0 \pi}(s_1, s_2) = \frac{1}{2\pi i} \int_{(m_{K^*}+m_K)^2}^{\infty} \frac{\operatorname{Disc}^{(\mathrm{sc})}_{K^* \bar{K}}(s_1, s_2')}{s_2' - s_2 - i\epsilon} \mathrm{d}s_2'. \tag{4.14}$$

As we validate by direct calculation, both Eq. (4.13) and Eq. (4.14) reproduce Eq. (4.4) as a function of s_2 when s_1 is fixed to the f_0 invariant mass squared as shown in Fig. 4.8. The two methods, Eq. (4.13) and Eq. (4.14) look algebraically the same, however, they turn out to have very different extension beyond perturbation theory.

The first method presented by Eq. (4.13) exploits the analytic structure in the subchannel variable ($\sigma \equiv m_{K\bar{K}}^2$ in that case). The diagram on the left panel of Fig. 4.9 is reminiscent of the unitarity equation for the production process where the $K\bar{K}$ appear from a decay. Using the terminology of Sec. 2.3 (see Eq. (2.41)), Eq. (4.13) is the "unitarization" of the "background" term which is given by the projection of the K^* resonance to the $K\bar{K}$ channel. In exactly the same way our triangle diagram appears in the iteration series of Khuri-Treiman (KT) equations [148, 149], which we discuss in Sec. 4.5. In order to account for the finite width of K^*, one can replace the K^* propagator in Eq. (4.9) by a complete $K\pi$ P-wave scattering amplitude.

The second approach (Eq. (4.14)) addresses the s-dependence ($m_{3\pi}^2$), which is controlled by three-body unitarity [5, 14, 150]. The triangle diagram also appears iteratively when the one-pion exchange diagram is attached to the production vertex similar to the left panel of Fig. 4.9. In order to take into account the width of K^* one would need to insert a $K\pi$ loop and put those particles on mass shell integrating over the K^* invariant mass (*i.e.* $K\pi$ invariant mass) leading to a convolution of Eq. (4.14) with the function $t_{K\pi}^*(\sigma')\rho(\sigma')t_{K\pi}(\sigma')$.

Using the example of the triangle diagram we established the interesting fact that the rescattering effects lead to a clear connection between the subchannel two-body unitarity and the overall dynamics of the system controlled by the three-body unitarity. In Ref. [5] we clarify the connection and show how the s-discontinuity, present due to the final-state interaction, helps to isolate genuine three-body effects.

4.2.4 Schmid's cancellation and conservation of probability

Along the lines of the kinematic explanations of the triangle singularity given in Sec. 4.2.1 we can discuss the rescattering mechanism using the Dalitz plot representation shown in Fig. 4.11. A decay $1 \to 3$ is considered in the center-of-mass frame. Points at the border of the Dalitz plot correspond to a situation when momenta of the final-state particles are aligned parallel to each other. For the quasi-stable "resonance" which decays to particles with momentum q_3 and k_2 on the left panel of Fig. 4.11, the particle with the momentum k_2 is collinear to $\vec{k}_3$ and it faster than k_3 only on the red arc. It is easy to see if we realize that the value q_1^2 is minimal (left tip of the red arc), when $\vec{k}_2 = \vec{k}_3$ such that they are both at rest their center-of-momentum; when the value of $(q_3 + k_2)^2$ approaches maximum (top tip of the red arc), $\vec{k}_2 = \vec{q}_3$, $\vec{k}_3 = 0$. On the other part of the Dalitz plot border either $|\vec{k}_2| < |\vec{k}_3|$, or the momenta point to opposite directions. The logarithmic divergence in the interaction amplitude as a function of $s_1 \equiv q_1^2$ appears exactly at the place where the "resonance" touches the red arc [151]. The band produced by the triangle singularity on the Dalitz plot (find TS line on the left panel of Fig. 4.11) can be observed in principle. However, it is extremely difficult to find a clean reaction where the initial state has well-defined quantum numbers, and a relatively narrow resonance touches the red arc.

The interesting question, if one can see the effect of the triangle singularity in the projection of the Dalitz plot, was addressed by Ch. Schmid [151]. He noticed that projections of a quasi-stable "resonance" (the width is infinitely small) to the two-body partial waves in the subchannel (k_2, k_3) is singular at those points where the resonance touches the Dalitz plot border. For the S-wave projection
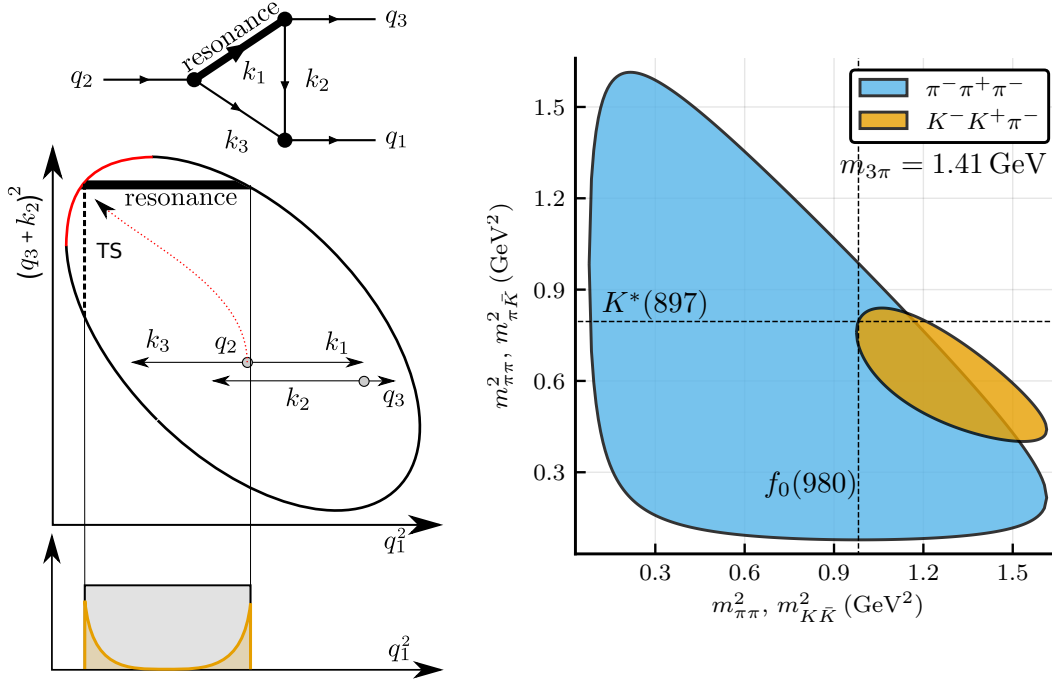
Figure 4.11: The left plot shows the kinematics of the rescattering which lead to the triangle singularity (see discussion in the text). Right plot: Dalitz plots for the 3π (blue) and the $K\bar{K}\pi$ (orange) systems at $w = 1.4\,\text{GeV}$. The invariant mass squared of the $\pi^+\pi^-$ or $K\bar{K}$ subsystem is along the x axis, the invariant mass squared of the other pion pair, $\pi^+\pi^-$, or the $K\pi$ subsystem is along the y axis. The horizontal dashed line indicates the K^* resonance, and the vertical dashed line shows the position of the $f_0(980)$ resonance for both the $K\bar{K}$ and $\pi\pi$ subsystems.

it reads,

$$f_0^{(\text{proj})}(s_1) = \int \frac{\mathrm{d}z}{2} \frac{1}{m_r^2 - k_1^2} = \frac{s_1}{\lambda^{1/2}(s_1, m_2^2, m_3^2)\lambda^{1/2}(s_1, s_2, s_3)} \log \frac{\tilde{C}+1}{\tilde{C}-1}. \qquad (4.15)$$

where as before, $k_1 = k_2 + q_3$, $z = \cos\theta$, and θ is the scattering angle in the center of momentum of the (k_2, k_3) pair. $\tilde{C}$ is given by Eq. (4.12). Schmid demonstrated that when the projection of the "resonance" from Eq. (4.15) is added to the amplitude calculated from the triangle diagram, the last term leads to a modification of the projection phase. In the vicinity of the singularity point,

$$\begin{aligned} f_0(s_1) &= f_0^{(\text{proj})}(s_1) + f_0^{(\text{tr})}(s_1) \\ &= f_0^{(\text{proj})}(s_1) + i\rho(s_1)t(s_1)f_0^{(\text{proj})}(s_1) = e^{i\delta_0}\, f_0^{(\text{proj})}(s_1). \end{aligned} \qquad (4.16)$$

The projection of the Dalitz plot is found as an incoherent sum of the squared partial-wave amplitudes, *i.e.* $\sum(2l+1)|f_l(s_1)|^2$. The phase factor drops the Dalitz plot projection does not show the effect of the triangle singularities as it was concluded by Ch. Schmid. He also showed that the final-state interaction cannot produce an enhancement in the total invariant mass of the system ($s_1 \equiv q_1^2$ in Fig. 4.11) as a consequence of probability conservation.
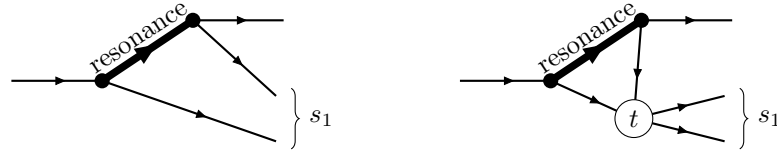
Figure 4.12: Two contributions to the partial-wave projection f_0 in Eq. (4.16). The left diagram shows a projection of the cross-channel resonance, while the right plot demonstrates the triangle loop diagram for the rescattering via an interaction $t(s_1)$ from the cross channel to the considered channel indicated in the plot by the curly bracket.

In 1995, V. Anisovich and A. Anisovich noticed that the Schmid theorem does not hold in the case of coupled channels [152]. The cancellation $1 + i\rho(s_1)t(s_1) = e^{i\delta_0}$ does not happen in presence of an inelasticity. The work [151] was generalized by A. Szczepaniak [153] who explicitly demonstrated that probability is still conserved and shared between the two channels. Recently, the influence of the "resonance" width was investigated (see Ref. [154]) in relation with the Schmid theorem. The authors concluded that the cancellation does not hold strictly in that case even for a single channel.

The general discussion on the Dalitz plot dynamics from Ref. [153] can be applied to a coupled system of 3π and $K\bar{K}\pi$. It gives a schematic explanation of the $a_1(1420)$ effect which is consistent with probability conservation. The Dalitz plot for $\pi^+\pi^-\pi^-$ superimposed on the one for $K\bar{K}\pi$ is shown in Fig. 4.11. The rescattering process from the K^*-resonance, being enhanced by the triangle singularity, leads to a "migration" of events from the $K\bar{K}\pi$ final state to the 3π final state. When we move the invariant mass $\sqrt{s_2}$, the sizes of both Dalitz plots change, so do the positions of their borders with respect to the subchannel resonances indicated in Fig. 4.11. When $\sqrt{s_2} = 1.4\,\text{GeV}$ the intersection of the dashed lines coincides with the border of the kaon Dalitz plot, *i.e.* the 3-momentum vectors of the decay products are aligned. In this case, events are redistributed from the intersection point along the $f_0(980)$ vertical dashed line. Since f_0 has both a $\pi\pi$ and a $K\bar{K}$ decay channel, this results in a migration of events from the $K\bar{K}\pi$ Dalitz plot to the 3π Dalitz plot.

4.2.5 Other triangles

Clearly, the rescattering process $K^*\bar{K} \to f_0\pi$ is not the only one contributing to the observed final state. All final states sharing the same quantum numbers $1^{++}0^+$ are coupled. Therefore, a valid question is whether the rescattering from the $K^*\bar{K}$ decay channel of the $a_1(1260)$ (i.e. "$(K^*K\bar{K})$-triangle") indeed produces the closest singularity to the physical region. We demonstrate this by calculating the intensity and the phase motion of the $J^{PC}M^\epsilon = 1^{++}0^+$ $f_0\pi$ P-wave rescattered via the triangle diagram from the other possible decay channels of the $a_1(1260)$.

Fig. 4.13 shows the intensities and relative phases for the six different triangles, which might contribute to the $J^{PC}M^\epsilon = 1^{++}0^+$ $f_0\pi$ P-wave. All plots feature a rise at threshold and a fall at high energies: the rise reflects the opening of the $f_0\pi$-channel, the fall comes from the $a_1(1260)$ propagator. The very narrow peak in the $(K^*K\bar{K})$ is accompanied by an extremely sharp phase motion near $M_{3\pi} = 1.4\,\text{GeV}$. It indicates the presence of the triangle singularity close to the physical region. For other channels, the phase moves as well but at different places and not as rapid. We find that the scattering-on-shell condition is not fulfilled for the remaining five configurations presented in Fig. 4.13. The motion of the phase corresponds to the threshold in the considered decay channel of a_1 which rescatters to the $J^{PC}M^\epsilon = 1^{++}0^+$ $f_0\pi$ P-wave.
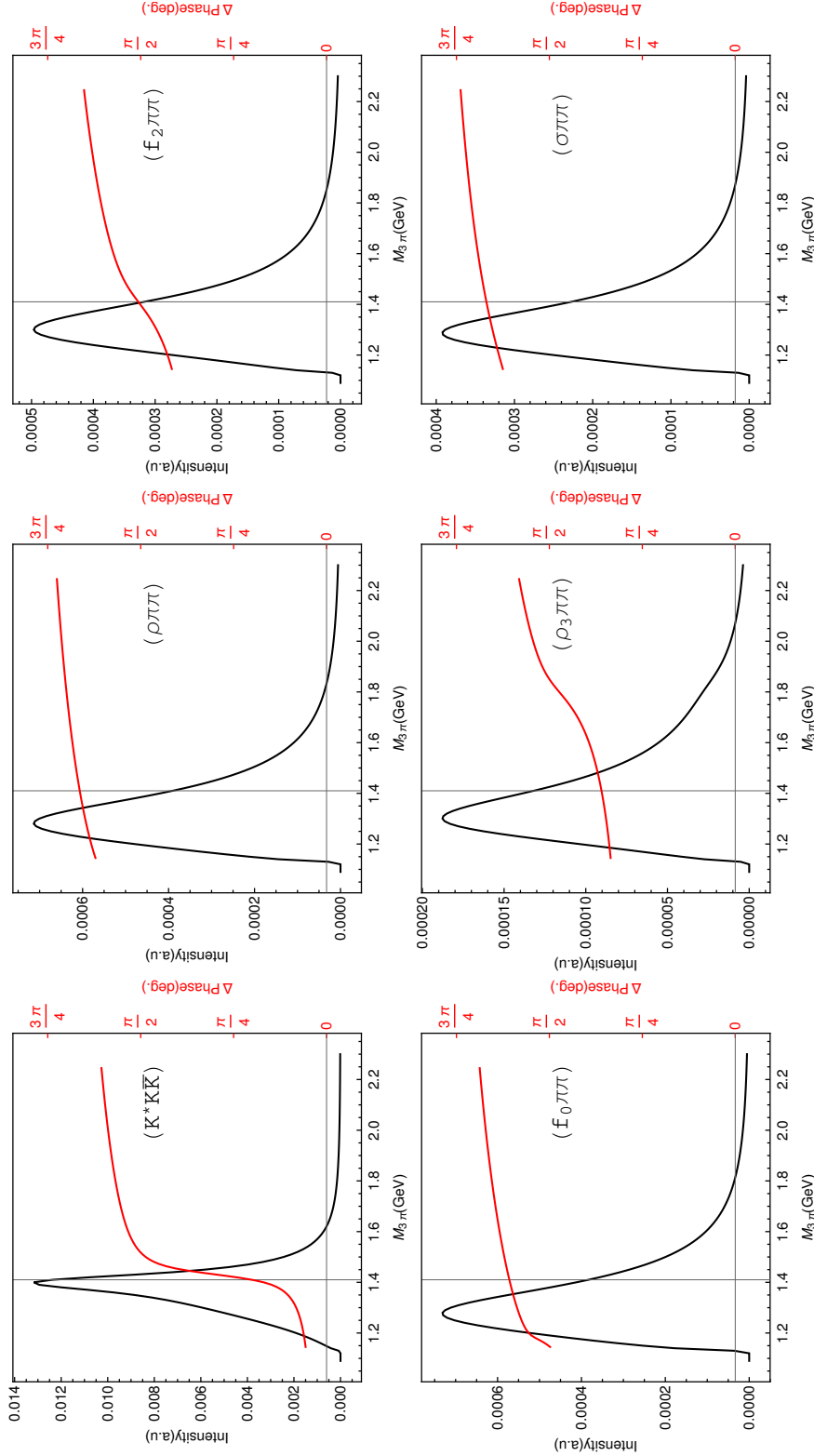
Figure 4.13: The results of calculations of the intensity (black line) and relative phase (red line) of the $J^{PC}M^\epsilon = 1^{++}0^+$ $f_0\pi$ P-wave with respect to the $J^{PC}M^\epsilon = 1^{++}0^+$ $\rho\pi$ S-wave for different triangle diagrams shown on the right plot of Fig. 4.5. The labels indicate the particles inside the triangle loop, i.e. $(G\,g\,r)$. The calculation is performed for scalar particles of nominal masses in the decay $a_1(1260) \to f_0\pi$, the amplitude is multiplied by the $a_1(1260)$ propagator parameterized by a Breit-Wigner propagator with constant width. The intensity is obtained by multiplying the matrix element squared to the two-body phase space (assuming stable f_0). The vertical line indicate $m_{3\pi} = 1.41$ GeV, the observed mass of the $a_1(1420)$ resonance.
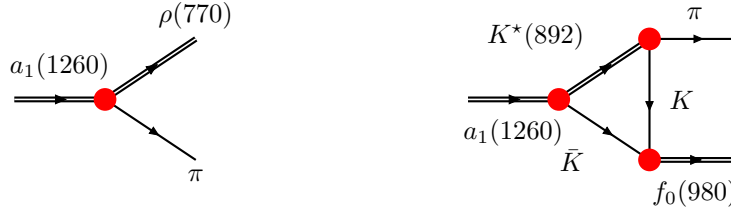
Figure 4.14: Simplistic diagrams representing decays $a_1(1260) \to \rho\pi$ and $a_1(1260) \to f_0\pi$ via $K^*\bar{K}$ rescattering. The vertex couplings discussed in the text are indicated by red dots.

The strength of the rescattering corrections can be read from Fig. 4.13. In these calculations no extra couplings were used (*e.g.* $a_1(1260)$ branching ratio). Hence, the strength indicates how close the triangle singularity is. As one would expect, the process with kaons is one order of magnitude stronger than the others. We conclude that other rescattering processes give a rather smooth contribution in the energy range of interest. The background used in the fit below is supposed to effectively account for these effects.

4.2.6 Strength of the effect

In order to estimate the intensity of the signal expected in the $f_0(980)\pi^-$ channel we calculate its intensity and phase difference with respect to the dominant $a_1^-(1260) \to \rho^0\pi^-$ decay, assuming that the signal in $f_0\pi^-$ is entirely due to the triangle singularity in the $a_1^-(1260) \to f_0(980)\pi^-$ decay. Then, the decay rate of $a_1 \to f_0(980)\pi^-$ P-wave is proportional to three squared couplings in the triangle vertices, $g_{a_1 K^*\bar{K}}$, $g_{f_0 K\bar{K}}$ and $g_{K^*\pi K}$ as indicated in Fig. 4.14, as well as to the squared amplitude for the triangle diagram and the branching ratio of $f_0 \to \pi\pi$. The decay rate of the $a_1 \to \rho\pi$ S-wave is related to the coupling constant $g_{a_1\rho\pi}$. We estimated the strength of the couplings and the branching ratios based on world-average data. The detailed discussion can be found in Ref. [1]. We will now briefly summarize the results. We estimated $g_{K^*\pi K}$ from the K^* decay width, the coupling constants $g_{f_0 K\bar{K}}$ and $g_{f_0\pi\pi}$ were extracted from results of Ref. [155]. The ratio of the constants $g_{a_1 K^*\bar{K}}$ and $g_{a_1\rho\pi}$ was estimated from the branching fractions of the $K\bar{K}\pi$ and $\rho\pi$ S-wave decay channels of $a_1(1260)$ measured in hadronic τ-decays [156–158]. Due to the poor knowledge of the $a_1(1260)$ couplings we were only able to give an order-of-magnitude estimate for the strength of the $J^{PC}M^\epsilon = 1^{++}0^+$ $f_0\pi$ P-wave with respect to $J^{PC}M^\epsilon = 1^{++}0^+$ $\rho\pi$ S-wave. The obtained peak-to-peak ratio, approximately 10^{-2}, agreed with the experimental result.

The estimation has large systematic uncertainties:

- In the calculations we assume that the decay of the $a_1(1260)$ resonance is the origin of $\rho\pi$ and $K^*\bar{K}$, which are rescattered to $f_0\pi$. However, there may be other processes which contribute to the same final state, *e.g.* non-resonant Deck-like processes [83]. We expect a rather large contribution of the Deck-like background to the $\rho\pi$ S-wave signal [83] as well as to the $K^*\bar{K}$ channel [159]. It might lead to a different branching ratio of $\rho\pi$ and $K^*\bar{K}$ channels than the one measured in τ-decays.

- A large uncertainty comes from the definition and the line shape of the f_0. As we discussed already in Sec. 3.4, the separation of $f_0(980)$ out of the $\pi\pi$ interaction in the S-wave is not well justified from the theory side. Therefore, the coupling constants used in the Flatté

parametrization are not well established. The relative intensity is proportional to $(g^2_{f_0\pi\pi}R_{K/\pi})^2$, therefore, it could easily change by a factor of 4 depending on the input values. The systematic uncertainty of the $f_0\pi$ P-wave due to the isobar parametrization is of the order of 20%, based on systematic studies of Ref. [78].

- Lastly, we neglected other possible contributions to the $f_0\pi$ final states such as various rescattering processes $\xi\pi \to f_0\pi$ as well as the non-resonant production of $f_0\pi$ via *e.g.* the Deck process. As shown in Fig. 4.13 the other rescattering processes are smooth and the phase motion is slow in the energy range under study. There is no reason to expect sharp enhancements in the projections due to the Deck process, however it might change the strength and shape of the signal by interference. From the fact that a clean $a_1(1420)$ signal *has been seen* in the $f_0\pi$ P-wave, we conclude that the other contributions are small. A factor of 2 uncertainty to the signal strength can be estimated from the amount of the intensity required by the background and interference in the mass-depend fit (*e.g.* compare the red and the blue line in Fig. 4.2).

4.3 Validation using the COMPASS data

To check our interpretation of the $a_1(1420)$ signal we performed a fit of the theoretical model presented above to the COMPASS SDM simultaneously for all bins of t'. A minimal set of waves is selected: the $J^{PC}M^\epsilon = 1^{++}0^+$ $f_0\pi$ P-wave with the $a_1(1420)$ signal, the $J^{PC}M^\epsilon = 1^{++}0^+$ $\rho\pi$ S-wave as an important reference wave for our interpretation, and the nearly background-free stable $J^{PC}M^\epsilon = 2^{++}1^+$ $\rho\pi$ D-wave incorporated in order to keep an external phase anchor. The models for the $J^{PC}M^\epsilon = 2^{++}1^+$ $\rho\pi$ D-wave and the $J^{PC}M^\epsilon = 1^{++}0^+$ $\rho\pi$ S-wave are the same as in the fits of Ref. [3, 124]: they are described in Sec. 3.3.3 by Eq. (3.30) for the $J^{PC}M^\epsilon = 1^{++}0^+$ $\rho\pi$ S-wave and Eq. (3.31) for the $J^{PC}M^\epsilon = 2^{++}1^+$ $\rho\pi$ D-wave. In our model, compared to the model of Ref. [3], the Breit-Wigner amplitude for the $J^{PC}M^\epsilon = 1^{++}0^+$ $f_0\pi$ P-wave is replaced by a product of the $a_1(1260)$ propagator from the $J^{PC}M^\epsilon = 1^{++}0^+$ $\rho\pi$ S-wave shown in Eq. (3.30) and the amplitude calculated for the triangle diagram (4.4). A coherent background in the parametrization of Eq. (3.29) is added to all waves, however, the background in the $J^{PC}M^\epsilon = 1^{++}0^+$ $f_0\pi$ P-wave is simplified with $b = c_1 = c_2 = 0$. The models for different t'-slices are coupled via the resonance parameters of a_1 and a_2 common for all slices. The strength of the signal and the background components are left free and complex in the fit. The fit model contained 134 free parameters. The range of the data is selected individually of all three waves to include relevant points around the studied $a_1(1420)$ phenomena as discussed. The fit procedure, studies of stability and uncertainties were performed by Mathias Wagner as his master project (find detailed discussion of the fit in Mathias' master thesis [143]). The analysis was summarized in the COMPASS Release Note [160]. A single slice of the fit model overlapping the data points from COMPASS SDM is presented in Fig. 4.15. We notice a very good agreement of the model with the data given the simplicity of the approach and the size of the error bars. The solid bulks of the fit are the $J^{PC}M^\epsilon = 1^{++}0^+$ $\rho\pi$ S-wave and the $J^{PC}M^\epsilon = 2^{++}1^+$ $\rho\pi$ D-wave for which the description is similar to the other studies [3, 161]. Although all parameters are released in the fit simultaneously, the model of the $J^{PC}M^\epsilon = 1^{++}0^+$ $f_0\pi$ P-wave seems to adjust in the fit based on the intensity (plot $[2, 2]$ of Fig. 4.15) and the relative phases (plots $[1, 2]$ and $[2, 3]$ of Fig. 4.15, which are however correlated through the phase in plot $[1, 3]$) for nearly fixed $J^{PC}M^\epsilon = 1^{++}0^+$ $\rho\pi$ S-wave and $J^{PC}M^\epsilon = 2^{++}1^+$ $\rho\pi$ D-wave models. The calculated rescattering amplitude shown by the blue curve in plot $[2, 2]$ requires a little shift to higher energy provided through the interference with the
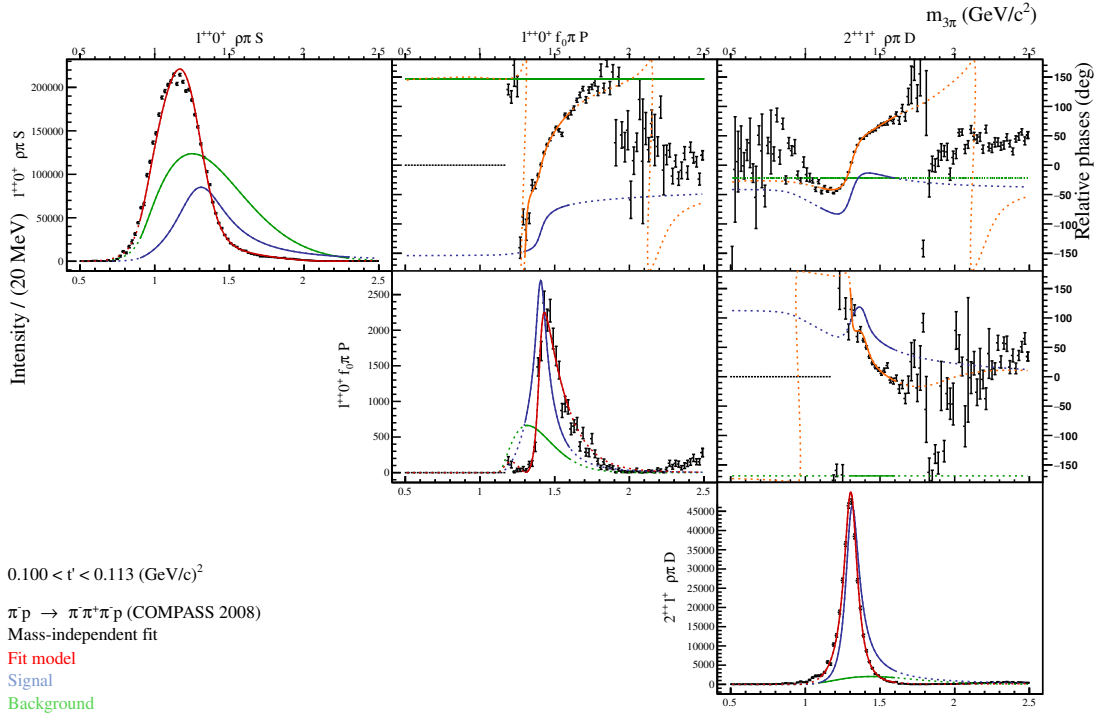
Figure 4.15: The combined plot of the fit results for the first slice in t' from Ref. [160]. The intensities of the $J^{PC}M^\epsilon = 1^{++}0^+ \rho\pi$ S-wave, the $J^{PC}M^\epsilon = 1^{++}0^+ f_0\pi$ P-wave, and the $J^{PC}M^\epsilon = 2^{++}1^+ \rho\pi$ D-wave are shown along the diagonal of the plot matrix. The off-diagonal plot $[i,j]$ show the phases difference $\mathrm{Arg}\,A_j - \mathrm{Arg}\,A_i$. The data points are results of the mass-independent PWA with statistical errors only. The red line presents the complete model adjusted to the data while the blue and green lines show the signal and the background components.

background shown by green curve. However the phase rise in the plot $[1,2]$ of the blue curve matches the place where the rapid motion is seen in the data points. We realize how exactly the interference with the background helps to change the motion of the phase looking at the Argand diagram in Fig. 4.16. There, the rescattering amplitude develops a circle which closely reminds the classical resonance circle. The background signal added coherently shifts every point collinearly as the phase of it does not depend on the energy $\sqrt{s}$. The total sum of the fit residuals is approximately 17 000, which on the largest extend comes from the description of the $J^{PC}M^\epsilon = 1^{++}0^+ \rho\pi$ S-wave and the $J^{PC}M^\epsilon = 2^{++}1^+ \rho\pi$ D-wave. To exclude these contributions from the estimation of the fit quality we sum up the weighted residuals for the $J^{PC}M^\epsilon = 1^{++}0^+ f_0\pi$ P-wave intensity and the phase difference with respect to the $J^{PC}M^\epsilon = 1^{++}0^+ \rho\pi$ S-wave over all t'-slices. The degrees of freedom are calculated counting for parameters of the $J^{PC}M^\epsilon = 1^{++}0^+ f_0\pi$ P-wave only. We obtained the ratio of the residuals divided by n.d.f, $R_{\mathrm{red}}^{(\mathrm{tr.})} = 4.19$. The number is high, however, the result cannot be interpreted in a sense of probability due to the fact that the data points themselves have systematic uncertainties that are not included in the fit.

The quality, though, can be estimated by a comparison with a similar fit in the alternative model. The genuine resonance model similar to the one presented in Ref. [124] is considered. For this
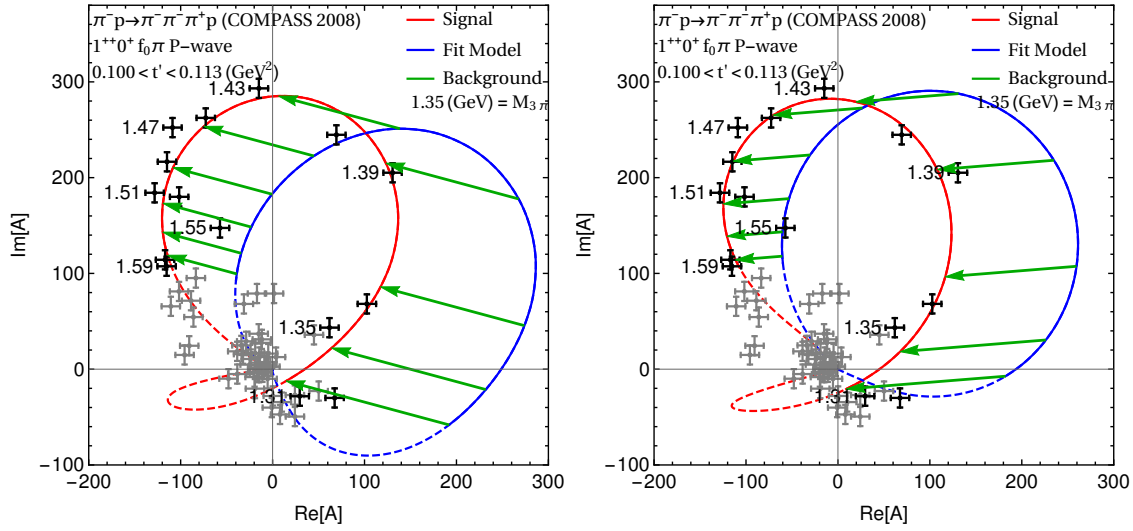
Figure 4.16: The Argand diagram for the $J^{PC}M^\epsilon = 1^{++}0^+ f_0\pi$ P-wave. The phase is measured with respect to the $J^{PC}M^\epsilon = 1^{++}0^+ \rho\pi$ S-wave. Two hypotheses are tested: the left plot is the result of the fit with the rescattering amplitude to describe the signal, the right plot the result with the Breit-Wigner parameterization of the signal. The data points are the result of the PWA in mass and t' bins preformed by COMPASS. The ones printed in black have been used for both fits while the grey ones are further away from the signal region and have not been taken into account. The full amplitude from the fit of the intensities of the $J^{PC}M^\epsilon = 1^{++}0^+ f_0\pi$ P-wave and the $J^{PC}M^\epsilon = 1^{++}0^+ \rho\pi$ S-wave waves and their relative phase is shown as red curve. The signal contribution is shown in blue for both fits, the non-resonant background by green arrows. It does not exhibit a phase motion but shifts the amplitude for both fits.

we replaced the rescattering amplitude by a relativistic Breit-Wigner amplitude and perform a fit analogous to Fig. 4.15. In that case the model for the $J^{PC}M^\epsilon = 1^{++}0^+ f_0\pi$ P-wave has two more parameters, the mass and the width of the $a_1(1420)$ resonance, which adjust the position of the peak in the signal amplitude. However, the quality of the fit did not improve, $R_{\text{red}}^{(\text{BW})} = 4.3$, due to a slightly worse phase description in this case.

4.4 Conclusions

The $a_1(1420)$ is changing the way we identify hadronic states in the spectrum. The signal has all attributes of the resonance: it was discovered in a PWA as an isolated peak with a significant motion of the phase with respect to other waves. However, based on the performed studies we conclude that the rescattering model is consistent with the observed features of the $a_1(1420)$. We find no need for the new resonance signal $a_1(1420)$.

Nevertheless, given a simplicity of the approach on the side of the theoretical calculations as well as the problems of the PWA model discussed in Sec. 3.4, we cannot completely exclude the existence of an exotic $a_1(1420)$ state. In this respect, we outline further important steps of the investigation:

- The freed-isobar results, *i.e.* Fig. 3.18, open an extra dimension in the problem. Since the rescattering effects influence the Dalitz plot distribution at the first place, it is extremely important to look for effects predicated by the rescattering in the subchannel invariant mass

distribution.

- The decay of $\tau \to 3\pi \, \nu_\tau$ is a clear complementary experiment which allows us to study the $a_1(1420)$ effect. An observation of the $J^{PC} M^\epsilon = 1^{++} 0^+ \, f_0 \pi \, P$-wave would clean up the list of interpretations at the first place, *e.g.* the Basdevant-Berger model [140] requires Deck-process which is absent in the τ-decay. Due to the simple production mechanism the dynamical models of the partial waves are simpler.

- The framework of the rescattering corrections has been further developed in order to make qualitative predictions and comparisons. Two main questions, which have not been addressed rigorously yet, are effects of the particles' spin and relative orbital angular momentum, and the importance of the higher order rescattering.

4.5 Outlook: Systematic approach to the rescattering

In this section we present a construction of the theoretical framework based on unitarity and analytic continuation which will allow to systematically address the final-state interaction (rescattering) in a system of three particles. The approach was named after Khuri and Treiman who first applied it for the decay $K \to 3\pi$ [148]. The formalism was further developed in Ref. [53, 149, 162–164]. The idea of the approach is to enforce the *two-body* unitarity relation to the subchannel interactions. Starting with the general isobar ansatz (3.7) we are going to relate the discontinuity of the isobar partial wave amplitude to the cross channel projections. A construction based on the dispersive relations leads to integral equations for the isobar amplitude. The total invariant mass is used as a tuning parameter which connects the physical scattering domain when s is small with the decay domain when s goes above the three-particle threshold.

The KT technique has been already applied to many decays: ω/ϕ [165, 166], $\eta \to 3\pi$ [167–169], $\eta' \to \eta\pi\pi$ [170], $D^+ \to K^- \pi^+ \pi^+$ [171], $D^+ \to K_S \pi^0 \pi^+$ [172]. However, it remains a state of art since for every individual case the formalism differs a little bit due to a different total J^{PC} of the system and different sets of isobar partial waves contributing to the final state. Here, we demonstrate how the formalism can be generalized using the advantages of helicity basis and LS-decomposition. We calculate the cross channel projections for arbitrary partial waves in a system of three pions under exact isospin symmetry.

A common procedure to build the model for the decay amplitude starts by writing all possible covariant structures which contract the polarization tensor of the decaying particle momenta of the final-state particles. Every covariant construction is supplied with a scalar amplitude which is a subject for the unitarity constraints. For example [9, 165, 173]:

$$A_{\omega \to 3\pi} = A(\sigma_1, \sigma_2, \sigma_3) \, \epsilon_{\alpha\beta\gamma\delta} \epsilon_\omega^\alpha p_1^\beta p_2^\gamma p_3^\delta, \tag{4.17}$$

$$A_{a_1 \to 3\pi} = B(\sigma_1, \sigma_2, \sigma_3) \, \epsilon_{a_1}^\mu (p_1 - p_2)_\mu + C(\sigma_1, \sigma_2, \sigma_3) \, \epsilon_{a_1}^\mu (p_2 - p_3)_\mu, \tag{4.18}$$

where A, B, and C are scalar functions. The main reason of complications in the customary construction is that one needs to calculate the partial wave projections for every tensor structure which appears in the covariant amplitude.

As a rather general case, we consider a three-pion production amplitude, where possible values of the total angular momentum J of the 3π system, with a projection M, are allowed. (The diffractive

production $\pi\, p \to 3\pi\, p'$, measured at COMPASS is a good example of the reaction where all values of J and M are allowed) We use the same notations for the three-particle partial waves as discussed in Sec. 3.3.1, and in Appendix C.1: S is the orbital angular momentum of $\pi\pi$, L stands for the relative orbital momentum between the $\pi\pi$ subsystem and the remaining pion. We will, however, drop the isospin coefficients for simplicity. These coefficients are presented in Appendix C.1, and it is not difficult to bring them back. The production amplitude is denoted by $A(\tau)$ (*cf.* Eq. (3.5)), where the kinematic variables τ are the subchannel invariant mass squared, σ_i and two pairs of spherical angles as discussed in Eq. (3.2). We will omit the t and s dependence of the amplitude A as these quantities enter as parameters in the formalism. The general constraint on the s dependence is subject of Chapter 7.

An expansion of the three-particle state leads to the general isobar decomposition (the decomposition for the $\pi^-\pi^+\pi^-$ system was discussed in Sec. 3.3.1, see Eq. (6.6) with Eq. (3.7) and Eq. (3.7)):

$$
A(\tau) = \sum_{JMLS} \left[F_{LS}^{JM}(\sigma_1) Z_{LS}^{JM*}(\Omega_1, \Omega_{23}) \right.
$$
$$
\left. + F_{LS}^{JM}(\sigma_2) Z_{LS}^{JM*}(\Omega_2, \Omega_{31}) + F_{LS}^{JM}(\sigma_3) Z_{LS}^{JM*}(\Omega_3, \Omega_{12}) \right], \quad (4.19)
$$

where the angular function Z_{LS}^{JM} is given by Eq. (3.9). Every isobar partial wave series is truncated for all channels (1), (2), and (3). We notice here that the full amplitude includes an infinite number of partial waves whatever channel is considered due to the cross-channel projections of the isobar partial wave. In Eq. (4.19), the same partial wave projected isobar amplitude F_{LS}^{JM} enters to all channels since the final-state particles are identical.

The projection of the full amplitude to the channel (1) partial waves is found by integrating over two pairs of the spherical angles, Ω_1 and Ω_{23}:

$$
A_{LS}^{JM}(\sigma_1) = \int \frac{d\Omega_1}{4\pi} \frac{d\Omega_{23}}{4\pi} Z_{LS}^{JM} A(\tau) \tag{4.20}
$$
$$
= F_{LS}^{JM}(\sigma_1) + \underbrace{\int \frac{d\Omega_1}{4\pi} \frac{d\Omega_{23}}{4\pi} Z_{LS}^{JM} \sum_{J'M'L'S'} \left[F_{L'S'}^{J'M'}(\sigma_2) Z_{L'S'}^{J'M'*}(\Omega_2, \Omega_{31}) + (\overrightarrow{123}) \right]}_{\hat{F}_{LS}^{JM}(\sigma_1)},
$$

where $\hat{F}_{LS}^{JM}$ is a projection of cross channels, $(\overrightarrow{123})$ indicates a symmetric term obtained by the $1 \to 2 \to 3 \to 1$ permutation from the first term in the square bracket. The integral in Eq. (4.20) can be simplified using properties of the Wigner D-functions and relations between rotations which are discussed in Ref. [91, 96] and are detailed in Appendix C.3. It reads:

$$
\sum_\lambda D_{M\lambda}^J(\phi_3, \theta_3, 0) D_{\lambda 0}^S(\phi_{12}, \theta_{12}, 0) = \sum_\lambda D_{M\lambda}^J(\phi_3, \theta_3, \phi_{12}) d_{\lambda 0}^S(\theta_{12})
$$
$$
= \sum_{\lambda\nu} D_{M\nu}^J(\phi_1, \theta_1, \phi_{23}) d_{\nu\lambda}^J(\hat{\theta}_3) d_{\lambda 0}^S(\theta_{12})
$$
$$
= \sum_{\lambda\nu} D_{M\lambda}^J(\phi_1, \theta_1, \phi_{23}) d_{\lambda\nu}^J(\hat{\theta}_3) d_{\nu 0}^S(\theta_{12}). \tag{4.21}
$$

The integrals over $d\theta_1$, $d\phi_1$, and $d\phi_{23}$ in Eq. (4.20) drop due to orthogonality of the D-functions. [5] We can also immediately conclude that only waves with the same $J' = J$, $M' = M$ contribute to the inhomogeneous term of $\hat{F}_{LS}^{JM}$.

$$
\hat{F}_{LS}^{JM}(\sigma_1) = \sum_{L'S'} \sum_{\lambda\nu} \sqrt{\frac{(2L+1)(2S+1)(2L'+1)(2S'+1)}{(2J+1)^2}} \langle L, 0; S, \lambda \,|J, \lambda\rangle \langle L', 0; S', \nu \,|J, \nu\rangle
$$
$$
\times \int \frac{d\cos\theta_{23}}{2} \Big[F_{L'S'}^{JM}(\sigma_3)\, d_{\lambda 0}^S(\theta_{23}) d_{\lambda\nu}^J(\hat{\theta}_3) d_{\nu 0}^{S'}(\theta_{12})
$$
$$
+ (-1)^{\lambda+\nu} F_{L'S'}^{JM}(\sigma_2)\, d_{\lambda 0}^S(\theta_{23}) d_{\lambda\nu}^J(\hat{\theta}_2) d_{\nu 0}^{S'}(\theta_{31}) \Big], \quad (4.23)
$$

where the angles $\hat{\theta}_3$, θ_{12}, $\hat{\theta}_2$, and θ_{31} can be expressed as functions of σ_1 and θ_{23}, or equivalently as functions of invariants σ_1, σ_2 and σ_3 as shown in Appendix C.3.

The unitarity constraint for the amplitude A_{LS}^{JM} analytically continued from the scattering domain reads:
$$
d_\sigma A_{LS}^{JM}(s, \sigma) = t_S^\dagger(\sigma)\, \rho(\sigma)\, A_{LS}^{JM}(s, \sigma), \qquad (4.24)
$$

where $t_S(\sigma)$ is the partial wave projected $\pi\pi$ scattering amplitude (to avoid confusion with the $(S = 0)$-wave we remind the reader that S stands for the $(\pi\pi)$-orbital angular momentum). Eq. (4.24) is nothing else but the production unitarity equation discussed in Sec. 2.3, *cf.* Eq. (2.34).

To relate the discontinuity of the amplitude A_{LS}^{JM} to $d_\sigma F_{LS}^{JM}$ we need to make one assumption on the analytic structure of F_{LS}^{JM}: the inhomogeneous term $\hat{F}_{LS}^{JM}$ does not contribute to the right-hand-side discontinuity of A_{LS}^{JM}. The unitarity equation for the isobar partial wave becomes, (*cf.* Eq. (2.37))
$$
d_\sigma F_{LS}^{JM}(\sigma) = i\, t_S^\dagger(\sigma)\, \rho(\sigma)\, (F_{LS}^{JM}(\sigma) + \hat{F}_{LS}^{JM}(\sigma)). \qquad (4.25)
$$

This equation can be inverted the same way as we demonstrated in Sec. 2.3. As a demonstration, we make a few unnecessary assumptions and write the final form of the integral equation.

1. $t_S(\sigma)$ does not have a left-hand cut.

2. $\hat{F}_{LS}^{JM}(\sigma)$ vanishes faster than $1/\sigma$ when $\sigma \to \infty$.

3. For the demonstration purposes, we are going to ignore the kinematic singularities of the of the function $F_{LS}^{JM}(\sigma)$ and $t_S(\sigma)$. [6]

---

[5] As a remark we notice that by applying a transformation from Eq. (4.21) to the original decomposition in Eq. (4.19), a common rotation function $D_{M\lambda}^{J*}(\phi_1, \theta_1, \phi_{23})$ can be pulled out of the square bracket:
$$
A(\tau) = \sum_{JMLS} \sqrt{(2L+1)(2S+1)} \sum_{\lambda\nu} D_{M\lambda}^{J*}(\phi_1, \theta_1, \phi_{23}) \times
$$
$$
\big[F_{LS}^{JM}(\sigma_1) \langle L, 0; S, \lambda \,|J, \lambda\rangle\, \delta_{\lambda\nu} d_{\nu 0}^S(\theta_{23})
$$
$$
+ F_{LS}^{JM}(\sigma_2) \langle L, 0; S, \nu \,|J, \nu\rangle\, d_{\lambda\nu}^S(\hat{\theta}_3) d_{\nu 0}^S(\theta_{12})
$$
$$
+ F_{LS}^{JM}(\sigma_3)(-1)^{\lambda+\nu} \langle L, 0; S, \nu \,|J, \nu\rangle\, d_{\lambda\nu}^S(\hat{\theta}_2) d_{\nu 0}^S(\theta_{31}) \big]. \qquad (4.22)
$$

When the orientation of the 3π production plane is not measured, the common rotation factor can be omitted.

[6] A consistent treatment of these singularities is, perhaps, the most tedious part of the problem (*e.g.* see the analysis of the kinematic singularities in B decays [2] and Λ_b decays [13])
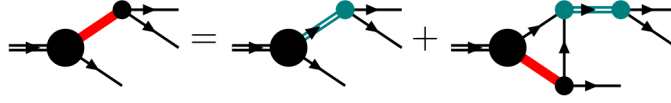
Figure 4.17: Diagrammatic representation of the KT equations (see Eq. (4.26)). The thick red line represents the amplitude F_{LS}^{JM}, the green double line denotes $t_S(\sigma)$, the large black circle replaces C_{LS}^{JM}.

The equation for the amplitude F_{LS}^{JM} then reads:

$$F_{LS}^{JM}(\sigma) = t_S(\sigma) \left[C_{LS}^{JM}(\sigma) + \frac{1}{2\pi} \int_{4m_\pi^2}^{\infty} \frac{\rho(\sigma')\hat{F}_{LS}^{JM}(\sigma')}{\sigma' - \sigma} \mathrm{d}\sigma' \right], \qquad (4.26)$$

where $C_{LS}^{JM}(\sigma)$ is an entire function of σ. The inhomogeneous term, $\hat{F}_{LS}^{JM}$, which stands under the integral, is related to F_{LS}^{JM} itself by Eq. (4.23) (see also Fig. 4.17), therefore, Eq. (4.26) is an integral equation. We see that these equations have a recursive form, and hence, can be solved by iterations. Let us suppose that $C_{LS}^{JM} = 1$, then, on the first interaction $(F_{LS}^{JM})^{(0)}$ takes the form of the known $(\pi\pi)$ amplitude, $t_S(\sigma)$, for all subchannels. The partial wave projection to one of the channels, however, includes not only the direct channel $t_S(\sigma)$, but also cross channel projections, Eq. (4.20). Such a partial wave projection amplitude cannot satisfy the unitary since $t_S(\sigma)$ by itself does. Hence, we have to modify the amplitude $(F_{LS}^{JM})^{(0)}$ in order to compensate (see discussion about Schmid cancellation in Sec. 4.2.4) for the cross channel projections, by adding a triangle diagram (second iteration). Since the cross channel amplitudes are modified accordingly, the projections of them change and we have to add the compensation term again which leads to the third iteration, and so on.

By a simple comparison, one can validate that the expression for the triangle diagram, calculated using the dispersive approach in Sec. 4.2.3, matches the first iteration of Eq. (4.26). The inhomogeneous term is a partial wave projection to the $K\bar{K}$-channel of the cross channel, with $K\pi$ amplitude in the $\pi K\bar{K}$ system.

Coherent background: non-resonance reactions

5.1 One pion exchange process
in diffractive production of a three-pion system

Exchange processes, especially the one-pion exchange, play very important roles for the 3π diffractive production at COMPASS. We have already noticed in Fig. 3.8 that the physics regime for the 3π production changes for $s \equiv m_{3\pi} > 3\,\mathrm{GeV}$. In this region, the cross-section is dominated by *near-to-forward* and the *near-to-backward* scattering in the system of the $\xi\pi^-$ where ξ is a $\pi^+\pi^-$-resonance (*e.g.* the system $\rho\pi$ selected for the Fig. 3.8). For the process where π^- scatters backwards in the CM frame of $\xi\pi^-$, it is straightforward to identify the closest singularity of the amplitude which governs the scattering. The one-pion exchange process embedded in the reaction $\pi^- p \to \pi^- \pi^+ \pi^- p$ shown in Fig. 5.1 contains a pole in the transferred momentum. Since the transferred momentum is bounded to be negative, the pion pole singularity is located outside of the physical region, however, still in the close proximity due to the small mass of the pion. The dominance of the exchange leads to the increase of the number of significant partial waves. A qualitative discussion of the relation is given by V. Gribov in his lecture series [39]. Considering the four-point reaction (which would be $\pi\mathbb{P} \to \xi\pi$ in our case), the mass of the exchange particle can be related to the interaction radius ρ_0 as $\rho_0 \approx 1/m_\pi$. It determines the total cross section as $\sigma_0 \approx 2\pi\rho_0^2$. From the other side, we can find an upper limit to the cross-section which includes J_0-partial waves in the inelastic limit (assumed to the equal to 8π, *i.e.* in the center of the unitary Argand circle) as $\sigma_0 \lesssim 4\pi J_0^2/s$ [39]. It gives an estimate for the number of partial waves one can expect to be significant:

$$J_0 \gtrless \sqrt{s}/(2m_\pi). \tag{5.1}$$

For $\sqrt{s} = 3\,\mathrm{GeV}$, the limit J_0 is already 10 which roughly matches our observation with the COMPASS data. In order to study the physics of resonances observed in partial waves, we are bound to understand the partial-wave projections of this exchange process. Our goal in this chapter is to construct a realistic model of the pion exchange for the reaction $\pi^- p \to \pi^- \pi^+ \pi^- p$ (see Fig. 3.8) and estimate its contribution to the COMPASS partial-wave results in the resonance region. The importance of this process for the diffractive reactions was first pointed out by R. Deck [40]. Later, extensive studies of the Deck model and the partial wave projections were performed by Ascoli et al. [91], which we closely follow here, and the ACCMOR collaboration [119]. The interplay between

the "direct" resonance production and the Deck process was discussed in Ref. [62, 174–178] using the unitarization method presented in Sec. 2.3. The latter is left outside of the scope of this chapter and we focus on the studies of the process shown in Fig. 5.1, which will be generally called the *Deck process*.

We present a systematic study of the Deck amplitude in the kinematic domain of the COMPASS experiment concentrating on the relevance of this process to the resonance region in the 3π system. In Sec. 5.2 we build the amplitude using the known $\pi\pi$ interaction in partial waves and the πp scattering amplitude in the high energy limit. In Sec. 5.3 we perform an analytic projection of the amplitude to the partial waves. The integrated intensities of waves are compared to the intensities extracted from the COMPASS data [78]. In Sec. 5.4 we investigate an expansion of the Deck amplitude in a truncated partial wave basis used for COMPASS PWA. We discuss effects of the fixed predetermined Isobar parametrization as well as an artificial "leakage" between waves caused by the cross-correlations between the waves due to the π^--symmetrization of the $\pi^-\pi^+\pi^-$ production amplitude.

5.2 The Deck amplitude
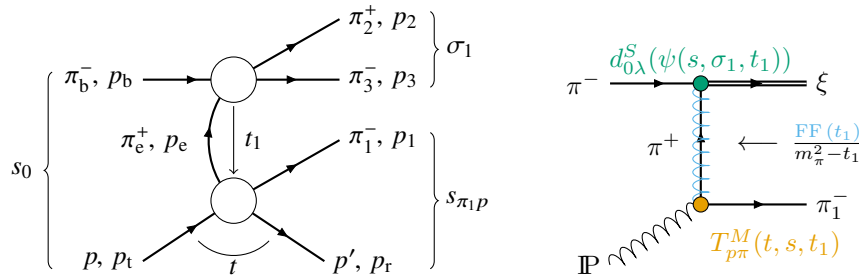
Figure 5.1: Left plot: One-pion-exchange diagram for the diffractive peripheral production of the three pion final state in the pion beam. Right plot: A schematic representation of the reduced Deck amplitude (*cf.* Eq. (5.23)). The $\pi\pi$-scattering amplitude is amputated, and $T_{\pi p}$ is projected to the states with a defined magnetic quantum number M. The remaining components of the amplitude factors can be identified with the vertices and the propagator.

The amplitude for the process is written as a product of three parts: the pion-proton scattering amplitude, the pion-pion scattering amplitude, and the pion propagator.

$$\mathfrak{B}^{(1)}_{\lambda'\lambda} = (T_{\pi_1 p})_{\lambda'\lambda} \frac{\text{FF}(t_1)}{m_\pi^2 - t_1} T_{\pi\pi} \tag{5.2}$$

where λ and λ' are helicities of the target proton and the recoil respectively, $\text{FF}(t_1)$ stands for the form-factor which modifies the behavior of the pion propagator far away from the pion pole. The superscript in the amplitude $\mathfrak{B}^{(1)}_{\lambda'\lambda}$ indicates the index of the pion, that is produced in the proton-pion subprocess. $T_{\pi\pi}$ denotes the $\pi_b^- \pi_e^+ \to \pi^- \pi^+$ scattering amplitude (see Fig. 5.1). For the calculation of the $\pi\pi$ scattering and the πp scattering with a virtual pion, we use on-shell dynamic amplitudes since the off-shell parametrizations are more complicated in general, and are not well established. Modifications to the simple pion propagator, which account for off-shellness and other exchanges, are discussed in Sec. 5.2.3.

Due to the Bose symmetry between the two π^- in the final state, the total amplitude of the process is symmetrized:

$$\mathfrak{B}_{\lambda'\lambda} = \mathfrak{B}^{(1)}_{\lambda'\lambda} + \mathfrak{B}^{(3)}_{\lambda'\lambda}. \tag{5.3}$$

We focus on the construction of the first term $\mathfrak{B}^{(1)}_{\lambda'\lambda}$. Thus, in the following discussion of this section the variable $s_{\pi p}$ refers to the invariant mass of the recoil proton p' and the bachelor pion π_1 which is used in the amplitude in Eq. (5.2) and in Fig. 5.1.

5.2.1 Pion-pion scattering

The $\pi\pi$ scattering amplitude at low energy is well described by a sum of a few partial waves: we are using $S \leq 2$, with S being the orbital angular momentum.

$$T_{\pi\pi}(\sigma, \cos\theta_{\pi\pi}) = \sum_S C_S^2 (2S+1) t_S(\sigma) P_S(\cos\theta_{\pi\pi}), \tag{5.4}$$

where $t_S(\sigma)$ is the partial wave amplitudes. Although the exchange pion is off-shell (*i.e.* $t_1 \neq m_\pi^2$), we neglect the dependence on the virtuality of the exchange pion and consider the off-shell parametrizations. The angle $\theta_{\pi\pi}$ is defined as an angle between vectors of pions π_b^- and π^- in the $\pi\pi$ rest frame, $C_S = \langle 1, -1; 1, +1 \,|\, I, 0 \rangle$ is an isospin Clebsch-Gordan coefficient where the negative pion appears first, consistently with the angular decomposition. The partial wave amplitude $t_S(\sigma)$ at the threshold is proportional to the break-up momentum k to the power $(2S)$. It is incorporated explicitly to the model:

$$t_S(\sigma) = h_S((kR)^2) \, \hat{t}_S(\sigma) \, h_S((kR)^2), \tag{5.5}$$

where $\hat{t}_S(\sigma)$ is a singularity free partial-wave amplitude. The $h_S(z)$ function includes threshold factors and the Blatt-Weisskopf factors (see Appendix E.3). $k = \sqrt{\sigma/2 - m_\pi^2}$ is the break-up momentum for the initial and the final pion pair. We use a standard value for the size parameter $R = 5\,\text{GeV}^{-1}$ [179]. The partial waves are parametrized as follows:

- $[\pi\pi]_S$-wave is from the analysis of Ref. [116]; it is shown in Fig. 3.16 by the dashed line.

- $[\pi\pi]_P$-wave is the ρ-meson represented by the relativistic Breit-Wigner amplitude; it is the same as used in the COMPASS basis. It is described in Appendix (D) and plotted in Fig. 3.11.

- $[\pi\pi]_D$-wave is the f_2-meson; it is parametrized by the Breit-Wigner amplitude with a constant width as given in Eq. (D.2). The parameters are chosen consistently with the COMPASS PWA. The absolute value squared and the phase of the amplitude are shown in Fig. 3.11.

We can already foresee some problem of decomposing those amplitude in the COMPASS basis: the $[\pi\pi]_S$ wave does not recall any of three scalar isobars used in the COMPASS basis. For the P-and D-wave we select exactly the same parametrizations, nevertheless, they are modified by the pion exchange propagator in Eq. (5.2). Therefore, the resulting line shapes do not match the partial-wave basis functions.

5.2.2 Proton-pion amplitude

As suggested in Ref. [83], the high energy limit of the helicity amplitudes in the Gottfried-Jackson frame can be approximated as follows.

$$(T_{\pi p})_{-+} = (T_{\pi p})_{+-} \approx 0, \quad (T_{\pi p})_{++} = (T_{\pi p})_{--} \approx s_{\pi p} e^{-\beta t}, \tag{5.6}$$

where the $\pm$ signs indicate proton helicities, $\pm 1/2$, t is a transferred momentum, $t = (p_\text{t} - p_\text{r})^2$, and β is a slope parameter. For the latter, we use the same value $\beta = 8\,\text{GeV}^{-2}$ as in Ref. [3], although this value does not have any influence of the three-pion spectrum which we are investigating in this chapter.

We can realize the same expression by considering a simple model of the Pomeron exchange for the πp scattering at high energy. The Pomeron trajectory, in coordinates of invariant mass squared $t \equiv M_\mathbb{P}^2$ against angular momentum J_e, crosses the smallest integer value $J_\text{e} = 1$ at $M_\mathbb{P}^2 = 0$. Therefore, in the physical region $t \approx 0$, we can view the Pomeron exchange as an exchange of the vector particle (see more discussion about the Pomeron treatment in Ref. [80, 180, 181]). We write the πp elastic scattering amplitude with a vector exchange as a product of the simplest spinor-spinor-vector vertex for Pomeron-proton coupling, a tensor of second rank which is orthogonal to $p_\mathbb{P} = p_\text{r} - p_\text{t}$ as the vector propagator, and the simplest scalar-scalar-vector vertex for the pion-Pomeron coupling. Omitting constant irrelevant factors, it reads,

$$(T_{\pi p})_{\lambda'\lambda} = \bar{u}(p_\text{r}, \lambda') \left[\gamma_\mu F(t) \right] u(p_\text{t}, \lambda) \left[g^{\mu\nu} - \frac{p_\mathbb{P}^\mu p_\mathbb{P}^\nu}{p_\mathbb{P}^2} \right] \frac{(p_1 - p_\text{e})_\nu}{2}, \tag{5.7}$$

where $u(\bar{u})$ is a Dirac spinor of the target (recoil) proton, the momenta are defined in Fig. 5.1, and $F(t)$ accounts for the t-dependence dominated by the proton form-factor and approximated by an exponential term, $F(t) = \exp(-\beta t)$. When we assume the scale hierarchy $s_0 \gg s \gg \sigma, t, t_1$, the momenta in the GJ-frame are approximated by $|\vec{p}_\text{t}| \approx |\vec{p}_\text{r}| \propto \sqrt{s_0}/2$, and $|\vec{p}_1| \approx |\vec{p}_\text{e}| \propto \sqrt{s}/2$. A series of algebraic manipulations results into the simple asymptotic relation, $\bar{u}(p_\text{r}, \lambda')\gamma_\mu u(p_\text{t}, \lambda) = 2p_\text{t}^\mu \delta_{\lambda'\lambda} + O((ss_0)^{1/2})$.

$$(T_{\pi p})_{++} \approx 2 \frac{(p_\text{t} + p_\text{r})_\mu}{2} \left[g^{\mu\nu} - \frac{p_\mathbb{P}^\mu p_\mathbb{P}^\nu}{p_\mathbb{P}^2} \right] \frac{(p_1 - p_\text{e})_\nu}{2} F(t), \tag{5.8}$$

where we replaced $2p_\text{t}$ with $p_\text{r} + p_\text{t}$ on the left side of the propagator by zero-addition $p_\mathbb{P} = p_\text{r} - p_\text{t}$ since the expression in the squared brackets is orthogonal to $p_\mathbb{P}$. We see that, in the high energy limit, the structure of the expression is the same as if the proton were a scalar particle. Assuming the particles to be massless, we express Eq. (5.8) through invariant variables.

$$(T_{\pi p})_{++} \approx -\frac{(p_\text{r} + p_1)^2 - (p_\text{t} - p_1)^2}{2} F(t) \approx -\frac{s_{\pi p}}{2} F(t). \tag{5.9}$$

Interestingly, Eq. (5.8) a matrix element for the scattering of scalar particles in s-channel via a vector resonance, which gives $(t - u)/2$, with t and u being the corresponding Mandelstam variables [59]. The expression (5.9) matches Eq. (5.6), up to irrelevant numerical factor, and completes the example.

5.2.3 Pion propagator

The simplest model for the pion exchange is a pole term $1/(m_\pi^2 - t_1)$ used in Eq. (5.2). It is only good approximation in the vicinity of this pole. In the kinematic domain of our diffractive reaction, the pion propagator needs be modified in order to make the model more realistic [90, 119]. One problem with the *Standard Deck model* is a dominance of S-wave at high energy [174, 178]. It can be seen in the high energy approximation (*cf.* Eq. (5.19)),

$$s_{\pi p} \approx \frac{s_0(m_\pi^2 - t_1)}{s - m_\pi^2} \tag{5.10}$$

which cancels the pion pole and remove the dependence on t_1, *i.e.* the scattering angle (see also Ref. [175]).

There are two common modifications of the pion propagator: *reggezation* and *form-factors*, which we consider as two alternative models. The reggezation is discussed in Ref. [90, 177, 178]; it suggests to modify the pion propagator as follows.

$$\frac{1}{m_\pi^2 - t_1} \to \frac{e^{-i\pi\alpha(t_1)/2}}{m_\pi^2 - t_1} \left(\frac{s' - u'}{2s_{\mathrm{sc}}}\right)^{\alpha(t_1)}, \tag{5.11}$$

where $\alpha(t_1) = t_1 - m_\pi^2$, $s_{\mathrm{sc}} = 1\,\mathrm{GeV}^2$ is a scale parameter, s', u' are Mandelstam variables calculated for the $2 \to 2$ kinematics, $(s' - u')/2 = s + m_\pi^2 + (t_1 - t - s_{\pi p})$. The phase factor $\exp(-i\pi\alpha(t_1)/2)$ has a large impact to the line shape of the amplitude, as well as to the phases of partial waves.

A modification of the pion propagator by a form-factor was suggested in Ref. [119]. An additional factor $\exp(b\,t_1)$ is added to the numerator to damp the amplitude. In the original analysis of the ACCMOR collaboration, the slope parameter $b_{\mathrm{ACCMOR}} = 2\,\mathrm{GeV}^{-2}$ was adjusted by comparison to the data. We use a slightly different value $b = 1.7\,\mathrm{GeV}^{-2}$ to be compatible with a model used in Ref. [3].

To summarize we outline three models for the numerator of the pion propagator $\mathrm{FF}\,(t_1)$:

$$\text{Standard Deck} \qquad \mathrm{FF}^{(I)} = 1, \tag{5.12}$$

$$\text{Reggeized Deck} \qquad \mathrm{FF}^{(II)} = e^{-i\pi\alpha(t_1)/2} \left(\frac{s' - u'}{2s_{\mathrm{sc}}}\right)^{\alpha(t_1)},$$

$$\text{Form-Factored Deck} \qquad \mathrm{FF}^{(III)} = e^{bt_1}, \quad b = 1.7\,\mathrm{GeV}^{-2},$$

and the explicit expression for the amplitude in Eq. (5.2) is

$$\mathfrak{B}^{(1)}(t, s, \tau_1) = s_{\pi p} F(t) \frac{\mathrm{FF}\,(t_1)}{m_\pi^2 - t_1} \left[\frac{2}{3}\, t^{(\sigma_1, f_0)}(\sigma_1) \right. \tag{5.13}$$

$$\left. - 3\, t^{(\rho)}(\sigma_1, t_1) P_1(\cos\theta_{\pi\pi}) + \frac{10}{3}\, t^{(f_2)}(\sigma_1, t_1) P_2(\cos\theta_{\pi\pi}) \right].$$

The differential distribution of the "Standard Deck" amplitude is shown in Fig. 5.2.
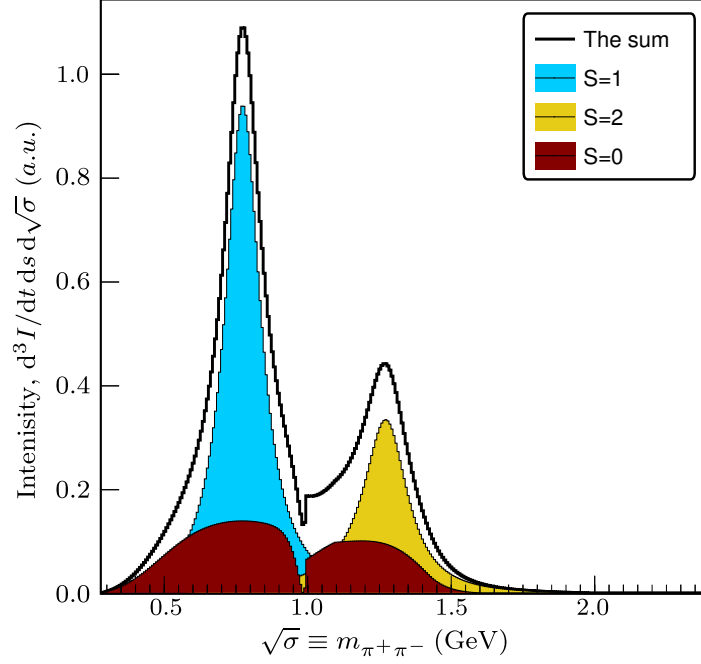
Figure 5.2: The $\pi\pi$ spectrum in the Deck model. The distribution $\mathrm{d}^3\Gamma/(\mathrm{d}t\,\mathrm{d}s\,\mathrm{d}\sigma)$ is calculated using a single non-symmetrized term $\mathfrak{B}^{(1)}$ from Eq. (5.2) for $s = (1.5\,\mathrm{GeV})^2$, $t = 0.1\,\mathrm{GeV}^2$. The contributions from the different isobars are shown by different colors. The differential distribution for the sum is shown by the blue area.

5.3 The partial-wave expansion of the Deck amplitude

It is important to realize that the transferred momentum t_1 determines the scattering angle of the Isobar in the 3π rest frame, and, therefore, the pion pole $1/(m_\pi^2 - t_1)$ produces an infinite series of the partial waves. An important question is how many of those waves are significant.

The permutation symmetry of the Deck amplitude in Eq. (5.3) matches the symmetry of the basis in Eq. (3.6). The expansion in the helicity basis takes the form:

$$\mathfrak{B}(t, s, \tau) = \sum_{JMS\lambda} \left[\mathfrak{B}_{S\lambda}^{JM}(t, s, \sigma_1) Z_{S\lambda}^{JM}(\Omega_1, \Omega_{23}) + \mathfrak{B}_{S\lambda}^{JM}(t, s, \sigma_3) Z_{S\lambda}^{JM}(\Omega_3, \Omega_{21}) \right], \quad (5.14)$$

The projections $\mathfrak{B}_{S\lambda}^{JM}$ can be found by integrating the non-symmetrized amplitude (5.13) over four angles with basis angular functions $Z_{S\lambda}^{JM}(\Omega_1, \Omega_{23})$. It reads,

$$\mathfrak{B}_{\lambda S}^{JM}(t, s, \sigma_1) = \int \frac{\mathrm{d}\Omega_1}{4\pi} \frac{\mathrm{d}\Omega_{23}}{4\pi} \mathfrak{B}^{(1)}(t, s, \sigma_1, \Omega_1, \Omega_{23}) Z_{\lambda S}^{JM}(\Omega_1, \Omega_{23}), \quad (5.15)$$

$$= \sqrt{(2J+1)(2S+1)} \int \frac{\mathrm{d}\Omega_1}{4\pi} \frac{\mathrm{d}\Omega_{23}}{4\pi} \mathfrak{B}^{(1)} D_{M\lambda}^J(\Omega_1) D_{\lambda 0}^S(\Omega_{23}), \quad (5.16)$$

where the notations are the same as introduced in Eq. (3.2). The arguments of the angular functions $Z_{S\lambda}^{JM}$ are the spherical angles which describe the decay chain as shown in Fig. 5.3: Ω_k (one index) are

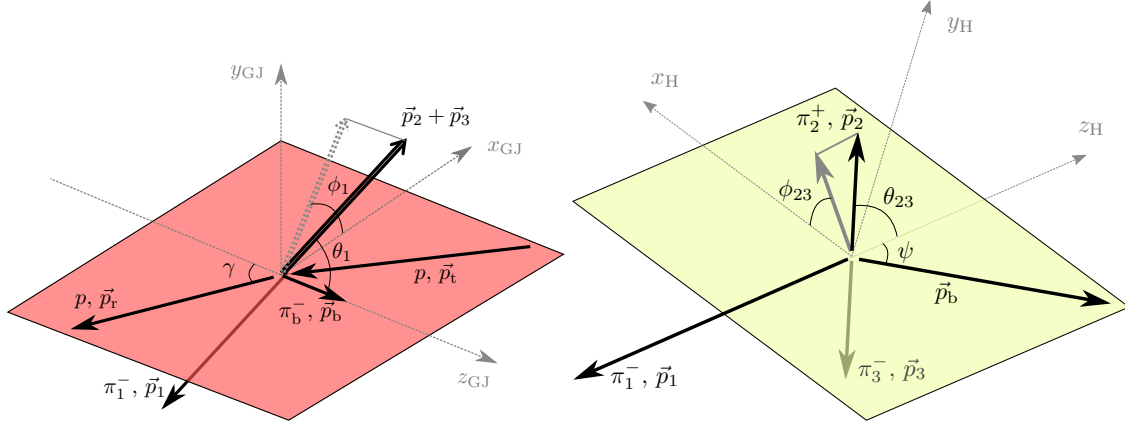Figure 5.3: Definition of angles used in the calculations (*cf.* Fig. 3.3). The left plot presents the definitions of the angles in the GJ-frame for the reaction $\pi_b^- \, p_t \to \pi_1^- \pi_2^+ \pi_3^- \, p_r$. The double line shows a combined momentum of particles 2 and 3, the spherical angles of which are denoted by $\Omega_1 = (\theta_1, \phi_1)$. The right plot shows the helicity frame of (23)-system where z_H-axis is defined along $-\vec{p}_1$, and the y_H axis is set by the direction on $\vec{p}_1 \times \vec{p}_b$. The spherical angles of the of the vector $\vec{p}_2$ are denoted by $\Omega_{23} = (\theta_{23}, \phi_{23})$.

angles of the Isobar in the 3π-rest frame (particularly, the GJ frame), and Ω_{ij} are angles of the a pion from the Isobar decay in the two-pion rest frame (the helicity frame of the Isobar). The projections to the canonical basis and the reflectivity basis used by the COMPASS analysis can be found by linear compositions of $\mathfrak{B}_{\lambda S}^{JM}$ according to Eq. (3.9) and Eq. (3.11). Since we are interested in a calculation of the total intensity, it is easier to work with the helicity basis, the total intensity requires a sum over all possible value of the Isobar helicity λ.

For the projections it is clear that the Isobar with spin S suppose to contribute to the partial waves with the same orbital momentum S between two pions. However, it is not straightforward to demonstrate the orthogonality since the expansion angles in $Z_{S\lambda}^{JM}$ and $T_{\pi\pi}$ are different: the partial-wave expansion in Eq. (5.13) is performed using the angle $\theta_{\pi\pi}$, between the beam pion and π_3^-. The projection angles, Ω_{23} in Eq. (5.15) are defined with respect to the z-axis in the same $\pi_2^+\pi_3^-$ rest frame that is particularly oriented ($z_H \uparrow\uparrow -\vec{p}_1$, $y_H \uparrow\uparrow (\vec{p}_b \times z_H)$, see Fig. 5.3). The relation between the angular functions is found in Ref. [91]:

$$P_S(\cos\theta_{\pi\pi}) = (-1)^{-S} P_S(-\cos\theta_{\pi\pi}) = (-1)^{-S} \sum_\lambda d_{0\lambda}^S(\psi) D_{\lambda 0}^{S*}(\Omega_{23}), \qquad (5.17)$$

where we changed the argument of the Legendre polynomial to a cosine of the angle between the beam and the π^+, that is $\pi - \theta_{\pi\pi}$. The properties of the Wigner D-functions were used to relate this angle with the variables of the basis. The additional angle ψ is the polar angle of p_b in the (23)-rest frame as shown in Fig. 5.3.

$$\cos\psi = \frac{(s + \sigma_1 - m_\pi^2)(t_1 + \sigma_1 - m_\pi^2) - 2\sigma_1(t + \sigma_1 - 2m_\pi^2)}{\lambda^{1/2}(s, \sigma_1, m_\pi^2)\lambda^{1/2}(t_1, m_\pi^2, \sigma_1)} \qquad (5.18)$$

An integral over the angle ϕ_1 in Eq. (5.15) projects the amplitude to the states M of the total angular momentum J. This integral can be performed analytically because the angle ϕ_1 enters only in

the expression for $s_{\pi p}$. Using the momenta and angles defined in the GJ frame (see the left plot of Fig. 5.3), we write:

$$
\begin{aligned}
s_{\pi p} &= (p_{\rm r} + p_1)^2 \\
&= m_p^2 + m_\pi^2 + 2E_r'E_3' - 2|\vec{p_{\rm r}}'||\vec{p_3'}|(\sin\theta_1\cos\phi_1\sin\gamma + \cos\theta_1\cos\gamma),
\end{aligned}
\tag{5.19}
$$

where the energies are $E_r' = (s_0 - s - m_p^2)/(2\sqrt{s})$ and $E_3' = (s + m_\pi^2 - \sigma_1)/(2\sqrt{s})$, as one can find by computing the expressions $s_0 = (p_{\rm r} + p_{3\pi})^2$ and $\sigma_1 = (p_{3\pi} - p_1)^2$ in the GJ-frame. The momenta are equal to $|\vec{p_{\rm r}}'| = \lambda^{1/2}(s_0, s, m_p^2)/(2\sqrt{s})$, $|\vec{p_3'}| = \lambda^{1/2}(s, \sigma_1, m_\pi^2)/(2\sqrt{s})$. The angle γ is an additional angle to the polar angle of $\vec{p_{\rm r}}$, it can be found using $(p_{\rm b} - p_{\rm r})^2 = u = 2m_p^2 + s + m_\pi^2 - s_0 - t$ evaluated in the GJ-frame,

$$
\cos\gamma = \frac{2s(s_0 + t - s - m_p^2) - (s + m_\pi^2 - t)(s_0 - s - m_p^2)}{\lambda^{1/2}(s, m_\pi^2, t)\lambda^{1/2}(s_0, s, m_p^2)} \xrightarrow[t, m^2 \ll s \ll s_0]{} 1,
\tag{5.20}
$$

where we indicated the limit of peripheral scattering at high energy. Now, the integral over the $d\phi_1$ is straightforward to calculate: the amplitude $T_{\pi p}$ can be written as $T_{\pi p}^0 + 2T_{\pi p}^1\cos\phi_1$;

$$
T_{\pi p}^M = \int \frac{d\phi_1}{2\pi} T_{\pi p}(\phi_1) e^{-iM\phi_1} =
\begin{cases}
T_{\pi p}^0, & \text{if } M = 0, \\
T_{\pi p}^1, & \text{if } M = \pm 1, \\
0, & \text{if } |M| > 1.
\end{cases}
\tag{5.21}
$$

We defined the projected amplitude $T_{\pi p}^M$, that follows from Eq. (5.19)

$$
T_{\pi p}^0 = (m_p^2 + m_\pi^2 + 2E_r'E_3' - 2|\vec{p_{\rm r}}'||\vec{p_3'}|\cos\theta_1\cos\gamma)\, F(t) \xrightarrow[t, m^2 \ll s \ll s_0]{} \frac{s_0}{2}(1 - \cos\theta_1)\, F(t),
\tag{5.22a}
$$

$$
T_{\pi p}^1 = -|\vec{p_{\rm r}}'||\vec{p_3'}|\sin\theta_1\sin\gamma\, F(t) \xrightarrow[t, m^2 \ll s \ll s_0]{} 0.
\tag{5.22b}
$$

An interesting consequence of our high energy model for the pion-proton scattering is a vanishing of $M = 1$ projections and an absence of the higher projections, $M > 1$. [1] In the high energy limit of $T_{\pi p}^0$, we recognize the $(1 - \cos\theta_1)$ term which supposedly cancels the pion pole as argued in Ref. [174].

The remaining expression for the partial wave projected Deck amplitude $\mathfrak{B}_{S\lambda}^{JM}$ includes a single integral over the scattering angle θ_1, that parametrizes the transferred momentum t_1 as shown by Eq. (3.3):

$$
\mathfrak{B}_{S\lambda}^{JM}(t, s, \sigma_1) = (-1)^S C_S\, \hat{t}_S(\sigma_1)\, h_S((kR)^2)\sqrt{2J+1} \int \frac{d\cos\theta_1}{2} d_{M\lambda}^J(\theta_1)\hat{\mathfrak{B}}_{S\lambda}^M(t, s, \sigma_1, t_1),
\tag{5.23}
$$

where $\hat{\mathfrak{B}}_{S\lambda}^M$ denotes the amputated pion exchange process, $h_S((kR)^2)$ is the Blatt-Weisskopf factors introduced in Eq. (5.5). The amplitude $\hat{\mathfrak{B}}_{S\lambda}^M$ contains exactly the factors which one would naively

---

[1] As a remark we notice that in the data of the COMPASS experiment the fraction of the $M = 2$ waves is less than 0.6%. It mostly comes from the $J^{PC}M^\epsilon = 2^{++}2^+ \rho\pi$ D-wave dominated by the a_2 resonance (see intensity fractions in Table V of Ref. [78]).
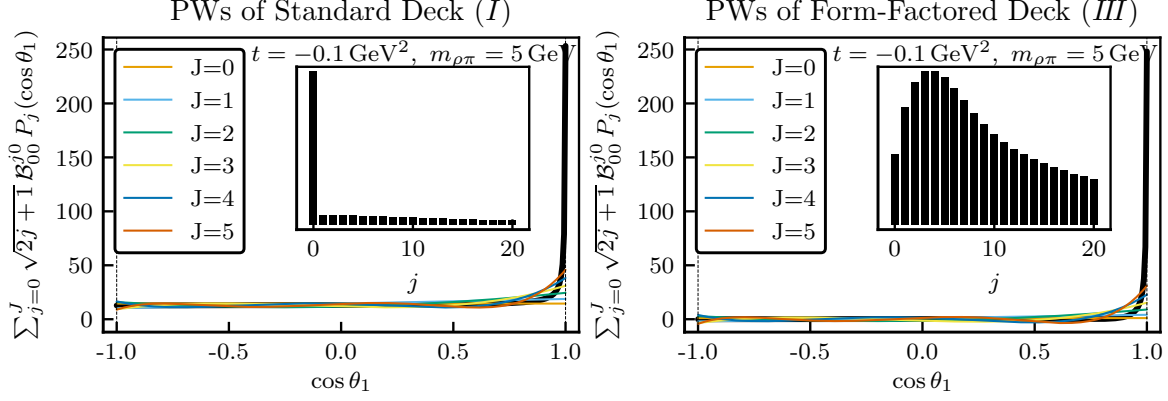
Figure 5.4: Approximations of the Deck amplitude by a partial wave series using the analytic decomposition from Sec. 5.3 calculated for fixed values of $\sqrt{s} = 5\,\text{GeV}$, $\sqrt{\sigma_1} = m_\rho$, $t = -0.1$. The thick solid line (behind the colored lines except the region $\cos\theta_1 \approx 1$) shows a full amplitude $\hat{\mathfrak{B}}_{S\lambda}^M$ for $S = M = \lambda = 0$, while the colored lines present an approximation of the curve by a sum of $J + 1$ Legendre polynomials (*cf.* Eq. (5.23) with $d_{00}^j = P_j$). The inset plot shows the expansion coefficients $\mathfrak{B}_{S\lambda}^{jM}$ for the first twenty projections.

expect considering a diagram on the right panel of Fig. 5.1,

$$\hat{\mathfrak{B}}_{S\lambda}^M(t, s, \sigma_1, t_1) = \sqrt{2S+1}\, C_S\, h_S((kR)^2) d_{0\lambda}^S(\psi) \frac{\text{FF}\,(t_1)}{m_\pi^2 - t_1} T_{\pi p}^M. \tag{5.24}$$

The partial-wave projections for different models reveal significant differences. Firstly, we look at the amplitude at high energy where we have a better intuition for the results. Fig. 5.4 shows a typical behavior of the expansion coefficients for the two models, *I* and *III*, from Eq. (5.12). We find that, for the "Standard Deck" without modifications of the pion pole (model-*I*), the pion pole is not canceled exactly (see the left panel of Fig. 5.4), *i.e.* the forward peak is well present. However, the amplitude does not vanish away from the forward region. The $J = 0$ wave, which corresponds to a homogeneous distribution, dominates over all other waves. The picture is very different for the model-*III*, with a form-factor suppression, shown on the right panel of Fig. 5.4. The forward peak, seen in the angular distributions, requires a large number of waves to be described. The sum of partial waves up to $J = 5$ is shown in Fig. 5.4 by the red line. It gives a sufficient description neither of Model-*I* on the left plot, nor of Model-*III* on the right plot. The Model-*II* with the Reggeized pion propagator shows a similar behavior as Model-*III*, however, the expansion coefficients are complex.

Having established the high energy behavior of partial wave projections we move to the low energy region which is the most important for our ultimate goal of spectroscopy studies. We suspect that many features found in the partial-wave analysis of the 3π dataset of the COMPASS experiment can be identified with the projections of the Deck model. To perform a direct comparison, we calculate the total intensity of the partial waves for different J^{PC} sectors and overlap them with the data as shown in Fig. 5.5. The total cross section is evaluated by squaring the amplitude and integrating over the phase space. We calculate the intensity distribution according to Eq. (3.18) and split it into the

contributions from the different waves:

$$I_{3\pi}^{\mathfrak{B}}(s,t) \approx \sqrt{s} \sum_{JM\lambda S} \int \left| \mathfrak{B}_{\lambda S}^{JM} Z_{\lambda S}^{JM} \right|^2 \, d\Phi_3 \tag{5.25}$$

$$= \sum_J \frac{\sqrt{s}}{(8\pi)^2 s} \int_{4m_\pi^2}^{(\sqrt{s}-m_\pi)^2} \frac{d\sigma}{2\pi} \frac{\lambda^{1/2}(\sigma, s, m_\pi^2) \lambda^{1/2}(\sigma, m_\pi^2, m_\pi^2)}{\sigma} \sum_{M\lambda S} \left| \mathfrak{B}_{\lambda S}^{JM}(t,s,\sigma) \right|^2, \tag{5.26}$$

where we neglected interference terms to simplify the phase space integration. This approximation affects the $J^{PC} = 0^{-+}$ sector the most, its impact to the other sectors is small (one sees it indirectly by comparing the left and the middle panels of Fig. 5.6).

We normalize the models (a single normalization constant for every of the three models) to to contribute a certain fraction of the total intensity of the COMPASS data. This normalization factors scales all projections simultaneously. This fraction is set to 30% as a compromise between an adjustment of the $J^{PC} = 4^{-+}$ and $J^{PC} = 3^{-+}$ as shown in Fig. 5.5.

All projections have a bump-like structure: there is a low-energy rise which is related to the threshold behavior; the intensity distribution peaks at the region $1 \ldots 2\,\mathrm{GeV}$, as higher as bigger J is; then, it starts falling and approaching its asymptotic limit. The "Standard Deck" model produces the broadest structures for all projections. For this model, the sum of waves with $J = 0$ is huge above $2\,\mathrm{GeV}$, that clearly contradicts the data. A significance of the $J = 0$ would mean that intensity does not vanish for the $\cos\theta_1 = 0$ (as in Fig. 5.4), while it is the opposite in the data (see $\cos\theta_{\mathrm{GJ}} \times m_{3\pi}$ distribution in Fig. 3.8).

The models *II* and *III* have similar projections which suggest a reasonable background for $J^{PC} = 1^{++}, 2^{-+}$. They also give a good justification for the $J^{PC} = 4^{++}$ and 3^{-+} distributions. For the $J^{PC} = 0^{-+}$, the enhancement in the data at $1.3\,\mathrm{GeV}$ could be suspected to be the $\pi(1300)$, previously observed in $p\bar{p}$ and e^+e^- annihilation as well as in diffraction [26]. [2] However, we see that a large fraction of this peak have to be attributed to the background. An interesting question for the further investigation is a sensitivity of this intensity to the parameters of the model. A non-negligible intensity of the Deck process is found in the exotic sector $J^{PC} = 1^{-+}$. It is in agreement with the result of the mass-dependent fit in Ref. [3] where a phenomenological parametrization of the background was used. The background intensity at $1.2\,\mathrm{GeV}$ hinders precise extraction of the resonance parameters of the exotic $\pi_1(1600)$.

5.4 Decomposition in the COMPASS basis

An expansion of the Deck amplitude using the COMPASS basis is not strictly equivalent to the partial-wave projections. The main reason is a predetermined $\sqrt{\sigma} \equiv m_{\pi\pi}$ dependence of the basis

---

[2] This state is not well established; measurements of the resonance parameters are controversial [182, 183]. In the COMPASS analysis [3], the wave $J^{PC}M^\epsilon = 0^{-+}0^+(\pi\pi)_S\pi$ S-wave was not included in the final fit due to the difficulties in describing it either by a resonance or a background component. The wave does not contain a significant phase motion around $1.3\,\mathrm{GeV}$, the observed t-dependence of the broad structure, which is reminiscent of the $\pi(1300)$, differs to the one for other well established resonances.
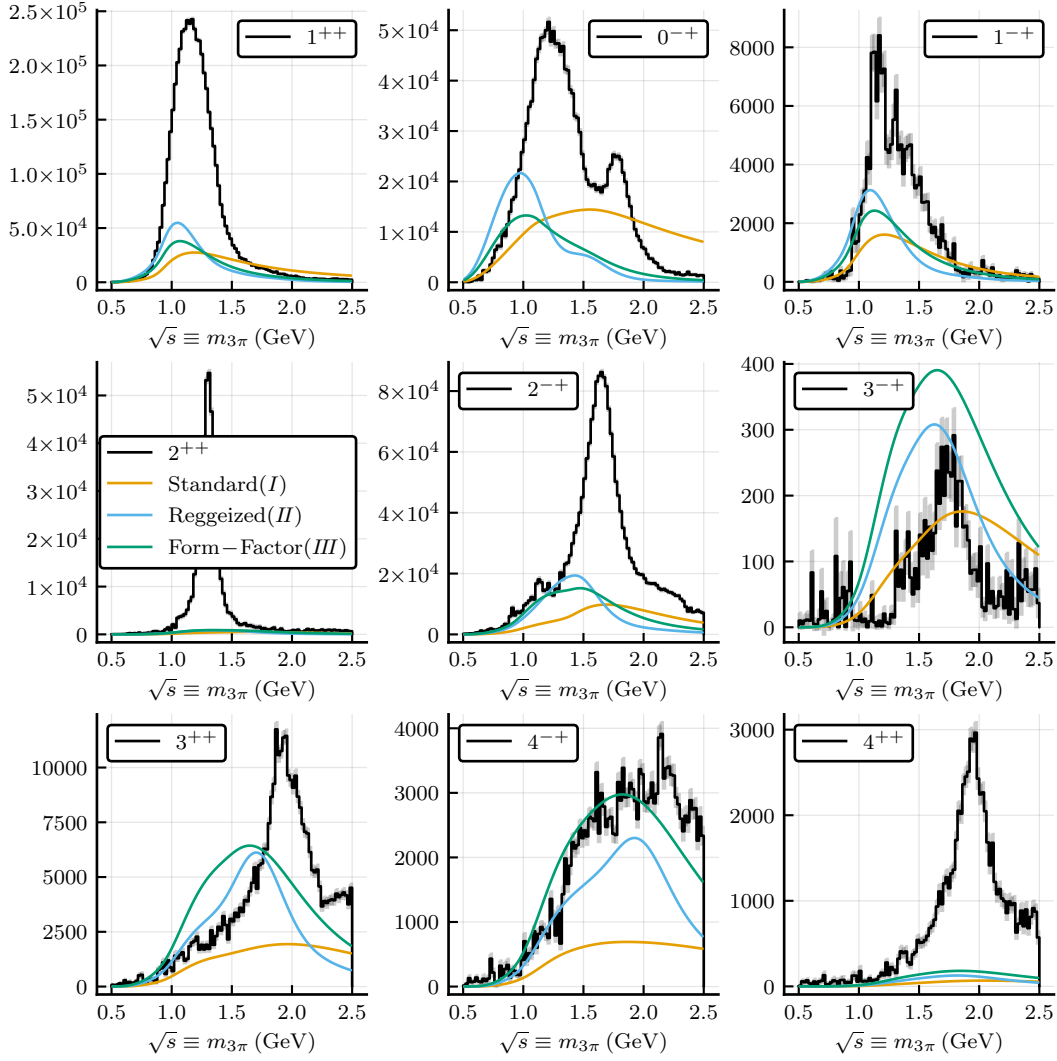
Figure 5.5: A comparison of intensities for the main J^{PC} from the COMPASS PWA and the calculations in three models for the Deck process. Partial wave intensities from the COMPASS PWA [78] summed for different J^{PC} sectors are overlapped by colored lines that correspond to the three Deck models discussed in the text. Data points are presented by the black histograms with gray errors. The Deck models are normalized to have 30% of total intensity of the data.

functions Ψ_w defined in Eq. (3.15). The approximation reads:

$$\mathfrak{B}(t,s,\tau) \simeq \sum_w \mathfrak{B}_w(t,s)\Psi_w(s,\tau). \tag{5.27}$$

The sign $\simeq$ implies that we need to find the coefficients $\mathfrak{B}_w(t,s)$ which approximate the original amplitude $\mathfrak{B}$ the best. It is important to agree how the measure of the mismatch is defined. In the PWA technique, the *intensity* is approximated: my minimizing likelihood, effectively the distance between the absolute value between the left and the right part of Eq. (5.27) is minimized. This numerical procedure is rather involved. [3] For the studies in this section we use another strategy, *algebraic-projection* method, in which we approximate the *amplitude* directly from Eq. (5.27). A system or linear equations for the coefficients $\mathfrak{B}_w$ can be obtained by multiplying both parts of Eq. (5.27) with Ψ_q^* and integrating over the phase space. The coefficients are found by inverting the integral matrix:

$$\mathfrak{B}_w(t,s) = \sum_q B_{wq}^{-1}(t,s) \int \mathfrak{B}(t,s,\tau)\Psi_q^*(s,\tau)\,\mathrm{d}\Phi_3, \tag{5.28}$$

where $\mathrm{d}\Phi_3$ is a three-body phase space integral, B_{wq} in the integral matrix defined in Eq. (3.20). The main difference of this algebraic method to the analytic method discussed above is the treatment of the subchannel energies. As for the PWA technique, we take the basis where the subchannel energy dependence is fixed (by $f_S(\sigma)$ in Eq. (3.15)). There are still two methods to proceed which deal differently with the symmetrization (see Eq. (5.3)) of the amplitude:

1. project the complete, symmetrized amplitude from Eq. (5.3) to the symmetrized basis from Eq. (3.15);

2. project only one term $\mathfrak{B}^{(1)}$ to the part of the basis which contains the partial-wave expansion in the corresponding subchannel. In this method, Eq. (5.28) have to be accordingly modified; the integral matrix becomes orthogonal for waves with distinguishable $J^{PC}M^\epsilon, LS$ quantum numbers.

We call the first method, the *symmetrized* projections, while the second is called *non-symmetrized*.

One may wonder what happens if the σ_k dependence of the amplitude $\mathfrak{B}^{(k)}$ is different to the one in our basis. For the non-symmetrized method, we obtain exactly the same projections since four angular integrals in $\mathrm{d}\Phi_3$ already guarantee orthogonality. However, the intensity are different since the specific line shape of the subchannel resonances, modified by the pion exchange, is not captured by the basis. In case of the symmetrized projections, the parasitic effects related to the fixed isobars are magnified due to the absence of strict orthogonality.

We restrict the discussion to the "Standard Deck" (Model-I) and address effects which appear due to the specific truncated basis. We can disentangle three issues:

1. A fixed shapes of the isobars in the basis lead to problems in description of the Deck model. Significant artifacts appear for waves where the $\pi\pi$ subsystem is in the S-wave.

---

[3] The partial-wave fit of the Deck process was pioneered by Ascoli et al. [83]. It was explored for the COMPASS kinematics by F. Haas and D. Ryabchikov Ref. [3, 77, 184]. The most of effects discussed in this section are also present in results of the fit method.

2. Symmetrization of the amplitude and the basis leads to a correlation between waves with the various L and S numbers within the same J^{PC}.

3. "Threshold effects": the number of waves in the PWA model changes from bin-to-bin, it results in the discontinuities of the waves' intensities.

To separate those problems we consider three procedures. The simplest and cleanest procedure is the algebraic projection of the non-symmetrized amplitude to the non-symmetrized basis. Next, we turn on the thresholds and check their influence. Lastly, we perform an expansion of the symmetrized model by the symmetrized basis.

We use the MC method to calculate the integral on the right side of Eq. (5.28). The amplitude $\mathfrak{B}_w(t, s)$ is discretized in 100 bins for $\sqrt{s} \equiv m_{3\pi}$ in the interval from $0.5\,\mathrm{GeV}$ to $2.5\,\mathrm{GeV}$, the value of the transferred momentum is fixed, $t = -0.1\,\mathrm{GeV}^2$. We generate 10^6 events distributed according to the phase space in each $m_{3\pi}$ bin. For every event we calculate the value of the Deck amplitude $\mathfrak{B}(t_e, s_e, \tau_e)$ as well as complex values for all basis functions $\Psi_w(s_e, \tau_e)$ where the subindex e points to a specific event e. The integral is calculated analogously to Eq. (3.20a). The coefficients $\mathfrak{B}_w$ are found for every bin independently.

The partial wave intensities as a function of $m_{3\pi}$ are shown in Fig. 5.6 in the same fashion as Fig. 3.13. As mentioned already, the intensities in the non-symmetrized projection method on the
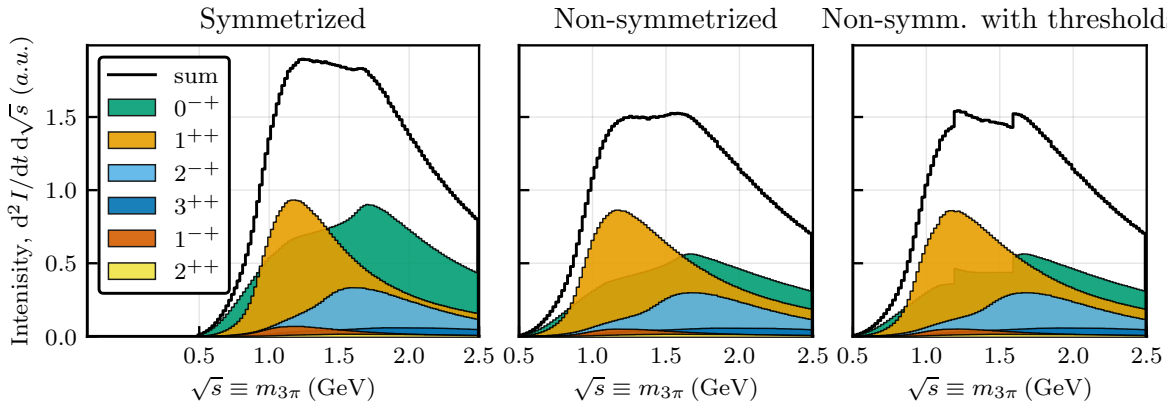
Figure 5.6: The intensities of the J^{PC}-sectors summed over the partial waves in the COMPASS basis. The left plot shows projections of the non-symmetrized Deck model to the non-symmetrized basis, the middle plot shows the projections of the symmetrized Deck model to the symmetrized basis. The right plot shows the effect of the "thresholding" while the amplitude as well as the basis is kept non-symmetrized.

middle panel of Fig. 5.6 agree with the analytic projections due to the orthogonality of the partial waves with respect to the all quantum numbers $(JM\epsilon LS)$. However, the basis contains several waves with $S = 0$ which share exactly the same quantum numbers but differ by the line shape of the $\pi\pi$-amplitude. The line shape of the $[\pi\pi]_S$ Deck amplitude (see Fig. 5.2) is similar to the $\pi\pi \to \pi\pi$ amplitude shown in the left panel of Fig. 3.16 (the difference comes from the σ-dependence of the pion propagator), while in the basis we have three functions with the predetermined line shapes: $(\pi\pi)_S$, $f_0(980)$, and $f_0(1500)$. The decomposition obtained in the algebraic-projection method is shown in Fig. 5.7. The description is far from being perfect: the shape is tilted and contains artifacts. As we can see on the left panel of the Fig. 5.7, the $f_0(1500)$ Breit-Wigner amplitude is eventually preferred over

Figure 5.7: Description of the $\pi\pi$-spectrum of the Deck amplitude by the partial-wave model in the COMPASS basis that is found by the algebraic-projection method (the non-symmetrized Deck to the non-symmetri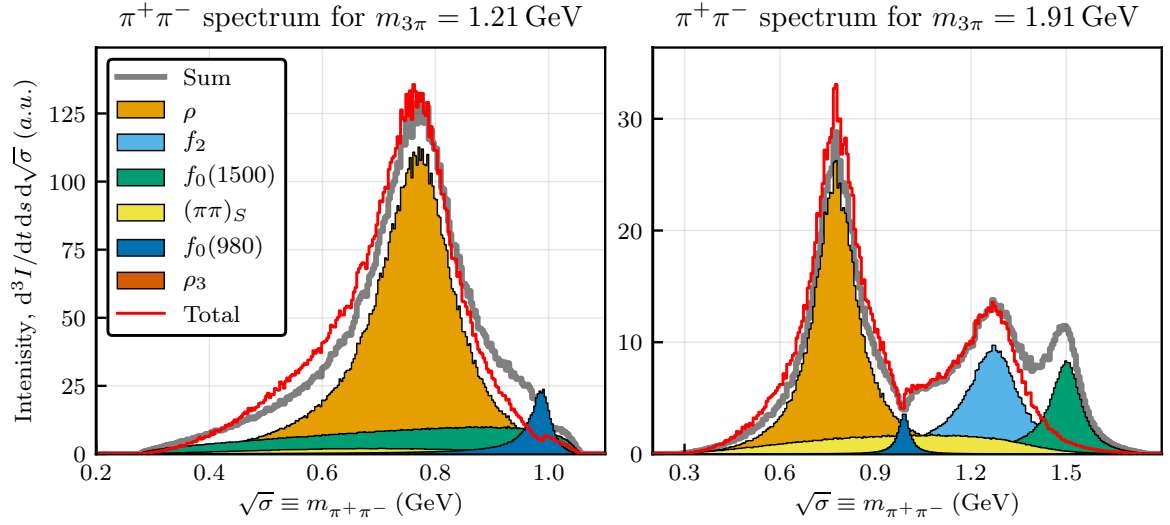zed basis). The intensity of the coherent sums of the waves $J^{PC}M^\epsilon \xi \pi L$ with the same Isobar ξ are shown by different colors. To plot the total intensity distributions we use the MC phase-space sample and weights w_e calculated for every event. For the total intensity shown by the red line $w_e = |\mathfrak{B}(t_e, s_e, \tau_e)|^2$, while for the other distributions $w_e = |\sum \mathfrak{B}_w(t_e, s_e, \tau_e)\Psi_w(s_e, \tau_e)|^2$.

the $(\pi\pi)_S$-Isobar for the description of the $\pi^+\pi^-$ spectrum of the Deck. It also causes a prominent $f_0(1500)$ peak in the $\pi\pi$ spectrum which is not present in the original Deck model on the right panel of the Fig. 5.7.

Problems in description of the amplitude lead to deviations of the integral intensity from the one calculated in the model (in contrast to the PWA technique, the number over events per bin is not constrained). The largest effect is observed in the $J^{PC} = 0^{-+}$ sector as can be seen by comparing the green distribution in the middle panel of Fig. 5.5 with the orange line in the middle-top panel of Fig. 5.7. The splitting of the total 0^{-+} intensity into contributions of the individual waves is presented in Fig. 5.8. One finds a peak around 1 GeV on the right panel in both $f_0(980)\pi$ S-wave and $f_0(1500)\pi$ S-wave, however, not in the total intensity. These two waves largely interfere in the expansion series. It has nothing to do with the physics: due to the pure model for the scalar waves, the found decomposition is preferred in the numerical procedure. The left plot of Fig. 5.8 shows how the decomposition changes when the wave with $f_0(1500)$ is artificially excluded from the basis below 1.7 GeV and the wave with the $f_0(980)$ is only added to the basis above 1.3 GeV.

As we mention above, the symmetrization introduces a non-orthogonality in the basis. It causes a "leakage" between waves. An example of this issue is shown in Fig. 5.9: $S = 3$ is not part of our Deck model, however, the $J^{PC}M^\epsilon = 2^{-+}0^+$ $\rho_3\pi$ P-wave gets non-zero weight, when the symmetrized amplitude is expanded in the symmetrized basis.
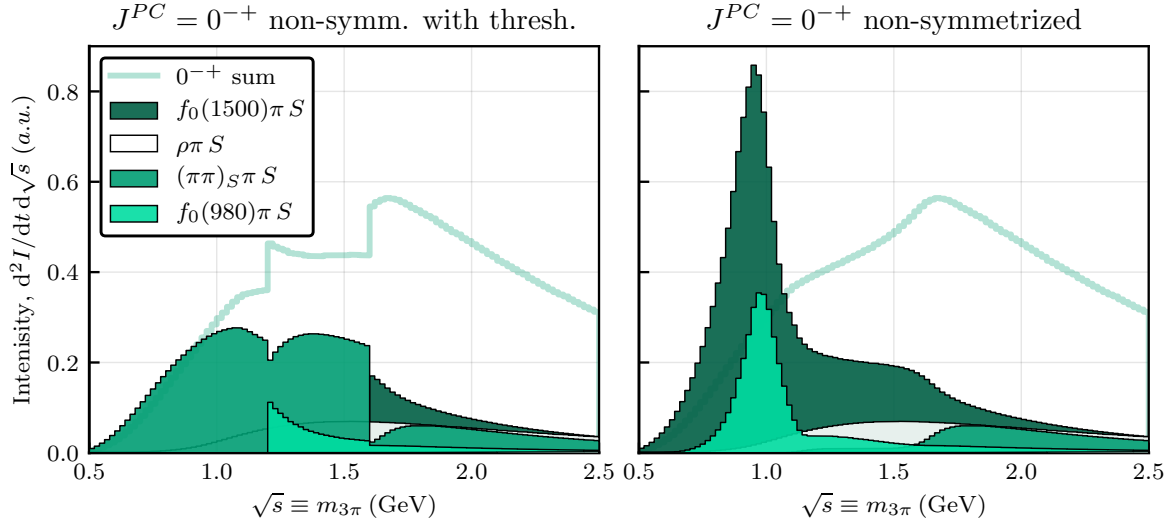
Figure 5.8: The decomposition of the 0^{-+}-sector in the COMPASS-PW basis obtained by the apgebraic method. The non-symmetrized Deck amplitude is projected to the non-symmetrized basis. Right plot: all 87 waves are used through out the whole mass range $m_{3\pi} \in [0.5, 2.5]$ GeV, Left plot: waves are included in the analysis only above the thresholds indicated in Table D.1.

5.5 Conclusions

We have explored three models for the Deck process which parametrize the exchange-pion propagator differently; the partial-wave expansion have been performed. The analytic decomposition of the amplitude allowed us to simplify the problem of the partial wave projection to a single integral over one scattering angle. The model with a simple, scalar propagator for the exchanged pion, was found to be inconsistent with the data at the high energy. The two models with a modified propagator look closer to the partial waves obtained from the analysis of the COMPASS data, especially for the sectors where no prominent resonances are known, *e.g.* $J^{PC} = 3^{-+}$ and $J^{PC} = 4^{-+}$. We have observed a similarity between the Deck projections and the background-like structures of the COMPASS PWA results for $J^{PC} = 0^{-+}$, 1^{-+}, 2^{-+}, and 3^{++} sectors. We saw that the Deck intensity for the 0^{-+} sector might develop a prominent peak structure around 1 GeV. The relevance of this structure to an observation of the $\pi(1300)$ strongly motivates a further investigation. We found that the Deck process also contributes significantly to 1^{-+}, shading the exotic $\pi_1(1600)$ signal.

Possible problems of the Deck amplitude expansion in a truncated set of waves with the predetermined isobars was discussed. Using an algebraic projection method, we found that the summed intensities for $J^{PC} M^\epsilon$ are rather well reproduced. However, a splitting the total intensity between the partial waves with the same quantum numbers based on the Isobar parametrization might be misleading. The wave thresholds partially cure the problem of unphysical intensities, however, they produce discontinuities in the model curve. The numerical problems are magnified by the symmetrization of the wave basis that relaxes of the basis orthogonality.

The results of the studies can be used to estimate the systematic uncertainties to our knowledge of the Deck projections. It is clear that the model dependence dominates over the basis-related issues. The shapes of the projections are rather ambiguous, while the relative strengths seem to be rather

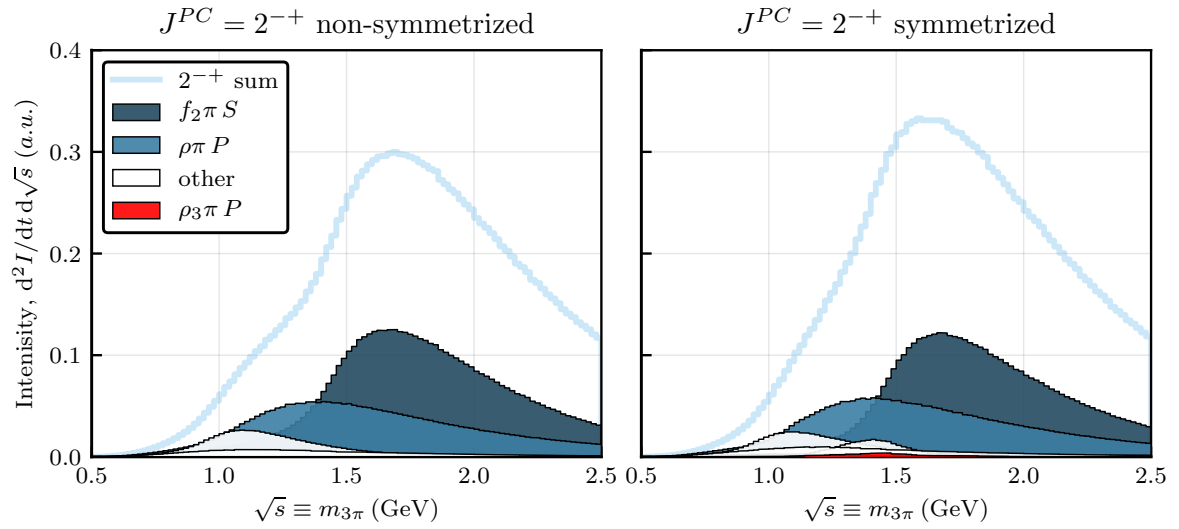Figure 5.9: The decomposition of the 2^{-+}-sector in the COMPASS partial wave basis. The left plot shows the projections of the non-symmetrized Deck amplitude to the non-symmetrized basis. The right plot presents the same decomposition for the Bose-symmetrized amplitude in the symmetrized basis.

stable. The uncertainty can be estimated by comparing the Regge model with the Form-factor model.

Properties of the $a_1(1260)$ from tau decays [1]

A large number of light meson resonances dominantly decay to three pions. This includes the enigmatic $a_1(1260)$ resonance, which is the lightest axial-vector meson with $J^{PC} = 1^{++}$. The properties of the a_1 resonance are difficult to assess, due to its large width that is affected by the three-pion dynamics. The $\pi\pi$ subchannel is dominated by the ρ resonance whose finite width is expected to be important for the extraction of the a_1 resonance properties. Indeed, a large part of the $a_1(1260)$ peak seen in the invariant mass distribution of three pions lays below the nominal $\rho\pi$ threshold. However, the pole of the resonance was previously addressed in Lagrangian-based models [185, 186], assuming a stable ρ-meson.

The $J^{PC} = 1^{++}$ three-pion state can be observed in the $\tau \to 3\pi\,\nu_\tau$ decay as well as in pion diffraction off a proton target $\pi\,p \to 3\pi\,p$. There appears to be a discrepancy in the a_1 resonance parameters extracted from the two reactions [26, 187]. The problem may be related to the presence of a large, coherent, non-resonant background, known as the Deck process in pion diffraction [3, 40, 62, 91]. This process happens to dominate in the $J^{PC} = 1^{++}$ partial wave and directly influences the extraction of the $a_1(1260)$ resonance parameters in pion diffraction. Thus, an independent determination of the $a_1(1260)$ resonance properties is not only relevant for a better understanding of this state but also to constrain the Deck process, which contributes significantly to other partial waves including the ones with the exotic quantum numbers 1^{-+} [3]. Therefore, we focus on the $\tau^- \to \pi^-\pi^+\pi^-\,\nu_\tau$ decay with the aim of extracting the $a_1(1260)$ resonance parameters.

6.1 The reaction model

We consider the reaction $\tau \to 3\pi\,\nu_\tau$ and derive an expression for the differential width which characterizes the 3π invariant mass spectrum [110, 188–191]. The differential width is calculated by averaging (summing) over the τ (ν_τ) polarizations and integrating the matrix element squared over the final-state momenta,

$$\mathrm{d}\Gamma = \frac{1}{2m_\tau} \cdot \frac{1}{2} \sum_{\lambda_\tau \lambda_\nu} \left| A_{\lambda_\nu, \lambda_\tau} \right|^2 \mathrm{d}\Phi_4, \tag{6.1}$$

where m_τ is the mass of the τ-lepton, $m_\tau = 1\,776\,\mathrm{MeV}$ [26], the neutrino is considered massless, $\mathrm{d}\Phi_4$ is the four-body differential phase space, and λ_x are the lepton helicities of the $x = \tau, \nu$. The

---

[1] A large part of this chapter has been published in Ref. [2] in collaboration with JPAC colleagues.
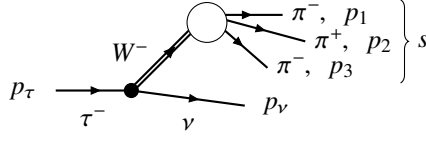
Figure 6.1: Diagram for the decay $\tau^- \to \pi^- \pi^+ \pi^- \nu_\tau$. The momenta of the τ lepton and ν_τ are denoted by p_τ and p_ν. The pions momenta are labeled by p_i, $i = 1, 2, 3$. s is the invariant mass of the three pions.

process is dominated by the emission of a W boson by the leptonic current,

$$\langle 3\pi\, \nu_\tau, \lambda_\nu |\, T\, |\tau, \lambda_\tau \rangle = -\frac{G_F}{\sqrt{2}} V_{ud}^* \, \bar{u}(p_\nu, \lambda_\nu) \gamma^\alpha (1 - \gamma^5) u(p_\tau, \lambda_\tau) \, \langle 3\pi |\, J_\alpha^{5-}(0)\, |0 \rangle, \qquad (6.2)$$

where $\langle 3\pi\, \nu_\tau, \lambda_\nu |\, T\, |\tau, \lambda_\tau \rangle = A_{\lambda_\nu, \lambda_\tau} (2\pi)^4 \delta^4(p_\tau - p_\nu - p_{3\pi})$, $G_F V_{ud}^* / \sqrt{2}$ is the Cabibbo-favored weak coupling, $p_{3\pi}$, p_τ, and p_ν are the four-momenta of three-pion system and the leptons, u ($\bar{u}$) are the Dirac spinors of the τ (ν_τ), see Fig. 6.1. Because of G-parity conservation the $\pi^- \pi^+ \pi^-$ system has positive C-parity. Hence, the vector current $\bar{u}\gamma^\alpha u$ does not couple it, and can be removed. Since the W^- is heavily off-shell, one should also consider the timelike polarization, which carries $J^{PC} = 0^{-+}$. However, the corresponding helicity amplitude is suppressed by the PCAC [188, 192]. This enables us to treat the off-shell W^- as purely axial. The polarization of the real W^- provides a complete basis which we use to expand the hadronic current,

$$A_{\lambda_\nu, \lambda_\tau} = \frac{G_F}{\sqrt{2}} V_{ud}^* \, \bar{u}(p_\nu, \lambda_\nu) \gamma^\alpha \gamma^5 u(p_\tau, \lambda_\tau) \sum_\Lambda \varepsilon_\alpha(\Lambda) A_\Lambda, \qquad (6.3)$$

where $\varepsilon^{\alpha*}(\Lambda) \langle 3\pi |\, J_\alpha^{5-}(0)\, |0 \rangle = A_\Lambda (2\pi)^4 \delta^4(p_\tau - p_\nu - p_{3\pi})$ is the helicity amplitude for the decay of the axial current to three pions. The squared matrix element summed and averaged over the ν_τ and τ helicities, respectively, is

$$\frac{1}{2} \sum_{\lambda_\tau \lambda_\nu} \left| A_{\lambda_\nu, \lambda_\tau} \right|^2 = G_F^2 |V_{ud}|^2 \left(p_\tau^\alpha p_\nu^\beta + p_\tau^\beta p_\nu^\alpha - g^{\alpha\beta}(p_\tau \cdot p_\nu) \right) \sum_{\Lambda, \Lambda'} \varepsilon_\alpha(\Lambda) \varepsilon_\beta^*(\Lambda') \, A_\Lambda A_{\Lambda'}^*. \qquad (6.4)$$

The explicit evaluation of the expression is performed in the τ-rest frame where $p_\tau \cdot \varepsilon(0) = (m_\tau^2 - s)/(2\sqrt{s})$, and $p_\tau \cdot \varepsilon(\pm) = 0$.

Using the recursive relation for the phase space, we split it into the $\tau^- \to W^- \nu_\tau$-phase space $d\Phi_2$, and the three-pion phase space $d\Phi_3$: $d\Phi_4 = \int d\Phi_2\, d\Phi_3\, ds/(2\pi)$, where $\sqrt{s}$ is the invariant mass of the hadronic system. To obtain the differential width $d\Gamma/ds$, we integrate explicitly over the neutrino angles,

$$\frac{d\Gamma}{ds} = \frac{G_F^2 |V_{ud}|^2}{64\pi^2 m_\tau^3} (m_\tau^2 - s)^2 \int d\Phi_3 \left(|A_+|^2 + |A_-|^2 + \frac{m_\tau^2}{s} |A_0|^2 \right). \qquad (6.5)$$

Here, one power of the factor $(m_\tau^2 - s)$ follows from the matrix element in Eq. (6.4), the other is given by the $W^- \nu_\tau$ two-body phase space. The expression for the $d\Phi_3$ is given in Appendix B. The integral is kept in the final expression to facilitate the further discussion on partial-wave expansion of the amplitude A_Λ.

The helicity amplitude A_Λ describes the coupling of the axial current to the three charged pions. The pions are labeled as follows, $\pi_1^- \pi_2^+ \pi_3^-$ (see Fig. 6.1). We use the isobar model to parametrize the dynamics and explicitly incorporate the $\pi_1^- \pi_3^-$ Bose symmetry,

$$A_\Lambda = A_\Lambda^{(3)} + A_\Lambda^{(1)}, \tag{6.6}$$

where the isobar amplitude $A_\Lambda^{(k)}$ includes only the subchannel interaction in a pion pair leaving the pion indexed k as a bachelor. In Eq. (6.6), we disregard the $\pi^- \pi^-$ interaction since it is negligible compared to the dominant ρ-meson in the $\pi^+ \pi^-$ subchannel. The pion momenta are denoted by p_i where $i = 1, 2, 3$ as shown in Fig. 6.1 and the subchannel invariant mass squared is denoted as $\sigma_k = (p_i + p_j)^2$. Here and below we use the circular convention, *i.e.* the bachelor pion has index k such that the (ijk) are numbers (123), (231) or (312).

Each isobar amplitude receives different contributions, often referred to as decay channels [26]. The importance of different decay channels can be estimated by the relative branching fractions of the $a_1(1260)$ decay. The latest measurements were carried out by the CLEO experiment from τ decay [156, 157] and by the COMPASS experiment in diffractive production [78]. The extraction of branching ratios is model-dependent and is influenced by the production mechanism; however, we get a rough estimate of their relative importance. The $\rho\pi$ S-wave channel is dominant with a branching ratio of $60\% - 80\%$. The second most important channel, $f_0(500)\pi$ P-wave, was estimated to contribute less than 20%. The combined branching ratio to the remaining channels ($\rho\pi$ D-wave, $f_2\pi$ P-wave, $K^*\bar{K}$ S, D-waves) does not exceed 10%. We thus limit the analysis to the main $\rho\pi$ S-wave channel. Including other decay channels would require the introduction of additional parameters for couplings and production strengths, which cannot be fixed by current publicly available data.

Therefore, we take the isobar amplitude to have the form,

$$A_\Lambda^{(k)} = \mathcal{C}^{(k)} a(s) f_\rho(\sigma_k) N_\Lambda(\Omega_k, \Omega_{ij}), \tag{6.7}$$

where $\mathcal{C}^{(k)} = \langle 1, \mu_i; 1, \mu_j | 1, 0 \rangle = \pm 1/\sqrt{2}$ is the Clebsch-Gordan coefficient relating the two pion with isospin projection $\mu_{i,j} = \pm 1$ to ρ^0 isospin states, thus, the sign depends on the index k. The $a(s)$ denotes the dynamical part of the amplitude $a_1 \to \rho\pi$ S-wave in the canonical basis [47, 79], $f_\rho(\sigma)$ is a parametrization for the ρ-meson decay amplitude, and $N_\Lambda(\Omega_k, \Omega_{ij})$ is the angular decay function for the decay chain $a_1 \to \rho\pi$, $\rho \to \pi\pi$,

$$N_\Lambda(\Omega_k, \Omega_{ij}) \equiv Z_{10}^{J\Lambda}(\Omega_k, \Omega_{ij}) = \sqrt{3} \sum_\lambda D_{\Lambda\lambda}^{1*}(\Omega_k) D_{\lambda 0}^{1*}(\Omega_{ij}), \tag{6.8}$$

where Z_{LS}^{JM} is introduced in Eq. (3.9). The three-pion center-of-mass (CM) frame is oriented by the direction of W in τ decay (W helicity frame). The momentum vector of the τ defines the xz plane, *a.k.a.* the production plane. $\Omega_k = (\theta_k, \phi_k)$ denotes the polar and azimuthal angles of the vector $\vec{p}_i + \vec{p}_j$ in the CM-frame. The $\Omega_{ij} = (\theta_{ij}, \phi_{ij})$ are the spherical angles of the pion i in the helicity frame of the isobar (ij). This helicity frame is obtained from the CM frame by active rotation $R^{-1}(\Omega_k)$ and boost along the z-axis. Equivalently, we can notice that the boost does not change azimuthal orientation, therefore, the y-axis direction $\vec{e}_y$ in the helicity frame can be found by $\vec{e}_z' \times \vec{e}_z$, where $\vec{e}_z'$ is the original orientation of the CM z-axis.

The line shape of the ρ-meson is given by the customary Breit-Wigner amplitude with dynamical

width [78, 179]

$$f_\rho(\sigma) = \mathcal{N} \frac{F_1\left((p(\sigma)R)^2\right)}{m_\rho^2 - \sigma - im_\rho\Gamma_\rho(\sigma)}, \tag{6.9}$$

where $p(\sigma) = \sqrt{\sigma/4 - m_\pi^2}$ is the pion break-up momentum, the function $F_1(pR)$ combines the threshold factor $p(\sigma)$ and the customary Blatt-Weisskopf barrier factor with size parameter $R = 5\,\mathrm{GeV}^{-1}$. Energy dependent width is described by Eq. (D.5) We use in the analysis $m_\pi = 139.57\,\mathrm{MeV}$, $m_\rho = 775.26\,\mathrm{MeV}$ [26]. For convenience we fix $\mathcal{N}$ so that the phase-space integral $\rho(s)$ defined below in Eq. (6.11a) approaches the two-body phase space asymptotic value, $1/8\pi$, in the limit $s \to \infty$ as shown in Eq. (D.3) in the Appendix. The normalization for $f_\rho(\sigma)$ fixes the normalization of $a(s)$.

Using Eqs. (6.6),(6.7) to substitute the amplitude A_Λ in Eq. (6.5), we get the expression for the differential width in terms of the dynamic amplitude $a(s)$.

$$\frac{\mathrm{d}\Gamma}{\mathrm{d}s} = \frac{G_F^2\,|V_{ud}|^2}{64\pi^2\,m_\tau^3}\left(2 + \frac{m_\tau^2}{s}\right)(m_\tau^2 - s)^2\,|a(s)|^2\rho(s). \tag{6.10}$$

where $\rho(s)$ is the effective $\rho\pi$ phase space. We will consider two models for $\rho(s)$'s:

$$\rho_{\mathrm{SYMM}}(s) = \frac{1}{2}\int \mathrm{d}\Phi_3 \left|f_\rho(\sigma_1)N_0(\Omega_1, \Omega_{23}) - f_\rho(\sigma_3)N_0(\Omega_3, \Omega_{12})\right|^2, \tag{6.11a}$$

$$\rho_{\mathrm{QTB}}(s) = \int \mathrm{d}\Phi_3 |f_\rho(\sigma_1)N_0(\Omega_1, \Omega_{23})|^2. \tag{6.11b}$$

The expression in Eq. (6.11a) strictly follows from Eqs. (6.6), (6.7), and (6.10). The label SYMM is introduced to emphasize the symmetrization between the decay channels, *i.e.* the $\rho\pi$ channels $k = 1$ and 3. The relative minus sign comes from the symmetry of the isospin coefficient in Eq. (6.7). The integral in Eq. (6.11a) is the same for all helicities Λ due to the properties of the Wigner d-functions, therefore we set $\Lambda = 0$ for simplicity. The interference term is only significant at low energy, where the overlapping region of the two ρ-mesons contributes to a substantial fraction of the Dalitz plot. The ρ_{QTB} (Quasi-Two-Body) in Eq. (6.11b) is a simplified phase space where the interference term is neglected. In this case, the integrals of the two decay chains squared are identical, which cancels the $1/2$ factor in front. This model treats the ρ-meson as quasi-stable and the interaction between the $\rho\pi$ as a two-body interaction. The simplification is suggested and discussed in Ref. [141] to treat the multiparticle final states. The same approximation is commonly used to account for 4π channel in the $\pi\pi/K\bar{K}$ coupled-channels problem [50, 193]). Finally, as shown in Fig. 6.2, the interference is rather small. Since this model is simpler, we would like to test it as an alternative.

Our model for the decay amplitude is constrained by the approximate three-body unitary [62, 141]. Turning general 3-body unitarity into some practically useful equations is cumbersome and not complete yet. A significant progress in this direction has been made in Refs. [38, 194–196]. In particular, one can separate the genuine three-body unitary from the subchannel unitarity related to rescattering between different isobars. These processes modify the line shape of the subchannel amplitudes [165, 166, 168, 169, 171, 197, 198]. A good example is the $\rho\pi$-dynamics studied in the 1^{--} sector in the decay of ω/ϕ [165, 166], where the final-state interaction were found to shift and skew the ρ-meson peak. Conversely, in our models we focus on the 3-body resonance dynamics,
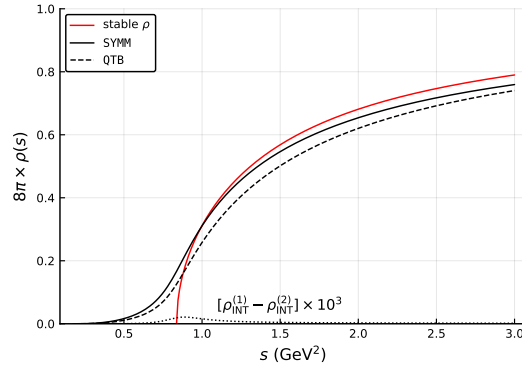
Figure 6.2: The phase space $\rho(s)$ calculated for different models. The black solid line shows the symmetrized ρ_{SYMM} from Eq. (6.11a). The dashed curve represents ρ_{QTB} from Eq. (6.11b), which neglects the interference between the two $\rho\pi$ decay chains. For reference we draw the two-body $\rho\pi$ phase space given by $\sqrt{(s-(m_\rho+m_\pi)^2)(s-(m_\rho-m_\pi)^2)}/(8\pi s)$ with a solid red line. Due to the chosen normalization in Eq. (D.3), all functions approach the same asymptotic limit. The dotted line shows the difference in the interference terms calculated in two different ways for $s+i\epsilon$ as discussed in Sec. 6.3.2.

and simplify the problem by neglecting the effects of the rescattering on the isobar line shapes. We introduce the $\rho\pi$ elastic scattering isobar amplitude $t(s)$, to impose the unitarity constraints for the amplitude $a(s)$:

$$2\,\text{Im}\,a(s) = t^*(s)\,\rho(s)\,a(s), \tag{6.12a}$$

$$2\,\text{Im}\,t(s) = t^*(s)\,\rho(s)\,t(s), \tag{6.12b}$$

where $\rho(s)$ is the effective phase space given by Eq. (6.11a) or Eq. (6.11b). The factor of 2 in the left-hand-side of Eq. (6.12) is kept for convenience.

The unitarity equations (6.12) can be satisfied by a certain choice of the parametrization.

$$t(s) = \frac{g^2}{m^2 - s - ig^2 C(s)/2}, \quad a(s) = \alpha(s)t(s), \tag{6.13}$$

where $C(s)$ is an analytic function constrained by condition $\text{Im}\,iC(s) = \rho(s)$. To describe the amplitude dominated by a single resonance, we added a first order polynomial $(m^2-s)/g^2$ to the denominator of $t(s)$, which is equivalent to have the K-matrix with a single pole [47]. The numerator function $\alpha(s)$ is supposed to incorporate the singularities specific to the production process into the amplitude $a(s)$. The final-state interaction required by unitarity is accounted for by the multiplicative form of the production amplitude in Eq. (6.13). It diminishes the differences between different possible production mechanisms, *e.g.* resonant vs. non-resonant production of $\rho\pi$. In the case at hand we use $\alpha = \text{const}$. There are two common constructions for $C(s)$ which both satisfy unitarity:

1. The models with $C(s) = \rho(s)$ will be called *non-dispersive*. Twhese models have left-hand singularities on the physical sheet inherited from the phase space, which are not motivated by physics.

Table 6.1: Summary of the models discussed for the 3π-scattered amplitudes in the τ decay. The numerator and denominator refer to Eq. (6.15).

Model	$\rho(s)$ in Numer.	$C(s)$ in Denom.	χ^2/n.d.f.	m (GeV)	g (GeV)
SYMM$-$DISP	$\rho_{\mathrm{SYMM}}(s)$	$\tilde{\rho}_{\mathrm{SYMM}}(s)$	94/100	1.205	6.64
SYMM	$\rho_{\mathrm{SYMM}}(s)$	$\rho_{\mathrm{SYMM}}(s)$	663/100	1.230	6.65
QTB$-$DISP	$\rho_{\mathrm{QTB}}(s)$	$\tilde{\rho}_{\mathrm{QTB}}(s)$	68/100	1.223	7.45
QTB	$\rho_{\mathrm{QTB}}(s)$	$\rho_{\mathrm{QTB}}(s)$	344/100	1.236	7.42

2. The *dispersive* models have $C(s) = \tilde{\rho}(s)$, with

$$i\tilde{\rho}(s) = l_0 + \frac{s}{\pi} \int_{9m_\pi^2}^{\infty} \mathrm{d}s' \, \frac{\rho(s')}{s'(s' - s - i\epsilon)}, \qquad (6.14)$$

where the subtraction constant l_0 is chosen such that the real part of $i\tilde{\rho}(s)$ is zero at the point $(m_\rho + m_\pi)^2$. The function $i\tilde{\rho}(s)$ has no singularities other than the unitarity cut as guaranteed by the Cauchy integral theorem. It is analogous to the Chew-Mandelstam function for the two-body scattering amplitude [62].

We note that the first construction with $C(s) = \rho(s)$ resembles the Breit-Wigner amplitude with a dynamical width [26]. In contrast, the dispersive amplitudes do not have the unmotivated left-hand cut generated by ρ in Eq. (6.11a). For all models, the structure of $C(s)$ ensures unitarity and extends the applicability of Eq. (6.13) from threshold to energy regions where higher-lying resonances or/and non-elastic channels become significant.

To summarize, the final expression for the differential cross section is.

$$\frac{\mathrm{d}\Gamma}{\mathrm{d}s} = \frac{1}{s} \left(1 - \frac{s}{m_\tau^2}\right)^2 \left(1 + \frac{2s}{m_\tau^2}\right) \frac{c\rho(s)}{\left|m^2 - s - ig^2 C(s)/2\right|^2}. \qquad (6.15)$$

Eq. (6.15) follows from Eq. (6.10). The constant c absorbs all energy-independent numerical factors; m, g, and c are real parameters which are fitted to data. The four models we are going to test are summarized in Table 6.1. Our primary model is SYMM$-$DISP, which is the one that incorporates the most of physical arguments. The SYMM model contains additional left-hand singularities with respect to SYMM$-$DISP. The QTB and QTB$-$DISP models do not include the interference between the two decay chains, but are much simpler to calculate on the real axis and continue to the complex plane. The $C(s)$ is calculated using the same $\rho(s)$ as in the numerator of Eq. (6.15), which is either ρ_{QTB} or ρ_{SYMM} as given in Table 6.1.

6.2 Fit results and resonance parameters

The largest public dataset for $\tau \to 3\pi \, \nu_\tau$ was collected by the ALEPH experiment in 2005 [199].[2] The distribution $\mathrm{d}\Gamma/\mathrm{d}s$ is binned in $0.025\,\mathrm{GeV}^2$ bins and normalized by the measured branching ratio. We

---

[2] An updated analysis was published in 2014 [200]. The main difference is related to the use of a new method to unfold detector effects from the mass spectra. However, the data were binned into wider bins with variable bin size, which makes it less straightforward to use. For this reason we stick to data of [199].
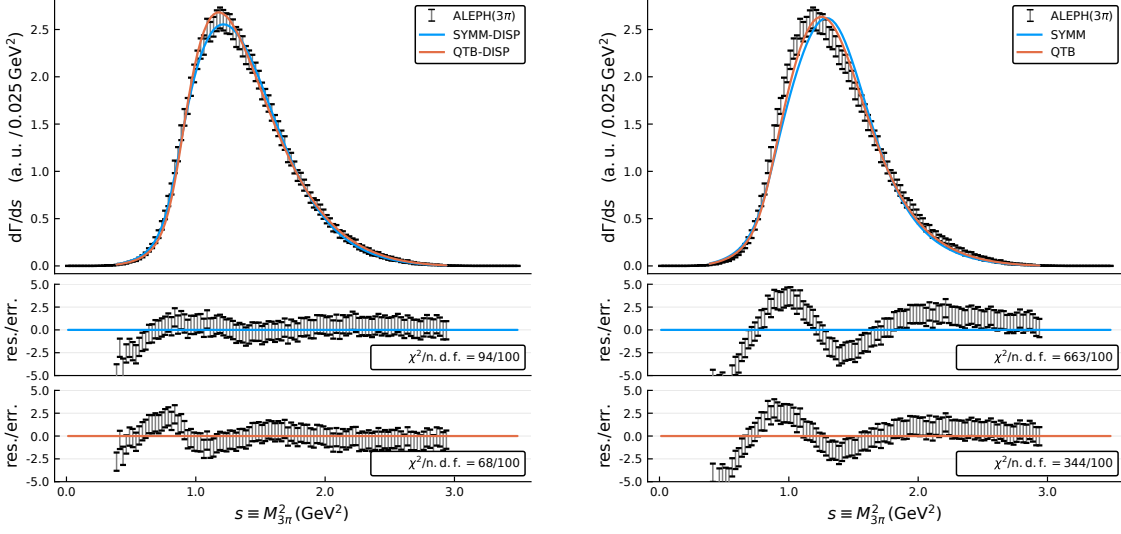
Figure 6.3: Fit to the ALEPH data with the four models described in the text. The models differ by either including the effect of interference between two $\rho\pi$ decay channels (SYMM) or not (QTB), and either using the dispersive integral over the phase space (DISP), or not. The lower panels show the normalized residues.

fit 103 data points in the range $0.38\,\mathrm{GeV}^2 \leq s \leq 2.94\,\mathrm{GeV}^2$. We minimize the χ^2-function taking into account the covariance matrix provided in Ref. [199],

$$\chi^2(c,m,g) = (\vec{D} - \vec{M}(c,m,g))^T C_{\mathrm{stat}}^{-1}(\vec{D} - \vec{M}(c,m,g)), \tag{6.16}$$

where $\vec{D}$ is a vector of the ALEPH data points, $\vec{M}(c,m,g)$ is a vector of the model predictions calculated for the centers of the bins. The matrix C_{stat} is the covariance matrix of the statistical errors. The systematic uncertainties are smaller than the statistical ones by a factor 5, and can be neglected. Nonzero correlations among different bins are introduced by the unfolding procedure. It is worth noticing the 3π spectrum does not show the expected random noise. As discussed in the follow up analysis of the ALEPH [200], the problem appears because the errors of the unfolding procedure were not correctly propagated. Hence, the absolute value of χ^2 we obtained does not have a strict statistical meaning. However, we assume that for the model characterization based on relative χ^2 values, the problem should not be critical.

The gradient minimization is performed using the `NLopt` optimizer and the `ND_MMA` algorithm [101] with the automatic differentiation provided by the `ForwardDiff.jl`-package [201]. The minimum we find is always stable and isolated, as checked by repeating the minimization from different starting values. Fits to the ALEPH dataset are shown in Figs. 6.3, and the fit parameters and χ^2 values are shown in Table 6.1. The non-dispersive models are not consistent with the data, with χ^2 at least three times worse than we have obtained for the dispersive models. In particular, they fail to reproduce the line shape around the peak and in the threshold region, and we do not consider them any further. On the other hand, the dispersive models show a good agreement with data, obtaining $\chi^2/\mathrm{n.d.f.} = 94/100$ and $\chi^2/\mathrm{n.d.f.} = 61/100$ for the $\mathrm{SYMM-DISP}$ and $\mathrm{QTB-DISP}$, respectively.

In the next section we will perform the analytic continuation of the amplitude to the second sheet and search for the $a_1(1260)$ resonance pole. For comparison with the PDG [26], we first provide the

customary Breit-Wigner parameters, that can be extracted on the real axis. We remind the reader that these are expected to be reaction-dependent, and do not provide an unambiguous characterization of the resonance. We define the Breit-Wigner mass squared m_{BW}^2 as the value of s when the denominator of the amplitude $t(s)$ in Eq. (6.13) becomes purely imaginary. The value of the denominator at this point gives the Breit-Wigner width, as it is equal to $-im_{\text{BW}}\Gamma_{\text{BW}}$. For QTB$-$DISP we get the Breit-Wigner mass and width as $(1246 \pm 3)\,\text{MeV}$ and $(394 \pm 5)\,\text{MeV}$; for SYMM$-$DISP, $(1254 \pm 3)\,\text{MeV}$ and $(461 \pm 8)\,\text{MeV}$, where the errors are statistical only.

6.3 Analytic continuation the pole position

Once the amplitude is fixed on the real axis, its analytic structure is unambiguously defined and can be explored. Unitarity introduces a branch cut along the real axis from the 3π threshold to infinity, which opens a non-trivial Riemann topology or sheet structure. The first Riemann sheet is the one containing the physical values of the amplitude slightly above the real axis. By construction, the amplitudes in the dispersive models contain no other singularity on the first sheet than the unitarity cut. Resonance poles are expected to lie on the second sheet, which is connected to the physical axis from below. The unitarity condition Eq. (6.12b) gives us a relation on the real axis that can be used to continue the amplitude in the complex s-plane. The real-axis relation followed from Eq. (6.12) reads

$$t_I^{-1}(s + i\epsilon) - \Delta t^{-1}(s) = t_I^{-1}(s - i\epsilon) = t_{II}^{-1}(s + i\epsilon), \tag{6.17}$$

where $\Delta t^{-1}(s) \equiv t_I^{-1}(s + i\epsilon) - t_I^{-1}(s - i\epsilon) = -i\rho(s)$ is the discontinuity across the cut, s is real, ϵ is an infinitesimal positive number, and the Roman subscript indicates the Riemann sheet. Thus, $t_{II}^{-1}(s) = t_I^{-1}(s) + i\rho(s)$ and the pole positions are determined by $t_{II}^{-1}(s) = 0$. The first sheet amplitude, $t_I^{-1}(s)$, is straightforward to calculate in the complex plane using the dispersive integral in Eq. (6.14). Continuation of the discontinuity, however, is more challenging since it is not explicitly analytical expression, as Eq. (6.11a) contains a modulus operator. Therefore, we need to find an analytic function which coincides with the discontinuity on the real axis. All singularities of the discontinuity $-i\rho(s)$ will be present in the second sheet amplitude according to Eq. (6.17). Among those, we expect the reflection of the $\rho\pi$ unitarity cut, which is pushed into the second sheet due to the unstable nature of the ρ-meson.

For the continuation to the complex s-plane, we need to evaluate $f_\rho(\sigma)$ and $f_\rho^*(\sigma)$ in Eq. (6.11a) and Eq. (6.11b) for complex argument σ. Along the physical axis $f_\rho(\sigma) = f_\rho^{(I)}(\sigma + i\epsilon)$ and the analytic function $f_\rho^{(II)}(\sigma + i\epsilon)$ coincides with $f_\rho^*(\sigma)$ due to the Schwarz reflection principle and the continuity of the Riemann sheet structure, since

$$f_\rho^*(\sigma) = f_\rho^{(I)*}(\sigma + i\epsilon) = f_\rho^{(I)}(\sigma - i\epsilon) = f_\rho^{(II)}(\sigma + i\epsilon). \tag{6.18}$$

6.3.1 Analytic continuation of the QTB$-$DISP model

We start with the QTB$-$DISP model, whose analytic continuation is simpler than the one of the SYMM$-$DISP model. The discontinuity across the unitarity cut is given by $-i\rho_{\text{QTB}}$ in Eq. (6.11b). The angular integrals in the phase space can be solved analytically due to the properties of the Wigner
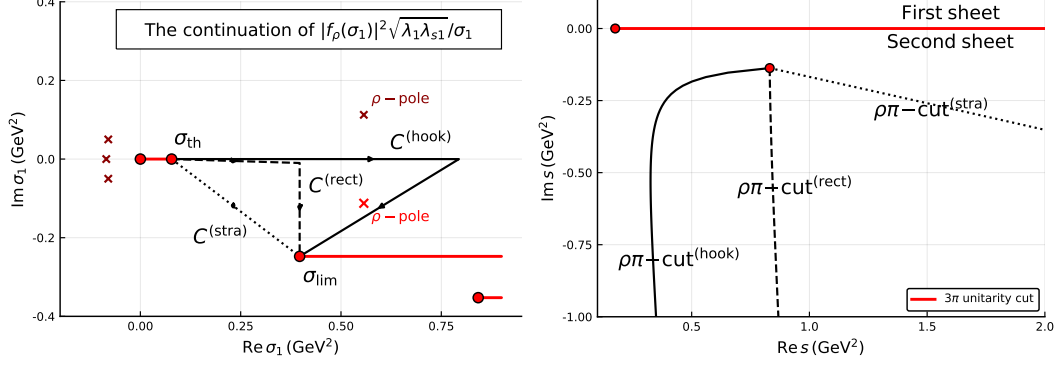
Figure 6.4: An illustration for the integral of the phase space from Eq. (6.19) in the complex plane. The left plot shows the complex plane of the integrand for $s = (0.6 - 0.35i)\,\text{GeV}^2$. The red circular markers are the square-root branch points, the crosses indicate positions of the poles. The integration paths from Eq. (6.20) are shown by the solid lines with arrows. The right plot presents the location of the $\rho\pi$ cut for the different integration paths.

D-functions. We obtain

$$
\rho_{\text{QTB}}(s) = \frac{1}{2\pi(8\pi)^2 s} \int_{4m_\pi^2}^{(\sqrt{s}-m_\pi)^2} f_\rho^{(II)}(\sigma_1) f_\rho^{(I)}(\sigma_1) \frac{\sqrt{\lambda_1 \lambda_{s1}}}{\sigma_1} \, d\sigma_1, \tag{6.19}
$$

where we used the definition $\lambda_i = \lambda(\sigma_i, m_\pi^2, m_\pi^2)$, $\lambda_{si} = \lambda(s, \sigma_i, m_\pi^2)$, with λ being the Källén function. Using Eq. (6.18), we replaced $\left|f_\rho(\sigma_1)\right|^2$ by the analytic expression $f_\rho^{(II)}(\sigma_1) f_\rho^{(I)}(\sigma_1)$. The function $f_\rho^{(I)}(\sigma_1)$ does not have singularities apart form cuts on the real axis, while the $f_\rho^{(II)}(\sigma_1)$ contains the pole of the ρ-meson in the complex plane. For complex values of s, the integral for the $\rho_{\text{QTB}}(s)$ in Eq. (6.19) has the upper endpoint in the complex plane, which requires a prescription for the path of integration. The value of the integral does not depend on the path of integration, unless there are singularities of the integrand in the complex plane. The integrand is plotted for complex values of σ_1 in Fig. 6.4. It has four branch points in the σ_1-variable: 0, $\sigma_{\text{th}} = 4m_\pi^2$, $\sigma_{\text{lim}} = (\sqrt{s} - m_\pi)^2$, and $(\sqrt{s} + m_\pi)^2$, coming from the product of the Källén functions,[3] and the resonance pole of the ρ-meson at $\sigma_p = (m_\rho^{(\text{pole})} - i\Gamma_\rho^{(\text{pole})}/2)^2$.[4] Singularities of the integral arise when the upper integration endpoint touches one of the singularities of the integrand. The ρ-meson pole in the integrand transforms into a branch singularity in the integral function. We find the branch point $s_{\rho\pi}$ by checking when the upper integration endpoint touches the ρ-meson pole; $s_{\rho\pi} = (m_\rho^{(\text{pole})} + m_\pi - i\Gamma_\rho^{(\text{pole})}/2)^2$. It is indeed a branch singularity, because for every s there are several ways to connect the integration limits in

---

[3] The branch points are connected by cuts. Since the integral is calculated numerically it is important to make sure that the integration path does not cross any cut between the integration end points. To illustrate the cut choice shown in Fig. 6.4, we write

$$
\lambda^{1/2}(\sigma, m_\pi^2, m_\pi^2)\lambda^{1/2}(s, \sigma, m_\pi^2) = \sqrt{\sigma}\sqrt{\sigma - 4m_\pi^2}\sqrt{(\sqrt{s} - m_\pi)^2 - \sigma}\sqrt{(\sqrt{s} + m_\pi)^2 - \sigma}.
$$

For real values of s, this expression has two short branch cuts on the real axis: one between 0 and σ_{th}, and the other between the points $(\sqrt{s} \pm m_\pi)^2$. When s is complex the first s-independent cut remains, while the second one splits into two straight cuts to the right with the branching points $(\sqrt{s} \pm m_\pi)^2$ as shown in Fig. 6.4.

[4] For the ρ-meson the pole parameters are very close to the Breit-Wigner parameters $m_\rho^{(\text{pole})} \approx m_\rho$, $\Gamma_\rho^{(\text{pole})} \approx \Gamma_\rho$.
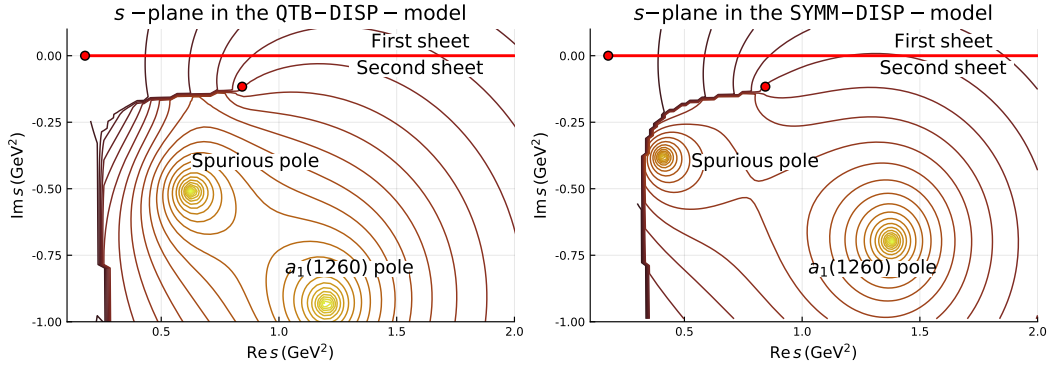
Figure 6.5: Analytic continuation of the amplitude $t(s)$ in Eq. (6.13) for different models: $\mathrm{QTB-DISP}$ (Left plot), $\mathrm{SYMM-DISP}$ (Right plot). Lines indicate the $|t(s)|$ equipotential levels. The poles of the amplitude are the bright spots. The red dots indicate branch points corresponding to the opening of decay channels.

Eq. (6.19) (see for example the solid and the dotted paths in the left panel of Fig. 6.4) which yield integral values differing by the residual of integrand in the ρ-meson pole. Practically, the choice of the integration path determines the location of the $\rho\pi$ branch cut in the complex s-plane as the loci of s values, for which the integration path goes through the pole. To demonstrate the evolution of the cut in the s-plane we consider the three different paths given in Eq. (6.20a):

$$C_\sigma^{(\mathrm{stra})} : \quad \sigma_{\mathrm{th}} \to \sigma_{\mathrm{lim}} \tag{6.20a}$$

$$C_\sigma^{(\mathrm{rect})} : \quad \sigma_{\mathrm{th}} \to \mathrm{Re}\,\sigma_{\mathrm{lim}} \to \sigma_{\mathrm{lim}}, \tag{6.20b}$$

$$C_\sigma^{(\mathrm{hook})} : \quad \sigma_{\mathrm{th}} \to 5\,\mathrm{Re}\,\sigma_{\mathrm{lim}} \to \sigma_{\mathrm{lim}}. \tag{6.20c}$$

The corresponding $\rho\pi$ cut locations are shown in the right panel of Fig. 6.4. The path $C_\sigma^{(\mathrm{hook})}$ rotates the $\rho\pi$ cut such that it opens up a larger area of the closest unphysical sheet and is used in the following for finding poles and illustration purposes.

The amplitude $t(s)$ in the complex s-plane for the $\mathrm{QTB-DISP}$ model is shown in the left panel of Fig. 6.5. Naively, one would expect a single pole in the complex plane, originating from the single K-matrix pole, $g^2/(m^2 - s)$, present in Eq. (6.13). In contrast to this expectation, two poles are observed. Furthermore, both are rather close to the physical region. The correspondence between the K-matrix poles and the complex poles can be established by varying the coupling g. In the limit $g \to 0$ the complex poles should approach the real axis at the position of the corresponding K-matrix poles. We find that the deep pole approaches the real axis at $s = m^2 = (1\,223\,\mathrm{MeV})^2$ (see Table 6.1 with the fit results), while the left pole goes to $s = 0$. Due to these observations, we identify the deep pole with $a_1(1260)$-pole label, *i.e.* corresponding to a resonance, and the left pole with a "spurious"-pole, *i.e.*, an artifact from our parametrization in Eq. (6.13). This exercise also helps us to understand the origin of the spurious pole: it is the $1/s$ singularity in ρ_{QTB} (see Eq. (6.19)). Clearly, this pole is an integral part of the model. In Sec. 6.4.2 we consider variations of the model attempting to get rid of the spurious pole. We show that its effect on the real axis is indeed required by the data. It effectively parameterizes the unphysical sheet singularities, *e.g.* the left-hand cuts related to the cross channel exchanges between pions in the final state. For now, we conclude by extracting the positions of the $a_1(1260)$ resonance pole in the $\mathrm{QTB-DISP}$ model. We use the convention $s_p = (m_p + i\Gamma_p/2)^2$,

obtaining

$$\mathrm{QTB-DISP}: \qquad m_p^{(a_1(1260))} = (1\,166 \pm 6)\,\mathrm{MeV}, \quad \Gamma_p^{(a_1(1260))} = (798 \pm 26)\,\mathrm{MeV}. \quad (6.21)$$

For the error estimation we used the bootstrap technique [103, 202]: 1000 sets of pseudo data were generated using the original data and the covariance matrices, with the correlations taken into account in the Gaussian approximation. By refitting the pseudo datasets, we collect samples of the parameters, which we use to estimate their uncertainties. The distributions of the mass and width of the pole obtained from the bootstrap are Gaussian to a good approximation. The fit results and the calculated error ellipses are shown in Fig. 6.9. The mean values of the bootstrap sample for the pole positions differ from the real data fit results by $< 0.2\sigma$ which indicate a good consistency and negligible bias of the bootstrap method [202].

6.3.2 Analytic continuation of the $\mathrm{SYMM-DISP}$ model

The evaluation of the discontinuity given by Eq. (6.11a) for complex s is more complicated since the angular integrals cannot be solved completely.

$$\rho(s) = \frac{1}{2}\int \mathrm{d}\Phi_3 \left| f_\rho(\sigma_1)N_0(\Omega_1,\Omega_{23}) - f_\rho(\sigma_3)N_0(\Omega_3,\Omega_{12}) \right|^2, \qquad (6.22)$$

where the convenient form of the differential three-body phase space is Eq. (B.5). We expand the squared expression in Eq. (6.22), use the normalization property, and combine the squared terms,

$$\rho_{\mathrm{SYMM}}(s) = \underbrace{\frac{1}{2\pi(8\pi)^2 s}\int |f_\rho(\sigma_1)|^2 \frac{\sqrt{\lambda_1 \lambda_{s1}}}{\sigma_1}\,\mathrm{d}\sigma_1}_{\rho_{\mathrm{QTB}}(s)} - \underbrace{\int \mathrm{d}\Phi_3 f_\rho(\sigma_1)f_\rho^*(\sigma_3)\,N_0(\Omega_1,\Omega_{23})N_0^*(\Omega_3,\Omega_{12})}_{\rho_{\mathrm{INT}}(s)},$$
$$(6.23)$$

where we used the observation that the last integral is real. Indeed, the term transforms to itself under complex conjugation due to the $1 \leftrightarrow 3$ symmetry of the differential phase space and the relation $N_0(\Omega_k,\Omega_{ij}) = -N_0(\Omega_k,\Omega_{ji})$ following from Eq. (C.28) in Appendix C.2, precisely Eq. (C.28) for $l=1$, which needs to be applied for both terms $N_0(\Omega_3,\Omega_{12})$ and $N_0(\Omega_1,\Omega_{23})$.

The interference term can be further simplified by integrating over three angular variables using Eq. (C.32) The expression for ρ_{INT} is simplified as follows:

$$\rho_{\mathrm{INT}}(s) = \frac{1}{(8\pi)^2 s}\int \frac{\mathrm{d}\sigma_1}{2\pi}\frac{\mathrm{d}\cos\theta_{23}}{2}f_\rho^*(\sigma_3)f_\rho(\sigma_1)\frac{\sqrt{\lambda_1\lambda_{s1}}}{\sigma_1}\sum_{\lambda,\lambda'}d_{\lambda 0}^1(\theta_{23})d_{\lambda\lambda'}^1(\hat\theta_3)d_{\lambda' 0}^1(\theta_{12}). \quad (6.24)$$

All angles expressed through the invariants are listed in Eq. (C.33). We combined the d-functions in Eq. (6.24) and get the expressions for the angular part through invariant variables [203]:

$$\sum_{\lambda,\lambda'}d_{\lambda 0}^1(\theta_{23})d_{\lambda\lambda'}^1(\hat\theta_3)d_{\lambda' 0}^1(\theta_{12}) = \cos(\theta_{12}+\hat\theta_3-\theta_{23}) = \frac{H(\sqrt{s},\sqrt{\sigma_1},\sqrt{\sigma_3})}{\lambda_1^{1/2}\lambda_3^{1/2}\lambda_{s1}\lambda_{s3}}, \qquad (6.25)$$

where $H(\sqrt{s},\sqrt{\sigma_1},\sqrt{\sigma_3})$ is a polynomial in $\sqrt{\sigma_1}$, $\sqrt{\sigma_3}$, and $\sqrt{s}$. The expression $H(\sqrt{s},\sqrt{\sigma_1},\sqrt{\sigma_3})$

is further factorized [204] and cancels terms zeros of the denominator which otherwise would be pole singularities in the physical reason.

$$
\begin{aligned}
H(s, \sigma_1, \sigma_3) =& \sqrt{\sigma_1 \sigma_3} \\
& \times (\sqrt{s} - \sqrt{\sigma_1} - m_\pi)(\sqrt{s} - \sqrt{\sigma_1} + m_\pi) \\
& \times (\sqrt{s} - \sqrt{\sigma_3} - m_\pi)(\sqrt{s} - \sqrt{\sigma_3} + m_\pi) \\
& \times W(\sqrt{s}, \sqrt{\sigma_1}, \sqrt{\sigma_3}),
\end{aligned}
\tag{6.26}
$$

with the polynomial $W(\sqrt{s}, \sqrt{\sigma_1}, \sqrt{\sigma_3})$ given by

$$
\begin{aligned}
W(a, b, c) =& - 4m_\pi^6 + 4m_\pi^2 s^2 - 4m_\pi^4 ab + 4m_\pi^2 a^3 b - 4m_\pi^4 ac \\
& + 4m_\pi^2 a^3 c - 9m_\pi^4 bc + 8m_\pi^2 a^2 bc + a^4 bc \\
& + 14m_\pi^2 ab^2 c + 2a^3 b^2 c + 9m_\pi^2 b^3 c - a^2 b^3 c \\
& - 4ab^4 c - 2b^5 c + 14m_\pi^2 abc^2 + 2a^3 bc^2 + 12m_\pi^2 b^2 c^2 \\
& - 6ab^3 c^2 - 4b^4 c^2 + 9m_\pi^2 bc^3 - a^2 bc^3 - 6ab^2 c^3 - 5b^3 c^3 \\
& - 4abc^4 - 4b^2 c^4 - 2bc^5.
\end{aligned}
\tag{6.27}
$$

The final expression for the interference term is

$$
\begin{aligned}
\rho_{\text{INT}}(s) =& \frac{1}{2\pi(8\pi)^2 s} \int_{4m_\pi^2}^{\sigma_{\text{lim}}} d\sigma_1 \int_{\sigma_3^-(\sigma_1, s)}^{\sigma_3^+(\sigma_1, s)} d\sigma_3 \frac{f_\rho^*(\sigma_1)}{\sqrt{\sigma_1 - 4m_\pi^2}} \frac{f_\rho(\sigma_3)}{\sqrt{\sigma_3 - 4m_\pi^2}} \\
& \times \frac{W(\sqrt{s}, \sqrt{\sigma_1}, \sqrt{\sigma_3})}{((\sqrt{s} + \sqrt{\sigma_1})^2 - m_\pi^2)((\sqrt{s} + \sqrt{\sigma_3})^2 - m_\pi^2)}.
\end{aligned}
\tag{6.28}
$$

Our next step is to make Eq. (6.28) analytic. It can be made as simple as substituting $f_\rho \to f_\rho^{(I)}$ and $f_\rho^* \to f_\rho^{(II)}$, however, the is one of the most complicated parts of the continuation as we explain on the following page.

$$
\begin{aligned}
\rho_{\text{INT}}(s) =& \frac{1}{2\pi(8\pi)^2 s} \int_{4m_\pi^2}^{\sigma_{\text{lim}}} d\sigma_1 \int_{\sigma_3^-(\sigma_1, s)}^{\sigma_3^+(\sigma_1, s)} d\sigma_3 \frac{f_\rho^{(II)}(\sigma_1)}{\sqrt{\sigma_1 - 4m_\pi^2}} \frac{f_\rho^{(I)}(\sigma_3)}{\sqrt{\sigma_3 - 4m_\pi^2}} \\
& \times \frac{W(\sqrt{s}, \sqrt{\sigma_1}, \sqrt{\sigma_3})}{((\sqrt{s} + \sqrt{\sigma_1})^2 - m_\pi^2)((\sqrt{s} + \sqrt{\sigma_3})^2 - m_\pi^2)}.
\end{aligned}
\tag{6.29}
$$

The function $W(a, b, c)$ is a multivariable polynomial defined in Eq. (6.27). Omitting constant factors, the function $f_\rho(\sigma)$ is given by

$$
f_\rho(\sigma) \propto \frac{\sqrt{F(\sigma)}}{m_\rho^2 - \sigma - im_\rho \Gamma(\sigma)}, \quad \Gamma(\sigma) \propto \frac{i\sqrt{4m_\pi^2 - \sigma}}{\sqrt{\sigma}} F(\sigma), \quad F(\sigma) \propto \frac{\sigma - 4m_\pi^2}{\sigma - 4m_\pi^2 + 4/R^2}.
\tag{6.30}
$$

A right-hand cut is introduced by $i\sqrt{4m_\pi^2 - \sigma}$. In addition, there are two branch points: one at
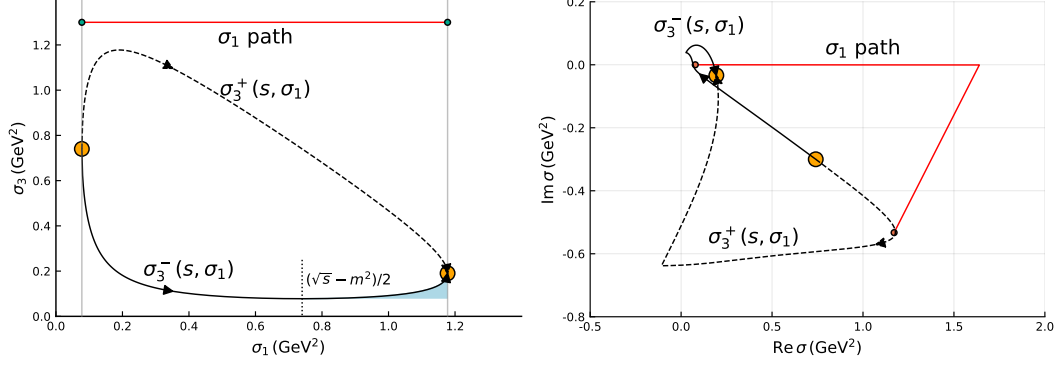
Figure 6.6: Integration paths in the complex σ-plane: while σ_1 is moving along the path $\sigma_{\text{th}} \to \sigma_{\text{lim}}$, the integration endpoints $\sigma_3^+(s,\sigma_1)(\sigma_3^-(s,\sigma_1))$ are traveling in the complex plane along the lines shown by black solid (dashed) curve The left plot shows the integration ranges of σ_1 and σ_3 for a real value of $s = 1.5\,\text{GeV}^2$. The red line is the straight integration path in σ_1. The yellow circles indicate the border of the integration domain when the integration endpoints in σ_3 coincide. In the right plot, the same lines are shown in the complex σ plane combined for σ_1 and σ_3 when $s = (1.5 - 0.6\text{i})\,\text{GeV}^2$. The points $4m_\pi^2$ and $(\sqrt{s} - m_\pi)^2$ are shown by the small orange dots. While σ_1 moves along the contour $C^{(\text{hook})}$ indicated by the red line, the integration limits $\sigma_3^\pm$ follow the dashed and the solid lines analogously to the left plot. The shaded area indicates the additional contribution to the phase-space integral discussed in Eq. (6.33).

$\sigma = 0$ from the phase space in the width $\Gamma(\sigma)$, and another one at $\sigma = 4m_\pi^2 - 4/R^2$ due to the Blatt-Weisskopf factor in the numerator. The break-up momentum singularity $\sqrt{\sigma - 4m_\pi^2}$ in the numerator of $f(\sigma)$ is canceled by the same factor which arises from the angular function (see Eq. (6.29)). The parametrization of $f_\rho(s)$ in Eq. (6.30) contains 5 poles, as one can count by the order of the polynomial which would give zeros of the denominator. They correspond to the ρ-meson poles at $(m_\rho \pm i\Gamma_\rho/2)^2$, and three spurious poles lying far away from the physical region as shown in Fig. 6.4. The integration endpoints of the σ_3 variable, $\sigma_3^\pm(\sigma_1, s)$, describe the border of the Dalitz plot for fixed value of s (Fig. 6.6, left panel),

$$\sigma_3^\pm(\sigma_1, s) = \frac{s + 3m_\pi^2 - \sigma_1}{2} \pm \frac{\sqrt{\lambda_1 \lambda_{s1}}}{2\sigma_1}. \qquad (6.31)$$

As soon as s becomes complex the endpoints depart from the real axis and move into the complex plane. The trajectories of the $\sigma_3^\pm$ as functions of σ_1 moving from $4m_\pi^2$ to $(\sqrt{s} - m_\pi)^2$ are non-trivial. As shown in Fig. 6.6, while σ_1 moves along the $C^{(\text{hook})}$ path (see Eq. (6.20c)), the σ_3^- circles around the branch point $4m_\pi^2$. When σ_3 crosses the unitarity cut, the sheet, on which it is evaluated, must be changed. However, if the σ_1 path goes exactly through the point $(s - m_\pi^2)/2$, σ_3^- just touches the branch point $4m_\pi^2$, (indeed, $\sigma_3^-((s - m_\pi^2)/2, s) = 4m_\pi^2$). In that case we are allowed to stay on the same sheet. Therefore, there are two ways to calculate ρ_{INT} for a complex argument (see Appendix E.1 for more details):

1. $\rho_{\text{INT}}^{(1)}$: We choose a special path in σ_1,

$$C_\sigma^{(\text{spec})}: \quad \sigma_{\text{th}} \to (s - m_\pi^2)/2 \to \sigma_{\text{lim}}, \qquad (6.32)$$
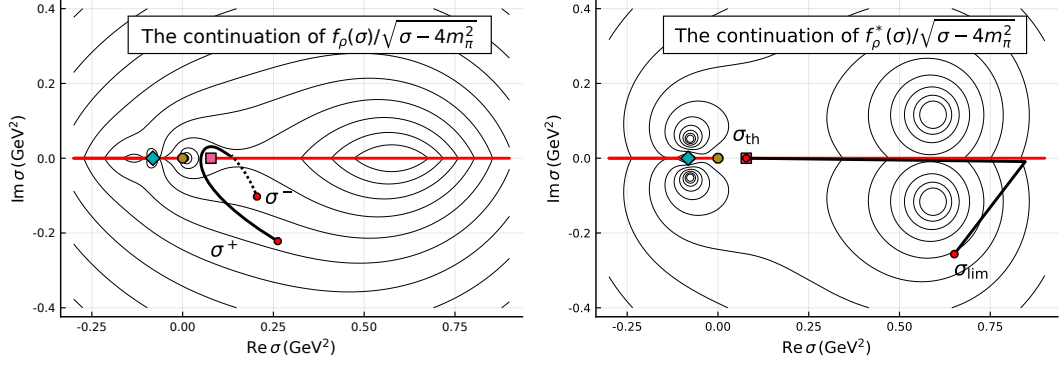
Figure 6.7: The complex sheets of the isobar amplitude $f_\rho(\sigma)$ and $f_\rho^*(\sigma)$. The left plot shows the analytic continuation of the function $f_\rho(\sigma)$ above and below the real axis. The function for positive imaginary part is the same as $f_\rho^{(I)}(\sigma)$; it is continuously connected to $f_\rho^{(II)}(\sigma)$ plotted for the negative imaginary part of σ. The right plot shows the analytic continuation of $f_\rho^*(\sigma)$, where the sheets are inverted. The lines are $|f_\rho(\sigma)|$ equipotential surfaces. The circular spots are the poles (see also red crosses in the left plot of Fig. 6.4). The markers on the real axis are the branch points of the left-hand cuts: the square marker shows the branch point from the break-up momentum located at $\sigma = 4m_\pi^2$, the diamond marker the $\sigma = 0$ branch point, the circular marker indicates the branch point related to the Blatt-Weisskopf factors in the numerator of the $f_\rho(\sigma)$ in Eq. (6.30).

the $\sigma_3^\pm$ always stay on the same sheet and can be connected with a straight (undistorted) path.

2. $\rho_{\text{INT}}^{(2)}$: We let σ_3^- circle around the branch point, changing sheets of $f(\sigma_3)$ appropriately. When $\sigma_1 = \sigma_{\text{th}}$, the integration limits $\sigma_3^\pm$ coincide. For certain values of σ_1, σ_3^- changes the sheet and, therefore, when σ_1 is in its upper limit σ_{lim}, the positions of $\sigma_3^\pm$ coincide, but they are on the different sheets. The integration path must be detoured around the branch point as shown in Fig. 6.7.

The first option provides a unique continuation of Eq. (6.28), however, the integration contour is bound to pass through $(s - m_\pi^2)/2$ which is non-analytic point of the integrand (see Appendix E.1). The integrand in the second option stays analytic on the integration contour, but in the limit of real s, the function $\rho_{\text{INT}}^{(2)}$ deviates from the original expression in Eq. (6.28). For $s = \text{Re}\, s + i\epsilon$, we change the sheet of σ_3^- when $\sigma_1 > (s - m_\pi^2)/2$, in contrast to the first option. The mismatch is calculated by integrating the discontinuity across the σ_3 unitarity cut over the shaded area of Fig. 6.6.

$$\rho_{\text{INT}}^{(1)}(s + i\epsilon) - \rho_{\text{INT}}^{(2)}(s + i\epsilon) = \int_{(s-m_\pi^2)/2}^{(\sqrt{s}-m_\pi)^2} d\sigma_1 \int_{\sigma_3^-(\sigma_1,s)}^{\sigma_{\text{th}}} d\sigma_3 \frac{\left[f_\rho^{(I)}(\sigma_3 + i\epsilon) - f_\rho^{(I)}(\sigma_3 - i\epsilon) \right]}{\sqrt{\sigma_3 - 4m_\pi^2}}$$

(6.33)

$$\times \frac{f_\rho^{(II)}(\sigma_1)}{\sqrt{\sigma_1 - 4m_\pi^2}} \frac{W(\sqrt{s}, \sqrt{\sigma_1}, \sqrt{\sigma_3})}{((\sqrt{s} + \sqrt{\sigma_1})^2 - m_\pi^2)((\sqrt{s} + \sqrt{\sigma_3})^2 - m_\pi^2)}.$$

The difference is practically negligible as shown in Fig. 6.2. The impact on the fit parameters and the values of the amplitude in the complex plane is a few orders of magnitude smaller than the statistical uncertainties. For the following discussion we use $\rho_{\text{INT}}^{(2)}(s)$ for the reason that the $\rho\pi$-cut can be rotated
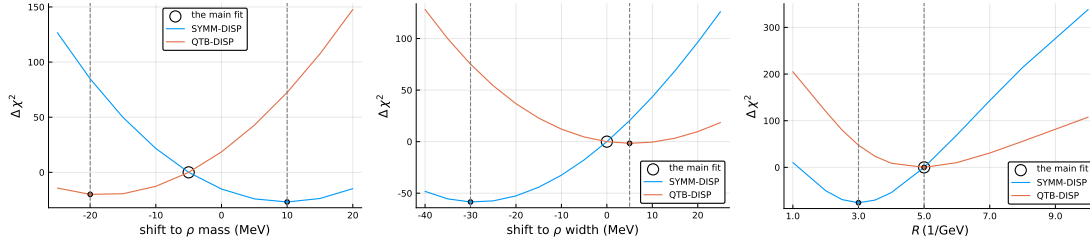
Figure 6.8: The change of the χ^2 is plotted against the ρ-meson parameters in Eq. (6.9): the mass m_ρ, the width Γ_ρ and the Blatt-Weisskopf size parameter R. The vertical lines indicate the estimated values where the minimum is found.

in the same way as before by using $C^{(\text{hook})}$ path in σ_1. Interestingly, an analogous problem appears in relation to the Khuri-Treiman equations (see Appendix in Ref. [194], Sec. IV in Ref. [162]). Ref. [205] gives arguments in favor of the first option.

As soon as the discontinuity is known for the whole complex plane, the amplitude on the unphysical sheet can be computed according to Eq. (6.17). The contour plot on the right panel of Fig. 6.5 presents the closest unphysical sheet of the amplitude, which is smoothly connected to the real axis. We find two poles and identify them as the $a_1(1260)$ resonance pole and the left "spurious" pole as shown in Fig. 6.5. for the same reasoning as in Sec. 6.3.1. The pole parameters are

$$\text{SYMM}-\text{DISP}: \quad m_p^{(a_1(1260))} = (1\,209 \pm 4)\,\text{MeV}, \quad \Gamma_p^{(a_1(1260))} = (576 \pm 11)\,\text{MeV}. \quad (6.34)$$

The statistical errors are obtained from a bootstrap analysis as described above in Sec. 6.3.1. The combined results are presented in Fig. 6.9.

6.4 Systematic uncertainties

6.4.1 Scan over the fixed parameters

The description of three-particle resonances is a difficult problem because of the complicated structure of final-state interactions, which induces an interplay between different decay channels. The latter manifests itself in the modification of the isobar line shape and the presence of interference terms. The importance of three-body effects is readily seen in the difference of $\text{SYMM}-\text{DISP}$ and $\text{QTB}-\text{DISP}$ pole positions, *cf.* Eqs. (6.34) and (6.21). Knowing that the interference between two $\rho\pi$ decay channels must be present, we now focus on systematic studies of $\text{SYMM}-\text{DISP}$, keeping $\text{QTB}-\text{DISP}$ for a mere comparison. The largest systematic uncertainty is the dependence of the $a_1(1260)$ pole position on the line shape of the subchannel resonance ρ. In principle, we know that final-state interactions shift and skew the ρ peak. The scale of the ρ-meson mass shift can be estimated from the studies of ω/ϕ decays using Khuri-Treiman equations [165, 166]. Fig. 3 of Ref. [165] suggests a shift of the real and imaginary parts of the isobar amplitude of the order of $10\,\text{MeV}$ before and after final-state interactions are taken into account. To estimate the effect on the $a_1(1260)$ pole position, we vary the parameters of $f_\rho(\sigma)$ in Eq. (6.9), *i.e.* the mass m_ρ, the width Γ_ρ and the Blatt-Weisskopf radius R, performing a χ^2 scan over each parameter, while keeping the others at their nominal values (Fig. 6.8). The new pole position obtained for the parameter value which minimizes

Table 6.2: The values m, g and χ^2 for fits described in Sec. 6.4. For scans over parameters m_ρ, R and Γ_p we present the values of m, g and χ^2 obtained in the minimum in the profile χ^2 plots shown in Fig. 6.8.

| | | QTB $-$ DISP | | | SYMM $-$ DISP | | |
#	Fit studies	m, GeV	g, GeV	χ^2/n.d.f.	m, GeV	g, GeV	χ^2/n.d.f.
1	$s < 2\,\mathrm{GeV}^2$	1.232	7.6	53/62	1.200	6.57	81/62
2	$R' = 3\,\mathrm{GeV}^{-1}$				1.211	7.00	18/100
3	$m'_\rho = m_\rho + 10\,\mathrm{MeV}$				1.207	6.85	83/100
4	$m'_\rho = m_\rho - 10\,\mathrm{MeV}$	1.204	7.23	37/100			
5	$m'_\rho = m_\rho - 20\,\mathrm{MeV}$	1.217	7.01	30/100			
6	$\Gamma'_\rho = \Gamma_\rho + 5\,\mathrm{MeV}$	1.223	7.45	66/100			
7	$\Gamma'_\rho = \Gamma_\rho - 30\,\mathrm{MeV}$				1.205	6.79	36/100

the χ^2 for each scan is then used to estimate the systematic error for the pole position of the main fit. The results of these studies are summarized in Table 6.2 (see fit studies #2-7, were #4 was introduced as an additional intermediate point outside of the minimum). The $a_1(1260)$ pole position is extracted, the results for the pole mass and width are represented in Fig. 6.9 by open ellipses.

We perform an additional test of the influence of heavier resonances, as the $a_1(1640)$, by excluding the region $s > 2\,\mathrm{GeV}^2$ from the fit. The fit quality does not change substantially, but get slightly worse due to the reduction of the degrees of freedom (see #1 in Table 6.2). The values for the pole position are shown in Fig. 6.9 and included to the systematic error of our final result.
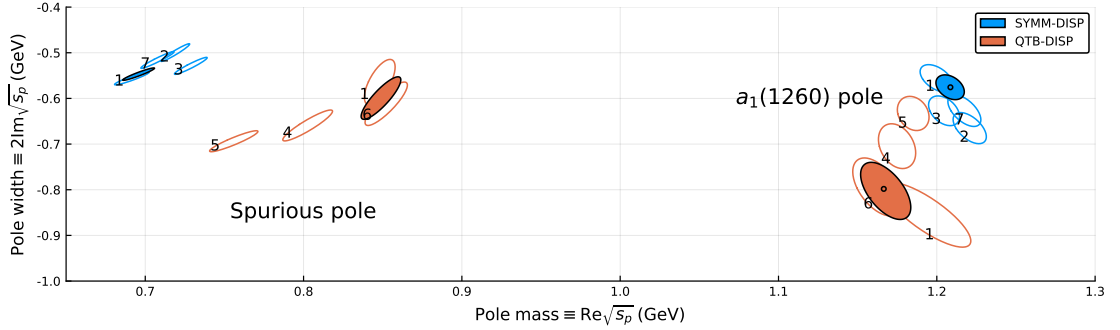

Figure 6.9: Extracted pole positions in the models QTB $-$ DISP and SYMM $-$ DISP: the resonance poles are on the right, the spurious poles are on the left. The ellipses show the 2σ contours of the statistical uncertainties obtained by the bootstrap method. The results of the systematic tests are shown by the open ellipses. The numerical labels correspond to the indices of the systematic tests described in Table 6.2.

The final systematic uncertainties are found by assigning the maximal deviation of the pole position in the systematic studies to the main fit SYMM $-$ DISP:

$$m_p^{(a_1(1260))} = (1209 \pm 4^{+12}_{-9})\,\mathrm{MeV}, \quad \Gamma_p^{(a_1(1260))} = (576 \pm 11^{+89}_{-20})\,\mathrm{MeV}.$$

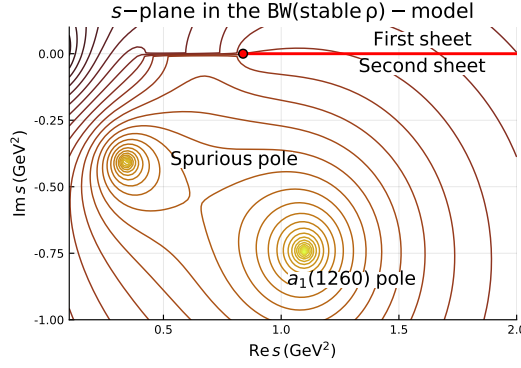where the first uncertainty is statistical and the second systematic.

Figure 6.10: Analytic continuation of the amplitude $1/D_{\mathrm{BW}}(s)$ from Eq. (6.35). Lines indicate the $|D_{\mathrm{BW}}|$ equipotential levels. The poles of the amplitude are the bright spots. The red dots indicate branch points for channel openings.

6.4.2 Studies of the spurious pole

Performing the analytical continuation in Sec. 6.3 we have shown that, in addition to the expected $a_1(1260)$ pole, there is a spurious pole rather close to the physical region. At first, the spurious pole looks surprising, however, it is clearly present in every Breit-Wigner-like model of a resonance decaying to particles of different masses. Indeed, the denominator of the Breit-Wigner amplitude with energy-dependent width decaying to two scalar particles in an S-wave reads:

$$D_{\mathrm{BW}}(s) = m^2 - s - im\Gamma(s), \quad \Gamma(s) = \frac{g^2}{16\pi m}\frac{\sqrt{(s-(m_1+m_2)^2)(s-(m_1-m_2)^2)}}{s}. \quad (6.35)$$

When $m_1 \neq m_2$, the equation $D_{\mathrm{BW}}(s) = 0$ has 4 complex roots, which we can identify by the order of the polynomial which gives those roots:

$$\left(16\pi s(m^2 - s)\right)^2 + g^4\left(s - (m_1+m_2)^2\right)\left(s - (m_1-m_2)^2\right) = 0 \quad (6.36)$$

Since all coefficients of the polynomial are real, the poles appear in conjugated pairs above and below the real axis. The two Breit-Wigner poles below the real axis are analogous to the $a_1(1260)$ and the spurious pole. To demonstrate this further, we draw the complex plane of the $1/D_{\mathrm{BW}}(s)$ function with $m = 1.2\,\mathrm{GeV}$, $g = 7.8\,\mathrm{GeV}$, $m_1 = m_\rho$, $m_1 = m_\pi$ in Fig. 6.10. We find that the spurious pole has no influence on the physical region as long as the resonance is far from threshold and rather narrow. Both poles become important for the real axis physics when the studied resonance is close to threshold or/and wider.

The spurious pole is a feature of Breit-Wigner-like models. It is generated by the $1/s$ singularity of the phase space in Eq. (6.35), and Eq. (6.19). In order to remove it, we try to exclude the $1/s$ factor from the dispersive term. Following the studies of $\mathrm{QTB-DISP}$, we consider a new model for scattering and production amplitudes $\hat{t}(s) = t(s)/s$ and $\hat{a}(s) = a(s)/s$, and modify the unitarity

Table 6.3: An extension of Table 6.1 with the additional models considered within the systematic studies. We added the last column to present additional parameters which enter in the models.

Model	$\rho(s)$ in Numer.	$C(s)$ in Denom.	χ^2/n.d.f.	m, MeV	g, GeV	h, m'^2 GeV^2
sQTB$-$DISP$^{(2)}$	$\rho_{\text{QTB}}(s)$	$\tilde{\rho}_{\text{QTB}}(s)$	979/100	1.915	17.94	$-$
sQTB$-$DISP$^{(3)}$	$\rho_{\text{QTB}}(s)$	$\tilde{\rho}_{\text{QTB}}(s)$	67/100	1.075	9.27	0.578
sQTB$-$DISP$^{(4)}$	$\rho_{\text{QTB}}(s)$	$\tilde{\rho}_{\text{QTB}}(s)$	42/100	1.229	6.01	$-39.3, 0.0$

equations accordingly.

$$2\,\text{Im}\,\hat{t}(s) = \hat{t}^*(s)\,(s\rho_{\text{QTB}}(s))\,\hat{t}(s), \tag{6.37a}$$

$$2\,\text{Im}\,\hat{a}(s) = \hat{t}^*(s)\,(s\rho_{\text{QTB}}(s))\,\hat{a}(s), \tag{6.37b}$$

where $s\rho(s)$ is free of the $1/s$ singularity. The parametrization which satisfies the unitarity constraints is

$$\hat{a}^{\text{sQTB}-\text{DISP}^{(k)}}(s) = \frac{c'}{K_k^{-1}(s) - is\tilde{\rho}_{\text{QTB}}(s)/2}, \tag{6.38}$$

where the index k gives the number of parameters in the function $K_k^{-1}(s)$, the models are labeled sQTB$-$DISP$^{(k)}$. The function $s\rho(s)$ has a $\sim s^1$ asymptotic behavior, therefore the dispersive integral must be subtracted twice. The integrand is thus the same as in Eq. (6.14), but the integral is multiplied by an extra factor of s as in Eq. (6.38). To make the dispersive integral independent of the subtraction points we must consider a polynomial of order $k \geq 2$. We consider three forms of functions $K_k(s)$,

$$K_2(s) = g^2/(m^2 - s), \tag{6.39}$$

$$K_3(s) = g^2/(s(m^2 - s) + h) \tag{6.40}$$

$$K_4(s) = g^2/(m^2 - s) + h'/(m'^2 - s) \tag{6.41}$$

The $K_2(s)$ and $K_4(s)$ are inspired by the K-matrix approach with one and two poles, respectively, while $K_3(s)$ is a special two-pole model which exactly coincides with QTB$-$DISP when $h = 0$.

In Fig. 6.11 we show the continuation of the sQTB$-$DISP$^{(2)}$ model, fitted to data. The spurious pole is no longer present. However, the quality of the fit is not acceptable: the best χ^2/n.d.f. is equal to 979/100. When we increase the freedom by taking the model sQTB$-$DISP$^{(3)}$ the fit quality significantly improves to yield a χ^2/n.d.f. $= 67/100$. Quite spectacularly, the picture of the complex plane is changed back: the place of the spurious pole is taken by the explicit pole introduced in the K-function (see the right plot of Fig. 6.11). The next relaxation of the setup in sQTB$-$DISP$^{(4)}$ overfits the data and gives χ^2/n.d.f. $= 42/100$. However, the positions of the resonance and spurious poles do not change much.

The position of the spurious pole was investigated for all systematic studies we performed in Sec. 6.4 as shown in Fig. 6.9.
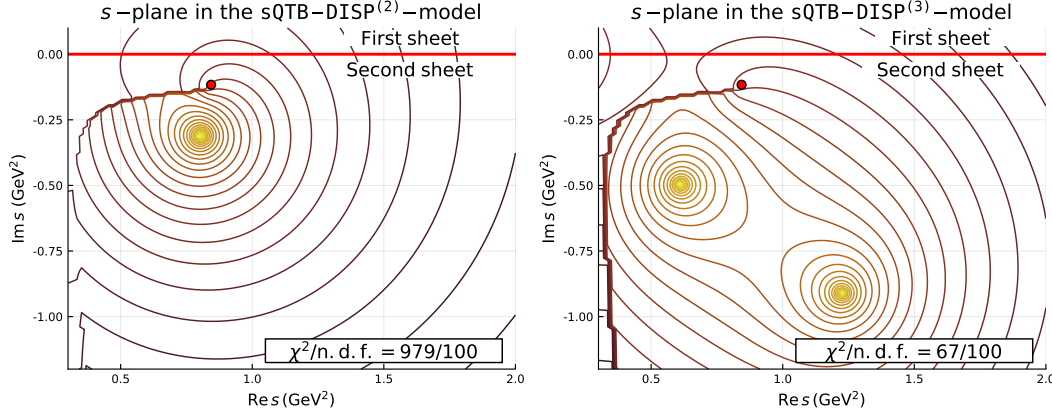
Figure 6.11: Analytic continuation of $t(s)$ in the model $\mathrm{sQTB-DISP}^{(k)}$. Lines indicate equipotential levels for the $|\hat{t}^{\mathrm{sQTB-DISP}^{(k)}}(s)|$ function from Eq. (6.38). The poles of the amplitude are the yellow spots. The red dots indicate branch points for channel openings: 3π-branch point and $\rho\pi$-branch point. The complex plane for the model $\mathrm{sQTB-DISP}^{(2)}$ (the models model $\mathrm{sQTB-DISP}^{(3)}$) fitted to the data is shown in the left (right) plot. The quality of the fit is indicated in the legend box on the right.

6.5 Conclusions

We have performed a new analysis of the lightest iso-vector axial-vector resonance $a_1(1260)$ decaying to three charged pions. Despite the fact that the corresponding $J^{PC} = 1^{++}$ partial wave dominates the hadronic weak decay of τ leptons as well as diffractive reactions of high-energy pions, the parameters of the $a_1(1260)$ are still poorly known. While the latter reactions suffer from an irreducible background due to non-resonant processes, the system of three pions produced in τ decay provides a very clean access to axial-vector resonances. Compared to a two-particle system, however, the system of three interacting particles exhibits additional phenomena, such as 3-particle rescattering or interference between different decay chains. These 3-body effects are taken into account using reaction models constraining the dynamics in the total invariant mass, however, without imposing subchannel unitarity. We have considered four analytic models of an isolated resonance decaying to three pions via the $\rho\pi$ channel. All these models satisfied approximate three-body unitary, but differ by the left-hand singularities and the treatment of the interference between the two $\rho\pi$ decay channels. Using the $\tau^- \to \pi^- \pi^+ \pi^- \nu_\tau$ data from ALEPH [199], we found that the dispersive models, having no left-hand singularities on the physical sheet, fit the data clearly better.

In order to find the pole position corresponding to the $a_1(1260)$ resonance, we have explored the analytic structure of the amplitude and performed its analytic continuation into the complex plane of the three-pion invariant mass squared, a challenging, and technically demanding task, requiring us to use a prescription for the integration paths in the two-pion invariant mass squared. We have searched for the singularities in the closest unphysical sheet, and have identified a pole as the $a_1(1260)$ resonance. The mass and width of the $a_1(1260)$ are given in terms of its pole position in the main $\mathrm{SYMM-DISP}$ model:

$$m_p^{(a_1(1260))} = (1209 \pm 4^{+12}_{-9})\,\mathrm{MeV}, \quad \Gamma_p^{(a_1(1260))} = (576 \pm 11^{+89}_{-20})\,\mathrm{MeV}.$$

The dominant source of systematic errors is the sensitivity to the details of the subchannel interactions. The simplified $QTB-DISP$ model, which neglects the interference between the two $\rho\pi$-channels, results in a significantly different pole position and a larger systematic uncertainty.

This analysis can be extended by further advancing the theoretical framework and constraining the model by fitting the Dalitz decay variables. This will be possible when the data from BelleII or BESIII become available. In addition, the results from this analysis will help to better constrain the non-resonant background in diffractive reactions, as measured by the COMPASS experiment.

Unified picture: theoretical framework [1]

The goal of this chapter is to construct a model for $3 \to 3$ scattering, which satisfies unitarity and analyticity and enables to separate the long-range interactions from the short-range QCD dynamics. While the former contain one particle exchange (OPE) processes germane to the three-particle system, the latter govern resonance formation that is the main interest of our studies. Unitarity in three-particle scattering has been extensively studied in the past in Ref. [38, 195, 196, 206–212] and here, in particular, we closely follow Ref. [195] in deriving three-body unitarity equations. In Ref. [195, 196] discontinuity relations for isobar-spectator partial waves were derived in all relevant variables and the N/D equations (see Ref. [213]) were formulated in a narrow resonance approximation for the underlying $2 \to 2$ amplitudes. Schematically, in the N/D approach the N function is determined by components of the partial-wave amplitude, that are unconstrained by unitarity in the studied scattering channel, often referred to as the driving terms. The D function is then constructed from N such that the full amplitude satisfies unitarity. In contrast, in our approach, we obtain a solution to the unitarity constraint without the need for solving the complicated N/D equations. Instead, for the long-range part one can solve a linear integral equation of the type of Blankenbecler and Sugar [214] developed in the context of the three-body problem in Ref. [150, 215–218]. We present a new method to incorporate the short-range part where the driving term is dressed by initial and final-state interaction via exchange processes. A complementary approach known as the Khuri-Treiman equations is developed, see Ref. [148, 149, 162–164, 194, 197, 219–221]. The model exploits the two-body unitarity condition to the system of three particles. The studies with Khuri-Treiman equations aimed to constrain the final-state interactions and rescattering effects on a Dalitz plot, however, could not address the overall three-body dynamics. In this work, we extend the investigation of Aitchison and Pasquier (Ref. [162, 194]) of a link between Khuri-Treiman equations and three-body unitarity and turn the former to a useful tool to dress three-body resonances.

7.1 Building a general unitary model

In order to simplify the ensuing discussion, the presentation is restricted to the case of three identical, scalar particles with unit mass for which interaction is only significant in the S-wave. The scattering

---

[1] A part of this chapter has been published in Ref. [5] in the collaboration with Y. Wunderlich and the JPAC group

matrix element M is defined as the expectation value of the transition operator T,

$$\langle p'_1 p'_2 p'_3 | T | p_1 p_2 p_3 \rangle = (2\pi)^4 \delta^4 (P - P') M(\kappa), \tag{7.1}$$

where the initial (final) particle momenta are denoted by p_i (p'_i), $i = 1, 2, 3$, and the total momentum is denoted P (P'). In general, the $3 \to 3$ amplitude depends on 8 kinematic variables, indicated by κ.

Details of the state definition and normalization are given in Appendix C.1. It is shown that the state of three identical particles can be written as,

$$|p_1 p_2 p_3 \rangle = \frac{1}{3} \sum_a |a\rangle, \tag{7.2}$$

where $|a\rangle$ is a three particle state, symmetric under permutation of momenta p_{a_2} and p_{a_3}, with $(a, a_2, a_3) \in \{(123), (231), (312)\}$. A subsystem of particles with these momenta is called *subchannel*. The partial-wave expansion for the state $|a\rangle$ is done in two steps: First, the state is expanded in variables of the subchannel, *i.e.* in the rest frame of $p_{a_2} p_{a_3}$, using the helicity basis (see Eq. (C.11)). Second, the partial-wave expansion is performed in the center-of-mass frame for the quasi-two-body system of the particle pair, and the remaining bachelor particle (see Eq. (C.17)).

Using the connectedness principle of S-matrix theory (*e.g.* see Ref. [38]), we split the interaction operator T into the (fully) *connected* interaction T_c and the (partially) *disconnected* interaction T_d: $T = T_c + 3T_d$, where the index 3 indicates three possible ways to choose the bachelor particle. For the connected diagrams there are 9 configurations. The scattering matrix element reads,

$$M = \frac{1}{3} \sum_{a,b} \left[(2\pi)^3 \delta^3 (p'_b - p_a) (8\pi) t(\sigma_a) + \frac{1}{3} T(\sigma'_a, s, \sigma_b) \right], \tag{7.3}$$

where s is the total invariant mass squared of the system $s = (p_1 + p_2 + p_3)^2$, the variable σ_a denotes the subchannel invariant mass squared $\sigma_a = (p_{a_2} + p_{a_3})^2$, with $(a, a_2, a_3) \in \{(123), (231), (312)\}$, the primed variables refer to the final-state invariant masses.

$$\langle b' | T_d | a \rangle = (2\pi)^4 \delta^4 (P' - P) \delta^3 (p'_b - p_a) (8\pi) t(\sigma_b), \tag{7.4}$$

$$\langle b' | T_c | a \rangle = (2\pi)^4 \delta^4 (P' - P) T(\sigma'_b, s, \sigma_a), \tag{7.5}$$

The disconnected piece is a part of the interaction where only two particles interact while the remaining third particle propagates through. A decomposition (7.3) falls under the name of *the general isobar model*, where with *isobar* is referred to the subchannel interaction in a specific partial wave. Assuming S-wave interaction in every channel the model is significantly simplified, however, we notice the partial-wave series of the complete amplitude M contains an infinite number of terms. In the S-wave approximation the total number of variables (see κ in Eq. (7.1)) the amplitude depends on is reduced to five: the total invariant mass of the system and two pairs of subchannel invariant masses squared, for the initial and the final state.

7.1.1 Unitarity relation

The unitarity condition for the interaction operator reads $T - T^\dagger = iT^\dagger T$. It translates to a constraint for the scattering amplitudes $T(\sigma', s, \sigma)$ and $t(\sigma)$ by calculating expectation values of the left-hand and right-hand side of the operator relation between three-particle states. To transform the right-hand part of the unitary equation we insert a resolution of the identity from Eq. (C.9) between the operators $T^\dagger$ and T.

$$\langle b|\, T - T^\dagger\, |a\rangle = \frac{i}{3}\int (\tilde{\mathrm{d}}p'')\, \langle b|\, T^\dagger\, |1''\rangle\, \langle 1''|\, T\, |a\rangle + \frac{2i}{3}\int (\tilde{\mathrm{d}}p'')\, \langle b|\, T^\dagger\, |2''\rangle\, \langle 3''|\, T\, |a\rangle. \quad (7.6)$$

Using the connectedness argument, the equation above is decomposed further. The left-hand side is seen to be separable very easily in an additive way, since it is only linear in T (as well as $T^\dagger$). Due to the product $T^\dagger T$, the right-hand side leads to different topologies [150] of the types "disconnected-disconnected", "disconnected-connected" and "connected-connected" (as well as their respective hermitian conjugates). A part of the "disconnected-disconnected" terms contain the spectator delta function and can be matched with the disconnected terms on the left-hand side. The remaining terms match the difference expression for the connected amplitude.

$$\langle b|\, T_{\mathrm{d}} - T_{\mathrm{d}}^\dagger\, |a\rangle = i\int (\tilde{\mathrm{d}}p'')\, \langle b|\, T_{\mathrm{d}}^\dagger\, |1''\rangle\, \langle 1''|\, T_{\mathrm{d}}\, |a\rangle, \quad (7.7)$$

$$\begin{aligned}
\langle b|\, T_{\mathrm{c}} - T_{\mathrm{c}}^\dagger\, |a\rangle = i\int (\tilde{\mathrm{d}}p'')\big[&\frac{1}{3}\, \langle b|\, T_{\mathrm{c}}^\dagger\, |1''\rangle\, \langle 1''|\, T_{\mathrm{c}}\, |a\rangle + \frac{2}{3}\, \langle b|\, T_{\mathrm{c}}^\dagger\, |2''\rangle\, \langle 3''|\, T_{\mathrm{c}}\, |a\rangle \quad (7.8)\\
&+ \langle b|\, T_{\mathrm{d}}^\dagger\, |1''\rangle\, \langle 1''|\, T_{\mathrm{c}}\, |a\rangle + 2\, \langle b|\, T_{\mathrm{d}}^\dagger\, |2''\rangle\, \langle 3''|\, T_{\mathrm{c}}\, |a\rangle\\
&+ \langle b|\, T_{\mathrm{c}}^\dagger\, |1''\rangle\, \langle 1''|\, T_{\mathrm{d}}\, |a\rangle + 2\, \langle b|\, T_{\mathrm{c}}^\dagger\, |2''\rangle\, \langle 3''|\, T_{\mathrm{d}}\, |a\rangle\\
&+ 6\, \langle b|\, T_{\mathrm{d}}^\dagger\, |2''\rangle\, \langle 3''|\, T_{\mathrm{d}}\, |a\rangle\,\big]
\end{aligned}$$

The disconnected constraint, Eq. (7.7), leads to the standard two-body unitarity equation.

$$t(\sigma) - t^\dagger(\sigma) = i\, t^\dagger(\sigma)\rho(\sigma)t(\sigma)\, \theta(\sigma - 4). \qquad\qquad (7.9)$$

where $\rho(\sigma)$ denotes the normalized two-body phase space $\rho(\sigma) = \sqrt{1 - 4/\sigma}$. The amplitude $t^\dagger(\sigma) \equiv t^*(\sigma)$ is defined as an expectation value of the operator $T^\dagger$ between S-wave projected two-particle states.

The three-body unitarity equation in the partial-wave projected form reads:

$$T(\sigma', s, \sigma) - T^\dagger(\sigma', s, \sigma) = \tag{7.10}$$

$$\frac{i}{3} \int_4^{(\sqrt{s}-1)^2} \frac{\mathrm{d}\sigma''}{2\pi} T^\dagger(\sigma', s, \sigma'') \rho(\sigma'') \rho_s(\sigma'') T(\sigma'', s, \sigma)$$

$$+ \frac{2i}{3} \iint_{\phi(\sigma_2'', \sigma_3'', s) > 0} \frac{\mathrm{d}\sigma_2'' \mathrm{d}\sigma_3''}{2\pi s} T^\dagger(\sigma', s, \sigma_2'') T(\sigma_3'', s, \sigma)$$

$$+ i\, t^\dagger(\sigma') \rho(\sigma') T(\sigma', s, \sigma)$$

$$+ 2i \frac{t^\dagger(\sigma')}{\lambda_s^{1/2}(\sigma')} \int_{\sigma^-(\sigma', s)}^{\sigma^+(\sigma', s)} \mathrm{d}\sigma_3' T(\sigma_3', s, \sigma)$$

$$+ i\, T^\dagger(\sigma', s, \sigma) \rho(\sigma) t(\sigma)$$

$$+ 2i \frac{t(\sigma)}{\lambda_s^{1/2}(\sigma)} \int_{\sigma^-(\sigma, s)}^{\sigma^+(\sigma, s)} \mathrm{d}\sigma_2 T^\dagger(\sigma', s, \sigma_2)$$

$$+ 6i \frac{2\pi s\, t^\dagger(\sigma') t(\sigma)}{\lambda_s^{1/2}(\sigma') \lambda_s^{1/2}(\sigma)} \theta(\phi(\sigma', \sigma, s)).$$

where the function $\rho_s(\sigma) = \lambda_s^{1/2}(\sigma)/s$ parametrizes the normalized three-body phase space, with $\lambda_s(\sigma) = \lambda(s, \sigma, 1)$ being the Källén function, and $T^\dagger(\sigma', s, \sigma) = T^*(\sigma, s, \sigma')$ due to hermitian propertied of T. [2] We notice that the unitarity equation (7.10) holds in the physical region, above the thresholds $\sigma, \sigma' > 4$ and $s > 9$. The term in the last line represent an exchange of real particle between the initial and the final system and, hence, contributes only in the decay region restricted by the condition $\phi(\sigma', \sigma, s) > 0$, where $\phi = \sigma\sigma'(3 + s - \sigma - \sigma') - (s - 1)^2$ is the Kibble function [222]. This function parametrizes the borders of the Dalitz plot in σ as functions of the variable σ' (in case s is fixed), or vice versa. The integration limits in Eq. (7.10) are the boundaries $\sigma^\pm(s, \sigma) = (s + 3 - \sigma)/2 \pm \lambda_s^{1/2}(\sigma)\lambda^{1/2}(\sigma)/(2\sigma)$, that are the solutions of the Kibble equation $\phi(\sigma^\pm, \sigma, s) = 0$.

To simplify equations we define an *amputated* amplitude $\mathcal{T}(\sigma', s, \sigma)$, for which the two-body interaction $t(\sigma)$ is removed from both sides.

$$T(\sigma', s, \sigma) = t(\sigma') \mathcal{T}(\sigma', s, \sigma) t(\sigma). \tag{7.11}$$

The terms on the left-hand side of Eq. (7.10) can be grouped as follows:

$$T(\sigma', s, \sigma) - T^\dagger(\sigma', s, \sigma) = \left[t(\sigma') - t^\dagger(\sigma') \right] \mathcal{T}(\sigma', s, \sigma) t(\sigma) + \tag{7.12}$$

$$+ t^\dagger(\sigma') \left[\mathcal{T}(\sigma', s, \sigma) - \mathcal{T}^\dagger(\sigma', s, \sigma) \right] t(\sigma) +$$

$$+ t^\dagger(\sigma') \mathcal{T}^\dagger(\sigma', s, \sigma) \left[t(\sigma) - t^\dagger(\sigma) \right].$$

---

[2] Under the time-reversal symmetry $\mathcal{T}^\dagger = \mathcal{T}^*$, however, as shown by Olive in Ref. [48], $T^\dagger$ can be consider as the opposite value of the analytic function $T^\dagger(\sigma', s, \sigma)$, then, the difference $T - T^\dagger$ gives the total discontinuity.

The discontinuities in the first and third line can be exactly matched to the third and the fifth terms of Eq. (7.10) due to the unitarity relation of $t(\sigma)$, *cf.* Eq. (7.9).

The three-body unitarity equation for the S-wave $\mathcal{T}(\sigma', s, \sigma)$ reads:

$$\mathcal{T}(\sigma', s, \sigma) - \mathcal{T}^\dagger(\sigma', s, \sigma) = \tag{7.13a}$$

$$2i \frac{1}{\lambda_s^{1/2}(\sigma')} \int_{\sigma^-(\sigma', s)}^{\sigma^+(\sigma', s)} \mathrm{d}\sigma_3' \, t(\sigma_3') \mathcal{T}(\sigma_3', s, \sigma) \tag{7.13b}$$

$$+ \frac{i}{3} \int_4^{(\sqrt{s}-1)^2} \frac{\mathrm{d}\sigma''}{2\pi} \mathcal{T}^\dagger(\sigma', s, \sigma'') \, t(\sigma'') t^\dagger(\sigma'') \, \rho(\sigma'') \rho_s(\sigma'') \, \mathcal{T}(\sigma'', s, \sigma) \tag{7.13c}$$

$$+ \frac{2i}{3} \iint_{\phi(\sigma_2'', \sigma_3'', s) > 0} \frac{\mathrm{d}\sigma_2'' \mathrm{d}\sigma_3''}{2\pi s} \mathcal{T}(\sigma', s, \sigma_2'') t(\sigma_2'') t(\sigma_3'') \mathcal{T}(\sigma_3'', s, \sigma) \tag{7.13d}$$

$$+ 2i \frac{1}{\lambda_s^{1/2}(\sigma)} \int_{\sigma^-(\sigma, s)}^{\sigma^+(\sigma, s)} \mathrm{d}\sigma_2 \, \mathcal{T}^\dagger(\sigma', s, \sigma_2) t^\dagger(\sigma_2) \tag{7.13e}$$

$$+ 6i \frac{2\pi s}{\lambda_s^{1/2}(\sigma') \lambda_s^{1/2}(\sigma)} \, \theta(\phi(\sigma', \sigma, s)). \tag{7.13f}$$

The three-body unitarity constraint is represented by a complicated integral equation. However, one can apply a very intuitive shorthand notation in order to rewrite such integral-constraints in a simpler form. In many cases, the underlying mathematical structure of the equations becomes more transparent, once they are written in this abbreviated form.

$$\mathcal{T} - \mathcal{T}^\dagger = \mathcal{D}\tau\mathcal{T} + \mathcal{T}^\dagger(\tau - \tau^\dagger)\mathcal{T} + \mathcal{T}^\dagger\tau^\dagger\mathcal{D}\tau\mathcal{T} + \mathcal{T}^\dagger\tau^\dagger\mathcal{D} + \mathcal{D}, \tag{7.14}$$

where we defined two additional functions, namely $\tau(\sigma) = t(\sigma)\rho_s(\sigma)/3$ and

$$\mathcal{D}(\sigma', s, \sigma) = 12\pi i \, s/(\lambda_s^{1/2}(\sigma')\lambda_s^{1/2}(\sigma)) \, \theta(\phi(\sigma', \sigma, s)). \tag{7.15}$$

The explicit indications of the variable dependencies of functions are suppressed in the shorthand notation. The rules for transitioning from the shorthand notation to full integral-expressions, and vice versa, are as follows. A multiplication by τ in the shorthand notation implies an integral over a energy variable shared by τ and all functions in the product. For instance, in case τ is pre-multiplied by an arbitrary function X and post-multiplied by an arbitrary function Y, the replacement rule becomes

$$X\tau Y \leftrightarrow \int_\alpha^{(\sqrt{s}-1)^2} \frac{\mathrm{d}\sigma}{2\pi} X(\ldots, s, \sigma)\rho_s(\sigma)t(\sigma)Y(\sigma, s, \ldots), \tag{7.16}$$

where the low limit of integral is not controlled by unitarity despite of a condition $\alpha < 4$. All integrals in (7.13) are truncated compared to Eq. (7.16). Such truncations are achieved by considering additional factors of $\mathcal{D}$, as well as the fact that the two-body unitarity constraint for τ (*cf.* Eq. (7.9)) also introduces a θ-function. Conventionally we fix $\alpha = -\infty$ for matching the forthcoming model of Sec. 7.2. Note that, according to Eq. (7.16), multiple factors of τ in a product are tantamount to multiple nested integrals. In the short form it is easy to notice that Eq. (7.14) matches unitarity equations derived in Ref. [150].

In an early work of G. Fleming [195], an expression similar to Eq. (7.13) was derived. The author

does not attempt to satisfy it as a whole but argues that it is allowed to split the total discontinuity into the left-hand side to discontinuities in the individual variables σ', s, σ and then match these discontinuities to terms on the right-hand side. The discontinuities in σ' and σ are matched to the terms (7.13b) and (7.13e), respectively. The rest is discussed with respect to the complex structure in the s-variable. The term (7.13f) arises from the u-channel pole singularity. However, the partial-wave projection to the total angular momentum induces a complex singularity surface, which depends on all three remaining variables σ', s, σ. Hence, a short-cut term (7.13f) contributes to the discontinuity in the subchannel variables, σ and σ'. Due to those general complications, we postpone the analytic continuation until Sec. 7.2 and for now confine ourselves to the relations (7.13) valid on the real axis.

Splitting interaction ranges

Our goal is now to solve the unitarity constraint in Eq. (7.13) or Eq. (7.14) for the S-wave $\mathcal{T}$ of the connected $3 \rightarrow 3$ amplitude. Although this constraint is represented by an involved integral equation which embodies complicated 3-body physics, we desire to obtain a solution which is straightforward and, in the end, simple. We found that a major step in this direction can be taken by decomposing the amplitude $\mathcal{T}(\sigma', s, \sigma)$ according to the following ansatz, which splits the *long-range* interactions, in the following described by what we call the *ladder* amplitude $\mathcal{L}$, as well as the *short-range* interactions implemented via the residual amplitude $\mathcal{R}$, additively:

$$\mathcal{T}(\sigma', s, \sigma) = \mathcal{L}(\sigma', s, \sigma) + \mathcal{R}(\sigma', s, \sigma). \tag{7.17}$$

In the remainder of this section, we will give meaning to the functions $\mathcal{L}$ and $\mathcal{R}$, one after the other. We show that, while the ladder $\mathcal{L}$, satisfies the three-body unitary equation by itself, the short-range part $\mathcal{R}$, requires the initial and the final-state interaction which is related to the $\mathcal{L}$.

7.1.2 The ladder amplitude

A straightforward and general model that satisfies three-body unitarity (Eq. (7.14)) was suggested in Ref. [150]. It was shown that an analytic function $\mathcal{L}$ written in the form of a integral equation, with kernel-function $\mathcal{B} \equiv \mathcal{B}\left(\sigma', s, \sigma\right)$,

$$\mathcal{L} = \mathcal{B} + \mathcal{B}\tau\mathcal{L}, \tag{7.18}$$

satisfies the unitary constraints (7.14), if the total discontinuity of the kernel $\mathcal{B}$ fulfills

$$\mathcal{B} - \mathcal{B}^\dagger = \mathcal{D}, \tag{7.19}$$

where the function $\mathcal{D}$ is defined in Eq. (7.15). The Eq. (7.18) was referred to as the Bethe-Salpeter ansatz in Ref. [150], however, we find it more appropriate to call it the Blankenbecler-Sugar ansatz [214]. We extend the validity of the proof given in Ref. [150] by demonstrating, in a series of steps that does not necessarily require operator inversions, that the relation follows from manipulations that are

essentially algebraic:

$$\mathcal{L} - \mathcal{L}^\dagger = \mathcal{L}^\dagger(\tau - \tau^\dagger)\mathcal{L} + (1 + \mathcal{L}^\dagger\tau^\dagger)\mathcal{L} - \mathcal{L}^\dagger(1 + \tau\mathcal{L}) \tag{7.20a}$$

$$= \mathcal{L}^\dagger(\tau - \tau^\dagger)\mathcal{L} + (1 + \mathcal{L}^\dagger\tau^\dagger)\mathcal{B}(1 + \tau\mathcal{L}) - (1 + \mathcal{L}^\dagger\tau^\dagger)\mathcal{B}^\dagger(1 + \tau\mathcal{L}) \tag{7.20b}$$

$$= \mathcal{L}^\dagger(\tau - \tau^\dagger)\mathcal{L} + (1 + \mathcal{L}^\dagger\tau^\dagger)\,\mathcal{D}\,(1 + \tau\mathcal{L}) \tag{7.20c}$$

$$= \mathcal{L}^\dagger(\tau - \tau^\dagger)\mathcal{L} + \mathcal{L}^\dagger\tau^\dagger\mathcal{D}\tau\mathcal{L} + \mathcal{D}\tau\mathcal{L} + \mathcal{L}^\dagger\tau^\dagger\mathcal{D} + \mathcal{D}. \tag{7.20d}$$

In the derivation, the first step imposed zero-additions using suitably defined terms. In the second step, we invoked the recursive definition of $\mathcal{L}$ (see Eq. (7.18)) and in the third step, we used our assumption on the total discontinuity of $\mathcal{B}$ (Eq. (7.19)).

Despite of the generality of the ansatz (7.18), we use this construction to incorporate only the long-range forces to our model. The amplitude $\mathcal{L}$ is defined entirely by the kernel function $\mathcal{B}$. In case $\mathcal{B}$ is given by an exchange process, the iterative definition (7.18) generates an infinite set of exchange diagrams which, from the shape of the diagrams that occur in the resummation, validates denoting $\mathcal{L}$ as a *ladder* amplitude.

One possible model for $\mathcal{B}$ that satisfies the condition $\mathcal{B} - \mathcal{B}^\dagger = \mathcal{D}$ is the one-particle-exchange suggested in Ref. [150]. In Ref. [14], advantages and problems of this particular choice are discussed. A very general and theoretically consistent class of unitary models emerges in case we only assume a priori that the 'ladder' amplitude is set and contains nothing but the long-range forces. For a more practical analysis method suggested later in this work, the ladder is generated by the Feynman triangle diagram as shown in Sec. 7.2. In this case, in addition to the one particle exchange diagram, $\mathcal{B}$ contains contributions from additional terms that generate a left-hand-side singularity.

7.1.3 Embodying the short-range physics

The *short-range* interaction contains all the resonance physics we are after and it is included via the amplitude $\mathcal{R}$ in our ansatz (7.17), as demonstrated in the following. Inserting the decomposition (7.17) into the unitarity equation (7.14) and canceling terms from the discontinuity of the ladder $\mathcal{L}$ (cf. eq. (7.20d)), we obtain the most general form of the unitarity constraint for $\mathcal{R}$, which in the shorthand notation reads

$$\mathcal{R} - \mathcal{R}^\dagger = \mathcal{R}^\dagger(\tau - \tau^\dagger)\mathcal{R} + \mathcal{R}^\dagger\tau^\dagger\mathcal{D}\tau\mathcal{R} \tag{7.21a}$$

$$+ \mathcal{D}\tau\mathcal{R} + \mathcal{L}^\dagger(\tau - \tau^\dagger)\mathcal{R} + \mathcal{L}^\dagger\tau^\dagger\mathcal{D}\tau\mathcal{R} \tag{7.21b}$$

$$+ \mathcal{R}^\dagger\tau^\dagger\mathcal{D} + \mathcal{R}^\dagger(\tau - \tau^\dagger)\mathcal{L} + \mathcal{R}^\dagger\tau^\dagger\mathcal{D}\tau\mathcal{L}. \tag{7.21c}$$

The structure of Eq. (7.21) is rather clear: the terms (7.21a) represent different intermediate states between $\mathcal{R}$, either with the matched isobar energies variable or with the recoupled ones. The terms (7.21b) and (7.21c) resemble the unitarity relation of the ladder $\mathcal{L}$, with the exchange interaction attached to $\mathcal{R}$ from the left- and the right-hand side. It motivates an introduction of the reduced amplitude $\hat{\mathcal{R}}$,

$$\mathcal{R} = (1 + \mathcal{L}\tau)\,\hat{\mathcal{R}}\,(\tau\mathcal{L} + 1). \tag{7.22}$$

Indeed, a successive attachment of the exchange processes can be achieved by introducing an integral over σ in the same way as it appears in the unitarity equation (7.13) (or a multiplication through τ in the algebraic shorthand notation). For instance, for the attachment of all exchange processes from the left, we can write: $\hat{\mathcal{R}} + \mathcal{B}\tau\hat{\mathcal{R}} + \mathcal{B}\tau\mathcal{B}\tau\hat{\mathcal{R}} + \cdots = (1 + \mathcal{L}\tau)\hat{\mathcal{R}}$. Using the three-body unitarity constraint for the ladder $\mathcal{L}$ (*cf.* Eq. (7.20d)), it is possible to demonstrate that

$$(1 + \mathcal{L}\tau)r - (1 + \mathcal{L}^\dagger\tau^\dagger)r = \left(\mathcal{D}\tau + \mathcal{L}^\dagger(\tau - \tau^\dagger) + \mathcal{L}^\dagger\tau^\dagger\mathcal{D}\tau\right)\left[(1 + \mathcal{L}\tau)r\right], \qquad (7.23)$$

which matches all terms in Eq. (7.21b). Thus, we see that by acting with $(1 + \mathcal{L}\tau)$ on $\hat{\mathcal{R}}$ from the left, we can reproduce all terms in the overall unitarity constraint in Eq.(7.21) for $\mathcal{R}$ that have $\mathcal{R}$ on the right. In exactly the same way, by applying the operator $(1 + \mathcal{L}\tau)$ or $(\mathcal{L}\tau + 1)$ to $\hat{\mathcal{R}}$ from the right, we can obtain all the terms in Eq. (7.21c), *i.e.* all terms with $\mathcal{R}$ on the left. The function $\hat{\mathcal{R}}(\sigma', s, \sigma)$ is denoted as the *resonance kernel*. A straightforward algebraic derivation, combining Eq. (7.21) with the decomposition (7.22), leads to the condition for $\hat{\mathcal{R}}$:

$$\hat{\mathcal{R}} - \hat{\mathcal{R}}^\dagger = \hat{\mathcal{R}}^\dagger(1 + \tau^\dagger\mathcal{L}^\dagger)\left[\tau - \tau^\dagger + \tau^\dagger\mathcal{D}\tau\right](1 + \mathcal{L}\tau)\hat{\mathcal{R}} \qquad (7.24)$$

$$= \hat{\mathcal{R}}^\dagger\left[\tau - \tau^\dagger + \tau\mathcal{L}\tau - \tau^\dagger\mathcal{L}^\dagger\tau^\dagger\right]\hat{\mathcal{R}}. \qquad (7.25)$$

This equation looks significantly much simpler than Eq. (7.14). It resembles a form of the two-body unitary equation: the expressions in the square bracket is nothing but the integration over the phase space of the two isobar-bachelor systems which are wither connected directly (isobar-to-isobar: $\tau - \tau^\dagger$) as shown in the diagram in Eq. (7.13c) ot crossed (isobar-to-bachelor: $\tau^\dagger\mathcal{D}$) as shown in Eq. (7.13d).

The Eq. (7.24) and Eq. (7.25) are the first important result of this chapter: a valid unitary amplitude that includes the long-range interaction can be extended by a function $\mathcal{R}$ in the form of Eq. (7.22) with the exchange processes dress amplitude $\hat{\mathcal{R}}$. Then, the unitarity requirement for $\hat{\mathcal{R}}$ can be written either as in Eq. (7.24), or as in Eq. (7.25). We notice that Eq. (7.25) admits a recursive solution for $\hat{\mathcal{R}}$, which reads $\hat{\mathcal{R}} = \mathcal{X} + \mathcal{X}(\tau + \tau\mathcal{L}\tau)\hat{\mathcal{R}}$, where $\mathcal{X}(\sigma', s, \sigma)$ does not have the right-hand-side cut and plays the role of a K-matrix used for $2 \to 2$ scattering. The latter resembles equations independently derived in Ref. [223] for purposes of lattice calculations on the $3 \to 3$ problem. We consider the separation of the long- and the short-range interaction as a convenient trick that allows us to simplify equations and emphasis the resonance physics. However, we would also like to stress that a separation between the ranges is not entirely necessary in a sense that one could obtain an equivalent model by including the kernel $\mathcal{X}$ into $\mathcal{B}$ as proposed in Ref. [14].

Despite of simplicity of Eq. (7.25) in what follows we demonstrate advantages of the form (7.24) and show how it gives benefits and a new angle of view to the problem.

7.2 Factorization of final-state interaction

The class of unitary models outlined in section 7.1, while being general, is difficult to implement for practical purposes. It still misses an important connection with the methods and tools of amplitude analysis we have mastered with two-body reactions. In this section we fill the gap by considering a plausible model for the long-range interaction inspired by the Khuri-Treiman approach. We also show that as soon as the resonance kernel $\hat{\mathcal{R}}$ factorizes in variables σ', s, and σ, the long-range interaction

can be taken into account by modifying the line shape of subchannel amplitudes following the Khuri-Treiman prescription, and the explicit calculation of the ladder amplitude, $\mathcal{L}$, becomes unnecessary. The three-body unitarity constraint given in Eq. (7.24) is obtaining an algebraic (multiplicative) form.

The the $3 \to 3$ scattering process cannot be observed experimentally. However, it is often the case that the system of three particles is produced in $2 \to 3$ scattering [224] or as a part of a $2 \to 4$ process [78]. On the other hand, the Dalitz plot analysis is a common task nowadays, due to an abundance of data on the three-particle states observed in the decay of narrow heavy meson states. For those reactions, the total invariant mass is fixed and the main dynamics accessible in the studies are given by the formation of subchannel resonances and the final-state interactions. Due to the non-perturbative character of the interaction, an approach based on unitarity and analyticity via dispersion relations becomes the main tool for theoretical studies. The Khuri-Treiman model was introduced in Sec. 4.5. We explore it further following the earlier studies by Aitchison and Pasquier [162, 194]. We demonstrate that a particular model for the ladder amplitude is generated implicitly by the form of the equations. Hence, we clearly identify the $(1 + \mathcal{L}\tau)$ operator with the final-state interaction via long-range exchanges that built the ladder $\mathcal{L}$.

7.2.1 A ladder from Khuri-Treiman equations

We consider a general production reaction, where the 3π-state is produced from some $|\text{source}\rangle$ state. The T-matrix element for the production is defined and approximated in the isobar model as

$$\langle 3\pi | \, T \, | \text{source} \rangle = (2\pi)^4 \delta^4(P - P') \, F(s, \sigma_1, \sigma_2, \sigma_3) \tag{7.26}$$

$$= (2\pi)^4 \delta^4(P - P') \sum_{i=1}^{3} \mathcal{F}(s, \sigma_i) t(\sigma_i), \tag{7.27}$$

where we follow the same level of simplification as before, *i.e.* the discussion is restricted to a system of three identical particles with unit masses. In Eq. (7.27), we write the decay amplitude F as a sum of a truncated partial-wave series which is stopped after the S-wave in all these subchannels, and introduce the amputated amplitude $\mathcal{F}(s, \sigma_i)$. The s-dependence of the amplitude $\mathcal{F}(s, \sigma_i)$ is not controlled in the formalism, instead, it is used as a tuning parameter: the reaction is considered in the scattering domain for a small value of s, the established relations are then used in the $1 \to 3$ decay domain by means of an analytic continuation [194].

We follow the same derivation of the Khuri-Treiman equations as in Sec. 4.5, however, the equations are much simpler due to our assumptions. Two-body unitarity for a given subchannel with invariant mass squared σ_i contains the *partial-wave projection* of the amplitude $F(s, \sigma_1, \sigma_2, \sigma_3)$, which involves a direct term $\mathcal{F}(\sigma_i) t(\sigma_i)$, as well as the partial-wave projections of the crossed channels, *i.e.* terms of the same structure as Eq. (7.13b). Using dispersive integrals, one builds a relation between a partial-wave amplitude $\mathcal{F}(\sigma_i)$ and the cross-channel projections (for the case in hand the cross-channel projections in Eq. (4.22) are equal to each other).

$$\mathcal{F}(s_+, \sigma) = \mathcal{C}(s, \sigma) + \frac{1}{\pi} \int_4^\infty \frac{\mathrm{d}\sigma'}{(\sigma' - \sigma)} \frac{1}{\lambda_{s_+}^{1/2}(\sigma')} \int_{\sigma^-(\sigma', s_+)}^{\sigma^+(\sigma', s_+)} \mathrm{d}\sigma'' \, t(\sigma'') \mathcal{F}(s, \sigma''), \tag{7.28}$$

where $\mathcal{C}(\sigma)$ is an entire function of σ. This might have a polynomial σ-dependence, which is not

controlled by the formalism. It is important to note that since the dispersive integral in σ' goes beyond the physical domain $4 < \sigma' < (\sqrt{s} - 1)^2$, the integration-limits $\sigma^{\pm}(\sigma', s)$ require an $i\epsilon$-prescription for the determination of their positions in the complex σ''-plane. As was shown by Bronzan and Kacser in Ref. [149], the determination using $s_+ \equiv s + i\epsilon$ leads to a perfect match between the first iteration of Eq. (7.28) and calculations performed in perturbation theory, *i.e.* the triangle loop diagram from Eq. (4.4). Eq. (7.28) can be solved for a every specific source term (subtraction coefficient) $C = k(\sigma)$ by multiple iterations [165–167, 169] or the numerical inversion suggested in Ref. [171] resulting in a function $\mathcal{F}(s, \sigma) = \mathcal{K}(s, \sigma)$. Importantly, the s-dependence of the solution $\mathcal{K}(s, \sigma)$ in case of the s-independent source $k(\sigma)$ entirely appears due to the specific form of Eq. (7.28). This s-dependence is not surprising since by iterating Eq. (7.28) one attaches further exchange processes.

For further analysis Eq. (7.28) is recast in the form of a so-called single variable representation (SVR). It is obtained once the order of the integrals over σ' and σ'' is swapped. One method for this transformation was suggested by I. Aitchison and R. Pasquier in Ref. [194] (we call it *Aitchison inversion*); an alternative technique was developed in Ref. [162] by R. Pasquier and J. Pasquier (*Pasquier inversion*). [3] In Appendix E.2 we clarify how the Pasquier inversion can be applied to Eq. (7.28). It results in the following equation.

$$\mathcal{F}(s, \sigma) = \mathcal{C}(s, \sigma) + \int_{-\infty}^{(\sqrt{s}-1)^2} \frac{\mathrm{d}\sigma''}{2\pi} \, \mathcal{B}_0(\sigma, s, \sigma'') \tau(\sigma'') \mathcal{F}(s, \sigma''). \tag{7.29}$$

Here $\tau(\sigma) = t(\sigma)\rho_s(\sigma)/3$, the function $\mathcal{B}_0(\sigma, s, \sigma'')$ is the Pasquier-kernel, which can be written as a complex integral along a complex contour (C') (see details of the contour in the Appendix E.2 in Fig. E.6).

$$\mathcal{B}_0(\sigma, s, \sigma'') = 6 \left[\theta(\sigma'') \int_{\sigma^-(\sigma''_+, s)}^{\sigma^-(\sigma''_{++}, s)} (C') - \theta(-\sigma'') \int_{\sigma^-(\sigma''_{++}, s)}^{\infty} (C') \right] \frac{\mathrm{d}\sigma'}{(\sigma' - \sigma)} \frac{1}{\lambda_{s_+}^{1/2}(\sigma')}, \tag{7.30}$$

where the function $\sigma^-(\sigma'', s)$ is given in Eq. (E.6), the values σ''_+ and σ''_{++} are the values slightly shifted to the complex plane as shown in Fig E.6. The heaviside θ-functions separate two ranges of the σ'' integral in Eq. (7.29): $0 < \sigma'' < (\sqrt{s} - 1)^2$ and $\sigma'' < 0$.

The integral (7.30) and its analytic structure are rather involved, but they have been discussed in detail in the references [162, 164, 194, 219, 226]. It was shown that $\mathcal{B}_0$ can be written as a sum of the S-wave projection of the one particle exchange diagram, *i.e.* $\mathcal{E} = \int \mathrm{d}z/(m_\pi^2 - u(s, \sigma, \sigma', z))$, where $u(s, \sigma, \sigma', z) = 1 + \sigma' - (s + 1 - \sigma)(s + \sigma' - 1)/(2s) + \lambda_s^{1/2}(\sigma)\lambda_s^{1/2}(\sigma') z/(2s)$, and an extra term $\mathcal{E}_{23}$ (referred to as $\Delta_{23}(\sigma, s, \sigma'')$ in the literature). Using the analytic form of $\mathcal{B}_0$ it can be shown that the extra terms do not contribute to the s-discontinuity such that the condition $\mathcal{B}_0 - \mathcal{B}_0^{\dagger}$ holds (this non-trivial fact requires the further studies and rigorous proof).

For our application, it is important that the kernel $\mathcal{B}_0$ satisfies the requirement (7.19) and, hence, it

---

[3] We also found useful a recent work of Peng Guo [225] where the Pasquier inversion is discussed in details.

generates a valid ladder amplitude for the $3 \to 3$ interaction. The iteration of Eq. (7.29) leads to

$$\mathcal{F}(\sigma', s) = \mathcal{C}(s, \sigma') + \int_{-\infty}^{(\sqrt{s}-1)^2} \frac{d\sigma''}{2\pi} \mathcal{L}_0(\sigma', s, \sigma'') \tau(\sigma'') \mathcal{C}(s, \sigma'') \quad \leftrightarrow \quad \mathcal{F} = (1 + \mathcal{L}_0 \tau)\mathcal{C},$$

(7.31)

where $\mathcal{L}_0(\sigma', s, \sigma)$ is defined by the integral equation $\mathcal{L}_0 = \mathcal{B}_0 + \mathcal{L}_0 \tau \mathcal{B}_0$ (written in the shorthand notation). The validity of $\mathcal{L}_0$ as a $3 \to 3$ model was extensively discussed in Ref. [162, 194]. A known problem of the kernel $\mathcal{B}_0 = \mathcal{E} + \mathcal{E}_{23}$ pointed out in Ref. [162] [4] is the time reversal symmetry of the generated ladder diagram. Looking at the definition of $\mathcal{B}_0$ in Eq. (7.30), one can suspect that $\mathcal{B}_0$ is not symmetric on permutation of σ and σ'. It was shown that the time-reversal symmetry is explicitly broken by the presence of $\mathcal{E}_{23}(\sigma', s, \sigma)$ term [219]. The scale of the violation is however unclear and should be addressed in numerical studies.

We see that our ansatz for the resonance part of the model in Eq. (7.22) appears in a new light. One realizes that the operator $(1 + \mathcal{L}\tau)$ attached to both sides of the resonance kernel $\hat{\mathcal{R}}$ indeed indicates a necessity for the initial- and the final-state rescattering, in a similar way as it is performed in the KT formalism.

7.2.2 The resonance kernel factorization

So far we have explored the two-body unitarity constraint to the production amplitude $\mathcal{F}$ which was a rather artificial construction obtained by the means of analytic continuation. Now, we can derive the three-body unitary constrains to the amplitude $\mathcal{F}$. Following the derivation of Eq. (7.6) we get:

$$\langle b| T - T^\dagger |\text{source}\rangle = \frac{i}{3} \int (\tilde{d}p'') \langle b| T^\dagger |1''\rangle \langle 1''| T |\text{source}\rangle$$
$$+ \frac{2i}{3} \int (\tilde{d}p'') \langle b| T^\dagger |2''\rangle \langle 3''| T |\text{source}\rangle .. \quad (7.32)$$

The derivation proceeds in a similar way as before, however, one realizes that the disconnected $3 \to 3$ scattering amplitude appears only on the right-hand side of the three-body unitarity equations.

$$\mathcal{F} - \mathcal{F}^\dagger = \mathcal{D}\tau\mathcal{F} + \mathcal{T}^\dagger(\tau - \tau^\dagger)\mathcal{F} + \mathcal{T}^\dagger\tau^\dagger\mathcal{D}\tau\mathcal{F},$$

(7.33)

where $\mathcal{F}^\dagger(s, \sigma)$ can be either related to the conjugated amplitude $\mathcal{F}^*$ when time-reversal symmetry holds, or related to the opposite border of analyticity function $\mathcal{F}(s, \sigma)$ [48]. The first term of Eq. 7.33 is associated with the σ-discontinuity of the function $\mathcal{F}(s, \sigma)$, leading to the Khuri-Treiman model as well as the decomposition $\mathcal{F} = (1 + \mathcal{L}_0 \tau)\mathcal{C}$, where the has s-dependence $\mathcal{C}(s, \sigma)$ is not constrained by the Khuri-Treiman equations, but rather by the three-body unitarity equations. We transform Eq. 7.32 using the decomposition (7.17) for the amplitude $\mathcal{T}$ with a given model for the ladder, $\mathcal{L}_0$, and $\mathcal{R} = (1 + \mathcal{L}_0 \tau)\hat{\mathcal{R}}(\tau\mathcal{L}_0 + 1)$. It results to:

$$\mathcal{C} - \mathcal{C}^\dagger = \hat{\mathcal{R}}^\dagger(1 + \tau^\dagger\mathcal{L}_0^\dagger) \left[\tau - \tau^\dagger + \tau^\dagger\mathcal{D}\tau\right] (1 + \mathcal{L}_0 \tau)\mathcal{C}.$$

(7.34)

---

[4] Ref. [227, 228] are also supposed be very valuable for the question, however, Ref. [227] could not be found by the Orsay Library, Ref. [228] is in French.

Although the equation is still complicated, we recognize the same construction as in Eq. (7.24). The final and the most powerful assumption we make is factorization of the functions $\hat{\mathcal{R}}$ and $\mathcal{C}$ in the variables s, σ, and σ'.

$$\hat{\mathcal{R}}(\sigma', s, \sigma) = k(\sigma')\mathfrak{R}(s)k(\sigma), \tag{7.35}$$

$$\mathcal{C}(s, \sigma) = \mathfrak{F}(s)k(\sigma). \tag{7.36}$$

where $k(\sigma)$ is an entire function of σ. [5] The factorization assumption seems to be a very natural given the fact that the resuduals are factorized in the resonance pole in general [39]. To proceed, we use $\mathcal{K}(\sigma, s)$ for a solution of the Khuri-Treiman equation (7.29) (or Eq. (7.28)) with a given source term $k(\sigma')$, *i.e.* $\mathcal{K}(\sigma, s) = k(1 + \tau\mathcal{L}_0)$. We arrive to fairly simple algebraic unitarity equations for the factorized kernels followed from Eq. (7.24) and Eq. (7.34).

$$\mathfrak{R}(s) - \mathfrak{R}^\dagger(s) = i\,\mathfrak{R}^\dagger(s)\Sigma(s)\,\mathfrak{R}(s), \tag{7.37}$$

$$\mathfrak{F}(s) - \mathfrak{F}^\dagger(s) = i\,\mathfrak{R}^\dagger(s)\Sigma(s)\mathfrak{F}(s), \tag{7.38}$$

where $\Sigma(s)$ is a dressed isobar-bachelor loop (the *self-energy function*) that includes the series of rescattering processes between three particles

$$\Sigma(s) = \mathcal{K}^\dagger(\tau - \tau^\dagger)\mathcal{K} + \mathcal{K}\tau^\dagger\mathcal{D}\tau\mathcal{K}. \tag{7.39}$$

The structure of the unitarity equation (7.37) is formally the same as that of the two-body unitarity constraint (7.9). The two-body phase-space factor is replaced by the function Σ, which averages rescattering contributions over the three-body phase space. The analogy with two-body unitary goes further: when the two-body interaction amplitude $t(\sigma)$ is dominated by an isolated narrow resonance, the effect of the final-state interaction, which is included via attaching the ladder in the form $(1 + \mathcal{L}\tau)$, becomes negligible. In this case, $\mathcal{K}(\sigma, s)$ is approximately equal to $t(\sigma)$. The second term in Eq. (7.39), which reflects the strength of the overlap of resonances in different crossed channels, vanishes, while the first term yields simply the two-body phase space $\rho_s(m_R^2)$, where m_R is a mass of the narrow resonance. If we only neglect the second term we arrive at the *quasi-two-body* approximation proposed in Ref. [141].

As an example, we can construct a model for an isolated three-body resonance, for instance $a_1(1260)$ observed in the system of 3π with $J^{PC} = 1^{++}$, which is fully consistent with three-body unitarity requirements as follows. Since the function $\Sigma(s)$ calculated along the real axis gives the imaginary part of the loop diagram that includes the cross-channel exchanges, the real part can be recovered

---

[5] It is important to mention usage of the same function $k(\sigma)$ for both $\hat{\mathcal{R}}$ and $\mathcal{C}$ a convenient simplification, however, it is not generally required. Perhaps, the most convenient practical approach is to expand of the functions $\mathcal{C}(s, \sigma)$ and $\hat{\mathcal{R}}(\sigma', s, \sigma)$ in polynomials in σ keeping the expansion coefficients functions of s.

$$\hat{\mathcal{R}}(\sigma', s, \sigma) = \mathfrak{R}_{00}(s) + \sigma'\mathfrak{R}_{10}(s) + \mathfrak{R}_{01}(s)\sigma + \sigma'\mathfrak{R}_{11}(s)\sigma + \dots,$$

$$\mathcal{C}(s, \sigma) = \mathfrak{F}_0(s) + \mathfrak{F}_1(s)\sigma + \dots.$$

In this case, one obtains a system of coupled equations.

using a dispersive integral:

$$\mathfrak{R}(s) = \frac{g^2}{m^2 - s - ig^2 \tilde{\Sigma}(s)/4}, \quad \tilde{\Sigma}(s) = \frac{s}{2\pi i} \int_9^\infty \frac{\Sigma(s')}{s'(s' - s)} \mathrm{d}s'. \tag{7.40}$$

It further extends the model used in Sec. (6) and includes the rescattering corrections consistently with the three-body unitarity. Although the model excludes explicit t-channel exchange processes, as we suppose, the effect of the latter can be incorporated effectively via left-hand-side singularities of the function $\mathfrak{R}(s)$, analogously to the common techniques used in analyses of two-body reactions. The reader observes that the explicit expression of $\mathcal{L}$ does not enter. Instead, the effect of the final-state interactions is absorbed into the function $\mathcal{K}(s, \sigma)$, which can be investigated separately, *e.g.* by solving the Khuri-Treiman equations.

7.3 Conclusions

We have outlined a general class of unitary models for the analysis of $3 \to 3$ processes based on a specific approach for the separation of the descriptions of long- and short-range forces. At first, the long-range interactions were introduced in terms of the ladder amplitude $\mathcal{L}$, which is a solution of an integral equation and iterates the kernel function $\mathcal{B}$ to all orders. The function $\mathcal{B}$ has been only restricted by the condition $\mathcal{B} - \mathcal{B}^\dagger = \mathcal{D}$, which is well satisfied by a one-particle exchange process, $\mathcal{E}$. It was shown that the ladder amplitude, $\mathcal{L}$ satisfies the three-particle unitarity constraint by itself.

The ladder amplitude has been extended additively by an a priori unknown function $\mathcal{R}$, which is used to parametrize the remaining short-range interactions. Unitarity implies a particular constraint on the total discontinuity of $\mathcal{R}$. We have shown how the unitarity constraint can be respected by a general ansatz for $\mathcal{R}$ introducing the resonance kernel $\hat{\mathcal{R}}$, dressed by initial- and final-state interaction operators constructed from $\mathcal{L}$. This dressing provides all relevant normal threshold singularities in the two-body subenergy variables.

The general class of unitary models, while being fully consistent, have been simplified further in order to be suitable for practical analyses. For this purpose, we introduced two further ideas. First of all, it has been pointed out how the known Khuri-Treiman formalism gives a specific model for the long-range kernel $\mathcal{B}_0$. Secondly, we have demonstrated how a factorization ansatz for the resonance kernel $\hat{\mathcal{R}}$, leads to a simplification of the three-body unitarity equations. We have obtained an algebraic equation in the for similar to the two-body unitary equation. The long-range interaction and the induced final-state rescattering have got packed into the dressed isobar-bachelor loop function (self-energy function). One of the main strengths of the final model is its analytic properties. Due to the usage of the dispersive Khuri-Treiman approach, the amplitude only contains the unitarity cuts the subchannel invariant mass squared. The analytic structure in the total invariant mass s is not effected by the subchannel variables σ, it can be set using dispersive methods. The three-body unitarity condition have been reduced to the form of the two-body unitary constraint therefore all common technique discussed in Sec. 2.1 and Sec. 2.3 become applicable.

Our model is a proposal suitable for studies of the three-particle resonances. Using the relation of the scattering amplitude and the production amplitude, the model can be applied to more complicated hadronic reactions, as for example the process $\pi^- p \to \pi^- \pi^+ \pi^- p$ discussed in Sec 3, or in hadronic tau decays, $\tau \to 3\pi\, \nu_\tau$ discussed in Sec. 6.

We have established an asymptotic limit of the formalism in the quasi-two-body unitarity approach [141] explored in Appendix (A.2) (final-state interaction is negligible), or, simply, the two-body unitarity [39, 47] (the subchannel interaction contains infinitely narrow resonance).

We have illustrated the basic ideas in the rather artificial context of a restriction to S-waves only. Thus, in the next step, the formalism should be extended for an arbitrary value of the total angular momentum (the first steps in this direction are done in Sec. 4.5). The system of three pions require also a consistent isospin treatment. The isospin symmetry seems to the straightforward to incorporate using the decomposition method presented in Appendix C.1. An extension of this work to the coupled-channel problem is required for further investigation of the $a_1(1420)$ phenomenon (see Chapter 4) in the $3\pi - K\bar{K}\pi$ coupled system. We have left aside a problem of the time-reversal symmetry which would be important to address in the practical cases.

Summary and Outlook

The studies of light-meson resonances are the main subject of this thesis. The central issue of this research is that the interaction between hadrons cannot be calculated from first principles. Although QCD is known and accepted to be the fundamental underlying theory of the strong interaction, the consequences for the hadron spectrum cannot be inferred from it due to the complicated, non-perturbative nature of this theory. Among several possible phenomenological treatments of hadron spectroscopy, we attempt to pursue the most general approach which is based on basic properties of the scattering amplitude: unitarity, analyticity and crossing symmetry. The approach allows us to strictly define the resonance characteristics such as the mass and width and remove a large arbitrariness of the phenomenological amplitude construction in other approaches.

The work is focused on the dynamics in the system of three charged pions ($\pi^-\pi^+\pi^-$) from measurements of diffractive reactions $\pi^- p \to \pi^-\pi^+\pi^- p$, performed at the COMPASS experiment. In Sec. 3 we have introduce the main featured of the three-pion physics seen in the diffractive production: The three-pion interaction incorporates numerous different excitations modes: the system couples to a few tens of hadronic states that arise either as excitation of a subsystem (two pions) or the excitation of the system as a whole. The identification, separation, and characterization of the excited mesonic states is a very challenging problem that has been investigated by physicists around the world for many years. Moreover, in addition to the hadronic excitations, the physics of the strong interaction exhibits the quantum phenomena of final-state. Attempting to advance the customary approach of modeling the energy dependence of the amplitude by several Breit-Wigner terms and a phenomenological background, we have performed exploratory studies in both theoretical and practical directions of research.

We have studied the origin of the new resonance-like phenomenon $a_1(1420)$, observed by the COMPASS experiment in 2015 in the $f_0\pi$ P-wave. We have suggested and developed an interpretation of the signals as a consequence of a peculiar 3π-$K\bar{K}\pi$ coupling. A close-to-mass-shell kaon exchange, when $K^*\bar{K}$ scatters to $f_0\pi$, has been found to produce an enhancement in the spectrum of $f_0\pi$ and a significant motion of the scattering phase. All features of the phenomenon established by the COMPASS data have been reproduced within a simple model (see Chapter 4). The understanding of the rescattering effect might shine light to the XYZ states discovered in the charmonium sector as well as the pentaquark states observed by LHCb. There are indications that some of these exotic-candidate signal might originate from rescattering effects. In this sense, the $a_1(1420)$ signal is a gift: due to the rather well-known interaction between light hadrons and thanks to high statistical precision of modern experiments, we have a chance to illuminate this tricky feature of the strong interaction.

In addition to rescattering effects, we have also studied a second long-standing issue in spectroscopy: how to formulate amplitudes in a theoretically cleaner way than the traditional approach of a sum of the Breit-Wigner amplitude. Starting from the well-established unitarity-based technique (see Chapter 2) for a system of two particles, we approach the 3π system where two pions are combined

into a quasi-stable intermediate state, *e.g.* the ρ-meson, or the f_2-meson. Since the diffractive reactions exhibit complicated production mechanisms including non-resonant background processes, we have applied our model to the hadronic decays of the τ-lepton, *i.e.* $\tau \to 3\pi\,\nu_\tau$. Using the publicly available data of the ALEPH experiment, we succeeded to fix the model parameters and to perform an analysis of the analytic structure of the scattering amplitude (see Chapter 6). The pole position of the spin-partner of the ρ-meson, the ground axial vector $a_1(1260)$ has been extracted for the first time. Using the ALEPH data we have tested our model which included the interference of two interaction chains ($\rho[\to \pi_1^-\pi_2^+]\pi_3^-$ and $\pi_1^-\rho[\to \pi_2^+\pi_3^-]$) against the simpler one of the quasi-stable ρ-meson and a bachelor pion resonating in the S-wave. The comparison has revealed a significant difference in the results of the two models; it has emphasized the importance of the fact that the 3π-system is not just a quasi-two-particle system.

A further important achievement of this thesis is the realization of a coherent framework which puts both the final-state interactions and the three-particle resonances to the same footing (Chapter 7). Using a simplified version of the 3π system (three identical scalar particles) we have derived the three-body unitarity requirements and suggested a model which manifestly satisfies them. We show that for a system with a significant subchannel interaction, the rescattering processes generate the long-range interaction amplitude which is a sum of ladder-like diagrams (the two-particle resonances in different subsystems are formed and decay via one-particle exchange). The three-particle resonances are incorporated into the model by short-range terms (*e.g.* contact terms). In order to preserve three-body unitarity, these terms need to be "dressed" with the ladder rescattering. A dedicated publication is being drafted.

The framework unifies several approaches applied to a system of three particles: in the limit of a stable subchannel resonance, it reduces to simple two-body unitarity-based constructions (*e.g.* the K-matrix); under a slightly weaker approximation, the framework leads to the approach used in the τ-decay analysis mentioned above. For a fixed value of the total invariant mass, the model for the subchannel dynamics of our general framework is reminiscent of the Khuri-Treiman model (see Sec. 4.5 and Sec. 7.2). It follows that the three-hadron scattering amplitude can be written and the N-over-D function (see Eq. (7.35) and Eq. (7.36) with $N = k(1 + \tau\mathcal{L}_0)$ and $1/D = \mathfrak{R}$) where the N includes the details of the production and decay chains, while the D describe the three-particle resonances (bare poles dressed by the hadronic loops). The final-state interaction modifies the line shape of the $\pi\pi$-subchannel resonances; it influences the results for the pole position of three-particle resonances (as we also found in the systematic studies of the τ-decay analysis in Sec. 6.4).

The framework is well suited for addressing the $a_1(1420)$ phenomenon, although it would require an extension to accommodate two coupled channels (3π and $K\bar{K}\pi$). The main question concerning the nature of the $a_1(1420)$ is either if the rescattering effects incorporated by the N function are sufficient to describe the data, or if the function D requires (develops) poles in addition to the expected axial states. It is important to notice, that the triangle singularity from the kaon exchange is present in the N-function as a part for the decay process. An investigation using this approach is ongoing.

Along the path of the investigation on the $a_1(1420)$, an essential next step would be a comprehensive analysis of the decay $\tau \to 3\pi\,\nu_\tau$. A simple test of the $a_1(1420)$ based on the dissection check discussed in Sec. 4.1 (see Fig. 4.3) can be done on the τ-sample ahead of the PWA. The conventional PWA (see Sec. 3.3.1) might be used to confirm the COMPASS observation of the $a_1(1420)$. The freed-isobar PWA discussed in Sec. 3.4 would give a model-independent extraction of the Isobar line shapes ($\pi^+\pi^-$ interaction with S- and P-waves in this case), distorted by the final-state interaction. Sequentially, these results have to be subjected to the dispersive unitarity-based approach such as the

Khuri-Treiman model. Subtraction constants need to be fitted for every fixed value of the 3π invariant mass. The final step of the "comprehensive analysis" is a dynamic description of the subtraction constants as functions of $m_{3\pi}$, using the general framework developed in Chapter 7 and the analytic continuation of the model to the complex plane. We admit that the project is ambitious: it would require a lot of research as well as large computational resources for every step of the sketched plan. It is not less important to have a sufficiently large and precise data sample. Belle and BaBar are the two experiments which have collected over 10^8 τ-pair events produced in e^+e^- collisions [229, 230].

Studies of the 3π system in diffractive reactions are more complicated due to the production mechanism. However, over the last years, COMPASS performed an outstanding work for breaking down this complex data into separate intensities for different J^{PC} sectors. With the recent result of the freed-isobar analysis, one gets access to the subchannel spectra distorted by the rescattering effects. Those results seems to be the best "data" to validate our understanding of the rescattering physics. For example, the exotic sector with $J^{PC} = 1^{-+}$ is found to couple exclusively (among the 3π waves in the COMPASS PWA) to the $\rho\pi$ P-wave. The Khuri-Treiman model in this case resembles the model for $\omega \to \pi^+\pi^-\pi^0$ studied in Ref. [165, 166] with a slight difference due to the total isospin [6] (an investigation has been started in collaboration with Tobias Isken and Bastian Kubis). We have performed the first steps in generalizing the KT-formalism for arbitrary J^{PC} quantum numbers of the system. The application of this approach to $J^{PC} = 1^{++}$ based on the COMPASS freed-isobar results is an ongoing JPAC project.

Combining the rescattering studies with the three-body resonance extraction is, however, difficult given the COMPASS data. An additional challenge with respect to the τ analysis is the non-resonant background process, the Deck process. The understanding of its effect on the three-particle spectrum is still far from being quantitative. everal partial waves in the COMPASS analysis [78] are believed to contain a significant contribution of this background. In Chapter 5 we have consider available models for the Deck processes and sorted out an important parameters. We have found that the line shapes of the partial-wave projections vary substantially depending on a model for the exchange-pion propagator. An adjustment of the background parametrization using the COMPASS data is the next mandatory step to move forward the understanding of diffractive reactions (this is an ongoing work).

An investigation of alternative production mechanisms, such as *e.g.* $\gamma p \to 3\pi p$, that are possible at the CLAS12 and GlueX experiments, will provide complementary access to the meson excitation spectrum. Interestingly, the CLAS partial-wave analysis of Ref. [231] reported no evidence for the exotic $\pi_1(1600)$ signal in $J^{PC} = 1^{-+}$ as well as no evidence for the $a_1(1260)$ in the $J^{PC} = 1^{++}$ sector. In this respect, the data from the GlueX experiment are looked forward to [232]. The techniques and methods developed in this thesis will be essential in the future analyses.

---

[6] Essentially, the inhomogeneous term in the KT framework contains two $\pi\pi$ cross channels in case of ω-decay: $J^{PC} = 1^{--}$, the total isospin is $I = 0$. For the 3π system with $J^{PC} = 1^{-+}$, $I = 1$, there are two $\pi^+\pi^-$ pairs.

Bibliography

[1] M. Mikhasenko, B. Ketzer, and A. Sarantsev, *Nature of the $a_1(1420)$*,
Phys. Rev. **D91** (2015) 094015, arXiv: `1501.07023` [hep-ph]
(cit. on pp. iv, 4, 47, 52, 53, 64).

[2] M. Mikhasenko et al., *Pole position of the $a_1(1260)$ from τ-decay*,
Phys. Rev. **D98** (2018) 096021, arXiv: `1810.00016` [hep-ph] (cit. on pp. iv, 70, 89).

[3] M. Aghasyan et al., *Light isovector resonances in $\pi^- p \to \pi^- \pi^- \pi^+ p$ at 190 GeV/c*,
Phys. Rev. **D98** (2018) 092003, arXiv: `1802.05913` [hep-ex]
(cit. on pp. iv, 4, 38, 40–42, 48, 65, 76, 77, 82, 84, 89, 146, 152, 153).

[4] A. Jackura et al.,
New analysis of $\eta\pi$ tensor resonances measured at the COMPASS experiment,
Phys. Lett. **B779** (2018) 464, arXiv: `1707.02848` [hep-ph]
(cit. on pp. iv, 8, 12, 17, 143, 179).

[5] M. Mikhasenko et al., *Three-body scattering: Ladders and Resonances*, JHEP **08** (2019) 080,
arXiv: `1904.11894` [hep-ph] (cit. on pp. iv, 60, 109).

[6] M. Mikhasenko et al., *Dalitz-plot decomposition for three-body decays*, (2019),
arXiv: `1910.04566` [hep-ph] (cit. on p. iv).

[7] M. Mikhasenko et al., *Unitarity approach to the mass-dependent fit of 3π resonance
production data from the COMPASS experiment*, EPJ Web Conf. **137** (2017) 05017
(cit. on pp. iv, 145).

[8] M. Mikhasenko and B. Ketzer,
Beyond the isobar model: Rescattering in the system of three particles.,
PoS **BORMIO2016** (2016) 024 (cit. on p. iv).

[9] M. Mikhasenko et al., *What is the right formalism to search for resonances?*,
Eur. Phys. J. **C78** (2018) 229, arXiv: `1712.02815` [hep-ph] (cit. on pp. iv, 68).

[10] M. Mikhasenko, *A triangle singularity and the LHCb pentaquarks*, (2015),
arXiv: `1507.06552` [hep-ph] (cit. on p. iv).

[11] J. Nys et al., *Features of $\pi\Delta$ Photoproduction at High Energies*, Phys. Lett. **B779** (2018) 77,
arXiv: `1710.09394` [hep-ph] (cit. on p. iv).

[12] A. Rodas et al., *Determination of the pole position of the lightest hybrid meson candidate*,
accepted by PRL (2018), arXiv: `1810.04171` [hep-ph] (cit. on pp. iv, 12, 42).

[13] A. Pilloni et al.,
What is the right formalism to search for resonances? II. The pentaquark chain,
Eur. Phys. J. **C78** (2018) 727, arXiv: `1805.02113` [hep-ph] (cit. on pp. iv, 70).

[14]   A. Jackura et al.,
Phenomenology of Relativistic **3** → **3** *Reaction Amplitudes within the Isobar Approximation*,
(2018), arXiv: `1809.10523` [`hep-ph`] (cit. on pp. v, 60, 115, 116).

[15]   M. Albaladejo et al., *Khuri–Treiman equations for* $\pi\pi$ *scattering*,
Eur. Phys. J. **C78** (2018) 574, arXiv: `1803.06027` [`hep-ph`] (cit. on p. v).

[16]   A. Pilloni et al., *Amplitude analysis and the nature of the* $Z_c(3900)$,
Phys. Lett. **B772** (2017) 200, arXiv: `1612.06490` [`hep-ph`] (cit. on p. v).

[17]   N. N. Achasov and A. A. Kozhevnikov, *On the Nature of C (1480) Resonance*,
Z. Phys. C **48** (1990) 121 (cit. on p. vii).

[18]   I. C. Brock,
Users Guide to Writing a Thesis in a Physics/Astronomy Institute of the Universität Bonn,
URL: `http://pi.physik.uni-bonn.de/pi_only/thesis.php` (cit. on p. viii).

[19]   F. W. Busser et al., *Observation of pi0 mesons with large transverse momentum in
high-energy proton proton collisions*, Phys. Lett. **46B** (1973) 471 (cit. on p. 1).

[20]   D. W. Sivers, S. J. Brodsky, and R. Blankenbecler, *Large Transverse Momentum Processes*,
Phys. Rept. **23** (1976) 1 (cit. on p. 1).

[21]   M. Breidenbach et al., *Observed Behavior of Highly Inelastic electron-Proton Scattering*,
Phys. Rev. Lett. **23** (1969) 935 (cit. on p. 1).

[22]   J. D. Bjorken and E. A. Paschos,
Inelastic Electron Proton and gamma Proton Scattering, and the Structure of the Nucleon,
Phys. Rev. **185** (1969) 1975 (cit. on p. 1).

[23]   R. P. Feynman, *The behavior of hadron collisions at extreme energies*,
Conf. Proc. **C690905** (1969) 237 (cit. on p. 1).

[24]   H. D. Politzer, *Reliable Perturbative Results for Strong Interactions?*,
Phys. Rev. Lett. **30** (1973) 1346, [,274(1973)] (cit. on p. 1).

[25]   D. J. Gross and F. Wilczek, *Ultraviolet Behavior of Nonabelian Gauge Theories*,
Phys. Rev. Lett. **30** (1973) 1343, [,271(1973)] (cit. on p. 1).

[26]   M. Tanabashi et al., *Review of Particle Physics*, Phys. Rev. **D98** (2018) 030001
(cit. on pp. 2, 11, 14, 24, 38, 40, 46, 51, 82, 89, 91, 92, 94, 95, 144–146, 187).

[27]   M. Gell-Mann, *A Schematic Model of Baryons and Mesons*, Phys. Lett. **8** (1964) 214
(cit. on pp. 2, 3).

[28]   D. Horn and J. Mandula, *A Model of Mesons with Constituent Gluons*,
Phys. Rev. **D17** (1978) 898 (cit. on p. 2).

[29]   P. Guo et al., *Gluelump spectrum from Coulomb gauge QCD*, Phys. Rev. **D77** (2008) 056005,
arXiv: `0707.3156` [`hep-ph`] (cit. on p. 2).

[30]   A. Esposito, A. Pilloni, and A. D. Polosa, *Multiquark Resonances*, Phys. Rept. **668** (2016) 1,
arXiv: `1611.07920` [`hep-ph`] (cit. on p. 2).

[31]   F.-K. Guo et al., *Hadronic molecules*, Rev. Mod. Phys. **90** (2018) 015004,
arXiv: `1705.00141` [`hep-ph`] (cit. on p. 2).

[32] S. L. Olsen, T. Skwarnicki, and D. Zieminska,
Nonstandard heavy mesons and baryons: Experimental evidence,
Rev. Mod. Phys. **90** (2018) 015003, arXiv: `1708.04012` [`hep-ph`] (cit. on p. 2).

[33] B. Ketzer, *Hybrid Mesons*, PoS **QNP2012** (2012) 025, arXiv: `1208.5125` [`hep-ex`]
(cit. on p. 2).

[34] C. A. Meyer and E. S. Swanson, *Hybrid Mesons*, Prog. Part. Nucl. Phys. **82** (2015) 21,
arXiv: `1502.07276` [`hep-ph`] (cit. on p. 2).

[35] J. J. Dudek, *The lightest hybrid meson supermultiplet in QCD*, Phys. Rev. **D84** (2011) 074023,
arXiv: `1106.5515` [`hep-ph`] (cit. on p. 2).

[36] J. J. Dudek et al., *Toward the excited meson spectrum of dynamical QCD*,
Phys. Rev. **D82** (2010) 034508, arXiv: `1004.4930` [`hep-ph`] (cit. on p. 2).

[37] G. Zweig, *An SU(3) model for strong interaction symmetry and its breaking*,
(1964), CERN-TH-401 (cit. on p. 3).

[38] R. J. Eden et al., *The analytic S-matrix*, Cambridge Univ. Press, 1966
(cit. on pp. 5, 7, 8, 53, 55, 57, 92, 109, 110).

[39] V. N. Gribov, Y. L. Dokshitzer, and J. Nyiri,
Strong Interactions of Hadrons at High Energies – Gribov Lectures on Theoretical Physics,
Cambridge University Press, 2009
(cit. on pp. 5, 8, 11, 13, 16, 24, 40, 53, 55, 73, 120, 122, 179).

[40] R. T. Deck, *Kinematical interpretation of the first pi - rho resonance*,
Phys. Rev. Lett. **13** (1964) 169 (cit. on pp. 5, 27, 73, 89).

[41] W. Heisenberg, *Die „beobachtbaren Größen" in der Theorie der Elementarteilchen*,
Zeitschrift für Physik **120** (1943) 513, ISSN: 0044-3328,
URL: `https://doi.org/10.1007/BF01329800` (cit. on p. 7).

[42] W. Heisenberg, *Die beobachtbaren Größen in der Theorie der Elementarteilchen. II*,
Zeitschrift für Physik **120** (1943) 673, ISSN: 0044-3328,
URL: `https://doi.org/10.1007/BF01336936` (cit. on p. 7).

[43] W. Heisenberg, *Die beobachtbaren Größen in der Theorie der Elementarteilchen. III*,
Zeitschrift für Physik A Hadrons and Nuclei **123** (1944) 93, ISSN: 0939-7922,
URL: `https://doi.org/10.1007/BF01375146` (cit. on p. 7).

[44] P. Collins and A. Martin, *Hadron Interactions*, 1st ed., Adam Hilger Ltd., 1984
(cit. on pp. 7, 11, 179).

[45] C. Itzykson and J. B. Zuber, *Quantum Field Theory*,
International Series In Pure and Applied Physics, McGraw-Hill, 1980,
ISBN: 9780486445687, 0486445682, URL: `http://dx.doi.org/10.1063/1.2916419`
(cit. on pp. 9, 15).

[46] M. J. Ablowitz and A. S. Fokas, *Complex Variables: Introduction and Applications*, 2nd ed.,
Cambridge Texts in Applied Mathematics, Cambridge University Press, 2003
(cit. on pp. 9, 15–17).

[47] A. Martin and T. Spearman, *Elementary Particle Theory*, 1st ed.,
North-Holland Publishing Company, 1970
(cit. on pp. 9, 11, 12, 14, 30, 91, 93, 122, 159, 162–164).

[48] D. I. Olive, *Unitarity and the evaluation of discontinuities*,
Il Nuovo Cimento (1955-1965) **26** (1962) 73, ISSN: 1827-6121,
URL: https://doi.org/10.1007/BF02754344 (cit. on pp. 10, 112, 119).

[49] J. L. Miramontes,
Hermitian analyticity versus real analyticity in two-dimensional factorized S matrix theories,
Phys. Lett. **B455** (1999) 231, arXiv: hep-th/9901145 [hep-th] (cit. on p. 10).

[50] A. V. Anisovich et al.,
Analysis of the meson-meson data in the framework of the dispersion D-matrix method,
Phys. Rev. **D84** (2011) 076001 (cit. on pp. 12, 92).

[51] A. M. Badalian et al., *Resonances in Coupled Channels in Nuclear and Particle Physics*,
Phys. Rept. **82** (1982) 31 (cit. on p. 12).

[52] S. U. Chung et al., *Partial wave analysis in K matrix formalism*, Annalen Phys. **4** (1995) 404
(cit. on pp. 12, 17).

[53] I. J. R. Aitchison, *Unitarity, Analyticity and Crossing Symmetry in Two- and Three-hadron
Final State Interactions*, (2015), arXiv: 1507.02697 [hep-ph] (cit. on pp. 12, 68).

[54] G. Costa and F. Ferrari, *Polology and ND-1 solutions in the multiple-channel problems*,
Il Nuovo Cimento (1955-1965) **22** (1961) 214, ISSN: 1827-6121,
URL: https://doi.org/10.1007/BF02829012 (cit. on p. 12).

[55] V. V. Anisovich, A. V. Sarantsev, and D. V. Bugg,
Analysis of the N N —> N Delta threshold using the coupled channel N/D method,
Nucl. Phys. **A537** (1992) 501 (cit. on p. 12).

[56] R. de L. Kronig, *On the Theory of Dispersion of X-Rays*, J. Opt. Soc. Am. **12** (1926) 547,
URL: http://www.osapublishing.org/abstract.cfm?URI=josa-12-6-547
(cit. on p. 14).

[57] H. A. Kramers,
La diffusion de la lumiére par les atomes Atti del Congresso Internazionale dei Fisici,
Como-Pavia-Roma **2** (1927) 545 (cit. on p. 14).

[58] J. S. Toll, *Causality and the Dispersion Relation: Logical Foundations*,
Phys. Rev. **104** (6 1956) 1760,
URL: https://link.aps.org/doi/10.1103/PhysRev.104.1760 (cit. on p. 14).

[59] M. E. Peskin and D. V. Schroeder, *An Introduction to quantum field theory*,
Addison-Wesley, 1995 (cit. on pp. 14, 53, 76).

[60] G. F. Chew and S. Mandelstam, *Theory of low-energy pion pion interactions*,
Phys. Rev. **119** (1960) 467 (cit. on p. 14).

[61] J. H. Reid and N. N. Trofimenkoff, *A GENERATING FUNCTION FOR A CLASS OF
EFFECTIVE CHEW-MANDELSTAM FUNCTIONS*, J. Math. Phys. **25** (1984) 3540
(cit. on pp. 14, 15).

[62] J. L. Basdevant and E. L. Berger,
      Unitary Coupled-Channel Analysis of Diffractive Production of the a1 Resonance,
      Phys. Rev. **D16** (1977) 657 (cit. on pp. 14, 17, 18, 52, 74, 89, 92, 94, 149).

[63] C. Adolph et al.,
      Odd and even partial waves of $\eta\pi^-$ and $\eta'\pi^-$ in $\pi^- p \to \eta^{(')}\pi^- p$ at $191\,\mathrm{GeV}/c$,
      Phys. Lett. B **740** (2015) 303, arXiv: `1408.4286` `[hep-ex]` (cit. on pp. 16, 144, 145).

[64] S. Dobbs, *Searching for Hybrid Mesons with GlueX*, PoS **Hadron2017** (2018) 047,
      arXiv: `1712.07214` `[nucl-ex]` (cit. on p. 16).

[65] P. Hoyer and T. L. Trueman, *Unitarity and Crossing in Reggeon-Particle Amplitudes*,
      Phys. Rev. **D10** (1974) 921 (cit. on p. 16).

[66] I. J. R. Aitchison, *K-MATRIX FORMALISM FOR OVERLAPPING RESONANCES*,
      Nucl. Phys. **A189** (1972) 417 (cit. on p. 17).

[67] K. M. Watson, *The Effect of final state interactions on reaction cross-sections*,
      Phys. Rev. **88** (1952) 1163 (cit. on p. 17).

[68] A. Švarc et al.,
      Introducing the Pietarinen expansion method into the single-channel pole extraction problem,
      Phys. Rev. **C88** (2013) 035206, arXiv: `1307.4613` `[hep-ph]` (cit. on p. 17).

[69] R. Omnès, *On the Solution of certain singular integral equations of quantum field theory*,
      Nuovo Cim. **8** (1958) 316 (cit. on pp. 17, 44).

[70] A. P. Szczepaniak, *Analytical improvements to the Breit-Wigner isobar models*, (2015),
      arXiv: `1510.00695` `[hep-ph]` (cit. on p. 18).

[71] F. Gautheron et al., *COMPASS-II Proposal*, CERN-SPSC-2010-014, SPSC-P-340, 2010
      (cit. on p. 19).

[72] P. Abbon et al., *The COMPASS Experiment at CERN*, Nucl. Instr. Meth. A **577** (2007) 455,
      eprint: `hep-ex/0703049` (cit. on p. 19).

[73] P. Abbon et al., *The COMPASS Setup for Physics with Hadron Beams*,
      Nucl. Instr. Meth. A **779** (2015) 69, arXiv: `1410.1797` `[physics.ins-det]`
      (cit. on pp. 19, 21).

[74] T. Szameitat,
      New Geant4-based Monte Carlo Software for the COMPASS-II Experiment at CERN,
      PhD thesis: Albert-Ludwigs-Universität Freiburg, 2016 (cit. on p. 20).

[75] T. Szameitat and C. Regali,
      A Geant4 based monte carlo simulation for the COMPASS-II experiment, 2016,
      URL: `https://na58-project-tgeant.web.cern.ch/` (cit. on p. 20).

[76] M. Brice, "View from the crane of the COMPASS experiment facility.", 2011,
      URL: `http://cds.cern.ch/record/1370231` (cit. on p. 20).

[77] F. Haas, *Two-Dimensional Partial-Wave Analysis of Exclusive $190\,\mathrm{GeV}$ $\pi^- p$ Scattering into
      the $\pi^-\pi^-\pi^+$ Final State at COMPASS (CERN)*, PhD thesis: Techn. Univ. München, 2014
      (cit. on pp. 21, 22, 25, 45, 84).

[78] C. Adolph et al.,
Resonance Production and $\pi\pi$ *S-wave in* $\pi^- + p \to \pi^-\pi^-\pi^+ + p_{recoil}$ *at 190 GeV/c*,
Phys. Rev. **D95** (2017) 032004, arXiv: `1509.00992 [hep-ex]`
(cit. on pp. 22, 23, 32, 37, 39, 45, 46, 48, 65, 74, 80, 83, 91, 92, 117, 125, 144–146, 170).

[79] P. Collins, *An Introduction to Regge Theory & High Energy Physics*, 1st ed.,
Cambridge University Press, 1977 (cit. on pp. 24, 30, 40, 91).

[80] A. Donnachie et al., *Pomeron Physics and QCD*, 1st ed., Cambridge University Press, 2002
(cit. on pp. 24, 76, 188).

[81] K. Gottfried and J. D. Jackson,
On the Connection between production mechanism and decay of resonances at high-energies,
Nuovo Cim. **33** (1964) 309 (cit. on p. 24).

[82] D. R. Giebink, *Relativity and spin in one-, two-, and three-body systems*,
Phys. Rev. **C32** (1985) 502 (cit. on p. 24).

[83] G. Ascoli et al., *Deck-model calculation of pi- p —> pi- pi+ pi- p*, Phys. Rev. D **9** (1974) 1963
(cit. on pp. 27, 64, 76, 84).

[84] A. Austregesilo, *Central Production of Two-Pseudoscalar Meson Systems at the COMPASS
Experiment at CERN*, PhD thesis: Techn. Univ. München, 2014 (cit. on p. 27).

[85] P. del Amo Sanchez et al., *Measurement of D0-antiD0 mixing parameters using D0 —> K(S)0
pi+ pi- and D0 —> K(S)0 K+ K- decays*, Phys. Rev. Lett. **105** (2010) 081803,
arXiv: `1004.5053 [hep-ex]` (cit. on p. 28).

[86] B. Aubert et al., *Dalitz Plot Analysis of B- —> D+ pi- pi-*, Phys. Rev. **D79** (2009) 112004,
arXiv: `0901.1291 [hep-ex]` (cit. on p. 28).

[87] R. Aaij et al., *Dalitz plot analysis of* $B^0 \to \overline{D}^0\pi^+\pi^-$ *decays*, Phys. Rev. **D92** (2015) 032002,
arXiv: `1505.01710 [hep-ex]` (cit. on p. 28).

[88] R. Aaij et al., *Dalitz plot analysis of* $B_s^0 \to \bar{D}^0 K^-\pi^+$ *decays*, Phys. Rev. **D90** (2014) 072003,
arXiv: `1407.7712 [hep-ex]` (cit. on p. 28).

[89] R. E. Mitchell et al., *Dalitz Plot Analysis of D+(s) —> K+K-pi+*,
Phys. Rev. **D79** (2009) 072008, arXiv: `0903.1301 [hep-ex]` (cit. on p. 28).

[90] G. Ascoli et al., *PARTIAL WAVE ANALYSIS OF THE 3 pi DECAY OF THE A2*,
Phys. Rev. Lett. **25** (1970) 962 (cit. on pp. 29, 77).

[91] G. Ascoli et al., *Partial-wave analysis of the deck amplitude for* $\pi N \to \pi\pi\pi N^*$,
Phys. Rev. **D8** (1973) 3894 (cit. on pp. 29, 69, 73, 79, 89).

[92] M. Mikhasenko, 2018, URL: `http://nbviewer.jupyter.org/github/mmikhasenko/`
`pwa_from_scratch/blob/master/PWA-FIT-NOCALLBACKS.ipynb` (cit. on p. 29).

[93] K. Buchner et al.,
Application of a unitarized veneziano model to the reaction k+ n —> k+ pi- p at 3 gev/c,
Nucl. Phys. **B34** (1971) 292 (cit. on p. 31).

[94] T. Schlüter,
The $\pi^-\eta$ *and* $\pi^-\eta'$ *Systems in Exclusive* 190 *GeV* πp *Reactions at COMPASS (CERN)*,
PhD thesis: Munich U., 2012 (cit. on p. 31).

[95] S. U. Chung and T. L. Trueman,
Positivity Conditions on the Spin Density Matrix: A Simple Parametrization,
Phys. Rev. **D11** (1975) 633 (cit. on p. 31).

[96] J. D. Hansen et al., *FORMALISM AND ASSUMPTIONS INVOLVED IN PARTIAL WAVE
ANALYSIS OF THREE - MESON SYSTEMS*, Nucl. Phys. **B81** (1974) 403 (cit. on pp. 31, 69).

[97] J. M. Blatt and V. F. Weisskopf, *Theoretical Nuclear Physics*, Wiley, 1952
(cit. on pp. 32, 179).

[98] F. Von Hippel and C. Quigg, *Centrifugal-barrier effects in resonance partial decay widths,
shapes, and production amplitudes*, Phys. Rev. **D5** (1972) 624 (cit. on pp. 32, 179).

[99] F. James, *Statistical methods in experimental physics*, 2006, ISBN: 9789812567956
(cit. on pp. 34, 35).

[100] F. James and M. Roos, *Minuit: A System for Function Minimization and Analysis of the
Parameter Errors and Correlations*, Comput. Phys. Commun. **10** (1975) 343 (cit. on p. 34).

[101] S. G. Johnson, *The NLopt nonlinear-optimization package*, 2011,
URL: `http://ab-initio.mit.edu/nlopt` (cit. on pp. 34, 95).

[102] J. Pumplin, D. R. Stump, and W. K. Tung,
Multivariate fitting and the error matrix in global analysis of data,
Phys. Rev. **D65** (2001) 014011, arXiv: `hep-ph/0008191 [hep-ph]` (cit. on p. 35).

[103] W. H. Press et al., *Numerical Recipes in FORTRAN: The Art of Scientific Computing*,
Press Syndicate of the University of Cambridge, 1992 (cit. on pp. 35, 99).

[104] M. Mikhasenko and S. Sehgal, *The statistical uncertainties of the mass-independent PWA*,
Talk at the COMPASS Analysis meeting, CERN, Switzerland, Novamber 10 – 11, 2018,
URL: `https://wwwcompass.cern.ch/compass/software/analysis/
transparencies/2018/am%5C_181011/talks/Mikhasenko%5C_20181011.pdf`
(cit. on p. 35).

[105] I. Kachaev and D. Ryabchikov, *Made up broad component* $(\pi\pi)_S$*-wave*,
Private communication () (cit. on pp. 36, 171).

[106] K. L. Au, D. Morgan, and M. R. Pennington,
Meson Dynamics Beyond the Quark Model: A Study of Final State Interactions,
Phys. Rev. **D35** (1987) 1633 (cit. on pp. 36, 171).

[107] S. M. Flatté,
Coupled - Channel Analysis of the pi eta and K anti-K Systems Near K anti-K Threshold,
Phys. Lett. B **63** (1976) 224 (cit. on p. 36).

[108] M. Alekseev et al., *Observation of a* $J^{PC} = 1^{-+}$ *exotic resonance in diffractive dissociation
of* $190\,\mathrm{GeV}/c\,\pi^-$ *into* $\pi^-\pi^-\pi^+$, Phys. Rev. Lett. **104** (2010) 241803,
arXiv: `0910.5842 [hep-ex]` (cit. on pp. 38, 46).

[109] F. Nerling, *Observation of a* $J^{PC} = 1^{-+}$ *exotic signal in the* $\pi^-\pi^0\pi^0$ *system diffractively
produced at COMPASS, and comparison to the charged decay mode*,
EPJ Web Conf. **37** (2012) 09025, arXiv: `1208.0474 [hep-ex]` (cit. on p. 38).

[110] M. G. Bowler, *The A1 Revisited*, Phys. Lett. **B182** (1986) 400 (cit. on pp. 39, 89).

[111] B. Hyams et al., $\pi\pi$ *Phase Shift Analysis from 600-MeV to 1900-MeV*,
Nucl. Phys. **B64** (1973) 134 (cit. on p. 43).

[112] G. Grayer et al., *High Statistics Study of the Reaction pi- p –> pi- pi+ n: Apparatus, Method of Analysis, and General Features of Results at 17-GeV/c*, Nucl. Phys. **B75** (1974) 189 (cit. on p. 43).

[113] B. Hyams et al., *A Study of All the pi pi Phase Shift Solutions in the Mass Region 1.0-GeV to 1.8-GeV from pi- p –> pi- pi+ n at 17.2-GeV*, Nucl. Phys. **B100** (1975) 205 (cit. on p. 43).

[114] J. T. Daub, C. Hanhart, and B. Kubis,
A model-independent analysis of final-state interactions in $\overline{B}^0_{d/s} \to J/\psi\pi\pi$,
JHEP **02** (2016) 009, arXiv: `1508.06841` `[hep-ph]` (cit. on pp. 43, 44).

[115] S. Ropertz, C. Hanhart, and B. Kubis, *A new parametrization for the scalar pion form factors*,
(2018), arXiv: `1809.06867` `[hep-ph]` (cit. on pp. 43, 44).

[116] R. Garcia-Martin et al., *The Pion-pion scattering amplitude. IV: Improved analysis with once subtracted Roy-like equations up to 1100 MeV*, Phys. Rev. **D83** (2011) 074004,
arXiv: `1102.2183` `[hep-ph]` (cit. on pp. 43, 75).

[117] F. Krinner et al., *Ambiguities in model-independent partial-wave analysis*,
Phys. Rev. **D97** (2018) 114008, arXiv: `1710.09849` `[hep-ph]` (cit. on p. 45).

[118] F. Krinner and D. Ryabchikov,
Extended freed-isobar PWA on $\pi^- + p \to \pi^-\pi^-\pi^+ + p$ *Compass data collected in 2008*,
COMPASS Release Note,
http://wwwcompass.cern.ch/compass/results/2017/september_3pi_mass_dependent_freedisobar/releaseNote.
2017 (cit. on p. 45).

[119] C. Daum et al., *DIFFRACTIVE PRODUCTION OF 3 pi STATES AT 63-GeV AND 94- GeV*,
Nucl. Phys. B **182** (1981) 269 (cit. on pp. 46, 73, 77).

[120] G. S. Adams et al., *Observation of a new J(PC) = 1-+ exotic state in the reaction pi- p –> pi+ pi- pi- p at 18-GeV/c*, Phys. Rev. Lett. **81** (1998) 5760 (cit. on p. 46).

[121] S. U. Chung et al.,
Exotic and qq resonances in the pi + pi - pi - system produced in pi -p collisions at 18 GeV/c,
Phys. Rev. **D65** (2002) 072001 (cit. on p. 46).

[122] R. Aaij et al., *Observation of the resonant character of the* $Z(4430)^-$ *state*,
Phys. Rev. Lett. **112** (2014) 222002, arXiv: `1404.1903` `[hep-ex]` (cit. on p. 47).

[123] R. Aaij et al., *Observation of* $J/\psi p$ *Resonances Consistent with Pentaquark States in*
$\Lambda_b^0 \to J/\psi K^- p$ *Decays*, Phys. Rev. Lett. **115** (2015) 072001, arXiv: `1507.03414` `[hep-ex]`
(cit. on p. 47).

[124] C. Adolph et al., *Observation of a New Narrow Axial-Vector Meson* a_1*(1420)*,
Phys. Rev. Lett. **115** (2015) 082001, arXiv: `1501.05732` `[hep-ex]`
(cit. on pp. 47–50, 65, 66).

[125] Y. Khokhlov et al., *Partial wave analyses of the* $\pi^-\pi^0\pi^0$ *and* $\pi^-\pi^0$ *systems with VES setup*,
PoS **Hadron2013** (2014) 088 (cit. on p. 47).

[126] F. Krinner, $\pi\pi\,S-$ *wave in* $190\,\text{GeV}\,\pi^- + p \to \pi^- \pi^- \pi^+ + p_{\text{recoil}}$ *at with COMPASS*,
COMPASS Release Note,
http://wwwcompass.cern.ch/compass/results/2015/may_3pic_deisobarred/release_note_de-isobarred_r305.pdf, 2015
(cit. on p. 48).

[127] J. J. Dudek et al., *Isoscalar meson spectroscopy from lattice QCD*,
Phys. Rev. **D83** (2011) 111502, arXiv: `1102.4299` `[hep-lat]` (cit. on p. 49).

[128] D. Ebert, R. N. Faustov, and V. O. Galkin,
Mass spectra and Regge trajectories of light mesons in the relativistic quark model,
Phys. Rev. **D79** (2009) 114029, arXiv: `0903.5183` `[hep-ph]` (cit. on pp. 50, 51).

[129] K. Chen et al., *Light axial vector mesons*, Phys. Rev. **D91** (2015) 074025,
arXiv: `1501.07766` `[hep-ph]` (cit. on pp. 50, 51).

[130] M. Karliner, J. L. Rosner, and T. Skwarnicki, *Multiquark States*,
Ann. Rev. Nucl. Part. Sci. **68** (2018) 17, arXiv: `1711.10626` `[hep-ph]` (cit. on p. 51).

[131] J. L. Friar, B. F. Gibson, and G. L. Payne,
ONE PION EXCHANGE POTENTIAL DEUTERON, Phys. Rev. **C30** (1984) 1084
(cit. on p. 51).

[132] M. Pavon Valderrama and E. Ruiz Arriola,
Renormalization of the deuteron with one pion exchange, Phys. Rev. **C72** (2005) 054002,
arXiv: `nucl-th/0504067` `[nucl-th]` (cit. on p. 51).

[133] Y. S. Kalashnikova and A. V. Nefediev, *One-pion exchange in the X(3872) revisited*,
Pisma Zh. Eksp. Teor. Fiz. **97** (2013) 76, [JETP Lett.97,70(2013)],
arXiv: `1212.2004` `[hep-ph]` (cit. on p. 51).

[134] P. Wang and X. G. Wang,
Study on X(3872) from effective field theory with pion exchange interaction,
Phys. Rev. Lett. **111** (2013) 042002, arXiv: `1304.0846` `[hep-ph]` (cit. on p. 51).

[135] V. Baru et al.,
Remarks on study of X(3872) from effective field theory with pion-exchange interaction,
Phys. Rev. **D91** (2015) 034002, arXiv: `1501.02924` `[hep-ph]` (cit. on p. 51).

[136] L. D. Landau and E. M. Lifshits, *Quantum Mechanics*, vol. v.3, Course of Theoretical Physics,
Butterworth-Heinemann, 1991, ISBN: 9780750635394 (cit. on pp. 51, 164, 178).

[137] H.-X. Chen et al., $a_1(1420)$ *resonance as a tetraquark state and its isospin partner*,
Phys. Rev. **D91** (2015) 094022, arXiv: `1503.02597` `[hep-ph]` (cit. on p. 51).

[138] T. Gutsche et al., *Test of the multiquark structure of* $a_1(1420)$ *in strong two-body decays*,
Phys. Rev. **D96** (2017) 114004, arXiv: `1710.02357` `[hep-ph]` (cit. on p. 51).

[139] H. Sundu, S. S. Agaev, and K. Azizi, *New* $\alpha_1(1420)$ *state: Structure, mass, and width*,
Phys. Rev. **D97** (2018) 054001, arXiv: `1711.05977` `[hep-ph]` (cit. on p. 51).

[140] J.-L. Basdevant and E. L. Berger, *Peak locations and relative phase of different decay modes
of the* a_1 *axial vector resonance in diffractive production*, Phys. Rev. Lett. **114** (2015) 192001,
arXiv: `1504.05955` `[hep-ph]` (cit. on pp. 52, 68).

[141] J. .-.-L. Basdevant and E. L. Berger,
Unstable Particle Scattering and an Analytic Quasiunitary Isobar Model,
Phys. Rev. **D19** (1979) 239 (cit. on pp. 52, 92, 120, 122, 146).

[142] E. L. Berger and J. T. Donohue, *Helicity Conservation and Meson Diffraction Dissociation*,
Phys. Rev. **D15** (1977) 790 (cit. on p. 52).

[143] M. Wagner, *Dispersive approach to $a_1(1420)$ phenomenon*,
MA thesis: Rheinische Friedrich-Wilhelms-Universität Bonn, 2001 (cit. on pp. 53, 65).

[144] L. Landau, *On analytic properties of vertex parts in quantum field theory*,
Nucl. Phys. **13** (1959) 181 (cit. on p. 53).

[145] R. Cutkosky, *Singularities and discontinuities of Feynman amplitudes*,
J. Math. Phys. **1** (1960) 429 (cit. on pp. 53, 57, 58).

[146] U.-G. Meissner,
Low-Energy Hadron Physics from Effective Chiral Lagrangians with Vector Mesons,
Phys. Rept. **161** (1988) 213 (cit. on p. 53).

[147] S. Coleman and R. E. Norton, *Singularities in the physical region*, Nuovo Cim. **38** (1965) 438
(cit. on p. 55).

[148] N. N. Khuri and S. B. Treiman, *Pion-Pion Scattering and $K^{\pm} \to 3\pi$ Decay*,
Phys. Rev. **119** (1960) 1115 (cit. on pp. 60, 68, 109).

[149] J. B. Bronzan and C. Kacser, *Khuri-Treiman Representation and Perturbation Theory*,
Phys. Rev. **132** (1963) 2703 (cit. on pp. 60, 68, 109, 118).

[150] M. Mai et al., *Three-body Unitarity with Isobars Revisited*, Eur. Phys. J. **A53** (2017) 177,
arXiv: `1706.06118` [`nucl-th`] (cit. on pp. 60, 109, 111, 113–115).

[151] C. Schmid, *Final-State Interactions and the Simulation of Resonances*,
Phys. Rev. **154** (1967) 1363 (cit. on pp. 60, 62).

[152] A. V. Anisovich and V. V. Anisovich,
Rescattering effects in three particle states and the Schmid theorem,
Phys. Lett. **B345** (1995) 321 (cit. on p. 62).

[153] A. P. Szczepaniak, *Dalitz plot distributions in presence of triangle singularities*,
Phys. Lett. **B757** (2016) 61, arXiv: `1510.01789` [`hep-ph`] (cit. on p. 62).

[154] V. R. Debastiani, S. Sakai, and E. Oset,
Considerations on the Schmid theorem for triangle singularities, (2018),
arXiv: `1809.06890` [`hep-ph`] (cit. on p. 62).

[155] R. García-Martín et al., *Precise determination of the $f_0(600)$ and $f_0(980)$ pole parameters
from a dispersive data analysis*, Phys. Rev. Lett. **107** (2011) 072001,
arXiv: `1107.1635` [`hep-ph`] (cit. on p. 64).

[156] D. Asner et al.,
Hadronic structure in the decay $\tau^- \to \nu_\tau \pi^- \pi^0 \pi^0$ and the sign of the tau-neutrino helicity,
Phys. Rev. **D61** (1999) 012002, arXiv: `hep-ex/9902022` [`hep-ex`] (cit. on pp. 64, 91).

[157] R. A. Briere et al., *Branching fractions of tau leptons decays to three charged hadrons*,
Phys. Rev. Lett. **90** (2003) 181802, arXiv: `hep-ex/0302028` [`hep-ex`] (cit. on pp. 64, 91).

[158] T. E. Coan et al.,
Wess-Zumino current and the structure of the decay tau- —> K- K+ pi- nu(tau),
Phys. Rev. Lett. **92** (2004) 232001, arXiv: `hep-ex/0401005` [`hep-ex`] (cit. on p. 64).

[159] E. Berdnikov et al., *Study of the reaction pi- A —> K+ K- pi- A at 37-GeV/c*,
Phys. Lett. B **337** (1994) 219 (cit. on p. 64).

[160] M. Wagner, M. Mikhasenko, and B. Ketzer,
Mass-dependent fit of $a_1(1420)$ via the "Triangle Singularity", COMPASS Release Note,
http://wwwcompass.cern.ch/compass/results/.html/2017/september_triangular_a1_1420/index.html,
2016 (cit. on pp. 65, 66).

[161] F. Haas,
Extraction of the $a_1(1420)$ from the $\pi^-\pi^-\pi^+$ Data using 3-Wave Fits, COMPASS Release Note,
http://wwwcompass.cern.ch/compass/results/2014/november_a1_1420_letter/rn_a1_1410letter_v2.pdf,
2014 (cit. on p. 65).

[162] R. Pasquier and J. Y. Pasquier,
Khuri-Treiman-Type Equations for Three-Body Decay and Production Processes,
Phys. Rev. **170** (1968) 1294 (cit. on pp. 68, 103, 109, 117–119, 175, 176).

[163] R. Pasquier and J. Y. Pasquier,
Khuri-treiman-type equations for three-body decay and production processes. 2.,
Phys. Rev. **177** (1969) 2482 (cit. on pp. 68, 109).

[164] I. J. R. Aitchison, *Dispersion Theory Model of Three-Body Production and Decay Processes*,
Phys. Rev. **137** (1965) B1070 (cit. on pp. 68, 109, 118).

[165] F. Niecknig, B. Kubis, and S. P. Schneider,
Dispersive analysis of $\omega \to 3\pi$ and $\phi \to 3\pi$ decays, Eur. Phys. J. **C72** (2012) 2014,
arXiv: `1203.2501` [`hep-ph`] (cit. on pp. 68, 92, 103, 118, 125).

[166] I. V. Danilkin et al., *Dispersive analysis of $\omega/\phi \to 3\pi, \pi\gamma*$*, Phys. Rev. **D91** (2015) 094029,
arXiv: `1409.7708` [`hep-ph`] (cit. on pp. 68, 92, 103, 118, 125).

[167] P. Guo et al., *Three-body final-state interaction in $\eta \to 3\pi$*, Phys. Rev. **D92** (2015) 054016,
arXiv: `1505.01715` [`hep-ph`] (cit. on pp. 68, 118).

[168] G. Colangelo et al., *$\eta \to 3\pi$: Study of the Dalitz plot and extraction of the quark mass ratio Q*,
Phys. Rev. Lett. **118** (2017) 022001, arXiv: `1610.03494` [`hep-ph`] (cit. on pp. 68, 92).

[169] M. Albaladejo and B. Moussallam, *Extended chiral Khuri-Treiman formalism for $\eta \to 3\pi$ and
the role of the $a_0(980)$, $f_0(980)$ resonances*, Eur. Phys. J. **C77** (2017) 508,
arXiv: `1702.04931` [`hep-ph`] (cit. on pp. 68, 92, 118).

[170] T. Isken et al., *Dispersion relations for $\eta^{'} \to \eta\pi\pi$*, Eur. Phys. J. **C77** (2017) 489,
arXiv: `1705.04339` [`hep-ph`] (cit. on p. 68).

[171] F. Niecknig and B. Kubis,
Dispersion-theoretical analysis of the $D^+ \to K^-\pi^+\pi^+$ Dalitz plot, JHEP **10** (2015) 142,
arXiv: `1509.03188` [`hep-ph`] (cit. on pp. 68, 92, 118).

[172] F. Niecknig and B. Kubis,
Consistent Dalitz plot analysis of Cabibbo-favored $D^+ \to \bar{K}\pi^+$ decays,
Phys. Lett. **B780** (2018) 471, arXiv: `1708.00446` [`hep-ph`] (cit. on p. 68).

[173] G. Colangelo, M. Finkemeier, and R. Urech, *Tau decays and chiral perturbation theory*,
Phys. Rev. **D54** (1996) 4403, arXiv: `hep-ph/9604279` [`hep-ph`] (cit. on p. 68).

[174] E. L. Berger, *Proceedings of the Daresbury conference on Three-Particle Phase Shift Analysis and Meson Resonance Production*, unpublished, 1975 (cit. on pp. 74, 77, 80).

[175] Stodolsky, *"Understanding" Kinematic Effects"*, () (cit. on pp. 74, 77).

[176] J. Dudek and A. Szczepaniak, *The Deck effect in pi N — pi pi pi N*,
AIP Conf. Proc. **814** (2006) 587 (cit. on p. 74).

[177] M. G. Bowler et al.,
Diffraction Dissociation, the Deck Mechanism and Diffractive Resonance Production,
Nucl. Phys. **B97** (1975) 227 (cit. on pp. 74, 77).

[178] I. J. R. Aitchison and M. G. Bowler, *Rescattering Effects in the Deck Model*,
J. Phys. **G3** (1977) 1503 (cit. on pp. 74, 77).

[179] J. Pisut and M. Roos, *The rho meson shape*, Nucl. Phys. **B6** (1968) 325 (cit. on pp. 75, 92).

[180] T. Arens et al., *Some tests for the helicity structure of the pomeron in e p collisions*,
Z. Phys. **C74** (1997) 651, arXiv: `hep-ph/9605376` [`hep-ph`] (cit. on p. 76).

[181] F. E. Close and G. A. Schuler,
Central production of mesons: Exotic states versus pomeron structure,
Phys. Lett. **B458** (1999) 127, arXiv: `hep-ph/9902243` [`hep-ph`] (cit. on p. 76).

[182] A. Abele et al., *Study of f0 decays into four neutral pions*, Eur. Phys. J. **C19** (2001) 667
(cit. on p. 82).

[183] P. Salvini et al., *anti-p p annihilation into four charged pions at rest and in flight*,
Eur. Phys. J. **C35** (2004) 21 (cit. on p. 82).

[184] D. Ryabchikov, *Modeling of non-resonant Deck-like contributions in diffractive-dissociation reactions at COMPASS*,
Talk at the German Pysical Society - Spring meeting, Munich, Germany, March 14 – 18,
2016, URL: `https://wwwcompass.cern.ch/compass/publications/talks/t2016/locked/ryabchikov%5C_dpg2016.pdf` (cit. on p. 84).

[185] L. Roca, E. Oset, and J. Singh,
Low lying axial-vector mesons as dynamically generated resonances,
Phys. Rev. **D72** (2005) 014002, arXiv: `hep-ph/0503273` [`hep-ph`] (cit. on p. 89).

[186] H. Nagahiro et al., *Composite and elementary natures of $a_1(1260)$ meson*,
Phys. Rev. **D83** (2011) 111504, arXiv: `1101.3623` [`hep-ph`] (cit. on p. 89).

[187] . Eidelman, *The $a_1(1260)$ and $a_1(1640)$*, 2003,
URL: `http://pdg.lbl.gov/2006/reviews/a11260_m010.pdf` (cit. on p. 89).

[188] J. H. Kuhn and E. Mirkes, *Structure functions in tau decays*,
Z. Phys. **C56** (1992) 661, [Erratum: Z. Phys.C67,364(1995)] (cit. on pp. 89, 90).

[189] N. Isgur, C. Morningstar, and C. Reader, *The a1 in tau Decay*, Phys. Rev. **D39** (1989) 1357
(cit. on p. 89).

[190] D. G. Dumm et al.,
       tau —> pi pi pi nu(tau) decays and the a(1)(1260) off-shell width revisited,
       Phys. Lett. **B685** (2010) 158, arXiv: `0911.4436` `[hep-ph]` (cit. on p. 89).

[191] I. M. Nugent et al.,
       Resonance chiral Lagrangian currents and experimental data for $\tau^- \to \pi^- \pi^- \pi^+ \nu_\tau$,
       Phys. Rev. **D88** (2013) 093012, arXiv: `1310.1053` `[hep-ph]` (cit. on p. 89).

[192] G. Colangelo et al., *Structure functions in semihadronic tau decays*,
       Nucl. Phys. Proc. Suppl. **55C** (1997) 325, [,325(1996)], arXiv: `hep-ph/9611329` `[hep-ph]`
       (cit. on p. 90).

[193] D. V. Bugg, B. S. Zou, and A. V. Sarantsev,
       New results on pi pi phase shifts between 600-MeV and 1900-MeV,
       Nucl. Phys. **B471** (1996) 59 (cit. on p. 92).

[194] I. J. R. Aitchison and R. Pasquier, *Three-Body Unitarity and Khuri-Treiman Amplitudes*,
       Phys. Rev. **152** (1966) 1274 (cit. on pp. 92, 103, 109, 117–119, 175, 176).

[195] G. N. Fleming,
       Recoupling Effects in the Isobar Model. 1. General Formalism for Three-Pion Scattering,
       Phys. Rev. **135** (1964) B551 (cit. on pp. 92, 109, 113).

[196] W. J. Holman, *Modified Isobar Approximation for $\pi - \rho$ Scattering*,
       Phys. Rev. **138** (5B 1965) B1286,
       URL: `https://link.aps.org/doi/10.1103/PhysRev.138.B1286` (cit. on pp. 92, 109).

[197] I. Aitchison and J. Brehm,
       ARE THERE IMPORTANT UNITARITY CORRECTIONS TO THE ISOBAR MODEL?,
       Phys. Lett. B **84** (1979) 349 (cit. on pp. 92, 109).

[198] I. Lorenz and E. Passemar, *a_1 properties in hadronic tau decays*,
       PoS **ICHEP2016** (2016) 539, arXiv: `1702.05432` `[hep-ph]` (cit. on p. 92).

[199] S. Schael et al., *Branching ratios and spectral functions of tau decays: Final ALEPH
       measurements and physics implications*, Phys. Rept. **421** (2005) 191,
       arXiv: `hep-ex/0506072` `[hep-ex]` (cit. on pp. 94, 95, 107).

[200] M. Davier et al.,
       Update of the ALEPH non-strange spectral functions from hadronic τ decays,
       Eur. Phys. J. **C74** (2014) 2803, arXiv: `1312.1501` `[hep-ex]` (cit. on pp. 94, 95).

[201] J. Revels, M. Lubin, and T. Papamarkou, *Forward-Mode Automatic Differentiation in Julia*,
       arXiv:1607.07892 [cs.MS] (2016), URL: `https://arxiv.org/abs/1607.07892`
       (cit. on p. 95).

[202] B. Efron and R. J. Tibshirani, *An Introduction to the Bootstrap*,
       Monographs on Statistics and Applied Probability 57, Chapman & Hall/CRC, 1993
       (cit. on p. 99).

[203] A. Meurer et al., *SymPy: symbolic computing in Python*,
       PeerJ Computer Science **3** (2017) e103, ISSN: 2376-5992,
       URL: `https://doi.org/10.7717/peerj-cs.103` (cit. on p. 99).

[204]   W. R. Inc., *Mathematica, Version 11.3*, Champaign, IL, 2018 (cit. on p. 100).

[205]   R. C. Hwa, *Singularities in the Unphysical Sheets and the Isobar Model*,
        Phys. Rev. **130** (6 1963) 2580,
        URL: https://link.aps.org/doi/10.1103/PhysRev.130.2580 (cit. on p. 103).

[206]   M. T. Grisaru, *Three-Particle Contributions to Elastic Scattering*,
        Phys. Rev. **146** (4 1966) 1098,
        URL: https://link.aps.org/doi/10.1103/PhysRev.146.1098 (cit. on p. 109).

[207]   S. Mandelstam et al., *Isobar approximation of production processes*,
        Annals of Physics **18** (1962) 198, ISSN: 0003-4916,
        URL: http://www.sciencedirect.com/science/article/pii/0003491662900672
        (cit. on p. 109).

[208]   D. R. Harrington, *Two-Particle Approximation for the Three-Pion Amplitude*,
        Phys. Rev. **127** (6 1962) 2235,
        URL: https://link.aps.org/doi/10.1103/PhysRev.127.2235 (cit. on p. 109).

[209]   W. R. Frazer and D. Y. Wong, *Width of Three-Pion Resonances*,
        Phys. Rev. **128** (4 1962) 1927,
        URL: https://link.aps.org/doi/10.1103/PhysRev.128.1927 (cit. on p. 109).

[210]   L. F. Cook and B. W. Lee, *Unitarity and Production Amplitudes*, Phys. Rev. **127** (1962) 283
        (cit. on p. 109).

[211]   J. S. Ball, W. R. Frazer, and M. Nauenberg,
        "Scattering and production amplitudes with unstable particles", *High-energy physics.*
        Proceedings, 11th International Conference, ICHEP'62, Geneva, Switzerland, Jul 4-11, 1962,
        1962 141 (cit. on p. 109).

[212]   R. C. Hwa, *On the Analytic Structure of Production Amplitudes*,
        Phys. Rev. **134** (5B 1964) B1086,
        URL: https://link.aps.org/doi/10.1103/PhysRev.134.B1086 (cit. on p. 109).

[213]   J. D. Bjorken, *Construction of Coupled Scattering and Production Amplitudes Satisfying*
        Analyticity and Unitarity, Phys. Rev. Lett. **4** (9 1960) 473,
        URL: https://link.aps.org/doi/10.1103/PhysRevLett.4.473 (cit. on p. 109).

[214]   R. Blankenbecler and R. Sugar,
        Linear integral equations for relativistic multichannel scattering, Phys. Rev. **142** (1966) 1051
        (cit. on pp. 109, 114).

[215]   R. D. Amado, *Minimal three-body equations with finite-range effects*,
        Phys. Rev. **C12** (1975) 1354 (cit. on p. 109).

[216]   R. D. Amado, *Minimal three-body scattering theory*, Phys. Rev. Lett. **33** (1974) 333
        (cit. on p. 109).

[217]   R. Aaron and R. D. Amado, *Analysis of three-hadron final states*,
        Phys. Rev. Lett. **31** (1973) 1157 (cit. on p. 109).

[218]   R. Aaron, R. D. Amado, and J. E. Young,
        Relativistic three-body theory with applications to pi-minus n scattering,
        Phys. Rev. **174** (1968) 2022 (cit. on p. 109).

[219] C. Kacser, *The Discontinuities of the Triangle Graph as a Function of an Internal Mass. II*, J. Math. Phys. **7** (1966) 2008 (cit. on pp. 109, 118, 119).

[220] I. J. R. Aitchison and J. J. Brehm, *Unitary Analytic Isobar Model for the Reaction Nucleon - Meson to Nucleon - Meson Meson*, Phys. Rev. **D17** (1978) 3072 (cit. on p. 109).

[221] I. Aitchison and J. Brehm, *MEDIUM-ENERGY N pi pi DYNAMICS. 1.*, Phys. Rev. **D20** (1979) 1119 (cit. on p. 109).

[222] T. W. B. Kibble, *Kinematics of General Scattering Processes and the Mandelstam Representation*, Phys. Rev. **117** (1960) 1159 (cit. on pp. 112, 166, 177).

[223] M. T. Hansen and S. R. Sharpe, *Expressing the three-particle finite-volume spectrum in terms of the three-to-three scattering amplitude*, Phys. Rev. **D92** (2015) 114509, arXiv: `1504.04248` `[hep-lat]` (cit. on p. 116).

[224] V. Sokhoyan et al., *High-statistics study of the reaction $\gamma p \to p\, 2\pi^0$*, Eur. Phys. J. **A51** (2015) 95, [Erratum: Eur. Phys. J.A51,no.12,187(2015)], arXiv: `1507.02488` `[nucl-ex]` (cit. on p. 117).

[225] P. Guo, *Analytic continuation of the Pasquier inversion representation of the Khuri-Treiman equation*, Phys. Rev. **D91** (2015) 076012, arXiv: `1412.3970` `[hep-ph]` (cit. on p. 118).

[226] I. J. R. Aitchison and C. Kacser, *Singularities and discontinuities of the triangle graph, as a function of an internal mass*, Il Nuovo Cimento A (1965-1970) **40** (1965) 576, ISSN: 1826-9869, URL: `https://doi.org/10.1007/BF02721045` (cit. on p. 118).

[227] R. Pasquier, *Orsay Report IPNO/TH 31*, unpublished, 1965 (cit. on p. 119).

[228] R. Pasquier, *Sur quelques aspects du problème à trois corps relativiste*, PhD thesis: Université Paris-Sud (Orsay), 1973, URL: `https://inis.iaea.org/collection/NCLCollectionStore/_Public/06/164/6164345.pdf` (cit. on p. 119).

[229] I. M. Nugent, *Invariant mass spectra of $\tau^- \to h^- h^- h^+ \nu_\tau$ decays*, Nucl. Phys. Proc. Suppl. **253-255** (2014) 38, arXiv: `1301.7105` `[hep-ex]` (cit. on p. 125).

[230] M. J. Lee et al., *Measurement of the branching fractions and the invariant mass distributions for $\tau^- \to h^- h^+ h^- \nu_\tau$ decays*, Phys. Rev. **D81** (2010) 113007, arXiv: `1001.0083` `[hep-ex]` (cit. on p. 125).

[231] M. Nozar et al., *Search for the photo-excitation of exotic mesons in the pi+ pi+ pi- system*, Phys. Rev. Lett. **102** (2009) 102002, arXiv: `0805.4438` `[hep-ex]` (cit. on p. 125).

[232] C. Salgado and E. S. Smith, *GlueX: Meson spectroscopy in photoproduction*, PoS **XLASNPA** (2014) 015 (cit. on p. 125).

[233] A. Jackura, M. Mikhasenko, and A. Szczepaniak, *Amplitude analysis of resonant production in three pions*, EPJ Web Conf. **130** (2016) 05008, arXiv: `1610.04567` `[hep-ph]` (cit. on p. 145).

[234] E. Klempt and A. Zaitsev,
Glueballs, Hybrids, Multiquarks. Experimental facts versus QCD inspired concepts,
Phys. Rept. **454** (2007) 1, arXiv: `0708.4016` `[hep-ph]` (cit. on p. 146).

[235] S. U. Chung, *SPIN FORMALISMS*,
(1971), CERN-71-08, Lectures given in Academic Training Program of CERN, 1969-1970
(cit. on p. 162).

[236] R. Kutsckhe, *An angular distribution cookbook*,
URL: `http://home.fnal.gov/~kutschke/Angdist/angdist.ps` (cit. on p. 162).

[237] G. Bonnevay, *A model for final-state interactions*,
Il Nuovo Cimento (1955-1965) **30** (1963) 1325, ISSN: 1827-6121,
URL: `https://doi.org/10.1007/BF02828791` (cit. on pp. 175, 177).

[238] M. Froissart, *Asymptotic behavior and subtractions in the Mandelstam representation*,
Phys.Rev. **123** (1961) 1053 (cit. on p. 178).

Other analyses

A.1 $\eta\pi/\rho\pi$ coupled channel amplitude

A single channel analysis of the $\eta\pi$ D-wave was performed by the JPAC collaboration and published in a JPAC-COMPASS combined paper [4]. The analysis was led by A. Jackura, I was responsible for the cross check of the results and tests of the systematic uncertainties due to coupling to $\rho\pi$ channel. Details of the developed coupled-channel model are described below.

Parametrization of the scattering amplitude

The transition amplitude is denoted by T_{ij}

$$\langle f|T|i\rangle = M_{if} (2\pi)^4 \delta^4(p_1 + p_2 - p_1' - p_2') \tag{A.1}$$

where i, f are the initial and the final state. Those are considered to be either $\eta\pi$ or $\rho\pi$. For the convenience the channels are labeled by 1 ($\eta\pi$) and 2 ($\rho\pi$). First, we dissect out the threshold factors,

$$M_{if} = h_2((p_i R)^2)\hat{M}_{if}h_2((p_f R)^2), \quad h_2^2(z) = \frac{z^2}{1 + z^2}, \tag{A.2}$$

where $p_1 = \lambda^{1/2}(s, m_\eta^2, m_\pi^2)/(2\sqrt{s})$, and $p_2 = \lambda^{1/2}(s, m_\rho^2, m_\pi^2)/(2\sqrt{s})$ with $\lambda(x, y, z) = x^2 + y^2 + z^2 - 2xy - 2yz - 2zx$ being the Källén function. R is the Blatt-Weisskopf size parameter (see Appendix E.3), we use $R = 5\,\text{GeV}^{-1}$. The reduced amplitude $\hat{M}$ is parametrized in the matrix form

$$\hat{M}(s) = K(s)[1 - i\tilde{\rho}(s)K(s)/2]^{-1} \tag{A.3}$$

where ρ, and K are matrices given by

$$K = \frac{1}{m_1^2 - s}\begin{pmatrix} g_1^2 & g_1g_2 \\ g_2g_1 & g_2^2 \end{pmatrix} + \frac{1}{m_2^2 - s}\begin{pmatrix} h_1^2 & h_1h_2 \\ h_2h_1 & h_2^2 \end{pmatrix}, \quad \tilde{\rho}(s) = \begin{pmatrix} \tilde{\rho}_1(s) & 0 \\ 0 & \tilde{\rho}_2(s) \end{pmatrix}, \tag{A.4}$$

Table A.1: Values of the parameters in the $\eta\pi/\rho\pi$ coupled-channel model for the scattering amplitude.

m_1^2, GeV^2	1.8089 ± 0.0013	m_1^2, GeV^2	2.950 ± 0.011
g_1, GeV	1.345 ± 0.011	h_1, GeV	2.51 ± 0.19
g_2, GeV	-3.381 ± 0.014	h_2, GeV	4.893 ± 0.067

Table A.2: Values of the parameters in the model of the production amplitude. Since the parameters are strongly correlated, we provide six significant digits for the main value.

parameters	$\eta\pi$ ($i = 1$)	$\rho\pi$ ($i = 2$)
$c_i^{(0)}$	59.20060 ± 3.02954	-61.65760 ± 1.05773
$c_i^{(1)}$	-83.9214 ± 37.5529	-280.032 ± 30.772
$c_i^{(2)}$	-8.82913 ± 160.63800	$-2\,231.93 \pm 313.14$
$c_i^{(3)}$	$4\,127.610 \pm 411.796$	$-10\,944.00 \pm 1\,207.15$
$c_i^{(4)}$	$10\,412.000 \pm 743.662$	$-16\,693.80 \pm 1\,636.41$

where $\rho_i(s)$ denotes the reduced phase-space factor. The $\tilde{\rho}$ is the dispersive form of ρ given by

$$\tilde{\rho}_i(s) = \frac{s}{\pi i} \int_{s_{\rm th}}^{\infty} \frac{\rho_i(s')\mathrm{d}s'}{s'(s' - s - i\epsilon)}, \qquad \rho_i(s) = \frac{1}{8\pi} \frac{2p_i}{\sqrt{s}} h_2^2((p_i R)^2)), \tag{A.5}$$

where ϵ is very small positive number (take 10^{-5}), $s_{\rm th}$ is the threshold in the corresponding channel, *i.e.* $(m_\eta + m_\pi)^2$ or $(m_\rho + m_\pi)^2$. The masses of the particles are $m_\pi = 0.13957\,\mathrm{GeV}$, $m_\eta = 0.547\,\mathrm{GeV}$, $m_\rho = 0.7755\,\mathrm{GeV}$ [26]. The values of parameters are given in the Table A.1.

Parametrization of the production amplitude

The production amplitude $F(s)$ is defined in Sec. 2.3. It is a vector with two components: $\eta\pi$ production amplitude and the $\rho\pi$ production amplitude. We use the method of production vector to parametrize it:

$$F_i(s) = h_2((p_i R)^2) \sum_j \hat{M}_{if}(s)\alpha_j(s), \tag{A.6}$$

where the functions $\alpha_j(s)$ is a two-component production vector. To model it, we use a polynomial series of the conformal variable $\omega(s)$.

$$\alpha_i(s) = \sum_{k=0}^{4} c_w^{(k)} \omega^k(s), \qquad \omega(s) = \frac{1 - \sqrt{s}}{1 + \sqrt{s}}, \tag{A.7}$$

where $c_w^{(i)}$ are real coefficients given in the Table A.2. To adjust the model, we use the COMPASS data. The $\eta\pi$ D-wave was extracted in Ref. [63]. The data are selected in the range of the squared transferred momentum t', $0.1 < t' < 1\,\mathrm{GeV}^2$. The $\rho\pi$ D-wave was extracted in the PWA in Ref. [78]. To use the same kinematic domain, we sum the intensities of the $J^{PC}M^\epsilon = 1^{++}0^+$ $\rho\pi$ S-wave in 11 t' slices incoherently.

A simultaneous fit of $\eta\pi$ and $\rho\pi$ channels is shown in Fig. A.1.
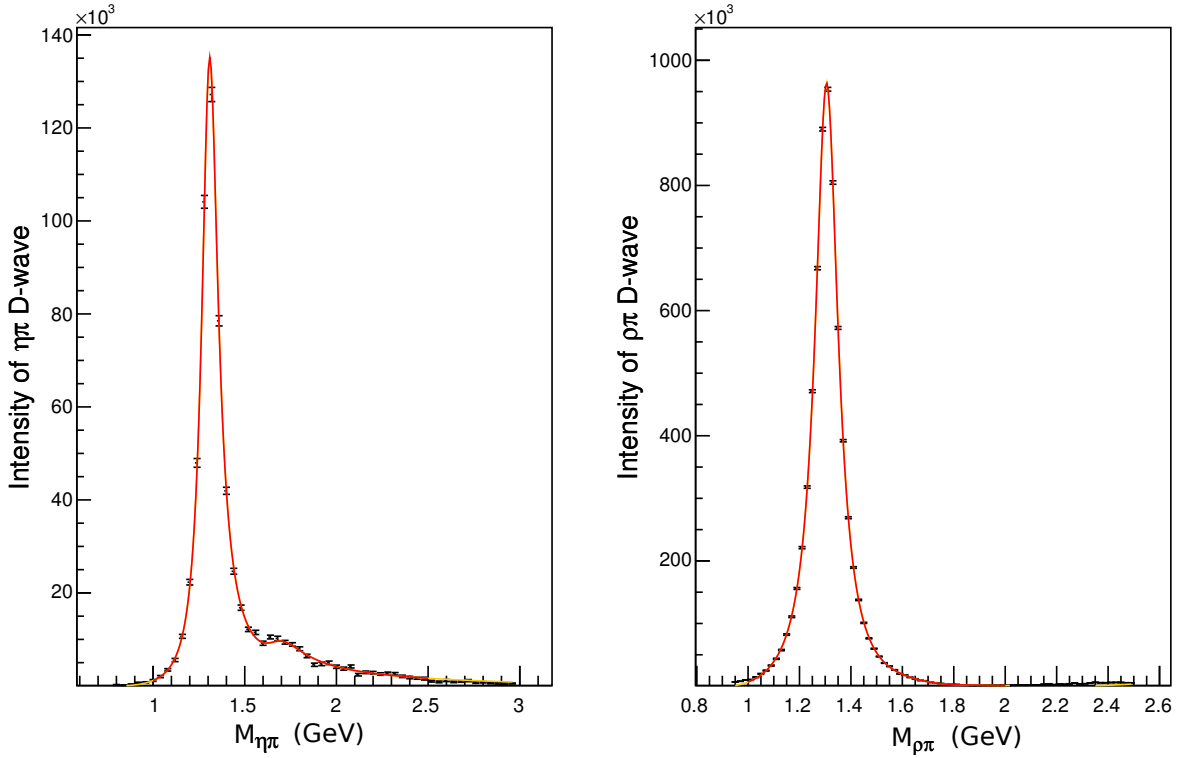
Figure A.1: A fit of the $\eta\pi/\rho\pi$ coupled-channel model to the COMPASS data The $J^{PC}M^\epsilon = 2^{++}1^+$ $\eta\pi$ D-wave is obtained in the PWA of the reaction $\pi p \to \eta\pi p$ [63], The $J^{PC}M^\epsilon = 2^{++}1^+$ $J^{PC}M^\epsilon = 2^{++}1^+$ $\rho\pi$ D-wave is from the PWA of the reaction $\pi^- p \to \pi^- \pi^+ \pi^- p$ [78]. The intensities are expressed in number of events. The red line shows the model curve in the intervals used for the fit. The extrapolation of the model beyond the fit range is shown by yellow line.

A.2 Mass-dependent fit of the 2^{-+} sector

This section summarizes an analysis aiming to extract the resonance parameters from the COMPASS data with a unitary model. The project was started in summer 2015 in collaboration with A. Jackura. Two years, 2016 and 2017, were dedicated to this problem in large extend. The intermediate results were pre-released (a cross-check has not been done) by the COMPASS collaboration and presented several times at conferences and workshops. Proceeding notes dedicated to the progress in the analysis have been published [7, 233]. Due to a lack of theoretical basis and remaining questions on systematic effects (particularly, the Deck effect) the analysis has not been finished. However, the project resulted in several developments which have been completed as separate works. Among of those are studies of the Deck model, *i.e.* Sec. 5, the $a_1(1260)$ investigation in Sec. 6, and the unified theory in Sec. 7.

$J^{PC} = 2^{-+}$ sector of the compass data

The main puzzle of the $J^{PC} = 2^{-+}$ sector is an interplay of the two states called $\pi_2(1670)$ and $\pi_2(1880)$, which have been seen to decay predominantly into 3π [26]. Both have identical quantum numbers, although, are only 200 MeV apart. This does not fit with quark model radial excitation
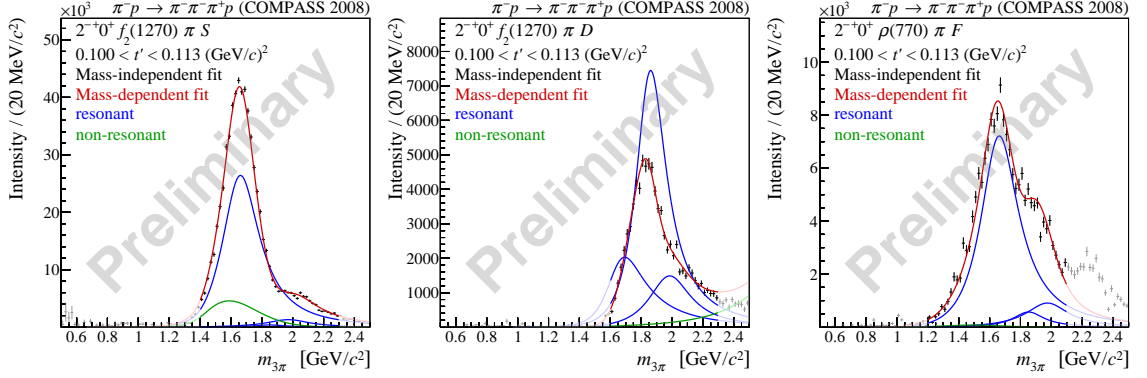
Figure A.2: A few partial waves in the $J^{PC}M^\epsilon = 2^{-+}0^+$ used in the resonance analysis of Ref. [3]: $f_2\pi$ S-wave (left), $f_2\pi$ D-wave (middle), and $\rho\pi$ F-wave (right). The data points are the wave intensities, *i.e.* elements of the SDM obtained as results of the mass-independent analysis of Ref. [78] for the first t'-slice (see the legends). The red curve shows the model adjusted to the data. Intensity distributions of the Breit-Wigner components of the model are shown by the blue curves. The green lines represent the intensity of the background component. The plots are from the Ref. [3].

trajectories or Regge trajectories of hadrons. The second state, $\pi_2(1880)$, is suggested to be a hybrid meson (see Ref. [234] and references therein). The parameters of those resonances are not well established. The mass dependent fit of the COMPASS data in the 2^{-+} sector indicated a striking need for a better dynamical model. In Ref. [3], it was found that the description of partial waves requires actually three π_2 resonances. Those states largely overlap and also require a coherent non-resonant background underneath (see Fig. A.2). In the conventional approach, the amplitudes for the partial waves are written as a sum of three resonance components parametrized by Breit-Wigner amplitudes (*cf.* Eq. (3.28)), and the non-resonant background (*cf.* Eq. (3.29)).

We develop a coupled-channel model which is based on the requirement of unitarity in the system of a subchannel resonance (Isobar) and the bachelor pion. The model was originally inspired by the quasi-two-body unitarity constraints proposed by Basdevant and Berger in Ref. [141]. One can derive this approach as a simplification of the general framework presented in Sec. 7.

Simplification 1: For the unitarity relation, we take into account only 3π intermediate states. Moreover, in a basis of the partial waves, we restrict our model to a few significant waves. The 3π elasticity approximation is justified below 2 GeV since the ground state $\pi_2(1670)$ decays to 3π with 95% branching ratio [26]. As discussed in Sec. 3.3.2, the COMPASS PWA model consists of 80 waves with positive reflectivity. The 2^{-+} consists of 17 waves. 8 waves contribute to the $J^{PC}M^\epsilon = 2^{-+}0^+$ sector, they are $f_2\pi$ S-, D-, H-waves, $\rho\pi$ P-, F-waves, $(\pi\pi)_S\pi$ D-wave, $f_0\pi$ D-wave, and $\rho_3\pi$ P-wave. In our analysis, we use a set of up to five major waves .

Simplification 2: We approximate the 3π system by the isobar-pion interaction and neglect interference terms in the rescattering. The $|3\pi\rangle$ state under the approximation is reduced to $|\xi\pi\rangle$, where ξ is an unstable Isobar. The production amplitude is denoted by $F(s,\tau)$. The partial-wave expansion reads,

$$F(s,\tau) = \sum_{JM\epsilon LS} \sum_I C_I F_{LS}^{JM\epsilon}(s,\sigma) Z_{LS}^{JM\epsilon}(\Omega_1,\Omega_{23}), \tag{A.8}$$

where, with respect to Eq. (3.7), we dropped the helicity indices for the proton, assuming a dominance

of the helicity non-flip amplitude. The function $Z_{LS}^{JM\epsilon}$ is defined in Eq. (3.9) with the reflectivity index introduced in Eq. (3.11). The isospin coefficient C_I is given in Eq. (3.8).

Simplification 3: We assume a factorization and a simple σ dependence of $F_{LS}^{JM\epsilon}$.

$$F_{LS}^{JM\epsilon}(s,\sigma) = \mathcal{F}_{LS}^{JM\epsilon}(s) h_L(s,\sigma) f_S(\sigma), \tag{A.9}$$

where $\mathcal{F}_{LS}^{J}(s)$ is an amputated dynamic production amplitude which does not depend on σ. The function $f_S(\sigma)$ is the isobar line shape as shown in Appendix D. The $h_L(s,\sigma)$ is a factor which ensures a correct threshold behavior and asymptotic limit. We use a simplified form of the Blatt-Weisskopf factors,

$$h_L^2 = \left(\frac{R^2 q^2}{1 + R^2 q^2}\right)^L, \quad q = 4\pi\rho_S\sqrt{s}. \tag{A.10}$$

In order to use the unitarity constraint we need to introduce the $3 \to 3$ scattering amplitude (see Sec. 7), which, under assumptions we made, reduces to $\xi\pi \to \xi'\pi$ scattering. In order to reduce the general model discussed in Sec. 7 to the quasi-two-body scattering, the *ladder interaction* has to be neglected. The full scattering amplitude T is parametrized by the *short-range* interaction. The partial-wave expansion of T reads,

$$T = \sum_{J} \sum_{L'S'LS} \sum_{M\epsilon} Z_{LS}^{JM\epsilon*}(\Omega_1', \Omega_{23}') T_{L'S'LS}^{J}(\sigma_1, s, \sigma_{23}) Z_{L'S'}^{JM\epsilon}(\Omega_1', \Omega_{23}'), \tag{A.11}$$

where we consistently use the factorization assumption,

$$T_{L'S'LS}^{J}(\sigma', s, \sigma) = f_{S'}(\sigma') h_{L'}(s,\sigma') \mathcal{T}_{L'S'LS}^{J}(s) h_L(s,\sigma) f_S(\sigma). \tag{A.12}$$

The amplitude T is independent of the production process. The relation to the production amplitude $\mathcal{F}_{LS}^{J}(s)$, is obtained through the unitarity relation:

$$2 \operatorname{Im} \mathcal{F}_{LS}^{JM\epsilon}(s) = \mathcal{T}_{LSL'S'}^{*J}(s) \Sigma_{L'S'}(s) \mathcal{F}_{L'S'}^{JM\epsilon}(s), \tag{A.13}$$

$$2 \operatorname{Im} \mathcal{T}_{LSL'S'}^{J}(s) = \mathcal{T}_{LSL''S''}^{*J}(s) \Sigma_{L''S''}(s) \mathcal{T}_{L''S''L'S'}^{J}(s), \tag{A.14}$$

where the quasi-two-body phase-space factor reads,

$$\Sigma_{LS}(s) = \frac{1}{(8\pi)^2} \int_{4m_\pi^2}^{(\sqrt{s}-m_\pi)^2} \frac{d\sigma}{2\pi} h_L^2(s,\sigma) \frac{\lambda^{1/2}(s,\sigma,m_\pi^2)\lambda^{1/2}(\sigma,m_\pi^2,m_\pi^2)}{s\sigma} |f_S(\sigma)|^2. \tag{A.15}$$

Parametrization of the scattering matrix and the pole search

The unitarity constraint to the scattering amplitude $\mathcal{T}$ in Eq. (A.14) can be built in using the K-matrix approach (see Sec. 2.2). In matrix notations over LS indices (J is fixed to 2), it reads,

$$\mathcal{T}(s) = K(s) \left[1 - i\,\tilde{\Sigma}(s)K(s)/2\right]^{-1}, \tag{A.16}$$

where $K(s)$ is a matrix of functions which is parametrized by the sum of pole terms, $\tilde{\Sigma}$ is a diagonal matrix with elements $\tilde{\rho}_{LS}$, that are given by a dispersive integral (*cf.* Eq. (A.17)),

$$\tilde{\Sigma}_{LS}(s) = \frac{1}{\pi i} \int_{s_{\text{th}}}^{\infty} \frac{\Sigma_{LS}(s')}{s' - s} \mathrm{d}s', \quad K_{LSL'S'}(s) = \sum_R \frac{g_{LS}^R g_{L'S'}^R}{s_R - s}. \tag{A.17}$$

The amplitude $\mathcal{T}$, is an analytic function, defined in the complex s-plane. Resonances in the $\xi\pi$ system are found by identifying poles in the unphysical Riemann sheets. The physical unitarity cut starts at the three pion threshold, $\sqrt{s} = 3m_\pi$. The sheet attached to the real axis from below is called the *second Riemann sheet*. Every quasi-two body channel of $\mathcal{T}$ introduces an additional cut which starts in the complex plane as demonstrated in details in Sec. 6.3.1. All those complex cuts need to be rotated (see Fig. 6.4) to give access to the closest unphysical sheet.

The scattering amplitude at the second Riemann sheet, T_{II}^{-1}, is calculated according to Eq. (2.32), where $\Sigma(s)$ used instead of the phase-space factor $\rho(s)$. Instead of looking for poles in T_{II}, we explore the inverse function T_{II}^{-1}, and find the point where it vanishes exactly. It is practically convenient to search for the solution of the equation, $\det(T_{II}^{-1}K) = 0$, which is equivalent to

$$\det\left(1 + i(\tilde{\Sigma}(s)/2 + \Sigma(s))K(s)\right) = 0. \tag{A.18}$$

Candidates for the solutions are found by minimization of the modulus of the left part. The minima are validated by a direct check of Eq. (A.18).

Two models of the production amplitude

Two production models, introduced in Sec. 2.3, are considered

- **Model–*I*: production vector.**
  The production amplitude is written as the scattering matrix multiplied by an arbitrary source vector, denoted by $\alpha_{LS}^{JM\epsilon}(s)$,

  $$\mathcal{F}_{LS}^{JM\epsilon}(s) = \sum_{L'S'} \mathcal{T}_{LSL'S'}^J(s)\, \alpha_{L'S'}^{JM\epsilon}(s). \tag{A.19}$$

  The functions $\alpha_{LS}^{JM\epsilon}(s)$, cannot have the a right-hand cut in order to preserve unitary. To model these functions, polynomial series of the conformal variable $\omega(s)$, are used.

  $$\alpha_w(s) = e^{i\phi_w} \sum \alpha_w^{(i)} \omega^i(s), \qquad \omega(s) = \frac{\sqrt{s_1} - \sqrt{s + s_0}}{\sqrt{s_1} + \sqrt{s + s_0}}, \tag{A.20}$$

  where we used a combined index $w = (JM\epsilon LS)$ for brevity of notation. The variables s_0 and s_1 are parameters of the conformal map: s_0 gives the position of the left-hand cut, while s_1 determines the slope of the s dependence. The expansion coefficients $\alpha_w^{(i)}$, are real, a single complex phase ϕ_w, is a free parameter of the fit. For indication of the parameter space, we introduce a superscript. Model–$I^{(n,m,l)}$ refers the n-channels amplitude with m poles in the K-matrix and l terms in the polynomial series.

- **Model–*II*: unitarized background.**
  The second model uses an explicit background term $\mathcal{B}_{LS}^{JM\epsilon}(s)$, which is incorporated according to Eq. (2.41).

$$\mathcal{F}_{LS}^{JM\epsilon}(s) = \mathcal{B}_{LS}^{JM\epsilon}(s) + \sum_{L'S'} \mathcal{T}_{LSL'S'}^{J} \left(c_{L'S'}^{JM\epsilon} + \frac{1}{2\pi} \int_{s_{\text{th}}}^{\infty} \frac{\mathcal{B}_{L'S'}^{JM\epsilon}(s') \, \Sigma_{L'S'}(s')}{s' - s} \mathrm{d}s' \right), \quad \text{(A.21)}$$

where $c_{L'S'}^{JM\epsilon}$ parametrizes the short-range interaction. These coefficients c, are complex constants adjusted in the fit. Eq. (A.21) resembles the model suggested by Basdevant and Berger in Ref. [62].

The background $\mathcal{B}_{LS}^{JM\epsilon}(s)$, is calculated by projecting the "Standard Deck" amplitude (see Sec. 5) to the partial waves. The projections, however, have σ dependence which cannot be addressed with the approximations stated above. An artificial method is used to get rid of this dependence. The subchannel invariant mass in those projections is set to the nominal mass of the isobar above the isobar-pion threshold, $\sqrt{s_{\text{th}}} = m_\xi + m_\pi$. Below the $\sqrt{s_{\text{th}}}$, the projections are evaluated for the value of σ that are on the interpolation between the nominam Isobar mass and the two-pion threshold, $\sqrt{\sigma_{\text{th}}} = 2m_\pi$. This way of omitting the σ dependence makes the background model unreliable (see the discussion on features of the projections in the COMPASS basis in Sec. 5.4). Moreover, there are large uncertainties on the line shape of the partial wave projections due to questions on the dynamic model for the pion propagator discussed in Sec. 5.3. Nevertheless, the obtained projections have two simple features of the background observed in the data. It rises near threshold s_{th}, and falls at high energies. The projections are purely real. Due to this large uncertainty, the relative strength of the background was not fixed. The background couplings are free parameters for all waves and all t' slices. Model–$II^{(n,m)}$ refers the n-channels amplitude with m poles in K-matrix and the unitarized background.

Fit to the COMPASS data and extracted poles

Free parameters of the models are positions of the K-matrix poles, the expansion coefficients of the production coefficients in Model–*I* and the strength of the "background" term and the "direct production" term in the Model–*II*. The data points from the COMPASS PWA are given in slices of t'. The differences in the intensity distributions for different t' slices, are attributed to the variations in the production mechanism. All data have to be fitted simultaneously using an independent set of production parameters for every t'-slice and one production-independent set of parameters for the scattering matrix.

To address the feasibility of the approach, many exploratory studies have been performed. The Model–*I* was found very flexible due to the large freedom of adjusting the production parameters (the model typically contains a few hundred free parameters). Due to the same reason, the model is found to have stability problems. Many local minima are barely distinguishable, and the fit parameters are largely correlated. Fig. A.3 and Fig. A.4 show the first t'-slice of the fit with Model–$I^{(3,3,6)}$ and Model–$I^{(4,4,7)}$, respectively. The plots demonstrate that the intensities can be described rather well within the Model–*I*. Most of the features seen in the data are reproduced in the fit. Namely, both the main peak and the shoulder of the $f_2\pi$ S-wave are described. The structure at $1.8\,\text{GeV}$ appears differently in different waves: it is a dip in the $(\pi\pi)_S\pi$ D-wave and a well pronounced peak in the
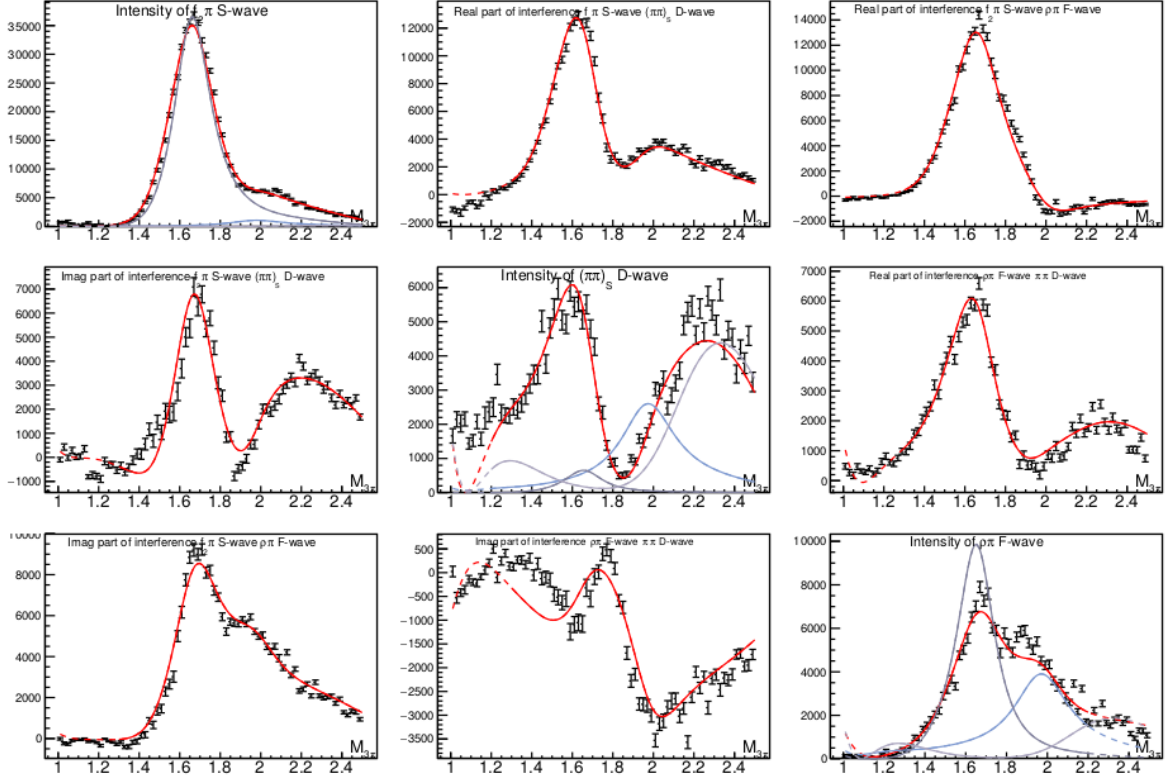
Figure A.3: The results of the fit of the dynamic model Model–$I^{(3,3,6)}$ to the COMPASS SDM with $J^{PC}M^\epsilon = 2^{-+}0^+$. The fit is performed simultaneously with all 11 t' slices, the first slice, $0.1 < t' < 0.112853\,\mathrm{GeV}^2$, is shown. The columns and rows are numbered from left to right and from top to bottom: they refer to the following waves: $f_2\pi$ S-wave, $(\pi\pi)_S\pi$ D-wave, and $\rho\pi$ F-wave. The wave intensities are shown on the diagonal of the plot matrix. The off-diagonal elements are the real (upper triangle) and imaginary (lower triangle) parts of the interference terms (see off-diagonal elements of the SDM in Eq. (3.25)). y-axis shows intensity of the waves and the interference terms expresses in the number of events, x-axis is the invariant mass of the three-pion system in GeV. The model includes three poles in the K-matrix and five expansion terms in the production vector for every channel. The other colored lines illustrate projections of the model to the intensities and interference terms when all but one K-matrix poles are turned off (couplings in Eq. (2.24) are set to zero). The range where the model has been fitted is indicated by solid lines, the dashed parts show the extrapolation of the model.

$f_2\pi$ D-wave as shown in Fig. A.6. The three hills of the $\rho\pi$ F-wave are reproduced in both models, however, we notice that the contribution of the K-matrix parameters is quite different for the two models, Model–$I^{(3,3,6)}$ and Model–$I^{(4,4,7)}$. Parameters of the K-matrix are not physical, and only the poles of T do identify hadronic resonances. However, there is an asymptotic correspondence between the K-matrix poles and the poles of T-matrix. When the K-matrix couplings in Eq. (2.24) are scaled simultaneously to zero, the T-matrix approaches K as seen in Eq. (A.16) (the inverted matrix in Eq. (A.16) is an identity in the limit). Therefore, for every pole which is put in the K-matrix, there is the corresponding pole in the complex plane.

The analytic continuation is presented in the Fig. A.5 for Model–$I^{(3,3,6)}$, and Fig. A.6 for the Model–$I^{(4,4,7)}$. In both attempts, three poles of the K-matrix have converged to values close to the range of the fit. The fourth K-matrix pole in Fig. A.6 ended up at higher energy outside of the fit
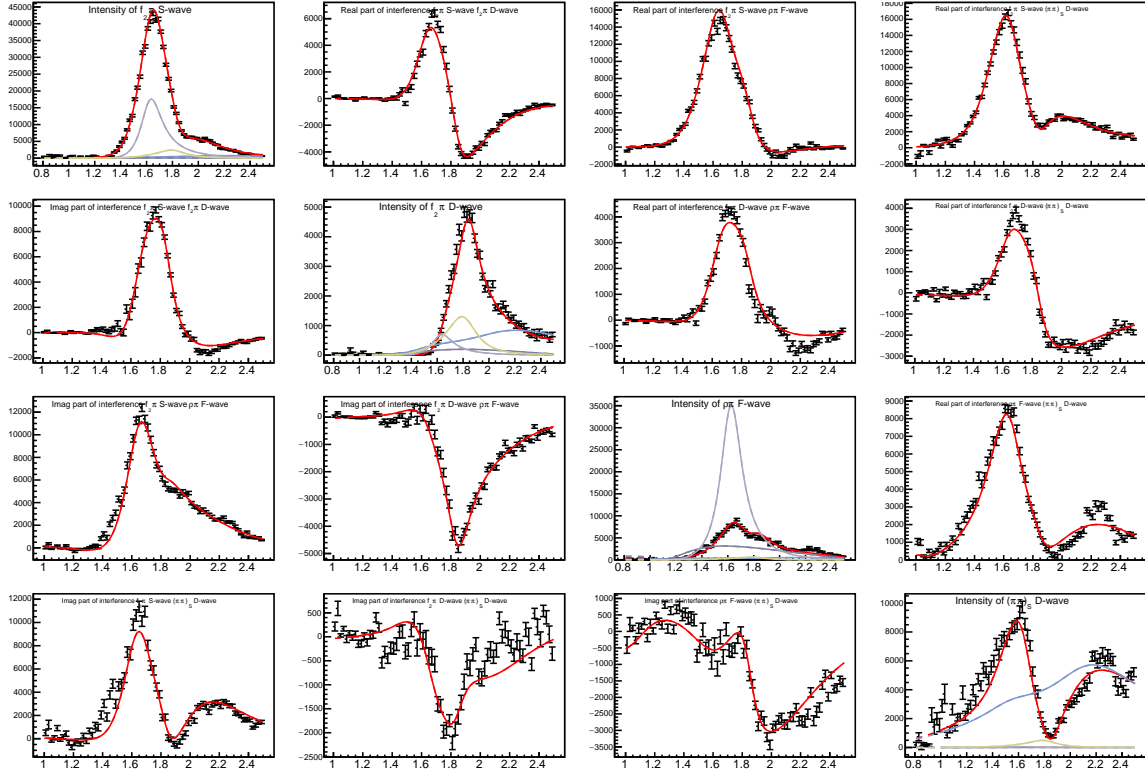
Figure A.4: Same as Fig. A.3 but with the $\text{Model--}I^{(4,4,7)}$. The used waves are $f_2\pi$ S-wave, $f_2\pi$ D-wave, $\rho\pi$ F-wave and $(\pi\pi)_S\pi$ D-wave. y-axis shows intensity of the waves and the interference terms expresses in the number of events, x-axis is the invariant mass of the three-pion system in GeV.

range. We find three resonance poles, which would correspond to $\pi_2(1670)$, $\pi_2(1880)$, and $\pi_2(2005)$. The positions of those poles, however, are not well determined.

The approach used in $\text{Model--}II$ has much fewer parameters, the minimum is better determined. On the other hand, it gives worse description of the data. Especially, the description of the $\rho\pi$ P-wave and $f_2\pi$ D-wave was found very problematic, possibly because these waves require a large background fraction. The largest set of the data which is reasonably described within the $\text{Model--}II$ is the three waves set presented in Fig. A.7. The main problem of this approach seems to be the simplistic and possibly incorrect background model. It is indirectly seen from the fact that the amplitude for the background, drawn by a light-green line in Fig. A.7, is nearly zero for $f_2\pi$ S-wave and the $\rho\pi$ F-wave. It seems to be preferred by the fit procedure, to assign the whole amplitude to the short-range component ("direct production"), because this part is more flexible, while the used background does not necessarily represent the physics right. The resonant poles found for the $\text{Model--}II^{(3,3)}$ are seen in Fig. A.8. The fit seems to prefer a narrow $\pi_2(1880)$ and a slightly lighter $\pi_2(1670)$. The distant $\pi_2(2005)$ does not look reliable. An isolated contribution of this pole is seen on the intensity plot for the $(\pi\pi)_S\pi$ D-wave. Its interference to the other components and the background is important, therefore, large correlations to the background shape are expected.

The results of the three models highlighted in the text are summarized in Table A.3. The poles are ordered by their mass and assigned to $\pi_2(1670)$, $\pi_2(1880)$, and $\pi_2(2005)$. In the conventional
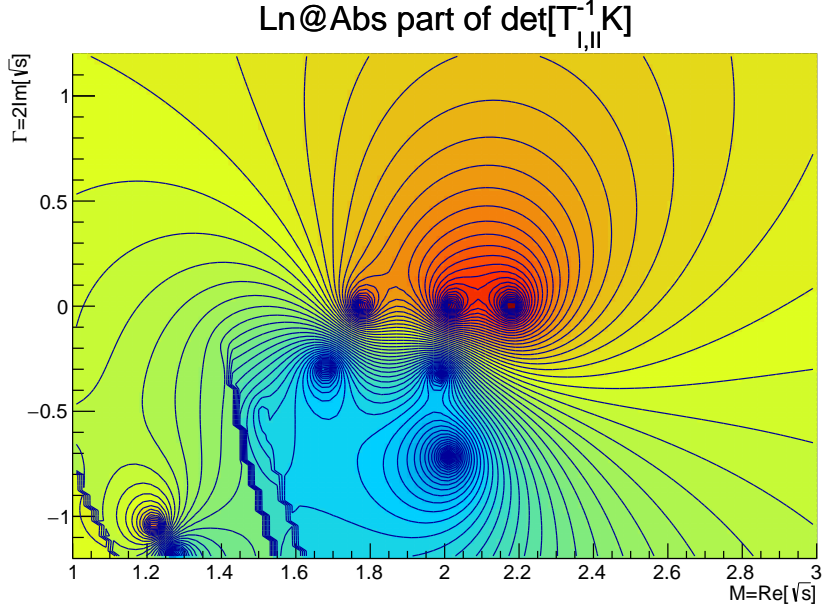
Figure A.5: Analytic continuation of the scattering amplitude in Model–$I^{(3,3,6)}$ to the unphysical sheet. The expression $|\det(T^{-1}K)|$ is calculated in the complex s plane at the points $s = (M - i\Gamma/2)^2$, where M in the units of GeV is given by the x coordinate, and Γ in the units of GeV is set by the y coordinate. For the positive values of Γ (y-axis), the expression $|\det(T(s)^{-1}K(s))|$ is presented by the color code, while for the negative values of Γ (nagative values along y-axis), the values of the expression $|\det(T_{II}(s)^{-1}K(s))|$ are presented. The red spots in the plot are zeros of the plotted expression. Those are positions of the K-matrix poles. The blue spots are resonance poles.

Table A.3: A summary of the limited systematic studies on the pole positions of the π_2 resonances are shown in black. The values state the limits for the pole parameters, they are found by comparing the three models presented in the text: Model–$I^{(3,3,6)}$, Model–$I^{(4,4,7)}$, and Model–$II^{(3,3)}$. Those number can be compared to the Breit-Wigner parameters obtained in the mass-dependent fit of Ref. [3] which are stated in gray. The pole positions for these parametrization are discussed in Sec. 3.3.3.

	m_p, MeV	Γ_p, MeV	m_{BW}, MeV	Γ_{BW}, MeV
$\pi_2(1670)$	$1640\ldots1720$	$250\ldots320$	1642^{+12}_{-1}	311^{+12}_{-23}
$\pi_2(1880)$	$1810\ldots1890$	$150\ldots220$	1847^{+20}_{-3}	246^{+33}_{-28}
$\pi_2(2005)$	$1950\ldots2350$	$850\ldots1050$	1962^{+17}_{-29}	269^{+16}_{-120}

approach of Ref. [3] the amplitude is modeled by a sum of Breit-Wigner amplitudes. In Sec. 3.3.3 we showed that the pole positions estimated from the Breit-Wigner parameters are close to these values, m_{BW} and Γ_{BW}. It makes it reasonable to compare it to our results from unitary based models. Our results have much large systematic uncertainties. The parameters of $\pi_2(1670)$ agree within their uncertainties, while we observe narrower $\pi_2(1880)$ and much wider $\pi_2(2005)$.
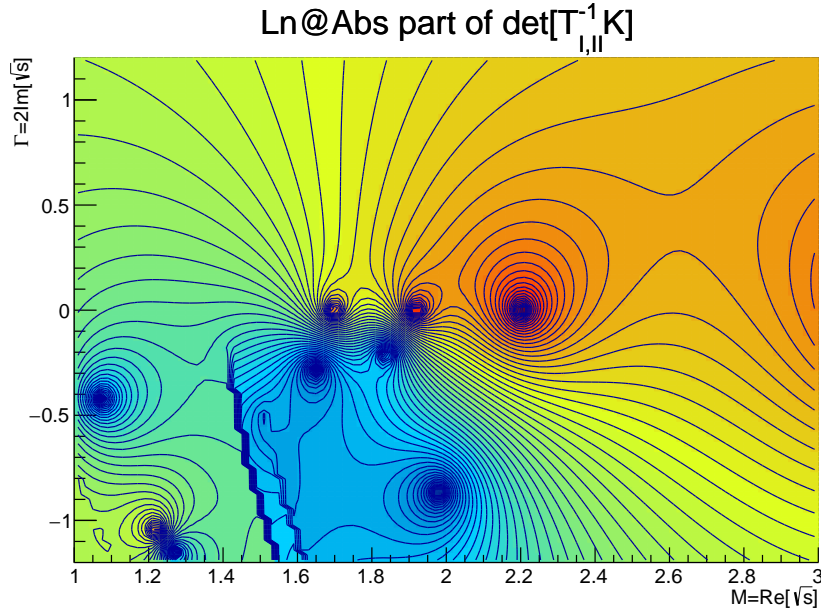
Figure A.6: Same as Fig. A.5 but with the $\mathrm{Model}{-}I^{(4,4,7)}$. M and Γ are the units of GeV.

Summary

We have performed fusibility studies of the unitarity based approach in the mass-dependent fit of the COMPASS data. We made a set of approximations which were required by the current model of the PWA: the final-state interaction was neglected in the production amplitude; we also neglected the ladder interaction in the scattering amplitude. The analysis was performed under the assumption of quasi-stable isobars.

We were able to describe a subset of 2^{-+} waves from the COMPASS PWA with a quality similar to the conventional Breit-Wigner analysis of Ref. [3]. Using methods of analytic continuation we extracted the pole position of the π_2 states. In agreement with the current understanding of the excited π_2 states, we found three resonances. We encounter several problems with the fit stability and multimodality of the solutions. In our model, the scattering isobar pion amplitude is well constraint, however, due to the unknown details of the production mechanism, the obtained pole positions have large systematic uncertainties. The preliminary results look promising and indicate a strong need for a better understanding of the background processes.
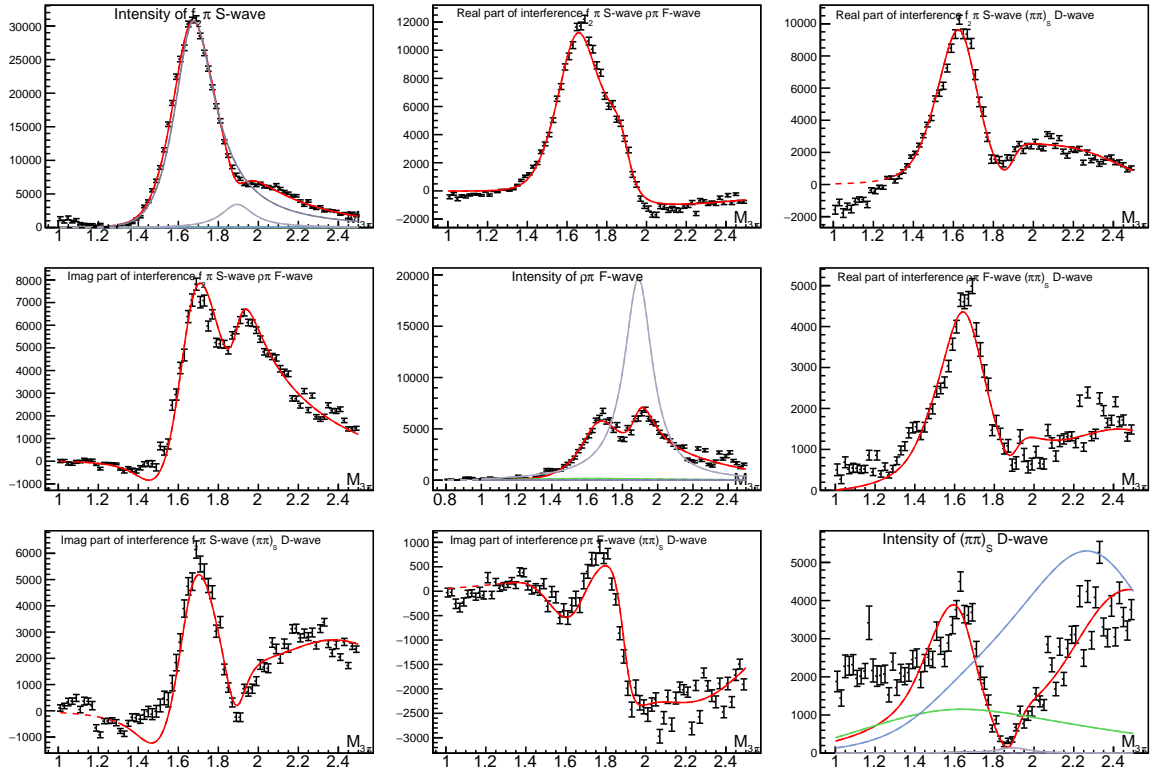
Figure A.7: Same as Fig. A.3 but with the $\mathrm{Model}{-}II^{(3,3)}$. The used waves are $f_2\pi$ S-wave, $\rho\pi$ F-wave and $(\pi\pi)_S\pi$ D-wave. y-axis shows intensity of the waves and the interference terms expresses in the number of events, x-axis is the invariant mass of the three-pion system in GeV.
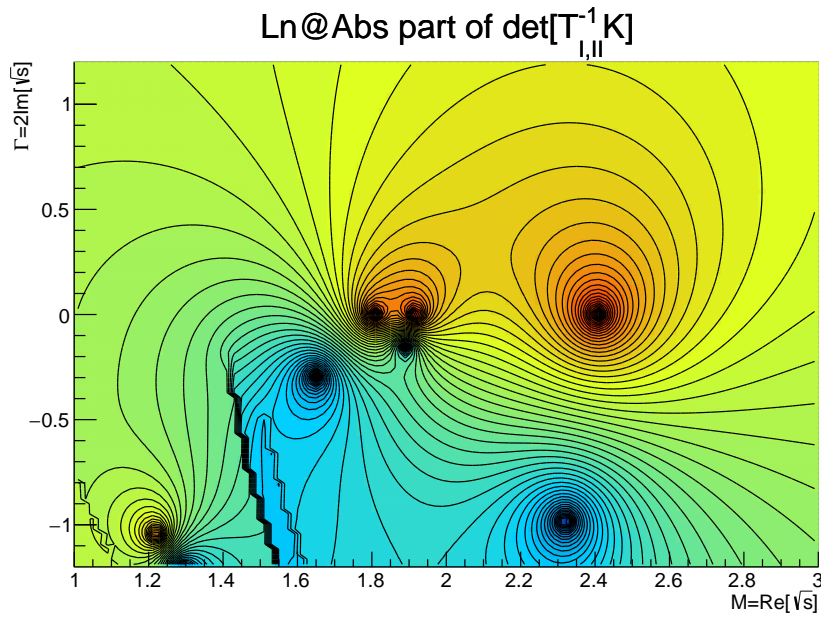
Figure A.8: Same as Fig. A.5 but with the Model–$II^{(3,3)}$. M and Γ are the units of GeV.

Phase space integrals

$$\mathrm{d}\Phi_n = \prod_{i=1}^{n} \frac{\mathrm{d}^3\vec{p}_i}{(2\pi)^3 \, 2E_i} \, (2\pi)^4 \delta^4(p_0 - \sum_{i=1}^{n} p_i), \tag{B.1}$$

where p_0 is a total momentum. The energy-momentum conservation conditions are presented by the δ-functions. Four integrals can be trivially solved using the δ-functions.

Two-body phase space

The two-body phase space space has two degrees of freedom.

$$\mathrm{d}\Phi_2 = \frac{1}{8\pi} \frac{2|\vec{p}^{\,*}|}{\sqrt{s}} \frac{\mathrm{d}\Omega}{4\pi} = \frac{1}{8\pi} \frac{\lambda^{1/2}(s, m_1^2, m_2^2)}{s} \frac{\mathrm{d}\Omega}{4\pi}, \tag{B.2}$$

where $\mathrm{d}\Omega = \mathrm{d}\cos\theta \, \mathrm{d}\phi$, the $\lambda^{1/2}(x, y, z)$ is a Källén function. For the $2 \to 2$ scattering, the integral over $\cos\theta$ can be related to the transferred momentum,

$$\mathrm{d}\Phi_2 = \frac{1}{8\pi} \frac{2|\vec{p}^{\,*}|}{\sqrt{s}} \frac{\mathrm{d}t}{4|\vec{p}^{\,*}||\vec{q}^{\,*}|} \frac{\mathrm{d}\phi}{2\pi} = \frac{1}{8\pi} \frac{\mathrm{d}t}{\lambda^{1/2}(s, m_1^2, m_2^2)} \frac{\mathrm{d}\phi}{2\pi}. \tag{B.3}$$

Three-body phase space

The three body phase space is given by the five dimensional integral.

$$\mathrm{d}\Phi_3 = \frac{\mathrm{d}\sigma}{2\pi} \mathrm{d}\Phi_2(s; \sigma, m_3^2) \mathrm{d}\Phi_2(\sigma; m_1^2, m_2^2) \tag{B.4}$$

$$= \frac{\mathrm{d}\sigma}{2\pi} \frac{1}{8\pi} \frac{\lambda^{1/2}(s, \sigma, m_3^2)}{s} \frac{\mathrm{d}\Omega_3}{4\pi} \frac{1}{8\pi} \frac{\lambda^{1/2}(\sigma, m_1^2, m_2^2)}{\sigma} \frac{\mathrm{d}\Omega_{12}}{4\pi} \tag{B.5}$$

$$= \frac{\mathrm{d}\sigma_1 \mathrm{d}\sigma_3}{2\pi(8\pi)^2 s \, \sigma} \frac{\mathrm{d}\Omega_3 \mathrm{d}\phi_{12}}{8\pi^2}. \tag{B.6}$$

Integrating over angles we find the expression for the three-body phase which is expressed as the single integral, which, however, cannot be solved analytically.

$$\Phi_3(s) = \frac{1}{(8\pi)^2} \frac{\mathrm{d}\sigma}{2\pi} \frac{\lambda^{1/2}(s, \sigma, m_3^2)}{s} \frac{\lambda^{1/2}(\sigma, m_1^2, m_2^2)}{\sigma}. \tag{B.7}$$

Four body phase space

It is convenient to write the 8 dimensional integral through the variables t, ϕ_{lab}, s, τ, with τ introduced in Eq. (3.2).

$$
\begin{aligned}
\mathrm{d}\Phi_4 &= \frac{\mathrm{d}s}{2\pi} \mathrm{d}\Phi_2(s_0; s, m_p^2)\, \mathrm{d}\Phi_3(s; m_1^2, m_2^2, m_3^2) \\
&= \frac{\mathrm{d}s}{2\pi} \frac{1}{8\pi} \frac{\mathrm{d}t}{\lambda^{1/2}(s_0, m_b^2, m_t^2)} \frac{\mathrm{d}\phi_{\text{lab}}}{2\pi}\, \mathrm{d}\Phi_3(s; m_1^2, m_2^2, m_3^2) \\
&= \frac{\lambda^{1/2}(s, \sigma_3, m_3^2) \lambda^{1/2}(\sigma_3, m_1^2, m_2^2)}{\lambda^{1/2}(s_0, m_b^2, m_t^2)} \frac{\mathrm{d}s\, \mathrm{d}t\, \mathrm{d}\phi_{\text{lab}}\, \mathrm{d}\sigma_3}{(2\pi)^3 (8\pi)^3 \sigma s_0 s \sigma} \frac{\mathrm{d}\Omega_3}{4\pi} \frac{\mathrm{d}\Omega_{12}}{4\pi}
\end{aligned}
$$

Manipulations with three-particle state

C.1 Definition of state vectors and partial-wave decomposition

Single-particle state

A single particle state is defined in the extension of the Hilbert space [47], it is written as a direct product of the momentum vector $|p\rangle$, the irreducible representation of the rotation group $|j\lambda\rangle$, and the isospin vector.

$$|p_1\rangle \otimes |j_1\lambda_1\rangle \otimes |i_1\mu_1\rangle \in V, \tag{C.1}$$

where the combined state is denoted by $|1\rangle$ for brevity of notations, the Hilbert space is denoted by V. The pion is scalar ($j = 0$) and isovector ($i = 1$), therefore, the notation can be simplified to $|p\mu\rangle$. The state has the standard relativistic normalization,

$$\langle p'_1\mu'_1 | p_1\mu_1 \rangle = 2E_1(2\pi)^3\delta^3(p'_1 - p_1)\delta_{\mu'_1\mu_1} = \tilde{\delta}(p'_1 - p_1)\delta_{\mu'_1\mu_1} = \tilde{\delta}_{1'1}, \tag{C.2}$$

where we demonstrate the short notations that are important for the further discussion on three-particle states.

Two-particle state and the partial-wave decomposition

A system of two identical particles has a state vector defined on the direct product of subspaces $V_I \otimes V_{II}$, where the spaces are identical $V_I \equiv V_{II} \equiv V$, roman indices label particles, *i.e.* we still can label particles as I and II, however, the state must be symmetric with respect to permutation of particle indices (pions are bosons).

$$|p_2\mu_2; p_3\mu_3\rangle = \frac{1}{2}\left[|p_2\mu_2\rangle \otimes |p_3\mu_3\rangle + |p_3\mu_3\rangle \otimes |p_2\mu_2\rangle \right] \in V \otimes V. \tag{C.3}$$

To perform a partial-wave expansion we first combine two isospin subspaces, then we expand direct products of the momentum states in partial waves for both terms in the sum (C.3). Since the isospin $SU(2)$ group permits a decomposition $3 \otimes 3 = 1 \oplus 3 \oplus 5$, the total isospin is $I \in \{0, 1, 2\}$. Hence, we

can choose a basis in the direct product which corresponds to irreducible representations of $SU(2)$.

$$|p_2\mu_2; p_3\mu_3\rangle = \frac{1}{2}\sum_{I,\mu_I} C^{I\mu_I}_{\mu_2\mu_3} \left[\, |p_2\rangle \otimes |p_3\rangle + (-1)^I |p_3\rangle \otimes |p_2\rangle \,\right] \otimes |I\mu_I\rangle \tag{C.4a}$$

$$= \sum_{I,\mu_I}\sum_{S,\lambda} \frac{1+(-1)^{S+I}}{2} C^{I\mu_I}_{\mu_2\mu_3} \sqrt{2S+1} D^S_{\lambda 0}(\Omega_{23}) \, |qS\lambda; I\mu_I\rangle\,. \tag{C.4b}$$

here $C^{I\mu_I}_{\mu_1\mu_2}$ is a Clebsch-Gordan coefficient $\langle 1,\mu_1; 1,\mu_2\,|I,\mu_I\rangle$ with $-I \leq \mu_I \leq I$. Orbital angular momentum S is a non-negative integer number, and helicity of the system λ varies from $-S$ to S. The angular function, $\sqrt{2S+1}D^S_{\lambda 0}(\phi_{23}, \theta_{23}, 0)$ performs decomposition of the little Hilbert space. To pull the common factor out, we use the symmetry of the Clebsch-Gordan coefficients $C^{I\mu_I}_{\mu_1\mu_2} = (-1)^I C^{I\mu_I}_{\mu_2\mu_1}$ and a symmetry of the spherical harmonics, $D^S_{\lambda 0}(\phi_{32}, \theta_{32}, 0) = D^S_{\lambda 0}(\pi + \phi_{23}, \pi - \theta_{23}, 0) = (-1)^S D^S_{\lambda 0}(\phi_{23}, \theta_{23}, 0)$. The inverse relation follows from Eq. (C.4b) if we multiply both sides by $\sqrt{2S'+1}\, D^{S'}_{\lambda' 0}(\Omega_{23})$ and integrate over angles, and also use orthogonality of the isospin indices.

$$|q_1 S\lambda; I\mu_I\rangle = \sum_{\mu_2\mu_3} C^{I\mu_I}_{\mu_2\mu_3} \int \frac{d\Omega_{23}}{4\pi} \, |p_2\mu_2, p_3\mu_3\rangle \sqrt{2S+1} D^{S*}_{\lambda 0}(\Omega_{23}) \tag{C.5}$$

We can find the normalization by acting on the state with a general identity operator.

$$\langle q'S'\lambda'I'\mu_I' \,|qS\lambda; I\mu_I\rangle = (2\pi)^4\delta^4(q_1' - q)\delta_{II'}\delta_{\mu_I\mu_I'} \frac{1}{\rho(\sigma)}, \tag{C.6}$$

$$\langle p_2'\mu_2'; p_3'\mu_3' \,|qS\lambda; I\mu_I\rangle = (2\pi)^4\delta^4(q_1' - q)\, C^{I\mu_I}_{\mu_2\mu_3}\, \sqrt{2S+1} D^S_{\lambda 0}(\Omega) \frac{1+(-1)^{S+I}}{2} \frac{1}{\rho(\sigma)}, \tag{C.7}$$

where $\rho(\sigma) = \sqrt{\sigma - 4m_\pi^2}/(8\pi\sqrt{\sigma})$.

Three-particle state

A state of three identical particles is symmetric under permutation of all particle indices.

$$|\equiv\rangle = \frac{1}{3!}\left(|p_1\mu_1\rangle |p_2\mu_2\rangle |p_3\mu_3\rangle + \text{symm.}\right) \tag{C.8a}$$

$$= \frac{1}{3}\sum_a |p_{a_1}\mu_{a_1}\rangle |p_{a_2}\mu_{a_2} p_{a_3}\mu_{a_3}\rangle = \frac{1}{3}\sum_a |a\rangle\,, \tag{C.8b}$$

where we introduced the shorthand notation for a state symmetrized with respect to permutation of two particles only, $|a\rangle$,

$$|a\rangle \equiv |p_{a_1}\mu_{a_1}\rangle |p_{a_2}\mu_{a_2} p_{a_3}\mu_{a_3}\rangle$$
$$\equiv |(p_{a_2}\mu_{a_2}, p_{a_3}\mu_{a_3}); p_{a_1}\mu_{a_1}\rangle,$$

which is symmetrized over permutation of the momenta p_{a_2} and p_{a_3} with the 3-tuple, $(a_1 a_2 a_3) \in \{(123), (312), (231)\}$. The semicolon used in the notation indicate a direct product of state components from different subspaces. We notice that there is a freedom to choose the bachelor subspace from the product $V \times V \times V$. The chosen one is denoted by V_P, $\mathrm{P} \in \{I, II, III\}$. For the brevity of notation we will omit this index since it does not play an important role in the further calculations.

We consider $\mathbb{I}$, the projection operator to the symmetrized three-particle space. Using the decomposition defined in Eq. (C.8), it can be expressed in terms of states $|a\rangle$,

$$
\begin{aligned}
\mathbb{I} &= \sum_{\mu_1\mu_2\mu_3} \int \frac{\mathrm{d}^3 p_1}{2E_1(2\pi)^3} \frac{\mathrm{d}^3 p_2}{2E_2(2\pi)^3} \frac{\mathrm{d}^3 p_3}{2E_3(2\pi)^3} |\equiv\rangle \langle\equiv| \\
&= \frac{1}{9} \sum_{\mu_1\mu_2\mu_3} \sum_{a,b} \int \frac{\mathrm{d}^3 p_1}{2E_1(2\pi)^3} \frac{\mathrm{d}^3 p_2}{2E_2(2\pi)^3} \frac{\mathrm{d}^3 p_3}{2E_3(2\pi)^3} |a\rangle \langle b| \\
&= \frac{1}{3} \sum_{\mu_1\mu_2\mu_3} \int \frac{\mathrm{d}^3 p_1}{2E_1(2\pi)^3} \frac{\mathrm{d}^3 p_2}{2E_2(2\pi)^3} \frac{\mathrm{d}^3 p_3}{2E_3(2\pi)^3} |1\rangle \langle 1| \\
&\quad + \frac{2}{3} \sum_{\mu_1\mu_2\mu_3} \int \frac{\mathrm{d}^3 p_1}{2E_1(2\pi)^3} \frac{\mathrm{d}^3 p_2}{2E_2(2\pi)^3} \frac{\mathrm{d}^3 p_3}{2E_3(2\pi)^3} |2\rangle \langle 3| \\
&= \frac{1}{3} \sum_{\mu_1\mu_2\mu_3} \int (\tilde{\mathrm{d}}p) |1\rangle \langle 1| + \frac{2}{3} \sum_{\mu_1\mu_2\mu_3} \int (\tilde{\mathrm{d}}p) |2\rangle \langle 3| ,
\end{aligned}
\tag{C.9}
$$

where we used a short notation for the product of integrals over the 3-momenta in the last line. The integral is fully symmetric under permutation of particle indices. Therefore, we are able to gather terms that mix bachelor indices and those that do not. For instance, the term $\int (\tilde{\mathrm{d}}p) |1\rangle \langle 1|$ translates to $\int (\tilde{\mathrm{d}}p) |2\rangle \langle 2|$ by interchanging the integration variables $p_1 \leftrightarrow p_2$ and using the symmetry of the state in Eq. (C.8) as follows,

$$
|(p_2\mu_2, p_3\mu_3); p_1\mu_1\rangle \xrightarrow{p_1 \leftrightarrow p_2} |(p_1\mu_1, p_3\mu_3); p_2\mu_2\rangle = |(p_3\mu_3, p_1\mu_1); p_2\mu_2\rangle .
\tag{C.10}
$$

The state $|a\rangle$ can be related to the partial wave projected states, $|qS\lambda; I\mu_I\rangle$, is a similar way as it done in Eq. (C.4). For example, the decomposition for the (23)-pair follows.

$$
|(p_2\mu_2, p_3\mu_3); p_1\mu_1\rangle \equiv \frac{1}{2} \big[|p_2\mu_2\rangle \otimes |p_3\mu_3\rangle + |p_3\mu_3\rangle \otimes |p_2\mu_2\rangle \big] \otimes |p_1\mu_1\rangle =
$$
$$
\sum_{I\mu_I} \sum_{S\lambda} C^{I\mu_I}_{\mu_2\mu_3} \frac{1+(-1)^{S+I}}{2} \sqrt{2S+1} D^S_{\lambda 0}(\Omega_{23}) |(q_3 S\lambda; I\mu_I); p_3\mu_3\rangle , \quad \text{(C.11)}
$$

The three-particle state is decomposed as,

$$
|\equiv\rangle = \frac{1}{3} \sum_{I\mu_I} \sum_{S\lambda} \sum_a \frac{1+(-1)^{S+I}}{2} C^{I\mu_I}_{\mu_{a_2}\mu_{a_3}} \sqrt{2S+1} D^S_{\lambda 0} |(q_i S\lambda; I\mu_I); p_a\mu_a\rangle ,
\tag{C.12}
$$

with $(a, a_2, a_3) \in \{(123), (231), (312)\}$.

In order to combine the two-particle states $|(q_i S\lambda; I\mu_I); p_i\mu_i\rangle$ with the bachelor state $|p_i\mu_i\rangle$ to the

basis of irreducible representation we follow the same steps as before in Eq. (C.4):

$$|(qS\lambda; I\mu_I); p\mu\rangle = \sum_{I\mu_I} \sum_{JM} C^{I\mu_I}_{\mu_I \mu} \sqrt{2J+1} D^J_{M\lambda}(\Omega) |P; JMS\lambda; I\mu_I\rangle, \tag{C.13}$$

where $P = q + p$ is a total momentum of the system, the total isospin state is $|I, \mu_I\rangle$, J is the total angular momentum, M is the momentum projection, and $\Omega = (\theta, \phi)$ are spherical angles of the vector q. As introduced before λ is the helicity of the subchannel state formed by two pions in a wave with orbital momentum S. The projection to basis $|P; JMS\lambda; I\mu_I\rangle$ is performed by the angular integration analogously to Eq. (C.5)

$$|P; JMS\lambda; I\mu_I\rangle = \sum_{\mu_I \mu_3} C^{I\mu_I}_{\mu_I \mu} \int \frac{d\Omega}{4\pi} \sqrt{2J+1} D^J_{M\lambda}(\phi, \theta, 0) |(qS\lambda; I\mu_I); p\mu\rangle. \tag{C.14}$$

Instead of working with the helicity basis it is often beneficial to introduce the LS-basis, related to the former one by a linear transformation [47, 235, 236].

$$|JMLS\rangle = \left(\frac{2L+1}{2J+1}\right)^{1/2} \sum_\lambda \langle L, 0; S, \lambda | J, \lambda\rangle |JMS\lambda\rangle \tag{C.15}$$

The expansion in Eq. (C.13) becomes

$$|(qS\lambda; I\mu_I); p\mu\rangle = \sum_{I_0 \mu_0} \sum_{JML} C^{I_0 \mu_0}_{\mu_I \mu} \langle L, 0; S, \lambda | J\lambda\rangle \sqrt{2L+1} D^J_{M\lambda}(\phi, \theta, 0) |P; JMLS; I_0 \mu_0\rangle \tag{C.16}$$

Combining Eq. (C.4b) and (C.16) we provide the partial-wave expansion of the three pion state.

$$|(p_2\mu_2, p_3\mu_3); p_1\mu_1\rangle = \sum_{JMLS} \sum_{I_0\mu_0 I\mu_I} \frac{1 + (-1)^{S+I}}{2} C^{I\mu_I}_{\mu_2\mu_3} C^{I_0\mu_0}_{\mu_I\mu_1} Z^{JM}_{LS}(\Omega_1, \Omega_{23}) |P; JMLS; I\mu\rangle, \tag{C.17}$$

where P is a total momentum, I_0 is the total isospin, μ_0 denotes the total isospin projection, the function Z^{JM}_{LS} takes care about the angular dependence,

$$Z^{JM}_{S\lambda}(\Omega_3, \Omega_{12}) = \sqrt{(2J+1)(2S+1)} D^J_{M\lambda}(\Omega_3) D^S_{\lambda 0}(\Omega_{12}), \tag{C.18a}$$

$$Z^{JM}_{LS}(\Omega_3, \Omega_{12}) = \sqrt{(2L+1)(2S+1)} \sum_\lambda \langle L, 0; S, \lambda | J, \lambda\rangle D^J_{M\lambda}(\Omega_3) D^S_{\lambda 0}(\Omega_{12}). \tag{C.18b}$$

For the angular variables we also use the circular notations or the spectator notations. For example, the index 3 in the argument of the $D^J_{M\lambda}$ function is referred to the angles of the vector $\vec{q}_3 = (\vec{p}_1 + \vec{p}_2)$ in the CM frame. As introduced before, Ω_{12} denotes spherical angles of particle 1 in the (12)-helicity frame. The twice partial wave projected three-pion state reads,

$$|\equiv\rangle = \frac{1}{3} \sum_i \sum_{JMLS} \sum_{I_0\mu_0 I\mu_I} \frac{1 + (-1)^{S+I}}{2} C^{I\mu_I}_{\mu_{i_2}\mu_{i_3}} C^{I_0\mu_0}_{\mu_I\mu_i} Z^{JM}_{LS}(\Omega_i, \Omega_{i_2 i_3}) |P; JMLS; I_0\mu_0\rangle_{i,P}, \tag{C.19}$$

where we broad back the bachelor subspace index P, and the bachelor momentum index, i. Importantly, the fully projected states within the same expansion indices $_{i,\mathrm{P}}$ are orthogonal.

$$_{i,\mathrm{P}}\langle P; J'M'; L'S'; I'\mu'_I \,|P; JMLS; I_0\mu_0\rangle_{i,\mathrm{P}} =$$
$$= (2\pi)^4 \delta^4(P'-P)\delta_{J'J}\delta_{M'M}\delta_{L'L}\delta_{S'S}\delta_{I'I}\delta_{\mu'_I\mu_I}\frac{1}{\rho_s(\sigma)}\frac{1}{\rho(\sigma)}, \quad \text{(C.20)}$$

where $\rho_s(\sigma) = \lambda^{1/2}(s,\sigma,m_\pi^2)/(8\pi s)$ with λ referring to a Källén function, $\rho(\sigma)$ is introduced below Eq. (C.7).

C.2 Properties of the angular functions

We use definitions of the Wigner D-functions given in the Appendix A of the "Elementary Particle Theory" book by Matrin and Spearman [47]. A few additional useful relations are inferred in what follows.

The Wigner D-function is related to the small Wigner d-function as,

$$D^j_{m_1 m_2}(\phi,\theta,\phi') = e^{-im_1\phi}d^j_{m_1 m_2}(\theta)e^{-im_2\phi'}. \quad \text{(C.21)}$$

The third angle is often zero, and the D-function is defined for a pair of arguments,

$$D^j_{m_1 m_2}(\Omega) \equiv D^j_{m_1 m_2}(\phi,\theta,0). \quad \text{(C.22)}$$

The normalization and the orthogonality relations for $D^j_{m_1 m_2}(\Omega)$ follow:

$$\int \frac{\mathrm{d}\Omega}{4\pi} D^{j*}_{m_1 m_2}(\Omega)D^{j'}_{m'_1 m_2}(\Omega) = \frac{\delta_{jj'},\delta_{m_1 m'_1}}{2j+1}, \quad \text{(C.23)}$$

where $\mathrm{d}\Omega = \mathrm{d}\cos\theta\,\mathrm{d}\phi$. Since the third argument of D-function is set to zero, the orthogonality on m_2 is not ensured.

It is often needed to evaluate the Wigner d-functions with special arguments,

$$d^j_{m_1 m_2}(0) = \delta_{m_1,m_2}, \qquad\qquad d^j_{m_1 m_2}(\pi) = (-1)^{j-m_1}\delta_{m_1,-m_2}. \quad \text{(C.24)}$$

The decay functions $Z^{JM}_{S\lambda}$ and Z^{JM}_{LS} are defined in Eq. (C.18). The orthogonality $Z^{JM}_{S\lambda}(\Omega,\Omega')$ follows straightforwardly from Eq. (C.23),

$$\int \frac{\mathrm{d}\Omega}{4\pi}\frac{\mathrm{d}\Omega'}{4\pi} Z^{JM*}_{S\lambda}(\Omega,\Omega')Z^{J'M'}_{S'\lambda'}(\Omega,\Omega') = \delta_{JJ'}\delta_{MM'}\delta_{SS'}\delta_{\lambda\lambda'}. \quad \text{(C.25)}$$

The decay functions Z^{JM}_{LS}, in the canonical basis are also orthogonal,

$$\int \frac{\mathrm{d}\Omega}{4\pi}\frac{\mathrm{d}\Omega'}{4\pi} Z^{JM*}_{LS}(\Omega,\Omega')Z^{J'M'}_{L'S'}(\Omega,\Omega') = \delta_{JJ'}\delta_{MM'}\delta_{SS'}\delta_{LL'}. \quad \text{(C.26)}$$

The proof of the latter requires an addition the orthogonality relation of Clebsch-Gordan coefficients.

$$\sqrt{(2L+1)(2L'+1)} \sum_\lambda \langle L, 0; S, \lambda \,|\, J, \lambda \rangle \langle L', 0; S, \lambda \,|\, J, \lambda \rangle = (2J+1)\delta_{LL'} \tag{C.27}$$

This identity can be derived from Eq. (A.17) and Eq. (A.18) of Ref. [47] or using properties of $3j$-symbols [136]. We can notice a symmetry relation of the functions Z, with respact to a flip of the second angle pair $\Omega = (\theta, \phi) \to (\pi - \theta, \pi + \phi) \equiv -\Omega$:

$$Z_{LS}^{JM}(\Omega, -\Omega') = (-1)^S Z_{LS}^{JM}(\Omega, \Omega'), \tag{C.28}$$

where we used that,

$$D_{\lambda 0}^S(\pi + \phi, \pi - \theta, 0) = e^{-i\lambda(\pi+\phi)} d_{\lambda 0}^S(\pi - \theta) \tag{C.29}$$

$$= (-1)^{S+\lambda} d_{\lambda 0}^S(\theta) \, (-1)^{-\lambda} e^{-i\lambda\phi} = (-1)^S D_{\lambda 0}^S(\phi, \theta, 0). \tag{C.30}$$

C.3 Relation between cross-channel angular functions

The kinematics of three particles is fully specified by five variables which are denoted by the combined variable τ (Eq. (3.2)). The choice of the variables in not unique, however, for every expansion chain there is the most convenient one,

$$\tau_k = (\sigma_k, \Omega_k, \Omega_{ij}).$$

The kinematic variables of the cross channels can be expressed through each other. The relations between the kinematic variables lead to convenient properties of the angular function from the channels.

Analytic approach

The product of Wigner D-functions from channel 3 is expressed through the angles of channel 1 as follows:

$$D_{M\lambda}^J(\Omega_3) D_{\lambda 0}^S(\Omega_{12}) = D_{M\lambda}^J(\phi_3, \theta_3, \phi_{12}) \, d_{\lambda 0}^S(\theta_{12}) = \sum_\nu D_{M\nu}^J(\phi_1, \theta_1, \phi_{23}) d_{\nu\lambda}^J(\hat{\theta}_3) \, d_{\lambda 0}^S(\theta_{12}), \tag{C.31}$$

where $\hat{\theta}_3$ is the angle between $\vec{p}_1$ and $\vec{p}_3$ in CM-frame. One can understand the relation in the following way. The $D_{M\lambda}^J(\Omega_3) = D_{M\lambda}^J(\phi_3, \theta_3, 0)$ and $D_{\lambda 0}^S(\Omega_{12}) = D_{\lambda 0}^S(\phi_{12}, \theta_{12}, 0)$ represent the rotations $[R_z(\phi_3)R_y(\theta_3)]^{-1}$ and $[R_z(\phi_{12})R_y(\theta_{12})]^{-1}$. The first transformation rotates the 3π system in the CM-frame such that the momentum $\vec{p}_1 + \vec{p}_2 = -\vec{p}_3$ is aligned to the z-axis as shown in Fig. C.1. When the system is boosted to the (12)-rest frame (helicity frame), the second transformation aligns $\vec{p}_1$ to the z-axis (we remind that Ω_{12} stands for the spherical angles of particle 1 in the (12)-helicity frame). Since the rotation $R_z(\phi_{12})$ commutes with the boost along z-axis, we can combine the three rotations in CM-frame, $R_z^{-1}(\phi_{12})R_y^{-1}(\theta_3)R_z^{-1}(\phi_3)$. The combined transformation has a clear meaning: it brings the 3π system to the $x \times z$ plane such that $\vec{p}_3$ points to $-z$-direction. The transformation $R_z^{-1}(\phi_{23})R_y^{-1}(\theta_1)R_z^{-1}(\phi_1)$ also brings the 3π system to the xz-plane while $\vec{p}_1$ is aligned with $-z$-direction. The difference between the results of the transformations is a rotation
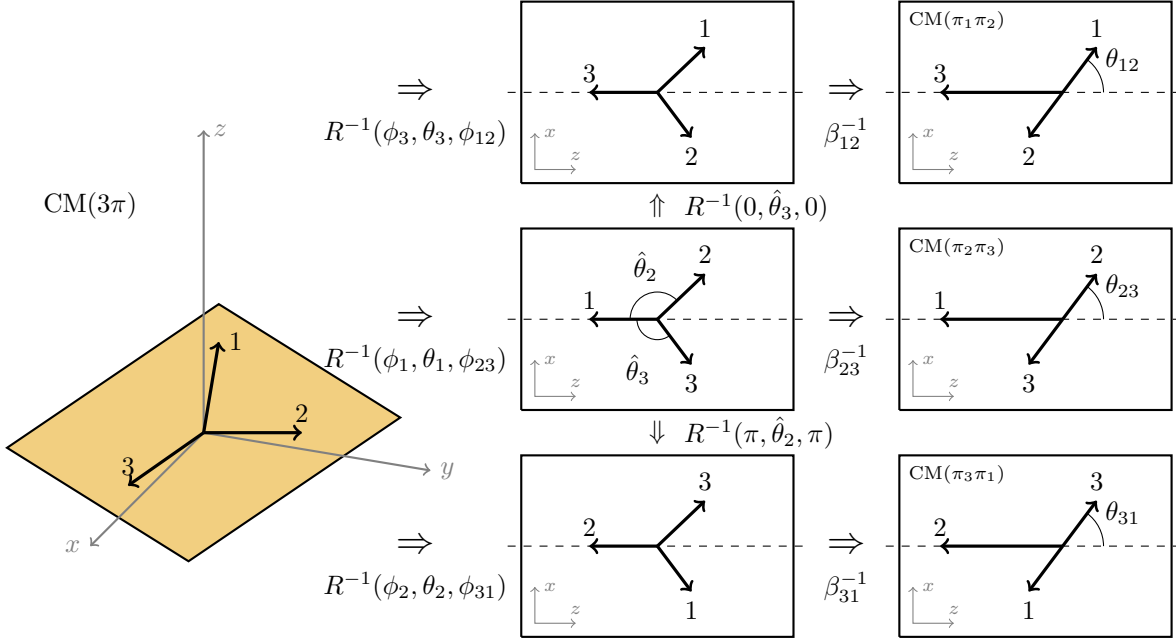
Figure C.1: The transformations of the three-pion decay plane. The left diagram shows pions momenta indicated by numbers 1, 2, 3 in the overall CM-frame. Transformations indicated under $\Rightarrow$ sign are applied to the pions momenta.

about y-axis, represented by $d^J_{\nu\lambda}(\hat{\theta}_3)$. The projection integral of the expansion chain of channel $k = 3$ to the channel $k = 1$ can be simplified analytically.

$$\int \frac{\mathrm{d}\Omega_1}{4\pi} \frac{\mathrm{d}\Omega_{23}}{4\pi} Z^{JM*}_{S\lambda}(\Omega_1, \Omega_{23}) Z^{J'M'}_{S'\nu}(\Omega_3, \Omega_{12}) = \frac{\delta_{J'J}\delta_{M'M}}{2J+1} \int \frac{\mathrm{d}\cos\theta_{23}}{2} d^S_{\lambda 0}(\theta_{23}) d^J_{\lambda\nu}(\hat{\theta}_3) d^{S'}_{\nu 0}(\theta_{12}).$$
(C.32)

where all angles are functions of the invariants,

$$\cos\theta_{23} = \frac{\sigma_1(\sigma_3 - \sigma_2)}{\sqrt{\lambda_1 \lambda_{s1}}}, \qquad \sin\theta_{23} = \frac{2\sqrt{\sigma_1}\sqrt{\phi(s,\sigma_1,\sigma_3)}}{\sqrt{\lambda_1 \lambda_{s1}}}, \qquad \text{(C.33a)}$$

$$\cos\theta_{12} = \frac{\sigma_3(\sigma_2 - \sigma_1)}{\sqrt{\lambda_3 \lambda_{s3}}}, \qquad \sin\theta_{12} = \frac{2\sqrt{\sigma_3}\sqrt{\phi(s,\sigma_1,\sigma_3)}}{\sqrt{\lambda_3 \lambda_{s3}}}, \qquad \text{(C.33b)}$$

$$\cos\theta_{31} = \frac{\sigma_2(\sigma_1 - \sigma_3)}{\sqrt{\lambda_2 \lambda_{s2}}}, \qquad \sin\theta_{31} = \frac{2\sqrt{\sigma_2}\sqrt{\phi(s,\sigma_1,\sigma_3)}}{\sqrt{\lambda_2 \lambda_{s2}}}, \qquad \text{(C.33c)}$$

$$\cos\hat{\theta}_3 = \sqrt{1 - \sin^2\hat{\theta}_3} \qquad \sin\hat{\theta}_3 = \frac{2\sqrt{s}\sqrt{\phi(s,\sigma_1,\sigma_3)}}{\sqrt{\lambda_{s1}\lambda_{s3}}}, \qquad \text{(C.33d)}$$

$$\cos\hat{\theta}_2 = \sqrt{1 - \sin^2\hat{\theta}_2} \qquad \sin\hat{\theta}_2 = \frac{2\sqrt{s}\sqrt{\phi(s,\sigma_1,\sigma_3)}}{\sqrt{\lambda_{s1}\lambda_{s2}}}. \qquad \text{(C.33e)}$$

where we introduced the Kibble function ϕ as it enters all $\sin\theta$ expressions [222],

$$\phi(s,\sigma_1,\sigma_3) = \sigma_1\sigma_2\sigma_3 - m_\pi^2(s-m_\pi^2)^2, \quad \sigma_2 = s + 3m_\pi^2 - \sigma_1 - \sigma_3. \tag{C.34}$$

Analogously, the relations can be derived for the chain (2) with a small difference shown in Fig. C.1. The system of three particles in CM frame orientated by the rotations $R^{-1}(\phi_1,\theta_1,\phi_{23})$ (first plot in the second row) needs to be rotated anti-clockwise (positive angle) to archive orientation required in the decay chain 2 (the first plot of the third row). It is equivalent to the rotation $R^{-1}(\pi,\hat\theta_2,\pi)$, which gives an additional sign factor,

$$D^J_{M\lambda}(\Omega_2)D^S_{\lambda 0}(\Omega_{31}) = \sum_\nu D^1_{M\nu}(\phi_1,\theta_1,\phi_{23})\,(-1)^{\nu+\lambda}\,d^J_{\nu\lambda}(\hat\theta_2)\,d^S_{\lambda 0}(\theta_{31}). \tag{C.35}$$

Kinematic approach

As mentioned, the sets of variables τ_i, $i=1,2,3$ are equivalent to each other. We are going to demonstrate explicitly how variables of one set can be expressed though the other using boosts and rotations. The derivation is performed for a general system of three particles with masses m_1, m_2, m_3.

The set of 5 variables $\tau_1 = (\sigma_1,\Omega_1,\Omega_{23})$ completely define the decay kinematics. As an example we show how to relate these variables to another set $(\sigma_3,\Omega_3,\Omega_{12})$. We start in the (23)-helicity frame. The particle 1 points to the negative direction of the z-axis. The particles 2 and 3 orientated at opposite directions, the solid angle of the particle 2 is Ω_{23}. The expression for σ_3 is found in this frame by explicit evaluation of $\sigma_3 = (p_1 + p_2)^2$:

$$\sigma_3 = m_1^2 + m_2^2 + \frac{1}{2\sigma_1}(\sigma_1 + m_2^2 - m_3^2)(s - m_1^2 - \sigma_1) + \frac{\lambda^{1/2}(\sigma_1,m_2^2,m_3^2)\lambda^{1/2}(s,\sigma_1,m_1^2)}{2\sigma_1}\cos\theta_{23}, \tag{C.36}$$

The direction Ω_3, is opposite to the particle 3 in the center of mass system. Therefore, we find it by a boost and a rotation of the vector $p_3^{(23)} = (E_3^{(23)}, \vec p_3^{(23)})$, with $E_3^{(23)} = (\sigma_1 + m_3^2 - m_2^2)/(2\sqrt{\sigma_1})$ and $|\vec p_3^{(23)}| = \lambda^{1/2}(\sigma_1,m_2^2,m_3^2)/(2\sqrt{\sigma_1})$

$$p_3^{\mathrm{CMS}} = \begin{pmatrix} 1 & & & \\ & & R_z(\phi_1)R_y(\theta_1) & \\ & & & \end{pmatrix} \begin{pmatrix} \gamma & & & \beta\gamma \\ & 1 & & \\ & & 1 & \\ \beta\gamma & & & \gamma \end{pmatrix} \begin{pmatrix} E_3^{(23)} \\ -\vec p_3^{(23)}\sin\theta_{23}\cos\phi_{23} \\ -\vec p_3^{(23)}\sin\theta_{23}\sin\phi_{23} \\ -\vec p_3^{(23)}\cos\theta_{23} \end{pmatrix}, \tag{C.37}$$

where $\gamma = (s + \sigma_1 - m_1^2)/(2\sqrt{s\sigma_1})$ is a relativistic factor of the (23) isobar in the CM frame. the minus sign in the vector components reflects that the angles Ω_{23} are measured by the direction of the particle 2 which in the (23) frame goes opposite to the particle 3.

$$\cos\theta_3 = -\frac{p_{3,z}^{\mathrm{CMS}}}{|\vec p_3^{\mathrm{CMS}}|} \tag{C.38}$$

$$\phi_3 = \mathrm{atan2}(-p_{3,y}^{\mathrm{CMS}}, -p_{3,x}^{\mathrm{CMS}}) \tag{C.39}$$

The variable $\cos\theta_{12}$ can be directly related to the invariant σ_3

$$\cos\theta_{12} = \frac{2\sigma_3(m_2^2 + m_3^2 - \sigma_1) + (\sigma_3 + m_2^2 - m_1^2)(s - m_3^2 - \sigma_3^2)}{\lambda^{1/2}(\sigma_3, m_1^2, m_2^2)\lambda^{1/2}(s, \sigma_3, m_1^2)} \quad \text{(C.40)}$$

The last angle ϕ_{12} is defined by the particle 1 in the (12) frame which is obtained from CM frame by the rotation $R_z(\phi_1)R_y(\theta_1)$ and the corresponding boost. The boost does not change azimuthal angle of the particle 1, therefore, it can be measured in the CMS-frame after the rotation is applied. Since the particle 1 is aligned with the z-axis in the (23)-helicity frame, its direction does not change when the boost to CMS is performed.

$$\vec{p}_{\perp 1}^{23} = \left(\quad R_y(-\theta_3)R_z(-\phi_3)\quad\right)\begin{pmatrix} -\sin\theta_1\cos\phi_1 \\ -\sin\theta_1\sin\phi_1 \\ -\cos\theta_1 \end{pmatrix}, \qquad \phi_{12} = \text{atan2}(p_{\perp 1,y}^{23}, p_{\perp 1,x}^{23}). \quad \text{(C.41)}$$

We can define an operator $O_{B.C.}$ which acts on the set of variables τ_1 and yields the set τ_3. A good check of the implementation of the basis transformation $O_{B.C.}$ is that being applied three times it gives identity.

$$O_{B.C.}(\sigma_1, \Omega_1, \Omega_{23}) = (\sigma_3, \Omega_3, \Omega_{12}), \quad \text{(C.42)}$$

$$O_{B.C.}^2(\sigma_1, \Omega_1, \Omega_{23}) = (\sigma_2, \Omega_2, \Omega_{31}), \quad \text{(C.43)}$$

$$O_{B.C.}^3(\sigma_1, \Omega_1, \Omega_{23}) = (\sigma_1, \Omega_1, \Omega_{23}). \quad \text{(C.44)}$$

Details on COMPASS partial waves

The model for the PWA is build using the isobar model presented in Eq. (3.6). Eq. (3.7) introduces the partial-wave expansion. An assumption enters in Eq. (3.13) when the isobar amplitude is written in the form,

$$(A_{\lambda'\lambda})^{JM\epsilon}_{LS}(s,\sigma) = (\mathcal{A}_{\lambda'\lambda})^{JM\epsilon}_{LS}(s)f_S(\sigma)\,h_L(s,\sigma), \tag{D.1}$$

where the amputated amplitude $(\hat{A}_{\lambda'\lambda})^{JM\epsilon}_{LS}(s)$ depends only on variable s, the functions $f_S(\sigma)$ describe the line shape of the Isobar-s, they are the same for all $m_{3\pi}$ bins, $h_L(s,\sigma)$ are given in Eq. (E.14) (in that case the break-up momentum is $k = \lambda^{1/2}(s,\sigma,m^2_\pi)/(2\sqrt{s})$, $x = (kR_L)^2$ with $R_L = 1/(0.2024\text{GeV})$) combine the threshold factor for the $\xi\pi$ L-wave state and the barrier factor. In this appendix we provide an exact parametrization for $f_S(\sigma)$ used in the analysis and provide a complete list of partial waves in Table D.1.

There are six isobars which used in the approach are motivated by the subchannel resonances. Three isobars which corresponds to $\rho(770)$, $f_2(1270)$, $\rho_3(1690)$, $f_0(1500)$ are parametrized by the Breit-Wigner-amplitude,

$$f_\xi(\sigma) = \mathcal{N}_\xi \frac{h_S(\sigma)}{m^2_0 - \sigma - im_0\Gamma(\sigma)}, \tag{D.2}$$

where the factor $h_S(\sigma)$ in the numerator corresponding to a one decay vertex. $\mathcal{N}_\xi$ is a normalization constant fixed by equation,

$$\int_{4m^2_\pi}^\infty \sqrt{1 - 4m^2_\pi/\sigma}\,|f_\xi(\sigma)|^2\mathrm{d}\sigma = 16\pi^2. \tag{D.3}$$

The energy dependence of the width is different for various isobars. For $f_2(1270)$ the width is proportional to the two-body phase space of the decay $f_2 \to \pi\pi$ and the factor h^2_2 which is a squared transition amplitude of the $f_2 \to \pi\pi$.

$$\Gamma(\sigma) = \Gamma_0\frac{q(\sigma)}{q_0}\frac{m_0}{\sqrt{\sigma}}\frac{h^2_2(q)}{h^2_2(q_0)}, \tag{D.4}$$

where the values of m_0 and Γ_0 are listed in Table D.2, $q(\sigma) = \sqrt{\sigma/4 - m^2_\pi}$, the constant q_0 is

Table D.1: A list of wave set used for mass-independent fit

A list of wave set used for mass-independent fit (from Ref. [78]): 80 waves with positive reflectivity, 7 with negative, and one incoherent isotropic wave (FLAT). The waves are only included in the analysis above their artificial threshold indicated in the table.

$J^{PC}M^\epsilon$	Isobar	L	Threshold [MeV]
FLAT			—
$0^{-+}0^+$	$(\pi\pi)_S$	S	—
$0^{-+}0^+$	$\rho(770)$	P	—
$0^{-+}0^+$	$f_0(980)$	S	1200
$0^{-+}0^+$	$f_2(1270)$	D	—
$0^{-+}0^+$	$f_0(1500)$	S	1700
$1^{++}0^+$	$(\pi\pi)_S$	P	—
$1^{++}1^+$	$(\pi\pi)_S$	P	1100
$1^{++}0^+$	$\rho(770)$	S	—
$1^{++}1^+$	$\rho(770)$	S	—
$1^{++}0^+$	$\rho(770)$	D	—
$1^{++}1^+$	$\rho(770)$	D	—
$1^{++}0^+$	$f_0(980)$	P	1180
$1^{++}1^+$	$f_0(980)$	P	1140
$1^{++}0^+$	$f_2(1270)$	P	1220
$1^{++}1^+$	$f_2(1270)$	P	—
$1^{++}0^+$	$f_2(1270)$	F	—
$1^{++}0^+$	$\rho_3(1690)$	D	—
$1^{++}0^+$	$\rho_3(1690)$	G	—
$1^{-+}1^+$	$\rho(770)$	P	—
$2^{++}1^+$	$\rho(770)$	D	—
$2^{++}2^+$	$\rho(770)$	D	—
$2^{++}1^+$	$f_2(1270)$	P	1000
$2^{++}2^+$	$f_2(1270)$	P	1400
$2^{++}1^+$	$\rho_3(1690)$	D	800
$2^{-+}0^+$	$(\pi\pi)_S$	D	—
$2^{-+}1^+$	$(\pi\pi)_S$	D	—
$2^{-+}0^+$	$\rho(770)$	P	—
$2^{-+}1^+$	$\rho(770)$	P	—
$2^{-+}2^+$	$\rho(770)$	P	—
$2^{-+}0^+$	$\rho(770)$	F	—
$2^{-+}1^+$	$\rho(770)$	F	—
$2^{-+}0^+$	$f_0(980)$	D	1160
$2^{-+}0^+$	$f_2(1270)$	S	—
$2^{-+}1^+$	$f_2(1270)$	S	1100
$2^{-+}2^+$	$f_2(1270)$	S	—
$2^{-+}0^+$	$f_2(1270)$	D	—
$2^{-+}1^+$	$f_2(1270)$	D	—
$2^{-+}2^+$	$f_2(1270)$	D	—
$2^{-+}0^+$	$f_2(1270)$	G	—
$2^{-+}0^+$	$\rho_3(1690)$	P	1000
$2^{-+}1^+$	$\rho_3(1690)$	P	1300
$3^{-+}1^+$	$\rho(770)$	F	—
$3^{-+}1^+$	$f_2(1270)$	D	1340

$J^{PC}M^\epsilon$	Isobar	L	Threshold [MeV]
$3^{++}0^+$	$(\pi\pi)_S$	F	1380
$3^{++}1^+$	$(\pi\pi)_S$	F	1380
$3^{++}0^+$	$\rho(770)$	D	—
$3^{++}1^+$	$\rho(770)$	D	—
$3^{++}0^+$	$\rho(770)$	G	—
$3^{++}1^+$	$\rho(770)$	G	—
$3^{++}0^+$	$f_2(1270)$	P	960
$3^{++}1^+$	$f_2(1270)$	P	1140
$3^{++}0^+$	$\rho_3(1690)$	S	1380
$3^{++}1^+$	$\rho_3(1690)$	S	1380
$3^{++}0^+$	$\rho_3(1690)$	I	—
$4^{++}1^+$	$\rho(770)$	G	—
$4^{++}2^+$	$\rho(770)$	G	—
$4^{++}1^+$	$f_2(1270)$	F	—
$4^{++}2^+$	$f_2(1270)$	F	—
$4^{++}1^+$	$\rho_3(1690)$	D	1700
$4^{-+}0^+$	$(\pi\pi)_S$	G	1400
$4^{-+}0^+$	$\rho(770)$	F	—
$4^{-+}1^+$	$\rho(770)$	F	—
$4^{-+}0^+$	$f_2(1270)$	D	—
$4^{-+}1^+$	$f_2(1270)$	D	—
$4^{-+}0^+$	$f_2(1270)$	G	1600
$5^{++}0^+$	$(\pi\pi)_S$	H	—
$5^{++}1^+$	$(\pi\pi)_S$	H	—
$5^{++}0^+$	$\rho(770)$	G	—
$5^{++}0^+$	$f_2(1270)$	F	980
$5^{++}1^+$	$f_2(1270)$	F	—
$5^{++}0^+$	$f_2(1270)$	H	—
$5^{++}0^+$	$\rho_3(1690)$	D	1360
$6^{++}1^+$	$\rho(770)$	I	—
$6^{++}1^+$	$f_2(1270)$	H	—
$6^{-+}0^+$	$(\pi\pi)_S$	I	—
$6^{-+}1^+$	$(\pi\pi)_S$	I	—
$6^{-+}0^+$	$\rho(770)$	H	—
$6^{-+}1^+$	$\rho(770)$	H	—
$6^{-+}0^+$	$f_2(1270)$	G	—
$6^{-+}0^+$	$\rho_3(1690)$	F	—
$1^{++}1^-$	$\rho(770)$	S	—
$1^{-+}0^-$	$\rho(770)$	P	—
$1^{-+}1^-$	$\rho(770)$	P	—
$2^{++}0^-$	$\rho(770)$	D	—
$2^{++}0^-$	$f_2(1270)$	P	1180
$2^{++}1^-$	$f_2(1270)$	P	1300
$2^{-+}1^-$	$f_2(1270)$	S	—

Table D.2: The Breit-Wigner parameters of the isobars. The size parameter of the Blatt-Weisskopf factors used in $h_S(\sigma)$ factors in Eqs. (D.2, D.4) is $R_\xi = 4.94\,\text{GeV}^{-1}$ (see Eq. (E.14) with $x = (qR)^2$)

isobar	mass	width
$\rho(770)$	$m_0 = 0.7685\,\text{GeV}$	$\Gamma_0 = 0.1507\,\text{GeV}$
$f_2(1270)$	$m_0 = 1.274\,\text{GeV}$	$\Gamma_0 = 0.185\,\text{GeV}$
$\rho_3(1690)$	$m_0 = 1.69\,\text{GeV}$	$\Gamma = 0.190\,\text{GeV}$
$f_0(1500)$	$m_0 = 1.507\,\text{GeV}$	$\Gamma = 0.109\,\text{GeV}$

Table D.3: Parameters of the $(\pi\pi)_S$ parametrization.

a_1	σ_p	α_0	α_1	α_2	α_3	m_K	m_{K^0}
0.1131	-0.0074	0.0337	-0.3185	-0.0942	-0.5927	0.493677	0.497614

calculate at the mass, $q_0 = q(m_0^2)$. For ρ-meson the expression is slightly modified by changing asymptotic behavior of the width: the tail of the ρ-meson is dumped stronger.

$$\Gamma(\sigma) = \Gamma_0 \frac{q(\sigma)}{q_0} \frac{h_1^2(q)}{h_1^1(q_0)}, \tag{D.5}$$

with parameters from Table D.2. The widths of ρ_3 and $f_0(1500)$ are constant values given in Table D.2.

The $(\pi\pi)_S$ is the broad component of the scalar sector. Historically, we used a parametrization which has never been explicitly suggested or published. It came from studies of I. Kachaev who modified the Au-Morgan-Pennington (AMP) parametrization [105, 106]. The idea of I. Kachaev was to get rid of the narrow dip and leave the shape of the broad component. It was achieved by setting to zero some of coefficients of the AMP parametrization. The actual expression used in COMPASS PWA is

$$f_{(\pi\pi)_S}(\sigma) = \frac{\mathcal{N}_{(\pi\pi)_S}}{M(\sigma) - i\sqrt{1 - 4m_\pi^2/\sigma}}, \qquad M(\sigma) = \frac{a_1}{\sigma - \sigma_p} + \sum_{k=0}^{3} \alpha_k \left(\frac{\sigma}{(m_K + m_{K^0})^2} - 1 \right)^k, \tag{D.6}$$

where the values of the parameters are specified in Table D.3, the normalization constant $\mathcal{N}_{(\pi\pi)_S}$ is calculated using Eq. (D.3).

The $f_0(980)$ is parametrized by the Flatté-formula, *i.e.* the energy-dependent width in Eq. (D.2) includes two channels $\pi\pi$ and $K\bar{K}$.

$$\Gamma(\sigma) = \frac{g_\pi}{m_0} \left(\sqrt{1 - \frac{4m_\pi^2}{\sigma}} + r_{K/\pi}\sqrt{1 - \frac{4m_K^2}{\sigma}} \right), \tag{D.7}$$

where $m_0 = 0.965$, $g_\pi = 0.165$, $r_{K/\pi} = 4.21$. below $K\bar{K}$ threshold the second square root expression in Eq. (D.7) needs to be calculated for the negative argument. One has to use it the form $i\sqrt{4m_K^2/\sigma - 1}$, where the new argument is positive for $\sigma < 4m_K^2$.

Miscellaneous

E.1 The Dalitz plot integral in the complex plane

To address the issues of the evaluation of Eq. (6.28) for complex values of s, we consider a simplified version of the problem:

$$X(s) = \int_{\sigma_{\text{th}}}^{\sigma_{\text{lim}}} d\sigma_1 \int_{\sigma_3^-(\sigma_1,s)}^{\sigma_3^+(\sigma_1,s)} d\sigma_3 \frac{1}{\sqrt{\sigma_3 - 4m_\pi^2}}, \tag{E.1}$$

where $\sigma_{\text{th}} = 4m_\pi^2$, $\sigma_{\text{lim}} = (\sqrt{s} - m_\pi)^2$, $\sigma_3^\pm(\sigma_1, s) = (s + 3m_\pi^2 - \sigma_1)/2 \pm \lambda_1^{1/2}\lambda_{s1}^{1/2}/(2\sigma_1)$. Similar to Eq. (6.28) this expression contains two nested integrals with the same limits. The integrand has a branch point at $4m_\pi^2$, the integration paths have to be modified in order to avoid crossing the cut. The position of the $\sigma_3^\pm$ are shown in Fig. E.1 for $s = \text{Re}\, s + i\epsilon$. We observe that the σ_3^+ has always positive imaginary part and stays far from the branch point $\sigma_3 = 4m_\pi^2$. The σ_3^- circles around the branch point changing the sheet of the integrand. When $\sigma_1 = \sigma_{\text{lim}}$, the σ_3 endpoints nearly coincide, $\sigma_3^\pm(\sigma_{\text{lim}}) = m_\pi(\sqrt{s} + m_\pi) \pm i\epsilon$, however, they are on the different sides of the integrand cut. In other words, if a straight line integration in σ_3 is done, we should observe a singularity related to the circling in the complex σ_1 plane. The inner integral can be solved analytically.

$$X(s) = 2 \int_{\sigma_{\text{th}}}^{\sigma_{\text{lim}}} d\sigma_1 \left(\sqrt{\sigma_3^+(\sigma_1, s) - 4m_\pi^2} - \sqrt{\sigma_3^-(\sigma_1, s) - 4m_\pi^2} \right), \tag{E.2}$$

where the first term does not give problems near the physical region since σ_3^+ stays away from $4m_\pi^2$. However, the second square root has two branch points at $(s - m_\pi^2)/2$ in the σ_1 plane. (Another example of a simple function with two adjoined square root branch points is $\sqrt{z^2}$.)

$$\sigma_3^+(\sigma_1, s) - 4m_\pi^2 = 0 \quad \rightarrow \quad (\sigma_1 - (s - m_\pi^2)/2)^2 = 0 \tag{E.3}$$

Fig. E.2 shows the σ_1 plane, where we see that a straight connection between σ_{th} and σ_{lim} is not allowed by the presence of the cut. Here, two options arise:

1. $X^{(1)}$: we draw the σ_1 path directly through the branch point $(s - m_\pi^2)/2$ (the point P in Fig. E.1
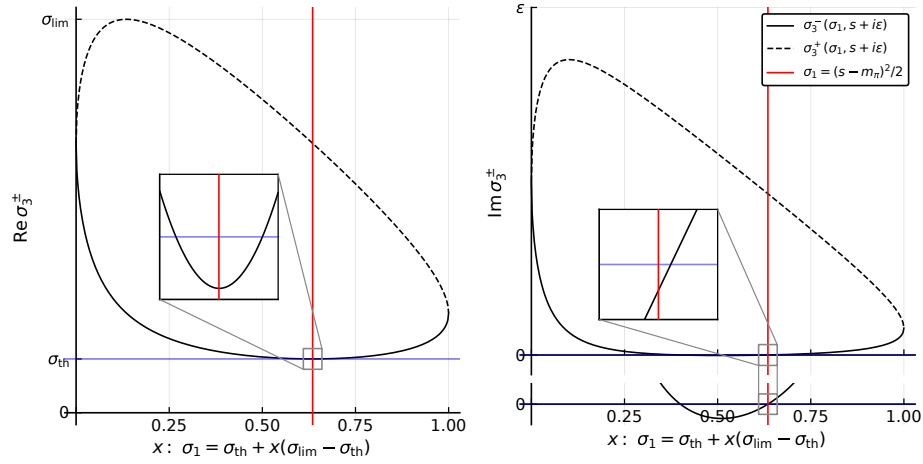
Figure E.1: The left (right) plot presents the real (imaginary) part of the $\sigma_3^{\pm}$ as a function of σ_1 for a fixed value of $s + i\epsilon$. The σ_1 is changed linearly between the integration limits. The zoomed plots show how the σ_3^{-} passes the real axis first below the branch point $\sigma_{\mathrm{th}} = 4m_\pi^2$, then returns above the branch point performing the circling. The red line indicates the closest point on the σ_1-path to the $(s-1)/2$ since it does not go exactly through it.
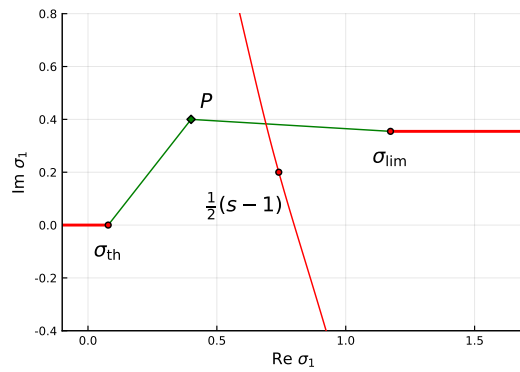
Figure E.2: Analytical structure of the integrand in Eq. (E.2). The branch points are shown by the red dots with the cuts indicated by the solid red lines. The arbitrary integration path $\sigma_{\mathrm{th}} \to \mathrm{P} \to \sigma_{\mathrm{lim}}$ is shown by the dashed green line.

can be aligned with the branch point $(s - m_\pi^2)/2)$. The point $\sigma_1 = (s - m_\pi^2)/2$ is special because when the path goes through it, the σ_3^- does not circle the branch point but just touches it.

2. $X^{(2)}$: we go analytically under the cut taking any arbitrary path. $X^{(2)}$ corresponds to the function which we would obtain connecting the points $\sigma_3^\pm$ properly, *i.e.* avoiding $1/\sqrt{\sigma_3 - 4m_\pi^2}$ cut.

The two options give two different analytical functions. Additional discussions on the subject can be found in Ref. [162, 194].

E.2 The Pasquier-Aitchison inversion

This appendix demonstrates how the integral Khuri-Treiman equation (see Eq. (7.28)) can be transformed into the single-variable representation, later referred as SVR (see Eq. (7.29)). Practically, it requires changing the order of two integrals in the following equation (*i.e.* Eq. (7.28) of the main text),

$$\mathcal{F}(s_+, \sigma) = \mathcal{C}(s, \sigma) + \frac{1}{\pi} \int_4^\infty \frac{d\sigma'}{(\sigma' - \sigma)} \frac{1}{\lambda_{s_+}^{1/2}(\sigma')} \int_{\sigma^-(\sigma', s_+)}^{\sigma^+(\sigma', s_+)} d\sigma'' \, t(\sigma'') \mathcal{F}(s_+, \sigma''), \qquad \text{(E.4)}$$

where $\lambda_{s_+}^{1/2}(\sigma') = \sqrt{\lambda(s, \sigma', 1)}$, $\sigma^\pm(\sigma', s) = (s + 3 - \sigma')/2 \pm \lambda_s^{1/2}(\sigma')\lambda^{1/2}(\sigma')/(2\sigma')$, $\lambda^{1/2}(\sigma') = \sqrt{\lambda(\sigma', 1, 1)}$, $t(\sigma)$ is a two-particle scattering amplitude, $\mathcal{F}(s, \sigma)$ is an amputated Isobar amplitude (see Sec. 7.2.1), and $\mathcal{C}(s, \sigma)$ is an entire function in σ. The s-dependence of the functions $\mathcal{F}$ and $\mathcal{C}$ is not important for the integral swapping since this transformation can be performed for a fixed value of s. The value, s_+ is set to be slightly imaginary to avoid that the integration ranges of the second integral, $\sigma^\pm$ hit singularities of integrand, $t(\sigma'')\mathcal{F}(s, \sigma'')$. We assume that both $t(\sigma'')$ and $\mathcal{F}(s, \sigma'')$ have a discontinuity on the real axis in the σ'' variable for $\sigma'' > 4$, and that there are no other singularities on the first Riemann sheet in σ''. The positions of the integration limits $\sigma^\pm(\sigma', s)$ are shown in the right panel of Fig. E.3. Due to the presence of the cut in the σ'' plane, these limits cannot always be connected with a straight line. Hence, the integration path has to be modified to avoid crossing of the cut. The analytic structure of the integrand in the σ' plane is also non-trivial. It has a pole, $1/(\sigma' - \sigma)$ and four branch points at $\sigma' \in \{0, 4, (\sqrt{s} \pm 1)^2\}$ due to the square-root expression in the integration limits $\sigma^\pm(\sigma', s)$ (see remarks in Ref. [237]). To define the internal integral on a path $\sigma' \in (4, \infty)$, the expression $\lambda_s^{1/2}(\sigma')$ has to be defined for all σ'. We fix the orientation of the cuts by writing, [1]

$$\lambda_{s_+}^{1/2}(\sigma') = i \sqrt{\sigma' - (\sqrt{s_+} - 1)^2} \sqrt{(\sqrt{s_+} + 1)^2 - \sigma'}, \qquad \text{(E.5)}$$

$$\sigma^\pm(\sigma', s_+) = \frac{s + 3 - \sigma'}{2} \mp \sqrt{\sigma' - (\sqrt{s_+} - 1)^2} \sqrt{(\sqrt{s_+} + 1)^2 - \sigma'} \frac{\sqrt{4 - \sigma'}}{2\sqrt{\sigma'}}. \qquad \text{(E.6)}$$

---

[1] We use a standard convention that the cut of $\sqrt{z}$ function is oriented to the left, *i.e.* $\sqrt{-1 + i\epsilon} = i$, and $\sqrt{-1 - i\epsilon} = -i$, with ϵ being an infinitesimal positive number.
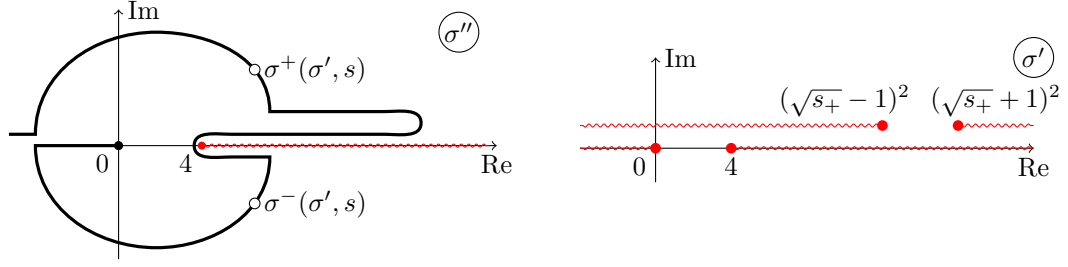
Figure E.3: Left: The location of the integration limits of the second integral, $\sigma^{\pm}(\sigma', s_+)$ for $s > 9$, and $\sigma' \in [4, \infty]$ are shown by the thick black line. The small white circle show an example: when σ' is outside of the physical domain $\sqrt{s} - 1 < \sqrt{\sigma'} < \sqrt{s} + 1$, the values $\sigma^{\pm}$ are located in the complex plane. The red broken line shows the cut along the real axis. Right: Location of the cuts of Eq. (E.6) in the σ' plane.

The left panel of Fig. E.3 shows locations of the cuts of Eq. (E.6) in the σ' plane.

There are two methods to transform Eq. (E.4) into the SVR, which we call the *Aitchison inversion* proposed in Ref. [194] and the *Pasquier inversion* given in Ref. [162]. The first method involves an additional integral, the dispersive representation of the integrand $\mathcal{F}(\sigma'')\, t(\sigma'')$ (see Eq. (2.26) in the introductory section), while the second method exploits modifications of the integration paths. Supposedly, both methods give the same result. We follow the *Pasquier inversion* method. It proceeds in three steps:

1. We change the integration paths as follows.

$$
\int_{4+i\epsilon}^{\infty+i\epsilon} \int_{\sigma^-(\sigma',s_+)}^{\sigma^+(\sigma',s_+)} = \int_{4+i\epsilon}^{\infty+i\epsilon} \int_{0}^{\sigma^+(\sigma',s_+)} - \int_{4+i\epsilon}^{\infty+i\epsilon} \int_{0}^{\sigma^-(\sigma',s_+)}
$$

$$
= \int_{4+i\epsilon}^{\infty+i\epsilon} \int_{0}^{\sigma^+(\sigma',s_+)} - \int_{4-i\epsilon}^{\infty-i\epsilon} \int_{0}^{\sigma^+(\sigma',s_+)} \tag{E.7}
$$

$$
= \left(\int_{\infty-i\epsilon}^{4-i\epsilon} + \int_{4+i\epsilon}^{\infty+i\epsilon} \right) \int_{0}^{\sigma^+(\sigma',s_+)} = \int_{+\infty-i\epsilon}^{+\infty+i\epsilon} (C) \int_{0}^{\sigma^+(\sigma',s_+)} (\Gamma) \,, \tag{E.8}
$$

where the first integral is performed in the σ' variable, the second one is is taken in the σ'' varible; we omitted the integrand expressions for simplicity (they do not change). To make the first step in Eq. (E.8), we noticed that $\sigma^-(\sigma' + i\epsilon) = \sigma^+(\sigma' - i\epsilon)$, since the sign in Eq. (E.6) is flipped by changing the side of the cut. The contours (C) and (Γ) are shown in Fig. E.5.

2. We change the order of the integrals. This step, in contrast to the first one, is well explained in the original Ref. [162]. The integration paths are fixed: the first integral, in the σ' plane is taken along the path (C) around the cut $[4, \infty]$; the second integral, in the σ'' plane is taken from 0 to $\sigma^+(\sigma', s)$. The path for the second integral can be arbitrary, however, it is natural to use a curve shown by the black thick line on the left panel of Fig. E.3 that connects 0 and $\sigma^+(\sigma', s)$. The path (C) is mapped into a variable x, $x \in (-\infty, \infty)$ such that 0 corresponds to the turning point, $\sigma' = 4$. The path (Γ) is mapped into a variable y, $y \in [0, \infty)$. [2] $\sigma^+(\sigma', s)$

---

[2] The coordinates x and y are called "cirvilinear abscissas" in the original work [162]
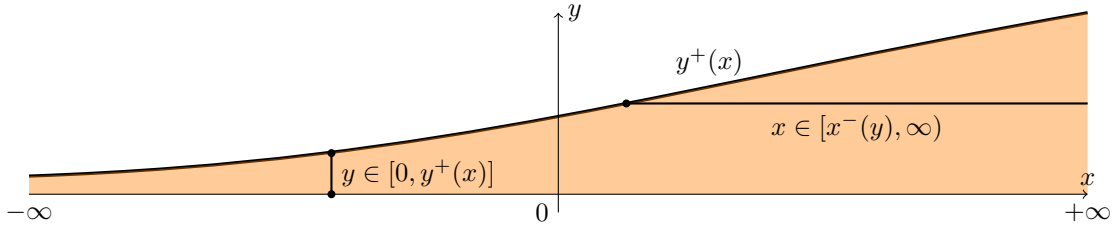
Figure E.4: A domain of the integration in the variables $x \times y$ is shown by the orange area. The joint intervals show ranges of integration over y (or x) by the vertical (or horizontal) line when this integral is the internal one. The transformation is clarified in Eq. (E.9).

gives the range of integration in y, *i.e.* a monotonously increasing function $y^+(x)$ as shown in Fig. E.4. The two integrals can be swapped:

$$\int_{-\infty}^{\infty} \mathrm{d}x \int_0^{y^+(x)} \mathrm{d}y = \int_0^{\infty} \mathrm{d}y \int_{x^-(y)}^{\infty} \mathrm{d}x, \tag{E.9}$$

where $x^-(y)$ is the inverse function to $y^+(x)$. The inverse function for the $\sigma'' = \sigma^+(\sigma', s)$ is, actually, $\sigma' = \sigma^-(\sigma'', s)$. This fact becomes clear based on the symmetry of the Kibble equation [222],

$$\sigma''\sigma'(3 + s - \sigma'' - \sigma') - (s-1)^2 = 0,$$

solutions of which are the functions $\sigma^{\pm}$. Eq. (E.4) becomes:

$$\mathcal{F}(s_+, \sigma) = \mathcal{C}(s, \sigma) + \frac{1}{\pi} \int_0^{-\infty} (\Gamma) \, \mathrm{d}\sigma'' \, t(\sigma'') \mathcal{F}(s_+, \sigma'') \int_{\sigma^-(\sigma'', s_+)}^{+\infty} (C) \, \frac{\mathrm{d}\sigma'}{(\sigma' - \sigma)} \frac{1}{\lambda_{s_+}^{1/2}(\sigma')}, \tag{E.10}$$

By changing the order or integrals, we modified the analytic structure in the σ'' variable. Since one of the integral limits of the internal integral (*i.e.* in the σ' plane) is given by $\sigma^-(\sigma'', s)$, there are four branch points in the σ'' plane: 0, 4 and $(\sqrt{s} \pm 1)^2$ (a remark about propagation of singularities from the integration limit can be found in Ref. [237]). The cuts are directed in the same way as shown on the right panel of Fig. E.3. The integration contours are kept the same: (Γ) in the σ'' plane and (C) in the σ' plane (see Fig. E.5).

3. The integration contour (Γ) in the σ'' plane is straighten to run around the cut that is made by the $(\sqrt{s} - 1)^2$ branch point. The integration contour in the σ' plane is modified accordingly as shown in Fig. E.6. As the contour (Γ) is continuously transformed into the contour (Γ') by just straightening the circular segments, the modification of the contour (C) into the (C') is also continuous. The latter can be realized by pulling a part of the contour through the gap between the branch points at $\sigma' = (\sqrt{s} - 1)^2$ (compare the right panels of Fig. E.5 and Fig. E.6).

The integral along the contour (Γ') shown in the left panel of Fig. E.6 contain three intervals: $[0, (\sqrt{s} - 1)^2]$ below the cut from the branch point $\sigma'' = (\sqrt{s} - 1)^2$, $[0, (\sqrt{s} - 1)^2]$ above this cut, and an infinite peace $(-\infty, 0]$ above the same cut. The first two parts can be combined into a discontinuity, *i.e.* a difference of the nested integral below and above the cut. Eq. (E.4) written in the final SVR
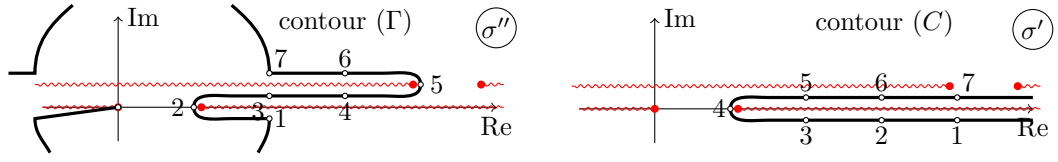
Figure E.5: The complex σ'' and σ' planes are shown un the left and right panels. The thick likes indicate the integration contours *before* the transformation described in the text as the third step of the Pasquier inversion. The function $\sigma^-(\sigma'', s)$ from Eq. (E.6) maps the points from the left panel to the right. The numbers label corresponding points.
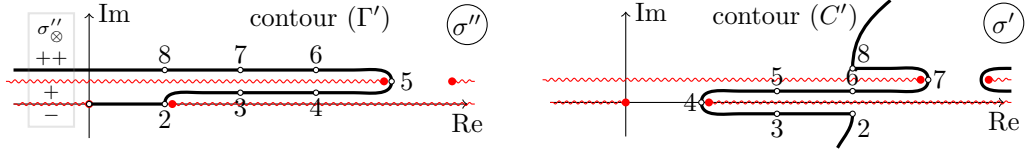
Figure E.6: The complex σ'' and σ' planes are shown in the left and right panels. The thick lines indicate the integration contours *after* the transformation described in the text as the third step of the Pasquier inversion. A part of the contour (C') on the right panel that joints the point 2 arrives from ∞. This contour also goes to the complex infinity after it takes off from point 8. Then, it is back to turn around the branch point $\sigma' = (\sqrt{s}+1)^2$ and match the peace of contour (C) from Fig. E.5 on the last part between the cuts.

form reads,

$$\mathcal{F}(s,\sigma) = \mathcal{C}(s,\sigma) + \int_{-\infty}^{(\sqrt{s}-1)^2} \mathcal{B}_0(\sigma, s, \sigma'') t(\sigma'') \mathcal{F}(s, \sigma'') \, d\sigma'' \tag{E.11}$$

with

$$\mathcal{B}_0(\sigma, s, \sigma'') = \frac{1}{\pi} \left[\theta(\sigma'') \int_{\sigma^-(\sigma''_+, s)}^{\sigma^-(\sigma''_{++}, s)} (C') - \theta(-\sigma'') \int_{\sigma^-(\sigma''_{++}, s)}^{\infty} (C') \right] \frac{d\sigma'}{(\sigma' - \sigma)} \frac{1}{\lambda_{s_+}^{1/2}(\sigma')}, \tag{E.12}$$

where σ''_+ is the value with small positive imaginary part that is still below the cut from $(\sqrt{s}-1)^2$, and σ''_{++} is the value with small positive imaginary that is above both cuts as shown in the left panel of Fig E.6. The heaviside θ-functions separate two ranges: $0 < \sigma'' < (\sqrt{s}-1)^2$ and $\sigma'' < 0$.

E.3 A comment on the Blatt-Weisskopf factors

We discussed the threshold factors which are square-root type singularities arising in the partial wave decomposition. The partial wave amplitudes for $2 \to 2$ scattering processes are proportional to $p^{L_1} q^{L_2}$, where p (q) are the initial (final) state break up momentum and the particles interact in an $L_1(L_2)$-wave configuration. This property is purely kinematical in nature. It is valid also in nonrelativistic potential scattering [136]. The behavior comes from the expansion of the amplitude at low energy. It cannot be (should not be) extended at higher energies. Generally, the asymptotic behavior of a scattering amplitude is bounded by the Froissart condition [238]. Thus, the amplitude cannot grow indefinitely as $p^{L_1} q^{L_2} \sim (\sqrt{s})^{L_1+L_2}$. Indeed, the asymptotic behavior is determined by

the t-channel exchange processes, *i.e.* it depends on the actual details of the dynamics. To enforce the correct threshold behavior and remove the problem at high energy, model-dependent form-factors are usually used. The most popular model was introduced in meson decays by Hippel and Quigg [98], based on the work of Blatt and Weisskopf [97] on α-particles emission from heavy nuclei. The latter formulates the Schrödinger problem, with the equivalent potential

$$U_l(r) = \begin{cases} -V_0 & \text{for } r \leq R \\ \frac{l(l+1)}{2mr^2} & \text{for } r > R \end{cases}, \tag{E.13}$$

where R is a well radius, V_0 is a depth of the well. We notice that peculiar dependence of potential on l makes it cumbersome: in order to compensate the centrifugal barrier for $r < R$, the original potential cannot be isotropic.

However, the problem is exactly solvable, and the so-called Blatt-Weisskopf factors h_l can be determined for any l from the transition amplitude. The $h_l(x)$ are functions of the dimensionless parameter $x = (kR)^2$, with k being the kinetic momentum in the system. The functions $h_l(x)$ have both the right threshold behavior and good asymptotics, $h_l \propto k^l$, and $h_l \xrightarrow{k \to \infty} 1$.

$$\begin{aligned} h_0^2(x) &= 1 \\ h_1^2(x) &= x/(1+x) \\ h_2^2(x) &= x^2/(9 + 3x + x^2) \\ h_3^2(x) &= x^3/(225 + 45x + 6x^2 + x^3) \end{aligned} \tag{E.14}$$

When the model is promoted to relativistic theory, the decay vertex form factor reads $v_{L_1}^{1/2}(p)$ (or $v_{L_2}^{1/2}(q)$) for the initial (or final) state. From the point of analyticity in the s-variable, the factors $v_l^{1/2}$ introduce left-hand singularities. The position of the singularities depend on the value of the range parameter R. The customary choice is $R = 1\,\text{fm}$, and the dependence of the results on this choice is usually considered as a systematic uncertainty. However, we have to stress that these factors are meaningful only in nonrelativistic potential theory. In addition to the behavior at thresholds and at high energy, the factors are required to be smooth in the physical region. Since there is no universal recipe to parameterize these factors, we have to accept some model dependence of the results. Here, we suggest alternative models to be tested in addition to the Blatt-Weisskopf factors. In a relativistic theory, the role of the potential is played by the exchange of resonances in the crossed channel. They generate left-hand singularities in the s-variable. The naïve projection of a t-channel exchange over s-channel partial waves gives an amplitude proportional to the Legendre function of the second kind Q_l [39, 44]. The projection is given by an expression as follows.

$$\int \frac{\mathrm{d}z}{2} \frac{P_l(z)}{M^2 - t} = \frac{1}{4k^2} Q_l \left(1 + \frac{M^2}{2k^2} \right). \tag{E.15}$$

In this case the relevant scale is given by the mass of the exchanged particles. The Q_l have the same asymptotic behavior as the Blatt-Weisskopf factors. Since there is no theoretical obstruction for the form factors to over-suppress the threshold behavior away from threshold one can also consider higher order poles as a model for the left-hand cuts, as in [4]. Whatever model is used to constrain the

high-energy behavior of the amplitude, we need to ensure that the singularities generated by them are far from the physical region, and affect the asymptotic high energy behavior only.

List of Figures

List of Tables

Glossary

Breit-Wigner amplitude or parametrization is commonly used approach to describe the resonance phenomenon [26]. The general form of the amplitude reads:

$$A_{\mathrm{BW}}(s) = \frac{1}{m^2 - s - im\Gamma(s)}.$$ (16)

The forms of the Breit-Wigner amplitudes used in this thesis:

- Standard Breit-Wigner with a constant width: $\Gamma(s) = \Gamma_0$,
- Breit-Wigner with a dynamic width is used for a resonance in a system of two particles with masses m_1 and m_2 in L-wave:

$$\Gamma(s) = \Gamma_0 \frac{p(s)\, m}{p(m^2)\sqrt{s}} \frac{h_L^2(p(s)R)}{h_L^2(p(m^2)R)},$$ (17)

where $h_L(z)$ are the Blatt-Weisskopf factors introduced by Hippel and Quigg, p is a break-up momentum, $p(s) = \lambda^{1/2}(s, m_1^2, m_2^2)/(2\sqrt{s})$.
. 32, 36, 38–43, 45, 67, 75, 85, 146, 152, 153, 169, 171, 185

DT0 is a COMPASS trigger for the diffractive reactions. It is formed as a coincidence of several independent signals:

- the beam trigger provided by scintillation detectors at the beam telescope,
- the signal from the recoil proton detector
- veto signal for particles leaving the target outside acceptance of the experiment
- veto signal for beam track downstream the spectrometer in order to suppress events without interaction.

The trigger selects events where the target proton obtains a significant momentum to leave the target material and cross two rings of the RPD detector.. 21

General Isobar Model A dynamic model for the decay amplitude which present the amplitude as a sum of the several truncated series of the Partial waves in different channels. The model has very natural intuitive meaning: it looks as the sum of various cascade reactions which proceed via different intermediate states.. 30

Isobar is an intermediate state in the cascade reaction with the well defined quantum numbers, spin and parity.. 30–32, 38, 74, 78, 79, 86, 87, 124, 146, 149, 169, 170, 175

Källén function is a commonly used function,

$$\lambda(x, y, z) = x^2 + y^2 + z^2 - 2xy - 2yz - 2zx. \tag{18}$$

It enters to the expression for the break-up momenta $|\vec{p}^{\,*}|$ when a particle with mass M decays to particles with the mass m_1 and m_2.

$$|\vec{p}^{\,*}| = \frac{\lambda^{1/2}(M^2, m_1^2, m_2^2)}{2M} \tag{19}$$

Pomeron is an exchange trajectory introduced to describe the high energy pp and π^+ scattering. This quasi-particle is often referred to as a ladder of the gluonic exchanges [80]..

production Production amplitude(reaction) is an amplitude of the process (or such a process) where a considered system of particles is produced. The terminology appears in a context of unitarity where in presence of a production channel with a negligible coupling the final-state interaction can still be assumed elastic..

Acronyms

CM Center-of-Momentum. 26, 73, 162, 165–167

GJ Gottfried-Jackson. 24, 26, 27, 31, 76, 79, 80, 181

KT Khuri-Treiman. 60, 71, 182

MC Monte-Carlo. 33, 34, 50, 85, 86

PWA Partial Wave Analysis. 28, 29, 34, 35, 37, 45, 47–50, 66, 67, 74, 75, 83–87, 124, 125, 144–146, 149, 153, 169, 171, 181, 182

QCD Quantum Chromodynamics. 1, 2, 5–7, 109, 123, 128, 129, 132, 135, 142

RPD Recoil Proton Detector. 19, 21, 22, 24, 187

SDM Spin Density Matrix. 34, 35, 39, 45, 65, 146, 150, 182, 183